Universität Stuttgart

Institut für Wasser- und Umweltsystemmodellierung

Mitteilungen

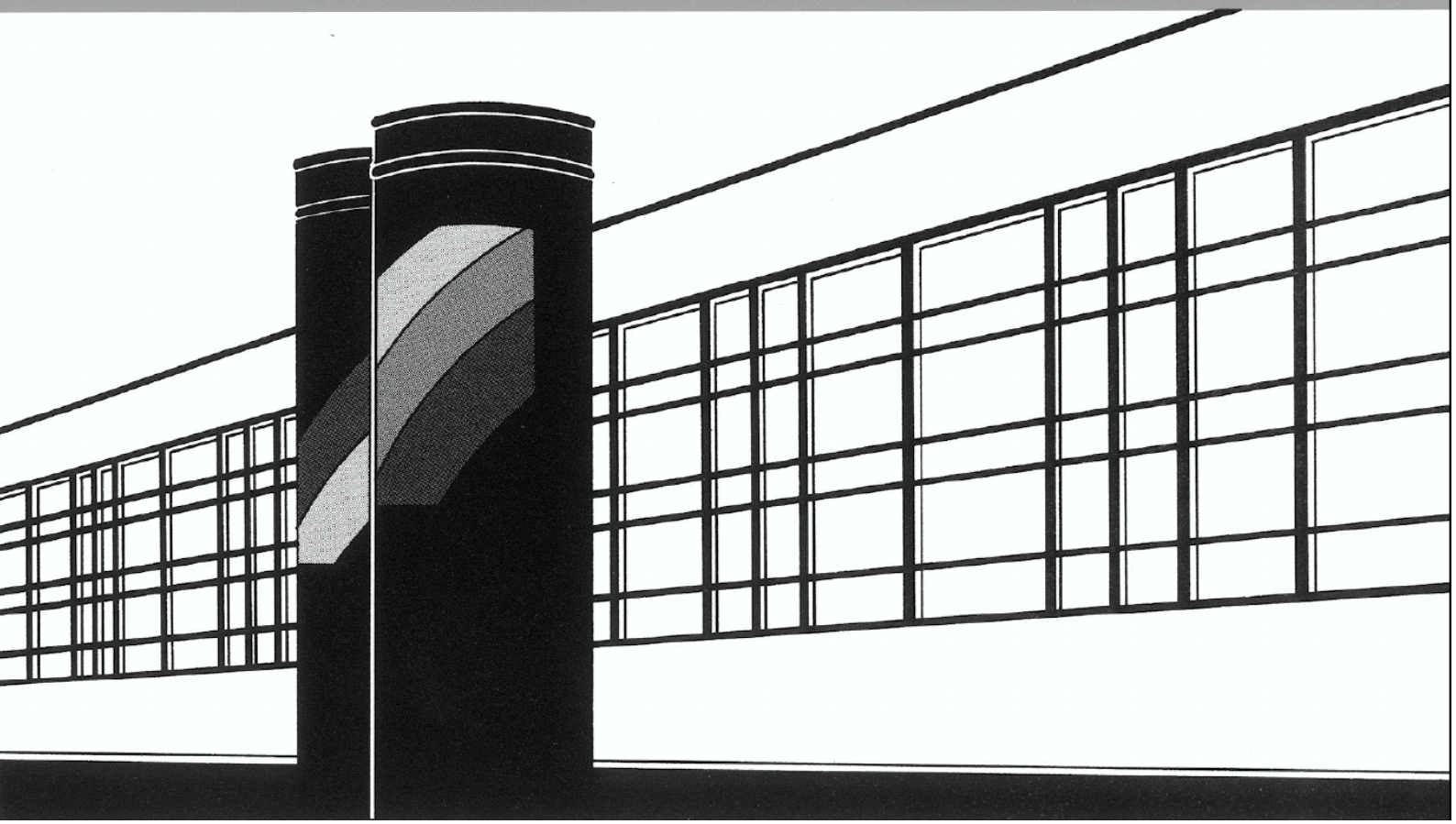

Heft 294

Daniela Pavía Santolamazza

Event-Based Flood Estimation Using a Random Forest Algorithm for the Regionalization in Small Catchments

Event-Based Flood Estimation Using a Random Forest Algorithm for the Regionalization in Small Catchments

von der Fakultät Bau- und Umweltingenieurwissenschaften der Universität Stuttgart zur Erlangung der Würde eines Doktor-Ingenieurs (Dr.-Ing.) genehmigte Abhandlung

vorgelegt von

Daniela Pavía Santolamazza

aus Barrancabermeja, Kolumbien

Hauptberichter:	Prof. Dr. rer.nat. Dr.-Ing. habil. András Bárdossy
Mitberichter:	Prof. em. Dr. Rolf Weingartner
Mitberichter:	Prof. Dr.-Ing. Henning Lebrenz M.Sc.

Tag der mündlichen Prüfung: 07. Juli 2022

Institut für Wasser- und Umweltsystemmodellierung
der Universität Stuttgart
2022

Heft 294

Event-Based Flood Estimation Using a Random Forest Algorithm for the Regionalization in Small Catchments

von
Dr.-Ing.
Daniela Pavía Santolamazza

Eigenverlag des Instituts für Wasser- und Umweltsystemmodellierung
der Universität Stuttgart

D93 Event-Based Flood Estimation Using a Random Forest Algorithm for the Regionalization in Small Catchments

Bibliografische Information der Deutschen Nationalbibliothek
Die Deutsche Nationalbibliothek verzeichnet diese Publikation in der Deutschen Nationalbibliografie; detaillierte bibliografische Daten sind im Internet über http://www.d-nb.de abrufbar

Pavía Santolamazza, Daniela:
Event-Based Flood Estimation Using a Random Forest Algorithm for the Regionalization in Small Catchments, Universität Stuttgart. - Stuttgart: Institut für Wasser- und Umweltsystemmodellierung, 2022

(Mitteilungen Institut für Wasser- und Umweltsystemmodellierung, Universität Stuttgart: H. 294)
Zugl.: Stuttgart, Univ., Diss., 2022
ISBN 978-3-942036-98-6

NE: Institut für Wasser- und Umweltsystemmodellierung <Stuttgart>: Mitteilungen

Herausgegeben 2022 vom Eigenverlag des Instituts für Wasser- und Umweltsystem-modellierung

Druck: DCC Kästl e.K., Ostfildern

Acknowledgment

"Caminante no hay camino se hace camino al andar"
Antonio Machado

I would like to start by thanking Prof. Bárdossy for his time and guidance during the past years of work. Thank you for finding time in your tight schedule for our meetings and discussions, which were key to the realization of this research. I appreciate very much your constructive criticism, the transfer of knowledge and your endless innovative ideas.

My gratitude also goes to Henning for giving me the opportunity to be part of his group. Thank you for your guidance, your suggestions and your comments. Thanks for pushing me to better represent my figures, so that I can better understand the data and critically assess them.

I would like to acknowledge the Fachhochschule Nordwestschwiez (FHNW) for the support on fulfilling this dissertation. Additionally, I would like to thank my colleagues, especially Anna, Julian and Sara, who were always ready to listen to me and motivated me to continue.

Thank you Astrid, for your help and advice with all the administration-related issues and for giving me moral support to keep going.

I want to take the opportunity to thank all the different federal institutions, cantonal offices and all other data providers. I want to express my gratitude for making the data available to me, so that this research could be carried out.

Many thanks to you Pirmin, for providing me the encouragement I needed to keep going and for your wise advises. Certainly, your patience, reviews and long discussions made me get over the finish line. Thanks for your English proofreading, which together with Annerose's and Pipe's corrections, made this document more readable, to whom I would also like to extend my sincere gratitude.

Last but not least thanks to my family and friends. Pa, Ma, Pipe and Nana thanks for listening to me in times of frustration, for the advice and encouragement. Finally, to all my friends thanks for your support and for understanding that my disappearance was only a sign of the amount of work I had to do.

Contents

List of Figures

List of Tables

List of Notations

α	Recession used for calculating API
API	Antecedent precipitation index
API^{FC}	API corresponding to a soil moisture equal to the field capacity
API^{WP}	API corresponding to a soil moisture equal to the wilting point
CN	Dimensionless Curve Number from the SCS rainfall-runoff model
CN_{eq}	Equivalent dimensionless Curve Number
$\boldsymbol{CO}$	Co-association matrix of a clustering ensemble
$D_{m,n}$	Kolmogorov-Smirnov maximum absolute distance
D_{kl}	Kullback-Leibler divergence
$D_{j,N}$	Precipitation duration with a data aggregation j and within N intervals
ε_R	Relative error
$\hat{f}(\boldsymbol{x})$	Random forest estimator
FC	Field capacity
H_R	Relative entropy
H_s	Association of precipitation triplets
H_t	Temporal precipitation entropy
I_a	Initial abstraction
K	Lin divergence
P	Accumulated precipitation depth
$p(i,j,k)$	Trivariate two state probabilities of precipitation triples exceeding a threshold
$p(i,j,k\|POT)$	Trivariate two state probabilities of triples exceeding a threshold given a POT
P_e	Effective precipitation
PVR	Peak to volume ratio
Q_p	Peak discharge
S	Potential maximum infiltration
$\bar{\boldsymbol{S}}$	Similarity matrix of a random forest ensemble
$\boldsymbol{S}$	Similarity matrix of a random forest
SW	Soil moisture
T_c	Concentration time
t_p	Time to peak
WP	Wilting point
W_n	Wilcoxon rank-sum statistic
Z_{flood}	Temperature's standard score at the occurrence of a flood
Z_W	Standarized Wilcoxon rank-sum statistic
λ	Regional constant

List of Abbreviations

AMF	Annual Maximum Flood
BWG	Bundestamt für Wasser und Geologie
CART	Classification and Regression Tree
DEM	Digital Elevation Model
DFH	Design Flood Hydrograph
EDF	Empirical distribution function
EPIC	Erosion/Productivity Impact Calculator model
FEH	Flood Estimation Handbook
FOAG	Federal Office for Agriculture
FOEN	Federal Office for the Environment
GEV	Generalized Extreme Value distribution
GPD	Generalized Pareto Distribution
GSTSP	Generalized Standard Two Sided Power distribution
HAKESCH	Hochwasser Abschätzung in Kleinen Einzugsgebieten der Schweiz
MDS	Multidimensional Scaling
ME	Mean Error
MSE	Mean Squared Error
NaN	None available Number
NSE	Nash Sutcliffe efficiency coefficient (NSE)
OOB	Out of Bag observations
PDF	Probability density function
POT	Peaks Over a Threshold
PREVAH	PREecipitation-Runoff-EVApotranspiration HRU Model
PUB	Predictions in Ungauged Basins
RF	Random Forest model
RMSE	Root Mean Squared Error
SCS	Soil Conservation Service methodology
Swisstopo	Federal office of topography
TSP	Two Sided Power distribution
WSL	Swiss Federal Institute for Forest, Snow and Landscape Research

Abstract

The hydrological cycle is a complex system, composed of multiple variables, which in most cases are not measured. This is one of the reasons why it is a challenge to have models that adequately represent the expected discharges. The Predictions in Ungauged Basins (PUB) initiative reinforces the need on having models that capture the different catchment interactions and represent various catchment processes. These models are more robust and thus can be more reliable to transfer to ungauged catchments. In recent years, the field of hydrological research has focused on understanding and explaining the different processes present in catchments. Nevertheless, few applications that include precipitation, the main responsible of runoff change, are found. Further understanding of the temporal and spatial dependence of the meteorological event triggering the floods is needed.

In this study, an analysis of the meteorological event triggering the floods was carried out. The concept of entropy was used to characterize the temporal distribution of precipitation. It was found that the precipitation temporal entropy is a better indicator of hydrograph shape than the duration or the intensity. Further, the geographical interdependence of the amount of precipitation and the temporal precipitation entropy causing the floods was described by looking at the association of stations triples. This suggested that, up until a given precipitation quantile, flood events are more likely caused by precipitation events of total coverage. However, for larger quantile values, it is observed that as the quantile increases the probability of observing joint occurrence in space decreases. The temporal distribution of precipitation events causing the floods showed to be more associated in space than the amount of precipitation triggering the floods. Nonetheless, this temporal distribution is not constant over all flood events, what can be attributed to different flood mechanisms. The antecedent precipitation index (API) was used to explain the soil moisture content. The empirical distribution of antecedent precipitation index (API) at the time of a flood was compared with empirical distributions of unconditioned API data series. For this purpose, the Wilcoxon statistic and the Kolmogorov-Smirnov distance were used to compare the empirical distributions. The results showed that the soil moisture that favor the occurrence floods is not an annual extreme, but rather a value close to the monthly maximum API. Further, it was observed that the longer memory of the catchment gives more information about the occurrence of the flood.

Additionally, in order to estimate the catchment reaction at the time of a flood, a region-

alization of the flood wave hydrographs was carried out. For this purpose, three methods of defining the similarity of the floods were considered. All three methods are based in the random forest algorithm. The novelty of this procedure was the use of a supervised random forest to describe the similarity of the flood events. The similarity matrix was obtained by calculating the joint occurrence of floods in the random forest space. To evaluate the performance, the estimations of the hydrograph peak and the time to peak were used. In all three methods, the same tendencies were observed, an overestimation of the peak and an underestimation of the time to peak. Moreover, an approach using an unsupervised random forest was compared to the supervised one. The unsupervised random forest yielded larger estimation errors.

For the estimation of the flood volume a rainfall-runoff model was modified to represent the study region. The model chosen in this study was the Erosion/Productivity Impact Calculator (EPIC). The model was calibrated to be more representative of the study region. For this purpose, the estimation errors in the space of the model parameters were studied. This allowed to find the model parameters that can better represent the study area. The values obtained were considered reasonable. For example, it is observed that the longer memory of the catchment is more representative of the study catchments, which are the same results as when analyzing the meteorological phenomenon causing the floods. Further, the values obtained for the regional constant, parameter modifying the initial abstraction of the catchment, were found to be smaller than the original ones obtained for United States catchments, which agrees with other studies in European catchments. Having the volume, only the duration is missing to denormalize the design hydrograph obtained from the random forest. For this purpose, an estimation of the duration was proposed by a simple linear regression model for which the precipitation duration and the concentration time of the catchments are considered.

Finally, a leave-one-out cross-validation of the flood estimation models showed that reasonable results of the estimation of floods in ungauged catchments, can be obtained with the models in this study. In particular, the estimation of the dimensionless flood wave hydrograph resulted in the lowest errors. Further studies should concentrate on understanding the uncertainties of the different precipitation mechanisms triggering the floods, and how the spatial association of precipitation can be described to be used as the input for the models.

Kurzfassung

Der Wasserkreislauf ist ein komplexes System, das aus zahlreichen Variablen besteht, die in den meisten Fällen nicht gemessen werden. Dies ist einer der Gründe, warum es eine Herausforderung ist, über Modelle zu verfügen, die die erwarteten Abflüsse angemessen darstellen. Die Initiative "Predictions in Ungauged Basins" (PUB) unterstreicht die Bedeutung von Modellen, die die verschiedenen Wechselwirkungen zwischen Einzugsgebieten erfassen und verschiedene Einzugsgebietsprozesse darstellen. Diese Modelle sind robust und können daher zuverlässig auf ungemessene Einzugsgebiete übertragen werden. In den letzten Jahren hat sich die hydrologische Forschung darauf konzentriert, die verschiedenen Prozesse in den jeweiligen Einzugsgebieten zu verstehen und zu erklären. Dennoch gibt es nur wenige Anwendungen, die den Niederschlag, den Hauptverantwortlichen der Abflussveränderung, einbeziehen. Ein besseres Verständnis der zeitlichen und räumlichen Abhängigkeit von dem meteorologischen Ereigniss, das die Überschwemmungen auslöst, ist erforderlich.

In dieser Studie wurde eine Analyse der meteorologischen Ereignisse, die die Überschwemmungen auslösen, durchgeführt. Das Konzept der Entropie wurde verwendet, um die zeitliche Verteilung des Niederschlags zu charakterisieren. Es wurde festgestellt, dass die zeitliche Entropie des Niederschlags ein besserer Indikator für die Form der Ganglinie ist als deren Dauer oder Intensität. Darüber hinaus wurde die geografische Abhängigkeit der Niederschlagsmenge und der zeitlichen Niederschlagsentropie, die die Überschwemmungen verursacht, anhand der Assoziation von Dreifachstationen beschrieben. Dies deutet darauf hin, dass bis zu einem bestimmten Niederschlagsquantil Überschwemmungsereignisse eher durch Niederschlagsereignisse mit vollständiger Überdeckung verursacht werden.Bei größeren Quantilwerten ist jedoch zu bemerken, dass die Wahrscheinlichkeit, ein gemeinsames Auftreten im Raum zu beobachten, mit steigendem Quantil abnimmt. Es zeigte sich, dass die zeitliche Verteilung der Niederschlagsereignisse, die zu den Überschwemmungen führten, räumlich stärker zusammenhängt als die Niederschlagsmenge, die die Überschwemmungen verursachte. Allerdings ist diese zeitliche Verteilung nicht über alle Hochwasserereignisse hinweg konstant, was auf unterschiedliche Hochwassermechanismen zurückzuführen ist. Zur Erklärung des Bodenfeuchtegehalts wurde der Vorregenindex (API) herangezogen. Die empirische Verteilung des API zum Zeitpunkt eines Hochwassers wurde mit empirischen Verteilungen von unkonditionierten API-Datenreihen verglichen. Zu diesem Zweck wurden die Wilcoxon-Statistik und der Kolmogorov-Smirnov-Abstand zum Vergleich der empirischen Verteilungen verwendet. Die Ergebnisse zeigten, dass die Bodenfeuchte, die die Über-

schwemmungen begünstigt kein jährlicher Extremwert ist, sondern ein Wert in der Nähe des monatlichen API-Maximums. Desweiteren wurde festgestellt, dass das längere Erinnerungsvermogen des Einzugsgebiets mehr Informationen über das Auftreten des Hochwassers gibt.

Um die Reaktion des Einzugsgebiets zum Zeitpunkt eines Hochwassers abschätzen zu können, wurde außerdem eine Regionalisierung der Hochwasserwellenganglinien vorgenommen. Zu diesem Zweck wurden drei Methoden zur Definition der Ähnlichkeit der Hochwasser in Betracht gezogen. Alle drei Methoden beruhen auf dem Random Forest Algorithmus. Das Neue an diesem Verfahren war die Verwendung eines supervised Random Forest zur Beschreibung der Ähnlichkeit der Hochwasserereignisse. Die Ähnlichkeitsmatrix wurde durch Berechnung des gemeinsamen Auftretens von Überschwemmungen im Random Forest Raum ermittelt. Zur Bewertung der Leistung wurden die Schätzungen des Spitzenwertes der Ganglinie und der Zeit bis zum Spitzenwert herangezogen. Bei allen drei Methoden wurden die gleichen Tendenzen beobachtet, nämlich eine Überschätzung der Spitze und eine Unterschätzung der Zeit bis zur Spitze. Darüber hinaus wurde ein Ansatz, der einen unsupervised Random Forest verwendet, mit dem supervised Ansatz verglichen. Der unsupervised Random Forest führte zu größeren Schätzfehlern.

Für die Abschätzung des Hochwasservolumens wurde ein Niederschlags-Abfluss-Modell modifiziert, um die Untersuchungsregion abzubilden. Das in dieser Studie gewählte Modell war der Erosion/Productivity Impact Calculator (EPIC). Das Modell wurde kalibriert, um für die Untersuchungsregion repräsentativer zu sein. Zu diesem Zweck wurden die Schätzungsfehler im Raum der Modellparameter untersucht. Auf diese Weise konnten die Modellparameter ermittelt werden, die das Untersuchungsgebiet besser repräsentieren können. Die ermittelten Werte wurden als angemessen angesehen. So ist beispielsweise festzustellen, dass das längere Erinnerungsvermogen des Einzugsgebiets für die untersuchten Einzugsgebiete repräsentativer ist, was den gleichen Ergebnissen entspricht wie bei der Analyse der meteorologischen Phänomene, die die Überschwemmungen verursachen. Die Werte für die regionale Konstante, die die anfängliche Entnahme des Einzugsgebiets modifiziert, sind kleiner als die ursprünglichen Werte für die Einzugsgebiete in den Vereinigten Staaten, was mit anderen Studien in europäischen Einzugsgebieten übereinstimmt. Nachdem das Volumen bekannt ist, fehlt nur noch die Dauer, um die aus dem Random Forest erhaltene Bemessungsganglinie zu denormalisieren. Zu diesem Zweck wurde eine Schätzung der Dauer durch ein einfaches lineares Regressionsmodell vorgeschlagen, bei dem die Niederschlagsdauer und die Konzentrationszeit der Einzugsgebiete berücksichtigt werden.

Schließlich zeigte eine Kreuzvalidierung, dass mit den vorgeschlagenen Modellen vernünftige Ergebnisse für die Schätzung von Hochwasser in unbeobachten Einzugsgebieten erzielt werden können. Insbesondere die Schätzung der dimensionslosen Hochwasserwellenganglinie führte zu den geringsten Fehlern. Weitere Studien sollten sich darauf konzentrieren, die Unsicherheiten der verschiedenen Niederschlagsmechanismen zu verstehen, die die Hochwässer auslösen, und darauf wie der räumliche Zusammenhang der Niederschläge beschrieben werden kann, um als Input für die Modelle zu dienen.

Chapter 1

Introduction

Around 2 billion Euros is the estimated financial damage of the floods, which took place in August 2005 at the northern part of Switzerland, according to Hilker et al. (2009). These flood events are identified as the most expensive over the past 100 years. The estimation of floods is an important economical and development planning tool, to prevent life losses and damages of infrastructure. Floods are complex processes derived from catchment responses to various meteorological inputs. Commonly summarized under one distribution function, representing the cumulative effect of all triggering events (Merz and Blöschl, 2009), although they are caused by different climatic conditions and have a different probability of occurrence. Hydrologists are challenged to estimate extreme discharges from catchments with data of relatively poor temporal and spatial resolution. Typically, the estimation of a small rapidly reacting catchment, whose flood peak takes place on a sub daily time scale, is made by means of daily records. Additionally, the characteristics of these catchments are often represented with coarse areal data, given that no other information is available (BWG, 2003).

Flood estimation methods can be roughly divided into those which purely relay on discharge measurements and those which use precipitation to estimate a runoff. For the case of the discharge measurements methods, their records must be long enough, so that they can represent the larger extremes. These long records are scarce, especially if a high temporal resolution is needed and the focus is on small catchments. Furthermore, if the objective is to account for the variability of different flood mechanisms, a classification of the extreme discharges into processes is required. This results in either having to accept lesser extremes for the estimations or using reduced records per considered flood mechanism, thus affecting the capability of estimating the floods with extreme value theory.

To overcome the lack of long series of discharge measurements, one can use the meteorological forcing to estimate flood volumes and describe the expected catchment reactions. Using precipitation has the advantage that the measurements are normally longer and that they have a denser spatial coverage. Where no discharge observations are present, a rainfall-

runoff model can be considered to estimate floods with different probabilities of occurrences. Over the past years hydrologists have spent time understanding the physical processes that generate different types of floods (Merz and Blöschl, 2003; Blume et al., 2007; Blöschl et al., 2013; Bárdossy and Filiz, 2005; Tarasova et al., 2019; Sikorska et al., 2015; Brunner et al., 2018d). Considering the occurrence of floods due to different factors and seasonal variability for flood classifications and estimation, either by means of a frequency analysis or a rainfall-runoff model, has increased and awakened the interest of the water community. However, there is still research potential to transfer the understanding of flooding mechanisms into the models and thus obtain better estimates. Especially considering that in each country the information available to develop the models is different, but also that the climate on the earth's surface has great spatial and temporal variability.

1.1 Motivation and Objectives

The focus of this study is to estimate floods in small catchments, making use of measurements with high temporal resolutions. The Northwestern Switzerland is chosen as the study area, region recurrently flooded over the past years. The emphasis will be specifically on small watersheds, exploring the added value of measurements with higher temporal and spatial resolution. Floods are known to be more diverse in small catchments than in lager catchments. Discharges in small catchments rapidly vary as a response to precipitation event, whereas larger catchments have slower reactions as the result of the aggregation of the reactions from smaller catchments that make them up (MacDonald and Fraser, 2014). Given the scarcity of discharge measurements, with long records of high temporal resolution, a rainfall runoff approach is preferred to profit from the length of precipitation records and its spatial coverage. In practice, engineering offices in Switzerland estimate floods in ungauged basins typically using the software *Hochwasser Abschätzung in Kleinen Einzugsgebieten der Schweiz (HAKESCH)*. It includes methods that estimate floods based on a selected critical precipitation event and some catchment characteristics (BWG, 2003). However, these methods merely estimate the peak discharge and do not consider other characteristics of the flood event as its volume, duration or hydrograph shape, which are crucial characteristics to estimate the storage capacity of the hydraulic structures (Gaál et al., 2015).

The main objective of this study is to regionalize the catchment reactions, considering the variability of the meteorological forcing causing the floods, which should be able to differentiate between various flood mechanisms. This has been an increasing area of research over the past years. Nevertheless, only approaches based on frequency analysis of discharge measurements were found in the study area, but none that considers rainfall-runoff methods. The idea is to regionalize not only the peak discharge or volume, but also the possible hydrograph shape. As the regionalization model a Random Forest (RF) algorithm is chosen, to evaluate the similarity of the catchment reactions at the occurrence of a flood and select the hydrographs donors for the estimation at the ungauged catchment. An analysis of the static catchment descriptors and the meteorological forcing responsible for different flood

mechanisms is carried out, to identify possible model predictors to use in the RF.

The estimation of flood volumes is done by means of an event based rainfall-runoff model. This model includes possible changes in the input (precipitation and soil water content), due to seasonal changes in the meteorological conditions. By combining both the rainfall-runoff model and the RF regionalization model, the estimation of floods in ungauged catchments is possible.

1.2 Outline

The work presented here is organized in the following way. Chapter 2 presents a theoretical background on flood estimations with a specific focus to the state of art in Switzerland. The study area and catchment descriptors are introduced in Chapter 3, with an overview of the discharge, meteorological and areal data available. In Chapter 4 the selection of the critical events, i.e. floods, and the method used for the separation of the hydrograph waves are explained. The focus on Chapter 5 is on the meteorological events causing the floods. An analysis of the temporal and spatial variability of precipitation is included, the antecedent precipitation index as an indicator of soil moisture triggering a flood is explored and the use of temperature measurements for the inclusion of snow melt is studied. In Chapter 6 a regionalization framework using a random forest algorithm to define the similarities of floods and its potential for flood estimation in ungauged catchments is investigated. A supervised approach is compared to an unsupervised one. In Chapter 7 an existing rainfall-runoff model is modified, to account for the catchment's characteristics of the study area and the seasonality of the meteorological forcing. This rainfall-runoff model is used in Chapter 8 with critical meteorological events and, together with the random forest model, a validation of the models for the estimation of floods in ungauged catchments is carried out. Finally, Chapter 9 gathers the main findings of this study and summarizes possible applications and potential research areas.

Chapter 2

Theoretical Background

In literature different methods for estimating floods in gauged and ungauged catchments can be found. These approaches can be roughly divided into two groups: those purely based on discharge measurements and those that use precipitation data together with a rainfall-runoff model for estimating the floods. No matter what type of model is used, for the estimation of floods in ungauged catchments, regionalization methods are required to transfer estimates from gauged catchments. This chapter gives a brief review of the estimation of floods in small catchments and points out some of its challenges, accounted to the more dynamic reaction of small catchments and the fact that various flood mechanisms might take place.

2.1 Estimation of Extreme Discharges

The estimation of runoff is not an easy task, given the great heterogeneity found in the catchments, such as different soil types, slopes, land use, vegetation, etc. In addition, the direct drivers of runoff change, such as precipitation and temperature, show great spatial and temporal variability (Sivapalan, 2003). Regardless of the type of model used, runoff estimates are associated with large uncertainties, which make the task of the estimation a difficult one (He et al., 2011). Hydrologists are faced with developing models with the available data, in order to describe the probability of occurrence of a given extreme discharge. For this purpose, two types of models are used, those which use only discharge observations and those that make use of the rainfall-runoff relationship to estimate the possible response of the catchment. Regardless of the model chosen for the estimation of the extremes, when the interest is to estimate ungauged catchments, a transfer of information from observed to ungauged catchments must take place. This poses an additional challenge, commonly solved with the so called regionalization models. This section gives an overview of the approaches typically used for estimating extreme discharge and the subsequent section will look at the regionalization models.

2.1.1 Frequency Analysis of Discharge Series

Flood frequency analysis methods use merely discharge measurements to describe the relationship between the flood peak and a given probability of occurrence Chow et al. (1988). Different probability distributions can be used. Typically, the Generalized Extreme Value (GEV) distribution or the Generalized Pareto Distribution (GPD) are considered. The choice of one or the other depends on which type of discharges are selected as extremes (Fischer, 2018). The parameters of the distribution are estimated using the discharge observations of the studied catchment.

The use of extreme value theory comes with the assumption that the data are independent and identically distributed (Rao and Hamed, 2000). This leads to the representation of different processes and different scales as a single independent identical distributed random variable (Klemeš, 2000). Additionally, extreme value theory presumes a stationary process. This means that there are no variations within the observation period (Coles, 2001), further no variations in the estimation period are expected. Yet, it is known that climate is not stationary, nor are land use and other parameters that influence runoff generation (Klemeš, 2000; Sivapalan et al., 2005). It is also assumed that the length of the observations is sufficient to estimate events larger as the observed ones. However, when the objective is to extrapolate to estimate a discharge with a return period greater as the observed period, one is faced with the problem of determining the extrapolated larger tail of the distribution by the behavior of the observations defining the lower tail of the distribution (Klemeš, 2000). Additionally, this analysis normally concentrates on the estimation of the peak discharge, leaving behind other important parameters of the hydrograph, which are crucial to estimate the storage capacity of the hydraulic structures (Gaál et al., 2015).

To overcome some of these limitations, separate frequency analysis approaches are developed to account for different event types and seasonality, furthermore multivariate approaches to estimate the peak and volume can be found. For example, Fischer et al. (2016) considered a seasonal mixed model, to account for the variability of flood mechanisms over the year, by separating the time series in seasons. Another approach, applied to catchments in Switzerland, is the identification of similar reactivity regions, which are used to estimate different catchment reactions, through an index method (Brunner et al., 2018b).

These methods often fall back on the need to include smaller events to have satisfactory amounts of data. In doing so, the smaller extremes are the events that determine the behavior of the larger events. As already identified by some authors, the record length is a strong source of uncertainty, when constructing synthetic design hydrographs though a frequency analysis of floods (Brunner et al., 2018c). Even if one subdivides the events to separate different flood mechanisms, and thus obtain subsamples that are more homogeneous (Fischer et al., 2016), the question about the validity of the extrapolation beyond the observation domain remains, as does the problem of whether a stationary process is present.

The estimation of floods by means of a rainfall-runoff model has benefits over the fre-

quency analysis but it also faces some drawbacks. One of the main advantages is the use of precipitation records, which in most countries have a greater spatial coverage and larger observation periods. In the following section the advantages and disadvantages are going to be discussed.

2.1.2 Rainfall-Runoff Models

As previously mentioned, the use of a rainfall-runoff model is an alternative to the frequency analysis of discharge methods. For this purpose, the understanding of the hydrological processes is used to describe the catchment reaction, assuming the model structure beforehand (Blöschl et al., 2013). When searching for rainfall-runoff models a large amount can be found. There are simple models, and more complex ones depending on the quantity of data used to characterize the catchment, the parameters of the meteorological forcing and the model structure.

There are different classifications of the rainfall-runoff models. According to the model approach, they can be grouped in event-based models or continuous simulations models (BWG, 2003). Event-based models use single meteorological events to describe the runoff. For this purpose, normally the precipitation and the soil moisture condition previous to the occurrences of a flood are used (Kjeldsen, 2007). These models are widely used, given the ease of obtaining estimates of the probabilities of occurrence of precipitation (Grimaldi et al., 2012; Blöschl et al., 2013). On the other hand, continuous simulation models estimate the catchment reactions within dry and wet periods (Patil, 2008). These models are not concentrated on isolated precipitation events as the previous ones, rather long series of observed or synthetic records are used to model the catchment reaction. The extreme discharges can then be extracted from the resulting discharge series, to determine the occurrences of floods (Grimaldi et al., 2012). These models are more complex and normally require a calibration with observed discharges.

Additionally, rainfall-runoff models can be classified according to their model structure. In this document, the classification from Wagener et al. (2004) is adopted, who uses three classes the metric, parametric and mechanistic models. The metric models, also recognized as empirical or black box models, are analytical models based purely on observations of the input and output of a catchment (Beven, 2012). They consider only the information obtained from the data and do not consider any physical knowledge of the hydrological cycle (Wagener et al., 2004). The parametric models, also known as conceptual models, use the concept of storage and removal from water contained in *buckets* to represent the main hydrological process (Wagener et al., 2004). The mechanistic models, or physically based models, are based on the physics of the underlying hydrological process (Beven, 2012). However, these models do not represent the totality of the physical processes, given the complexity of the hydrological cycle (He et al., 2011).

Rainfall-runoff models have different applications, one of those is to extrapolate to un-

observed extremes. In this case, the use of an empirical model purely based on data, can question the robustness of the model. If there is no confidence that the models properly represent the hydrological processes on the observed period, the uncertainty that it can represent future scenarios is large. Nevertheless, through a validation of the transferred physical relationships, one could establish if the model behaves in a reasonable manner (Patil, 2008). It can also suggest areas where there is a lack of theoretical understanding (Beven, 2012). For the case of using a conceptual model, the difficulty comes with the need of the calibration of the model parameters, which is done with observations that are not available for the case of ungauged catchment (He et al., 2011). Furthermore, it has not been demonstrated yet that the use of complex physically based models achieves a much better performances than simpler models (Beven, 2012).

A large variety of rainfall-runoff models are used in literature. There is no single model that outperforms the rest. Due to the complexity of the hydrological process and the uncertainties present in the observations themselves, some models are better for the estimation of water balance, others for the estimation of low flows and others for the estimations of floods. Regarding the size of the catchment and its characteristics different performances can also be observed. Here, merely some considerations relevant in the context of this study are included. For other examples and applications, the reader can refer to Wagener et al. (2004); Beven (2012).

In Switzerland, the PREecipitation-Runoff-EVApotranspiration HRU Model (PREVAH) model has been developed as a continuous parametric model, to simulate runoff in mountain environments (Viviroli et al., 2009b). The term HRU stands for hydrological response units, which are clusters of similar hydrological response (Viviroli et al., 2009c). As recognized by Viviroli et al. (2009b), one of the main limitations is the estimation in small catchments ($<$10 km^2). Additionally, there are software tools as HAKESCH, which integrate the use of different rainfall-runoff models for the estimation of floods in small ungauged catchments. There has been no update of this methods, to include observations of new catchments, at least none known by the author. Apart from HAKESCH, no event-based rainfall-runoff model approach was found for the estimation of floods in small catchments.

When it comes to the estimation of floods by means of a rainfall-runoff model, Blöschl et al. (2013) give a good summary of the main advantages and disadvantages of the different approaches. The authors recognize on the one side the benefit of using precipitation records, which are normally longer and denser than discharge measurements. Additionally, the authors highlight that these models can represent different catchment processes due to their nature. This has the advantage that the extrapolation to estimate the extremer discharges to unobserved periods is more reliable. However, when it comes to the estimation of the rainfall-runoff model parameters in ungauged catchments, there are many uncertainties involved, especially when using complex models. In this study, the Erosion/Productivity Impact Calculator (EPIC) is considered, looking for a simple event-based approach to estimate the runoff process. Therefore, a basic description of this model is given in the following section.

One disadvantage of using a rainfall-runoff model is that the frequency distribution of the floods is not directly obtained. An estimate of the severity of the floods is key to develop the flood management plan, design flood protection structures and identify risk zones (Winter et al., 2019). This problem can be solved using derived distribution methods, which allow to relate the frequency of the floods by combining a precipitation model with a runoff generation model (Gottschalk and Weingartner, 1998). The derived distributions methods involve three main steps (Sivapalan et al., 2005): (1) A statistical model of the meteorological event triggering the floods. This model determines the rainfall responsible of the floods, which can either be obtained by means of a design rainfall event, described by an intensity duration curve, or through a stochastic rainfall model, where an ensemble of precipitation events is generated (Blöschl et al., 2013). It can also include an estimation of the catchment soil moisture and other important model inputs. (2) A rainfall-runoff model to translate the meteorological event in runoff volume by means of the characteristics of the catchment. (3) Finally, a method to connect (1) and (2) is included.

2.1.3 EPIC Model

The Erosion/Productivity Impact Calculator (EPIC) is a modification of the Soil Conservation Service (SCS) model to account for changes in soil water content and differentiate the catchment slope when calculating the runoff (Shaperly and Williams, 1990). It is based on the following water balance equations (Singh and Mishra, 2003)

$$P = I_a + F + Q\,, \tag{2.1}$$

$$\frac{Q}{P - I_a} = \frac{F}{S}\,, \tag{2.2}$$

$$I_a = \lambda S\,, \tag{2.3}$$

where P is the precipitation sum, I_a the initial abstraction, F cumulative infiltration excluding I_a, Q is the runoff volume, λ a regional constant dependent on geology and climate factors and S the potential maximum infiltration. A combination of these 3 equations leads to the popular SCS model

$$Q = \begin{cases} \frac{(P-I_a)^2}{P-I_a+S} & P > I_a \\ 0.0 & P \leq I_a \end{cases}\,, \tag{2.4}$$

where, given the case that the precipitation is smaller as the initial abstraction, no runoff is generated.

The potential retention S is expressed as a function of the dimensionless curve number CN. According to the soil type, land use and vegetation cover, CN assumes values from 0 to 100 depending on soil moisture, soil type and land use (Singh and Mishra, 2003). There are different tables in literature, where the values of CN can be found according to the characteristics of the soil. The value of CN found in the tables, typically represents the average soil moisture condition CN_2. However, depending on soil moisture conditions previous to the occurrence of the flood event, CN_2 should be corrected to have CN_1 or CN_3, representative of drier or wetter soil conditions respectively. Further, CN_1 and CN_3 can be estimated from the tables of the SCS model or with the following equations:

$$CN_1 = CN_2 - \frac{20(100 - CN_2)}{100 - CN_2 + \mathrm{e}^{2.533 - 0.0636(100 - CN_2)}}\,, \tag{2.5}$$

$$CN_3 = CN_2\, \mathrm{e}^{0.00673(100 - CN_2)}\,. \tag{2.6}$$

A modification of the EPIC model is the inclusion of the catchment slope for a correction of the abstraction parameter, by adjusting CN_2, the average soil moisture condition, as

$$CN_{2s} = \frac{1}{3}(CN_3 - CN_2)(1 - 2\mathrm{e}^{-13.86s}) + CN_2\,, \tag{2.7}$$

where CN_{2s} is the slope adjusted CN value of the SCS model, s is the mean catchment slope and CN_2 and CN_3 are the CN table numbers of the SCS model.

The potential maximum retention S of the catchment is a function of the soil and land use properties and the actual soil moisture. It is defined in the EPIC model as

$$S = S_1 \left(1 - \frac{FFC}{FFC + \mathrm{e}^{(w_1 - w_2 FFC)}}\right)\,, \tag{2.8}$$

with

$$FFC = \frac{SW - WP}{FC - WP}\,, \tag{2.9}$$

where FFC is the fraction of field capacity, SW the soil water content, WP the wilting point, FC the field capacity and S_1 is the retention parameter corresponding to CN_1. The coefficients w_1 and w_2 are shape parameters obtained by solving Eq. 2.8. For this purpose, it is assumed that $S = S_2$ when $FFC = 0.5$ and $S = S_3$ when $FFC = 1$ and having that S_1, S_2 and S_3 are the retention parameters corresponding to CN_1, CN_2 and CN_3 respectively. When solving as explained, the following relations are obtained

$$w_1 = \ln\left(\frac{1}{1-\frac{S_3}{S_2}} - 1\right) + w_2\,, \tag{2.10}$$

$$w_2 = 2\left(\ln\left(\frac{0.5}{1-\frac{S2}{S1}} - 0.5\right) - \ln\left(\frac{1}{1-\frac{S3}{S1}} - 1\right)\right)\,. \tag{2.11}$$

To compute S_1, S_2 and S_3 the following relationship with the dimensionless curve number of the SCS can be used,

$$S_x = \frac{25400}{CN_x} - 254\,, \tag{2.12}$$

where x corresponds to the curve number considered. Additionally, if information about the distribution of water content over the root zone is available the EPIC model includes a modification to account for the variation of soil moisture within the soil depth (Shaperly and Williams, 1990). Nevertheless, in this study it is considered to be uniform.

Regardless of the model used for the estimation in an ungauged catchment it is necessary to have a function that can transfer the knowledge from observed to ungauged catchments. On the following section, an overview of regionalization approaches is going to be given.

2.2 Regionalization to the Ungauged Catchment

As pointed out by Beven (2012) the regionalization problem in hydrology is known to be the challenge modelers constantly face: to estimate runoff in ungauged catchments. In literature, there is a plethora of regionalization methods addressed to resolve this problem. In this section, an overview of some of these methods is given, mentioning those considered important in the context of this study. For this purpose, the general classification by He et al. (2011) is adopted. The authors divide the regression methods into regression-based and distance-based.

2.2.1 Regression-Based Regionalization Methods

The regression-based approach is built on the use of regional transfer functions to transfer model parameters from observed to ungauged catchments. Its fundamental base lies on the assumption that catchments in homogeneous regions react similar and, therefore, the relationships between model parameters and hydrological characteristics are consistent (Patil,

2008). The linear regression is the transfer function most commonly used in hydrological applications (He et al., 2011). Although, it is known that the relationships between model parameters and hydrological characteristics are not linear, they are approximated by a linear model (Blöschl et al., 2013). In some cases, the variables are transformed to reduce the correlation between them and/or to satisfy linear models, typically a logarithmic transformation or dimensionality reduction methods are used. Generally, a multilinear regression model is fitted to the data, by means of statistical fitting techniques, which identify independent variables that have a significant contribution to explain the dependent variables (Beven, 2012).

Viviroli et al. (2009a) used a linear model as one of the regionalization approaches, to estimate discharge hydrographs in Swiss mesoscale catchments, using the continuous rainfall-runoff model PREVAH. The linear model is not the only one that has been used for the estimation of runoff in ungauged catchments. Other regressions structures have been applied to find a functional approximation between model parameters and hydrological characteristics. In Switzerland, Brunner et al. (2018a) used tree-based techniques to regionalize design flood estimates and unit hydrographs. However, this approach is based on flood frequency analysis and not in a rainfall-runoff model, which is the objective of this study. Additionally, nonlinear methods have been applied to other study areas. For example, artificial neural networks have been applied in the UK, Germany and other countries (Shu and Ouarda, 2007; Patil, 2008; Blöschl et al., 2013; Wagener et al., 2004).

The regression technique is strictly statistical, it finds correlations between the hydrological characteristics and the catchment response. However, it is not easy to deduce whether they are physically correct, e.g. catchments with steeper slopes resulting in faster runoff generation (Blöschl et al., 2013; Beven, 2012). There are approaches in which the model parameters are modified and with the obtained results it is possible to analyze whether the model behaves as expected, such as that applied in Patil (2008).

Although regression methods assume there is a regional similarity of the catchments included in the regression, this similarity is not measured, nor used for the regionalization itself. On the contrary, distance-based methods do include the similarity in the regionalization, as is explained in the following section.

2.2.2 Distance-Based Regionalization Methods

Distance-based regionalization methods are based on the idea of similarity. The idea behind it, is to find donor catchments that allow the transfer of estimates to ungauged catchments. Thus, catchments most similar to the interest location are chosen for the estimation of the ungauged location (Merz and Blöschl, 2005). The difficulty is that the similarity of the catchments can be defined in multiple ways (Beven, 2012).

The must simple way of defining similarity is through geographical distance. The logic

behind this metric is that catchments that are close to each other will have comparable runoff regimes since climate and catchment conditions will only change gradually in space (Merz and Blöschl, 2004). Geo-statistical models are more advanced approaches to describe the spatial dependance of a variable by means of a variogram, which is not purely based on the geographical distance (Lebrenz and Bárdossy, 2017). In Swiss catchments Kriging has been applied in regionalization approaches (Viviroli et al., 2009a; Brunner et al., 2018a).

Yet, catchments that are close to each other in geographical space, have been observed to have different hydrological reactions and catchments further apart can exhibit similar catchment response to a given meteorological input (Beven, 2012; Merz and Blöschl, 2005). Alternative approaches for measuring the similarity of the catchments have been explored in hydrology to conform the group of donors. They are based on the hydrological closeness of the catchments rather than on the geographical closeness. For example, in the Flood Estimation Handbook (FEH) a pooling group is used. The catchments belonging to this pooling group, to be used as donors are identified with a distance measured based on an optimal combination of catchment descriptors, which are for example the catchment area, the annual average rainfall, etc. These optimal descriptors are identify using a linear regression approach (Kjeldsen et al., 2008).

In general, these approaches start with the definition of a distance measure to evaluate the similarity of the catchments (Merz and Blöschl, 2005). There are many applications, and they mainly differ in the manner the similarity is defined. For the case of Switzerland, for example Brunner et al. (2018a) used three regionalization methods based on the hydrological similarity of the catchments: (1) six defined catchment characteristics known to be hydrologically meaningful, (2) a random set of characteristics that minimizes the Hosking and Wallis homogeneity statistic and (3) catchment characteristics obtained through canonical correlation analysis. Other approaches for delineating the catchments donors' space are those applied by Shu and Burn (2004) to UK catchments, who used genetic algorithms or fuzzy rules based systems.

However, as it was the case of the regression-based approaches, it is important to determine if the catchments groups agree with the hydrological reasoning or if they are the result of the model used (Blöschl et al., 2013). There are less applications found that consider the dynamic trigger of the floods. As highlighted by Merz and Blöschl (2005), the dynamic input is responsible for the different flood processes and its inclusion should lead to more reliable regionalization approaches.

Chapter 3

Study Area and Static Catchment Descriptors

The focus of this research is to understand flood mechanisms in Northwestern Switzerland, with the aim of deriving a model to estimate floods. The model should capture the complexity of the system and it should be transferable to ungauged catchments. This chapter provides an overview of the study area and the data available for describing the catchments. Specifically, parameters considered as the static input of the system are addressed, those, which do not change on the short term and are, therefore, not event specific. The parameters that change according to the flood event, which represent the dynamic input of the model, will be included in the other chapters.

3.1 Study Area and Database

The study area of this research is the Northwestern Switzerland. Catchments with areas ranging between 0.5 km^2 and 200 km^2 are considered, to have enough data for regionalization purposes. Figure 3.1 gives an overview of the study area and the researched catchments. The catchments are delineated using the 2 meters resolution Digital Elevation Model (DEM) of the Federal office of topography (Swisstopo). Since some of the catchments overlay each other, for matters of visualization in the bottom panel of Fig. 3.1 the catchments are represented as a circle positioned at its centroid. The size of this circles indicates the catchment size. This type of visualization will be chosen in this study to represent spatial results.

For this study, data from different owners were collected. Specific focus is put on obtaining discharge and precipitation data with the highest available temporal resolution. This type of measurements can be collected by various state agencies and municipalities of Switzerland or by private operators. The length of discharge records with a high temporal resolution (10

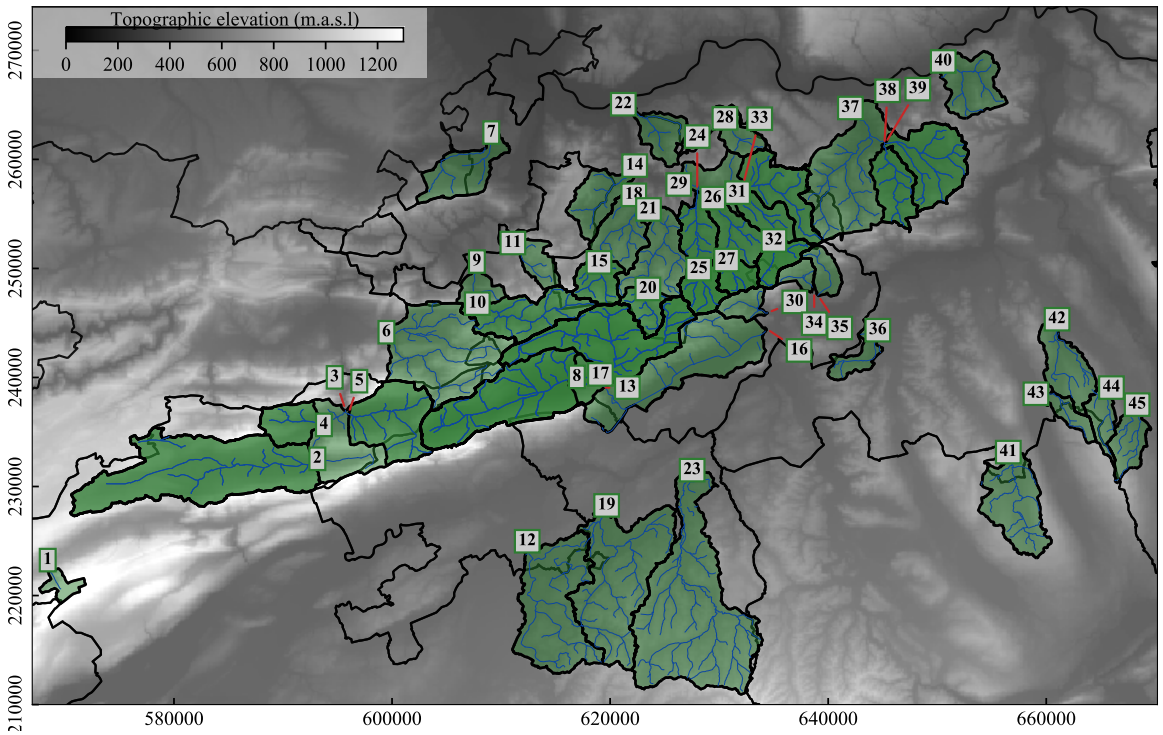

(a)

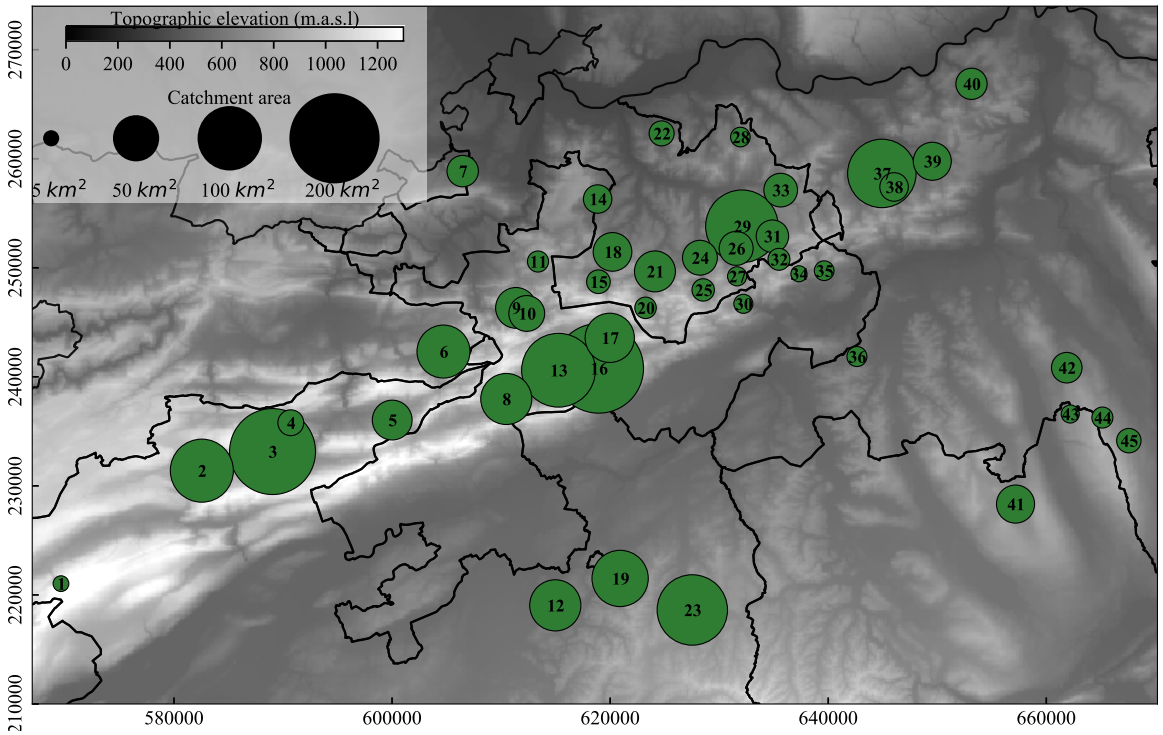

(b)

Figure 3.1: Study area and measured catchments with areas smaller than 200 km^2. For visualizations reasons the catchments will be represented throughout this study as in (b) where circles are plotted on the catchment centroid and its size is representative of the catchment area.

minutes or 15 minutes) found in the study area variate from a couple of years to 44 years. As stated by Tarasova et al. (2019), the value of an application that includes different causation of catchment reactions decreases if the length of the records is short. Therefore, in this study only catchments with at least 7 years of records are included (these are the ones included in Fig. 3.1). A number of 7 years is chosen as a tradeoff to achieve an acceptable spatial coverage with representative records length. For the selected study catchments, the mean records length is 23 years with a standard deviation of 12 years.

The precipitation stations in the study area also showed a high variability in record lengths. Figure 3.2 shows the precipitation stations available in the study area with measurements every 10 minutes. The different markers are used for indicating the number of years with records. The blue, red and yellow markers represent stations with at least 1, 5 and 10 years of measurements respectively. As demonstrated Fig. 3.2 the number of stations measuring with a sub-hourly temporal resolution has increased over the past years. The stations for this study are selected as a tradeoff between (1) reducing the distance of the precipitation station to the catchment centroid, (2) maximizing the length of 10 minutes precipitation measurements and (3) having long precipitation records to represent a given number of floods per catchment.

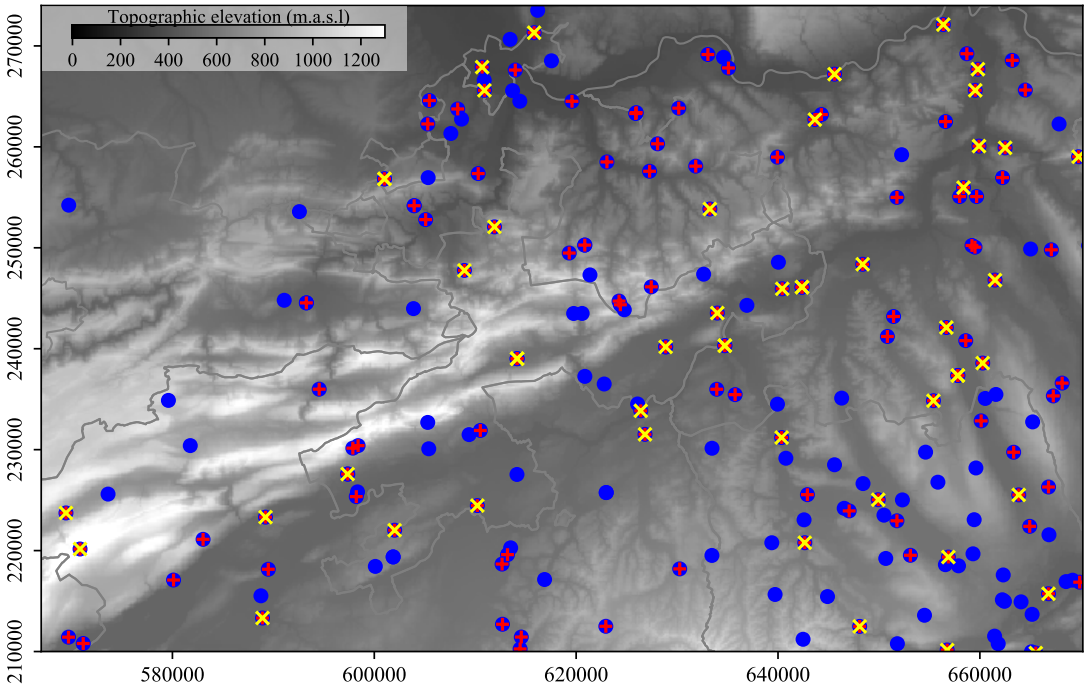

Figure 3.2: Precipitation stations on study area with measurements every 10 minutes. The different colors give the records length. Blue markers for > 1 year, red marker for > 5 years and yellow marker for > 10 years.

A screening of the stations was done according to the observed quality of the data. The quality of the data is assessed by looking first at the number of None available Number

(NaN), thus, dropping stations with a high content of NaNs. Special care must be taken when looking for outliers, in order to ensure the value is an outlier and not an observed extreme, as the focus of the research is on extreme events. Outliers are considered non-physical values, for example temperature exceeding 50°or below -40°, which are not plausible in the study area. An overview, of the type of measurements for discharge, precipitation and temperature used in this study, is given in Tab. A.1, with the corresponding resolutions and data providers.

3.2 Static System Input: Long-Term Catchment Descriptors

In this section the long-term catchment descriptors considered in this study are introduced. These are the catchment parameters that do not change in short time scales or if they do, the change is so small that it can be neglected. They are also recognized in other studies as the catchment controls. Long-term catchment descriptors are indicators of the spatial variability of the events and can be helpful to determine existing runoff trends (Merz and Blöschl, 2009). In this study, the catchment descriptors are divided in two groups: catchment characteristics and climatic factors.

3.2.1 Catchment Characteristics

Catchment characteristics are those indicators of the properties of a catchment, as the geometry, formation, geology, land use, aquifer formation, etc. A summary of the characteristics of each catchment is given in Tab. A.2, with information about the measured river and data owner. A brief explanation of the catchment characteristics is included in the following.

Geometry

The area of a catchment is one of the most important parameters when determining the water balance, given that it gives the extents to quantify the runoff volume. Among with the area, the perimeter of a catchment and some shape indices are typically used for describing expected hydrological signatures (Bárdossy and Schmidt, 2002).

In Fig. 3.3 a scatter plot of the areas versus the form factor is given. The form factor is calculated as $F = A/L^2$, where F is the form factor, A the catchment area and L the catchment length. A value of F close to 0 represents an elongated narrow catchment, that can have a different hydrological regime as a more irregular catchment (Horton, 1932). It can be observed in Fig. 3.3 that there is no constant shape for a given catchment area. This variability can have an influence on the respond of a catchment to a given precipitation.

Other shape indices used in this study can be found in Tab. A.2.

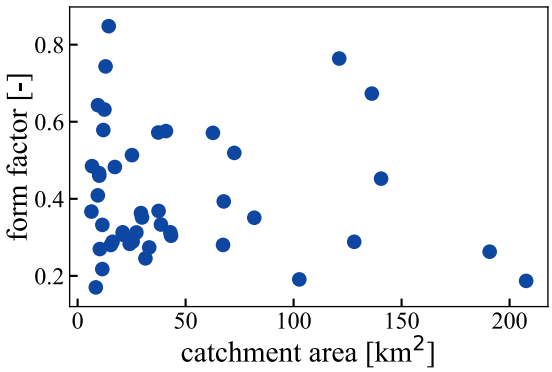

Figure 3.3: Catchment area versus form factor.

Topographic Characteristics

Topography is an indirect indicator of changes in the runoff generation processes. For instance, steeper slopes have an accelerated effect, resulting in rapid runoff building (Weingartner et al., 2003; Blöschl et al., 2013). Different altitudes can have effects on snow and rainfall, given that rainfall and snow cover tend to increase with the elevation (Merz and Blöschl, 2009). The mean and standard deviation of the slopes and elevations are chosen for describing the topography of the catchments. To calculate them, the same DEM from Swisstopo mentioned before is used.

The values of the topographic characteristics can be found in Tab. A.2. As an example, in Fig. 3.4 the standard deviations of the elevations of the catchments are plotted in space. It can be observed that the catchments located on the west of the Jura Mountains (left in Fig. 3.4) have a larger difference in elevations than those catchments on the east part of the Jura (right in Fig. 3.4).

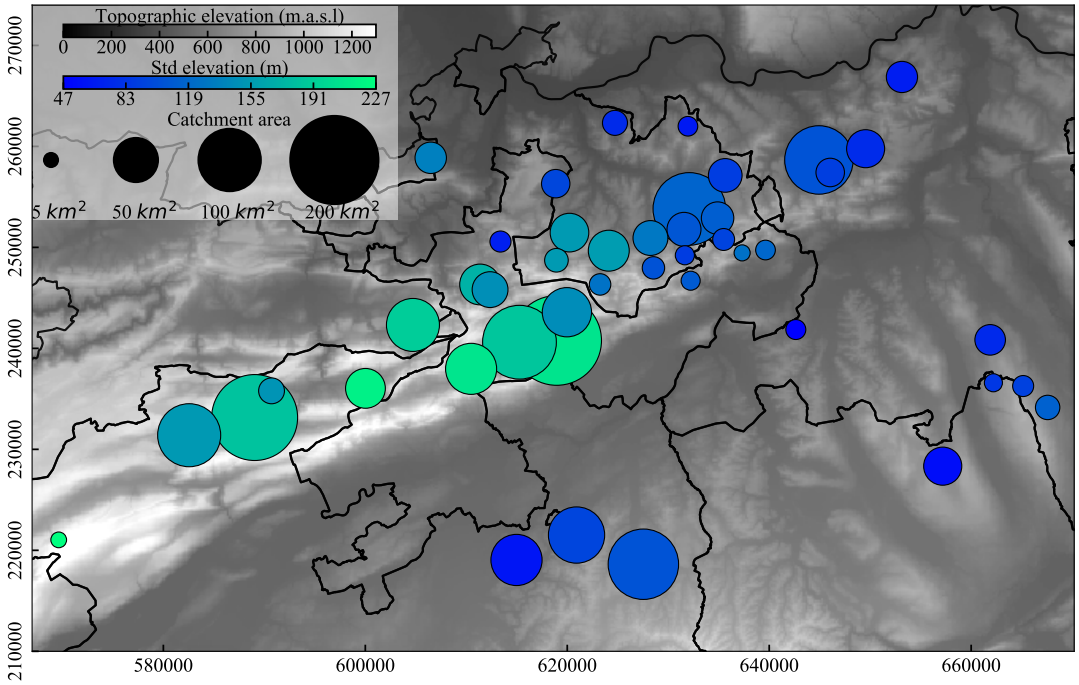

Figure 3.4: Standard deviation of the elevations of the studied catchments.

Land Use

The type of land use can affect the amount of water that can be infiltrated and retained in a catchment. However, it is not the only factor controlling runoff. There might be different soils under different vegetation covers, which can result in different runoff. The land use by its own might not be enough to explain the spatial variations of runoff in a catchment (Weingartner et al., 2003). Anyway, it is an important indicator, which together with other characteristics of the catchment can help explain differences of catchment reactions. For the calculation of the land use of each catchment the classes from the CORINE Land Cover raster obtained from the Swiss Federal Institute for Forest, Snow and Landscape Research (WSL) are used.

In Fig. 3.5 the proportion of the catchments having settlement, agriculture or forest areas are given. It can be observed that the majority of the catchments have almost no settlement areas and they are mainly rural catchments with large areas of agriculture and forest. The agricultural and forest areas are more or less equally divided in all catchments. However, there are some catchments for which the agricultural areas are larger than the forest areas. It is possible that these catchments react differently to extreme discharge.

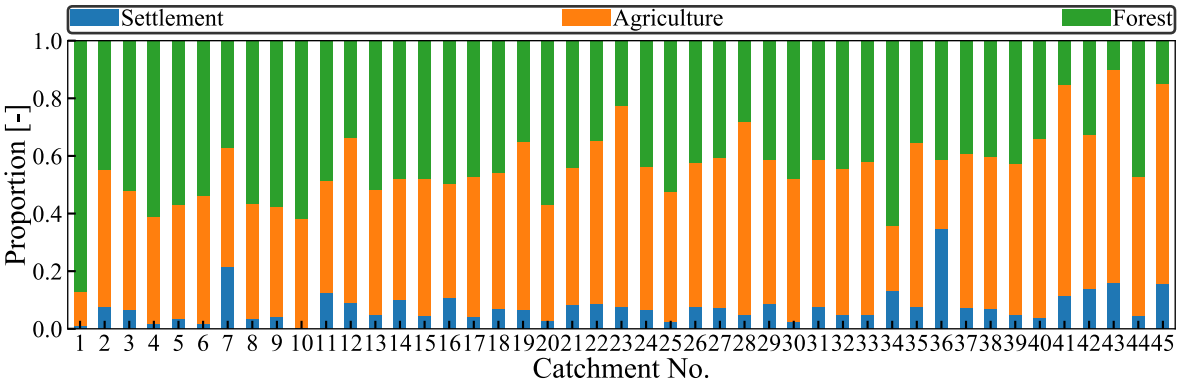

Figure 3.5: Land use proportions of the studied catchments.

Soils

The soil characteristics play a fundamental role in the partitioning of precipitation into surface and subsurface flow: not all precipitation falling in a catchment can reach the outlet (Blöschl et al., 2013). The soil, together with the vegetation cover, control the amount of water that can be infiltrated into the ground. Thus, they are indicators of the potential soil moisture of a catchment.

There are different soil classifications in the study area. Some more complex than others if complexity is measured by the number of soil groups. In this study, a simple soil classification is preferred to not over-parametrize the model. Many classes may lead to catchments having a lot of zeros for a given soil group. The digital soil suitability map of Switzerland from the Federal Office for Agriculture (FOAG) is used to classify the soils of the catchments. Figure 3.6 shows the proportions of the distribution of soils in each catchment. It can be observed that the catchments do not only have different soil distributions between each other, but there is also a high spatial variability of the soils in the catchment itself. This can be observed in the uneven distribution of soils and number of soil classes between the catchments. For instance, catchments 1 to 6 and 41 to 45 have an uniform spatial distribution of soils, with one predominant soil class. However, catchments 1 to 6, although show also a uniform distribution with one predominant soil, they have more permeable soils than catchments 41 to 45.

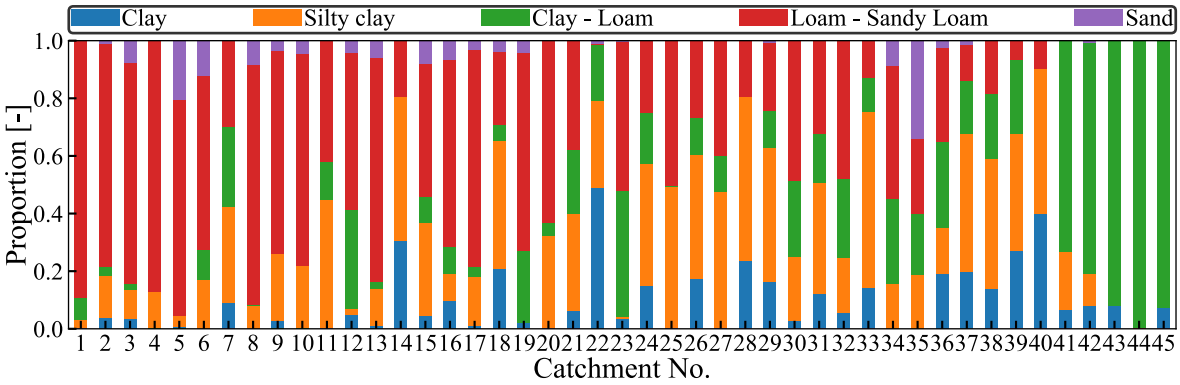

Figure 3.6: Soil distribution of the studied catchments.

Catchment Orientation

Catchment orientation helps to identify the possible influence of given fronts or big meteorological events. Exposition to orographic enhancement of precipitation can be responsible to some extent of the variability in mechanisms, it is an indicator of possible floods more prone to a given wind or storm direction patterns (Martínez-Goytre et al., 1994). It can help recognize different mechanisms and flood magnitudes. In this study it is calculated as the angle of the vector formed from the catchment outlet (gauge station) to the furthest point of the catchment. This is the point that maximizes the distance between catchment outlet and the exterior coordinates that delineate the catchment. An example is given in Fig. 3.7. It can be observed that the vector for calculating the orientation (in purple) has an angle of around 45°. This angle represents a cardinal direction of a South-West orientation (in orange). As it is shown in the top panel of Fig. 3.1, most of the catchments have an orientation between 180°and 360°, which corresponds to the North-East and the North-West quadrants.

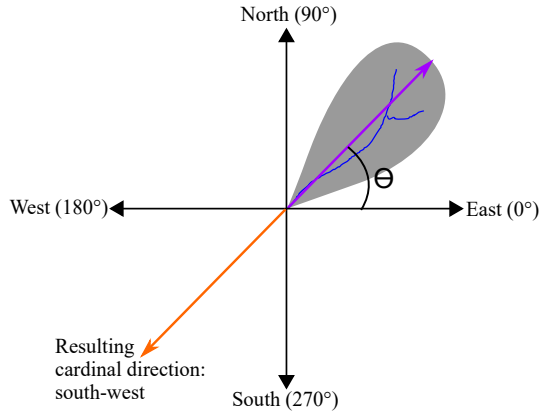

Figure 3.7: Catchment orientation: the angle θ of the purple vector formed from the catchment outlet to the furthest point on the perimeter gives the orientation. The actual cardinal direction that θ represents is the opposite vector (orange).

Drainage Density

Drainage density, as defined by Horton (1945), characterizes the stream system of a catchment. It is defined as the sum of the river lengths divided by the catchment area. Drainage density is an indicator of the magnitude of a flood and the velocity in which it can take place, assuming that runoff travels faster on streams as on land (Pallard et al., 2009). A larger drainage density represents a better drained catchment, which has a faster reaction and hence it has larger runoff coefficients (Gottschalk and Weingartner, 1998). Additionally, it represents how the topography, soil and vegetation have interactively change over the years (Blöschl et al., 2013). It is a complex parameter that can help explain flooding.

The drainage density of the study catchments is calculated using the rivers information from Federal Office for the Environment (FOEN) (Einzugsgebietsgliederung Schweiz EZGG-CH) and the catchments areas delineated for this study. Figure 3.8 gives the drainage density of the catchments in this study. It can be observed that the drainage density is not dependent on the catchment area, as there is no constant value according to the size of the catchment. Rather some regional trends are observed of similar drainage densities for catchments that are close to each other. This is expected, because similar soil formations, wind patterns and other characteristics might be found in the same regions and thus resulting in similar drainage densities.

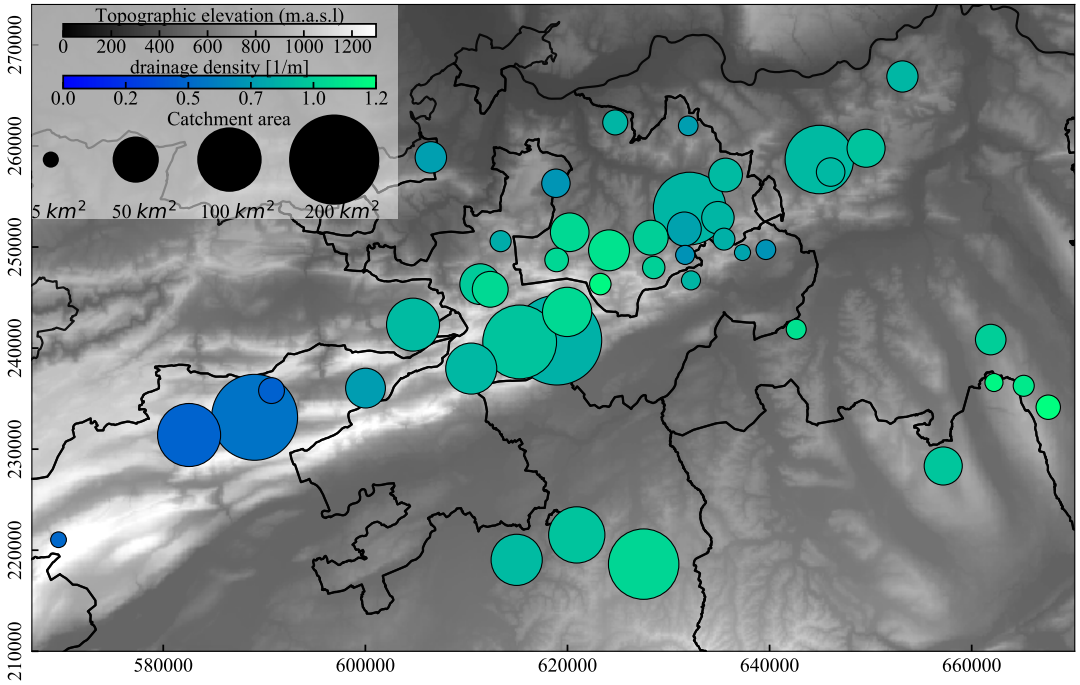

Figure 3.8: Drainage density of the studied catchments.

Concentration Time

The concentration time of the catchment is the time a water drop takes to move from the farthest point of the catchment until the outlet. It is an indicator of the time required until the whole catchment contributes to the runoff (Chow et al., 1988). In this study it is considered using the method from Kirpich as:

$$T_c = 0.06625 \cdot \left(\frac{L}{I_f^{0.5}} \right)^{0.77}, \tag{3.1}$$

where T_c is the concentration time, L the river length and I_f the average slope.

In Fig. 3.9 the Kirpich T_c is plotted against the catchment areas. Although a strong correlation between the catchment and T_c can be observed, there is also some variability within a constant catchment area, given that T_c is not a direct function of the catchment size but of the slope and length. Larger catchments are expected to have longer L and, therefore, longer T_c. Nevertheless, differences in the catchment characteristics give a variability to L.

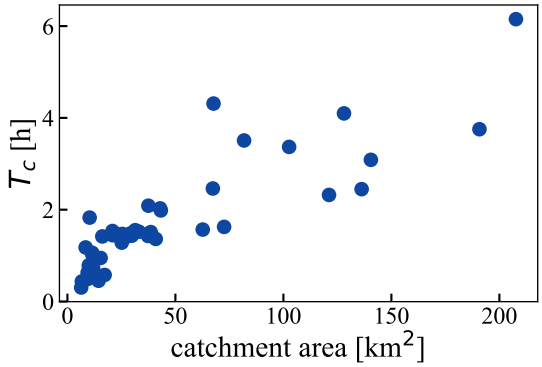

Figure 3.9: Catchment area versus concentration time.

Aquifer Formation

In Switzerland the hydro-geological conditions can be divided in three main aquifer groups. These are the unconsolidated aquifer, fissured aquifer and karst aquifer. According to the type of aquifer water moves at different velocities. In the unconsolidated aquifer water flows slowly and evenly. In fissured aquifer water flows more inhomogeneous and faster, some 100 meters per day. Finally, water flows faster in karst aquifer, some 100 meters per hour (Sinreich et al., 2012). Karst aquifers because of the strong iteration with surface water are the most influential in flooding processes. Karst aquifers are complex and highly heterogeneous. A catchment reaction to the same precipitation event can be completely different according to the fissured system of the aquifer. This has a direct influence on the hydrograph, where the

occurrence of the peak is faster, if caves and conduits are more interconnected. On the other hand, if the aquifer has narrower conduits water will flow slower (Bonacci et al., 2009).

The aquifers of the study catchments are identified using the hydro-geological overview map of Switzerland from the FOEN. In Fig. 3.10 the ratios of the study catchments having a given aquifer are given. Those catchments with predominate karst aquifer are located in the Jura Mountains. Whereas the catchments that have mostly fissured aquifers are on the south and east of the study area.

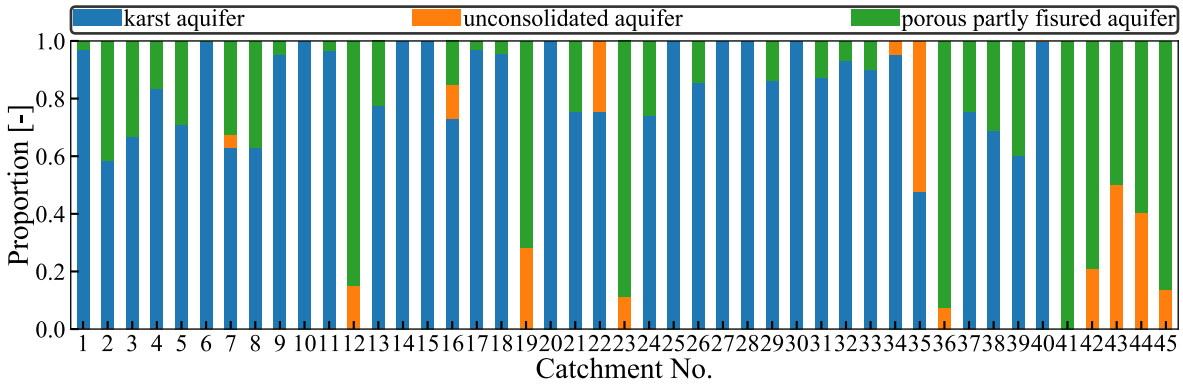

Figure 3.10: Aquifer proportions of the studied catchments.

3.2.2 Climatic Factors

Climatic factors or signatures are those parameters that identify the mean hydrological schema of the catchment. Given that the study period is short, these signatures are assumed to be constant for each catchment. In this study, the similarity of climate is characterized using precipitation observations. Herein, the the probability of a given amount of precipitation are used and the inter-annual variability of precipitation is described using a trigonometric function.

Daily precipitation quantiles are indicators of the likeliness of precipitation volumes. The knowledge of the expected precipitation volumes gives differences between drier and wetter catchments. For this purpose, the probabilities of having 5, 10, 15 and 20 mm of precipitations are considered. Chapter 5 will elaborate more on this subject.

The seasonal variability of precipitation is characterized by fitting a trigonometric function to mean daily precipitation data. This function $f(t)$ is defined as

$$f(t) = a_0 + a_1 \cdot \cos t + a_2 \cdot \sin t = a_0 + A \cos(t + \phi) \ , \tag{3.2}$$

where a_0, a_1 and a_2 are the coefficients of the function, t is the time interval of the observations, A is the amplitude of the wave and ϕ is the phase. The function is fitted to only

one period. For this purpose, the calendar days are transformed to values between 0 and 2π, where 0 is January 1st, π is around July 1st and 2π corresponds to December 31st. The function has it minimum at a value of $t = \phi$ and it maximum at the value of $t = \phi + \pi$. At this t values the function achieves $a_0 \pm A$.

As indicators of seasonality the values of the amplitude and the phase are used. The amplitude A represents how large the precipitation peak is and the phase ϕ gives the shift of the trigonometric function in the horizontal position. It is used as an indicator of the occurrence of precipitation peak and its magnitude. In Fig. 3.11 two examples are given where different precipitation regimes can be identified. The blue scatter points represent the observed daily precipitation means and the red line is the obtained $f(t)$. As it can be observed the plot on the left panel has a smaller ϕ than the one on the right. This means that the larger precipitations are expected to occur earlier in the year, sometime around Juli, whereas this peak is shifted more towards autumn for the case of the observations of the right panel. Regarding A, a larger value is obtained for the left panel than for the right one. This indicates that larger precipitation volumes are expected on the left panel as for the right panel. It can be concluded that the station on the right panel has a smaller inter-annual variability, for which similar precipitation volumes are expected around the whole year.

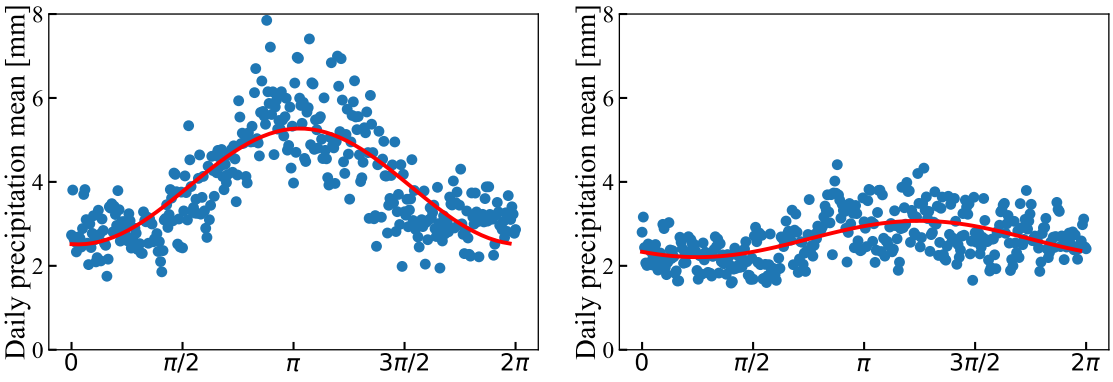

(a) $\phi = 0.09, A = 1.38$ **(b)** $\phi = 0.78, A = 0.43$

Figure 3.11: Difference of the inter-annual variability of precipitations for two stations. The blue scatter points are the observe mean daily precipitations. The red line is the fitted trigonometric function.

In this chapter the study area and the static catchment characteristics are described. Giving an insight to the complexity of the hydrological responses of the catchment. Nevertheless, no information is given about the differences of flood mechanisms, nor from the main drivers of different catchment reactions, i.e. the meteorological forcing causing the floods. In the following two chapters, first the catchments' respond by itself will be analyzed and second the variability of the meteorological input triggering the floods will be studied.

Chapter 4

Characterization of Extreme Discharges

The aim of this study is to characterize extreme discharges not only by their peak but by including their volume and hydrograph shape. In this chapter an explanation on the sampling of extreme discharges and how the flood waves are separated from the time series is given. Finally, the fit of a probability density function (PDF) to the flood waves is studied in order to describe the reaction of the catchment at the occurrence of a flood.

4.1 Sampling of Extreme Discharges

The first step when analyzing extreme discharges is to define which observations to select as a flood. A flood, as described by Field et al. (2012), is considered as the event of the water level exceeding the embankment of a water body or covering areas that normally are not under water. This is a rather wide definition that can change from one study site to the next and requires detailed catchment information not always available. As pointed out by Lang et al. (1999), a stochastic approach for determining extreme discharges is to consider the Annual Maximum Flood (AMF), the highest observed discharge per year. If more than one flood takes place within the same year, by using the AMF approach the information about the less extreme ones is going to be lost. To overcome this problem an approach with increasing popularity over the past years can be considered, the Peaks Over a Threshold (POT), also known as partial duration series. With this approach, a discharge threshold is selected to separate the events that will be considered as extremes. A common method is to select an average number of floods per year, which will give the value of the discharge that is set as the threshold to obtain the POT.

Throughout this study, different POT thresholds are used, which allows to compare different extremes. These are identified by the number of selected POT on average per recorded year with the abbreviation xPOT, where x is the number of POT selected on average per year. For example, a 4POT sample refers to the sampling of four POT on average per year. When

sampling extremes with a POT approach, consecutive events can be selected. To solely retain the independent floods, an inter-flood duration criteria is applied. A duration of ten days as inter-flood time is considered. One could argue that it is a high duration, especially for the catchment sizes within the study area. Nevertheless, it is observed that when selecting shorter inter-flood durations and sampling 4POT, the smaller extreme events already begin on the recession limb of higher peak events. In order to avoid this and to maintain consistency and simplicity a constant inter-flood duration of ten days is set for all catchments.

Figure 4.1 gives the frequency of occurrence of floods over the calendar months for all the catchments in the study area. In Fig. 4.1a the AMFs are sampled and in Fig. 4.1b the 1POT. These plots suggest that if one defines the floods as AMFs, important summer floods are missed. For example, the number of floods in June will be underestimated (≈ 125 for AMF instead of ≈ 160 for POT). The occurrence of floods in winter and summer when sampling the floods as the AMFs seems to be of comparable importance, due to the large number of floods occurring in January. If one looks at the 1POT samples this picture is different: by allowing the occurrence of multiple events per year, a more dominant summer flooding season is present. It is also observed that the importance of floods taking place in fall can be underestimated when looking at the AMFs. On the other hand, when using a POT approach, the sample size of the fall events increases, resulting in a more balanced data base, which is a benefit when the seasonality of the flood events is important for identifying flood mechanism as highlighted by Brunner et al. (2017) and Fischer (2018).

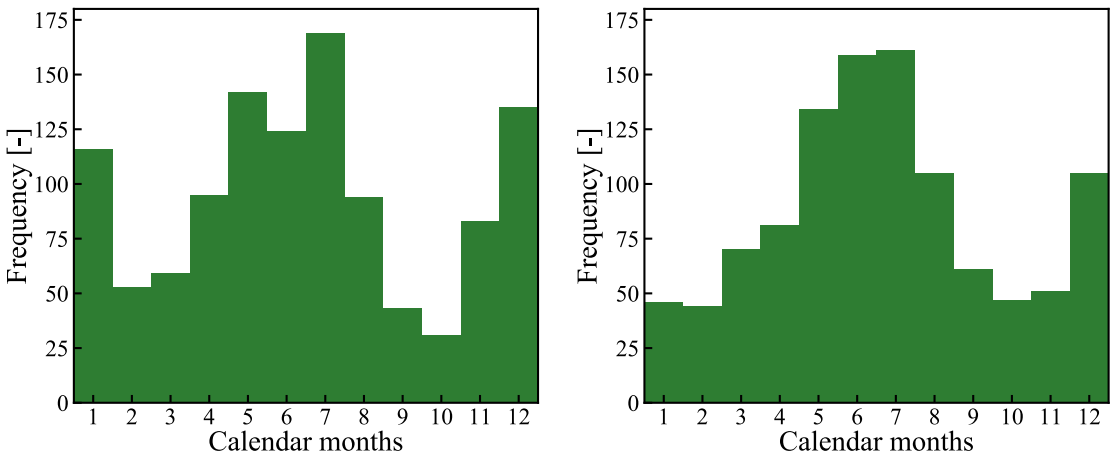

(a) AMF **(b)** 1POT

Figure 4.1: Frequency of occurrence of floods over the calendar months, given for the AMF sample **(a)** and the 1POT sample **(b)**.

As part of the Predictions in Ungauged Basins (PUB) initiative, Blöschl et al. (2013) pointed out that there is a need to understand the patterns and processes behind the runoff generation to be able to extend knowledge beyond individual catchments. A hydrograph flood wave is the resulting signature of a given meteorological event modified by the specific

characteristics of the catchment. Focusing only on the peak of the flood wave hampers the identification of the mechanism causing the floods. If full discharge series are available, further information about the flood can be obtained using a hydrograph separation technique, explained on the next section.

4.2 Hydrograph Separation

By means of a hydrograph separation it is possible to capture the start and end of the flood, separate the baseflow and calculate the flood volume. In this study the limits of the flood waves are identified using a method like the one applied in Bárdossy and Filiz (2005). The authors used the lag differences of discharge time series to identify increases in runoff due to weather conditions. The discharge lag differences are defined as:

$$\Delta Q(t) = Q(t) - Q(t - \Delta t)\,, \tag{4.1}$$

where $\Delta Q(t)$ is the corresponding lag series, $Q(t)$ is the discharge time series, t the time interval and Δt the time window. Figure 4.2 shows an example of a hydrograph of a 62 km^2 catchment. The left vertical axis corresponds to $Q(t)$ and the right axis corresponds to $\Delta Q(t)$. A $\Delta Q(t) > 0$ represents the increase of the discharge before the occurrence of the peak and it is the indicator of the start of the flood. On the other hand, $\Delta Q(t) < 0$ occurs after the peak on the recession of the hydrograph and it helps to identify the end of the flood. As mentioned in Chap. 3, discharge measurements with 10 and 15 minute resolutions are used. For a better performance on the identification of the flood limits, the hydrograph curves are smoothed, aggregating the observed discharges within some time intervals. The number of intervals chosen for the aggregation of the records depends on the size of the catchment, catchments with longer concentration times are aggregate using more time intervals.

In Figure 4.2 one can see that the start and end of the flood correspond to those points where the $\Delta Q(t)$ series approach zero. The displacement of $\Delta Q(t)$ with respect to $Q(t)$ is given by the data aggregation and the fact that one interval less is considered when calculating $\Delta Q(t)$. This method allows for identifying floods with different durations, in contrast to the approach of considering the flood wave within a fixed period (a given time before and after the peak). For different flood mechanisms and catchment sizes one would expect variations in shape and flood duration. Once the start and end of the flood hydrograph are specified, the baseflow is assumed to be linear and it gives the separating boundary between direct runoff and base flow (see green dashed line Fig. 4.2).

As mentioned by Fischer et al. (2016) there is no objective method to evaluate an automatized discharge separation. The hydrographs are assessed visually, to define the $\Delta Q(t)$ that better separates the hydrographs and the optimal number of time intervals for the aggregation.

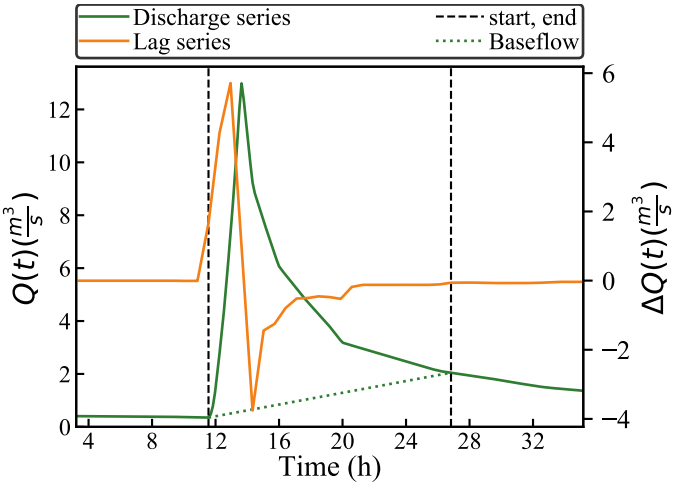

Figure 4.2: An example of the hydrograph separation approach. The left vertical axis corresponds to the scale of the $Q(t)$ and the right vertical axis to the scale of $\Delta Q(t)$. The hydrograph (green) corresponds to a 62 km^2 catchment. The start and end of the flood wave are identified using the lag series of the discharge data (orange). A linear behavior of the baseflow is assumed for separating the direct runoff, here plotted as the green dashed line.

4.3 Hydrograph Shape

Depending on the meteorological input causing the floods and the characteristics of the catchment, a variation on the shape of the hydrograph can be expected. For instance, if convective precipitation is the trigger of the flood, a hydrograph with a sharp shape, a large peak and a small volume is likely to occur. In contrast, if snowmelt is the generator, a longer hydrograph is expected with higher volumes. Figure 4.3 gives as an example the hydrographs for the ten biggest observed POT for two catchments of different sizes. The hydrographs are plotted in different colors according to the season when the flood occurred. As it can be observed on the left panel, the shape variation of the yellow hydrographs, suggests events happening in summer with different genesis. The events with shorter durations and smaller volumes can be a result of convective precipitation, whereas the event with a longer duration and larger volume can be the result of a weather front or precipitation caused due to orographic effects. The winter and spring events have longer durations and can be allocated to snow melt or rain over snow. A similar behavior is observed on the right panel although event shapes have less variability than for the smaller catchment.

The peak to volume ratio (PVR) is a useful indicator of the shape of the flood wave and can be used for differentiating flood mechanisms. It is defined as

$$PVR = \frac{Q_p}{V}\,, \tag{4.2}$$

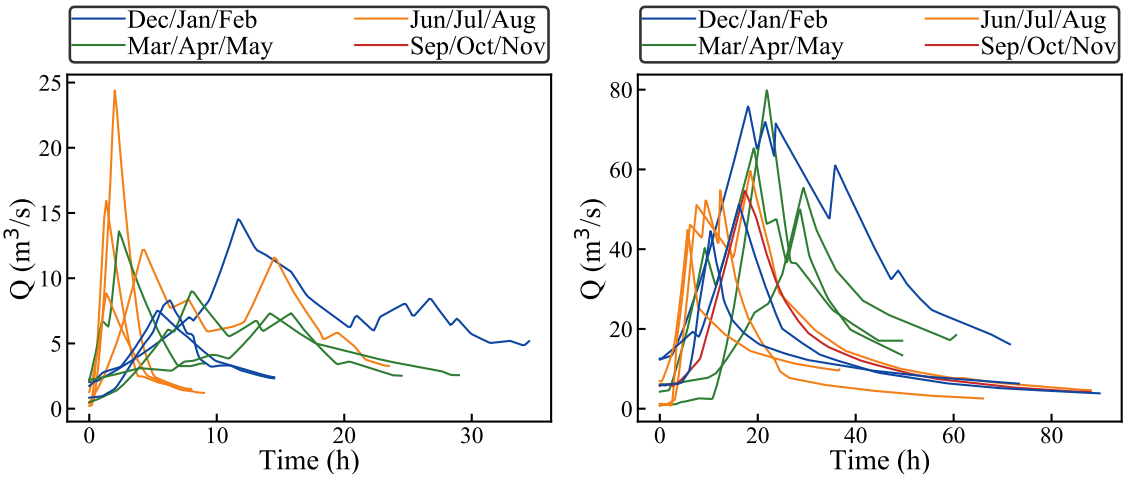

(a) Catchment No. 32 (12 km^2) **(b)** Catchment No. 29 (136 km^2)

Figure 4.3: Flood hydrographs of the five biggest POT for two selected catchments, the different color identify the season of the flood occurrence.

where Q_p is the peak discharge and V the volume of the separated flood wave. A large PVR stands for a hydrograph with most of the volume concentrated within the time intervals close to the flood peak, indicating a sharp hydrograph with rapidly increasing and decreasing limbs. On the contrary a small PVR represents hydrographs where the volume is distributed along the duration of the flood with smoother limbs. The largest summer peak in Fig. 4.3a has a PVR of 0.48 whereas the largest winter peak has a PVR of 0.12.

Figure 4.4 gives the average PVR over the different seasons for all the catchments included in this study. On the left panel a box plot with the distribution of the average seasonal PVR is given. The largest median PVR occurs in summer, which is expected given a more frequent occurrence of convective precipitation triggering flash floods. The catchments marked as outliers, i.e. the small circles in Fig. 4.4a, are just an effect of using a box plot for the representation and should not be interpreted as implausible values. Nonetheless, it is observed that catchments having larger $PVRs$ in summer and fall tend to have either large ratios of impermeable soils, large agricultural coverage or steep slopes. In winter the PVR are on average smaller, what is explained by the dominating occurrence of other flood mechanisms, i.e. snowmelt or rain over snow.

On the right panel of Figure 4.4 the relationship between the mean PVR and catchment area is plotted, with a color code to identify the seasons. It shows the expected tendency of larger $PVRs$ for the summer events with a decreasing trend of PVR as the catchment area increases. There is a high variability of the PVR especially for small catchments in summer. This means that there are different hydrograph shapes taking place when a flood event occurs. The information in PVR can be used for recognizing similarities within catchments at the event scale and represent the various flood mechanisms. Nonetheless, the use of the catchment area to characterize the shape is not sufficient, other factors influencing the hydrograph shape must be included. For example, the characteristics of the meteorological

event triggering the floods can be considered as it is the main driver of floods. This will be analyzed in Chap. 5, in which the relationship to the hydrograph shape is analyzed.

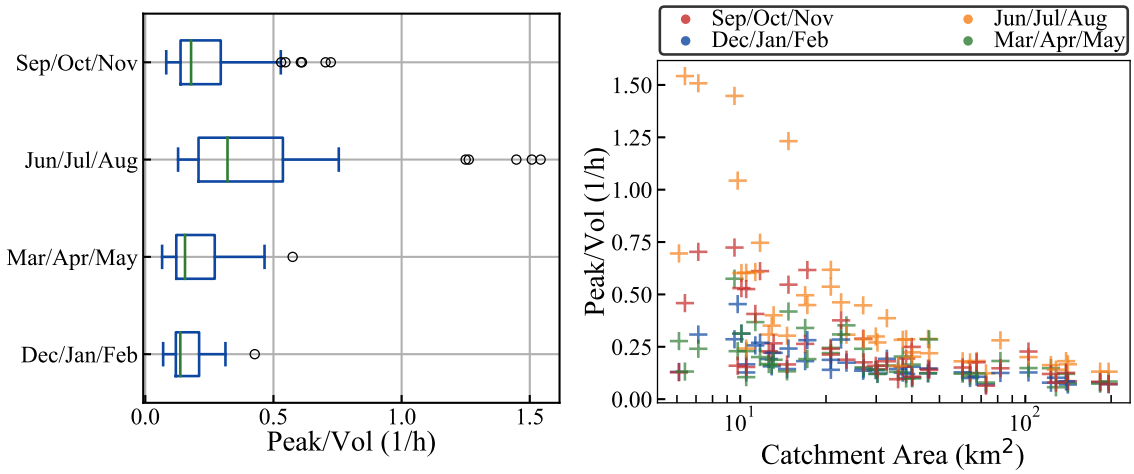

(a) PVR seasonal distribution

(b) PVR vs. catchment area

Figure 4.4: Average seasonal PVR for the study catchments of the 4POT samples. In (a) a box plot of seasonal average PVR is given and in (b) the relationship of PVR and catchment area is plotted.

4.3.1 Design Flood Hydrograph

Even though the PVR is shown to have a strong relationship with the hydrograph shape, it is only an indicator of the possible shape. The design of hydraulic structures for flood protection measures requires a reasonable representation of the whole flood wave, a Design Flood Hydrograph (DFH). Yue et al. (2002) classify the existing methods for deriving a DFH into four categories: traditional unit hydrograph, synthetic unit hydrograph, typical hydrograph and statistical methods. In this study the last approach is used, applying a probability density function (PDF) to represent the observed flood wave. In particular, the use of a Beta distribution is proposed by Yue et al. (2002). To fit the Beta distribution to the observations, the hydrograph must be normalized, given that the domain of the Beta distribution is [0,1] and the area underneath the curve must be equal to one. This is achieved by dividing the base of the hydrograph with the duration D and multiplying the discharge series $Q(t)$ by the ratio D/V resulting in the observed dimensionless hydrograph $f(t)$.

For fitting a PDF and obtaining $f(t)$, the dimensionless DFH, one possibility is to use the method of moments with the statistical properties (mean and variance) of the hydrograph (Yue et al., 2002). One can also use the hydrograph characteristics to estimate $f(t)$, as pointed out by Nadarajah (2007). The idea behind using a DFH is not to achieve perfect agreement with the observed hydrograph, but to resemble its shape and maintain the peak Q_p and the occurrence of the peak at t_p. Nadarajah (2007) proposes to estimate the parameters

by solving $Mode = t_p$ and $f(Mode) = Q_p$. For which $Mode$ is the value of t that maximizes the PDF $f(t)$. The denormalized hydrograph is obtained via

$$Q(t) = f(t)\frac{V}{D}\,. \tag{4.3}$$

In this research eight PDFs are studied: Beta, Fréchet, Gamma, Inverse Gamma, Lognormal, Weibull, Two Sided Power (TSP) and Generalized Standard Two Sided Power (GSTSP). The first six mentioned distributions are bell curves and the last two distributions, TSP and TSP, have sharp peaks. These two are included because they could be representative of hydrographs in small catchments (Serinaldi and Grimaldi, 2011). Table 4.1 gives an overview of the expressions for the PDFs.

Table 4.1: Probability density functions used to describe the shape of the flood waves.

Distribution name	Probability distribution functions
Beta	$Q(t;a,b) = \frac{1}{B(a,b)}t^{a-1}(1-t)^{b-1}$
Weibull	$Q(t;\kappa,\lambda) = \frac{\kappa}{\lambda}\left(\frac{t}{\lambda}\right)^{\kappa-1}\mathrm{e}^{-t\frac{\kappa}{\lambda}}$
Gamma	$Q(t;\tau,\theta) = \frac{t^{\tau-1}}{\theta^{\tau}\Gamma(\tau)}\mathrm{e}^{-\frac{\tau}{\theta}}$
Inverse Gamma	$Q(t;\alpha,\beta) = \frac{\beta^{\alpha}t^{-\alpha-1}}{\Gamma(\alpha)}\mathrm{e}^{-\frac{\beta}{t}}$
Lognormal	$Q(t;\mu,\sigma) = \frac{1}{t\sigma\sqrt{2\pi}}\mathrm{e}^{-\frac{(\ln(t)-\mu)^2}{2\sigma^2}}$
Fréchet	$Q(t;\alpha,c) = \frac{c\alpha^{\alpha}}{t^{c+1}}\mathrm{e}^{-(\frac{\alpha}{t})^{c}}$
TSP	$Q(t;n,m,b) = \begin{cases} \frac{n}{b}\left(\frac{t}{m}\right)^{(n-1)} \,\&\, \text{if } 0 \le t \le m \\ \frac{n}{b}\left(\frac{b-x}{b-m}\right)^{(n-1)} \,\&\, \text{if } m \le t \le b \end{cases}$
GSTSP	$Q(t;\theta,n_1,n_3) = \begin{cases} \left(\frac{n_1 n_3}{\theta n_3+(1-\theta)n_1}\right)\left(\frac{t}{\theta}\right)^{(n_1-1)} \,\&\, \text{if } 0 \le t < \theta \\ \left(\frac{n_1 n_3}{\theta n_3+(1-\theta)n_1}\right)\left(\frac{1-t}{1-\theta}\right)^{(n_3-1)} \,\&\, \text{if } \theta \le t < 1 \end{cases}$

For the Beta function the value of $B(a,b)$ normalizes the distribution and is given as follows

$$B(a,b) = \frac{\Gamma(a)\Gamma(b)}{\Gamma(a+b)},$$

where $\Gamma(n)$ is the gamma function, which also appears in the Gamma distribution and is given as

$$\Gamma(n) = (n-1)!,$$

with n being a positive integer. Additionally, the fit parameters n_1 and n_3 of the GSTSP are obtained via the following system of equations

$$n_1 = \frac{t_p f(t_p)}{F(t_p)}$$
$$n_3 = \frac{f(t_p)(1-t_p)n_1}{n_1 - t_p f(t_p)},$$

where $F(t;\theta,n_1,n_3)$ is the density of the GSTSP distribution, which is given as

$$F(t;\theta,n_1,n_3) = \begin{cases} 0 & \text{if } t \leq 0 \\ \frac{\theta n_3}{\theta n_3+(1-\theta)n_1}\left(\frac{t}{\theta}\right)^{n_1} & \text{if } 0 \leq t < 0 \\ 1 - \left(1 - \frac{\theta n_3}{\theta n_3+(1-\theta)n_1}\right)\left(\frac{1-t}{1-\theta}\right)^{n_3-1} & \text{if } \theta \leq t < 1 \\ 1 & \text{if } t \geq 1 \end{cases}$$

All eight distributions are fitted to the separated hydrographs of the 4POT sample. Figure 4.5 gives an example of an observed hydrograph and the corresponding fitted PDF. For this specific example the PDF fits are very similar, the biggest difference is observed on the recession limb, with a "fat tail" representation for the TSP and GSTSP distributions.

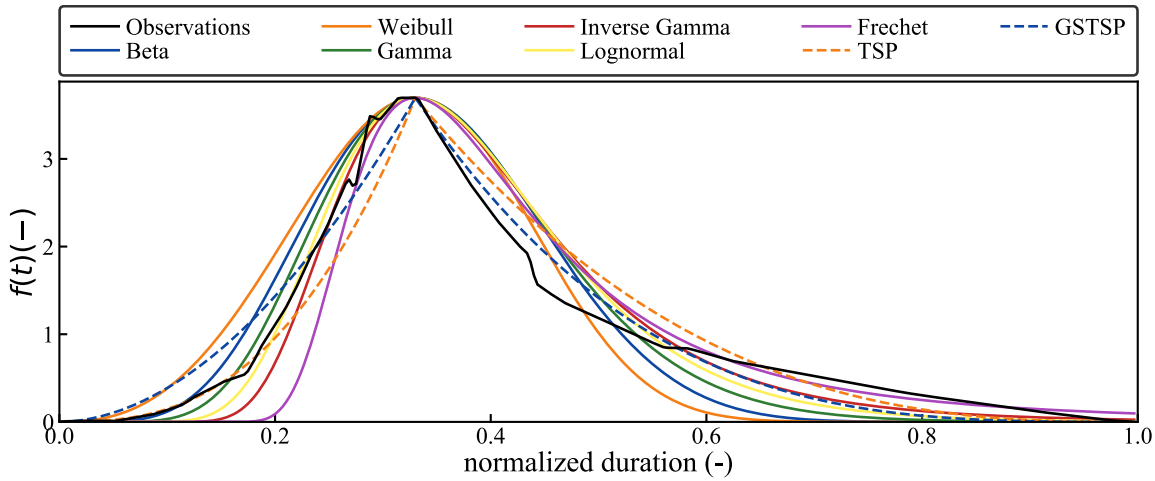

Figure 4.5: Example of fitted design flood hydrographs for one flood wave. The observed hydrograph is given in black, and the different PDFs are color coded.

The quality of the PDFs fits is evaluated using the Nash-Sutcliffe efficiency coefficient (NSE) as

$$NSE = 1 - \frac{\sum_{i=1}^{N}(\hat{y}_i - y_i)^2}{\sum_{i=1}^{N}(y_i - \bar{y})^2} \tag{4.4}$$

where $\hat{y}_i$ is the estimated value, y_i is the observed value and $\bar{y}$ is the mean of the observations. Here, N are the number of time intervals of each hydrograph. Additionally, for

comparing the fits in terms of the shape of the hydrograph the Mean Squared Error (MSE) of the observed and the fitted entropy are calculated as

$$MSE = \frac{1}{N}\sum_{i=1}^{N}(\hat{y}_i - y_i)^2 \tag{4.5}$$

in this case $\hat{y}_i$ and y_i are also the estimated and the observed values respectively, but of the entropy of the estimated and observed hydrographs. Here, N represents the number of flood hydrographs in each catchment. The entropy is considered for the time intervals before the peak, after the peak and for the whole hydrograph.

Figure 4.6 gives a summary of the goodness of fit for the eight distributions. For this purpose, for each catchment a NSE is calculated per fitted hydrograph. The hydrographs used correspond to those in the 4POT sample. On the left panel of Fig. 4.6 the average of the NSE obtained for each catchment are used to generate the box plot. It can be observed that, the sharp peak distributions have larger NSE, i.e. they fit better, the median NSE for the TSP and GSTSP is around 0.78. In terms of the median, the worst fit is obtained with the Weibull and the Fréchet distributions with a NSE of 0.64. However, the Fréchet distribution has catchments that in average presented a larger average NSE, indicating better fit than the Weibull for catchments. The Beta distribution has the catchment with the lowest performance (NSE of 0.15). The Lognormal has the best fit of the bell shaped distributions with a median NSE of 0.61, this agrees with the observations of Brunner et al. (2017). Looking at the fit quality in terms of the difference between the entropies of the observed and the fitted distributions is more significant than looking at the goodness of fit over all data points of the hydrograph as evaluated with the NSE. The right panel of Fig. 4.6 gives a box plot with the MSE between the entropies of the observed and the fitted distributions. Here, also the average MSE for each catchment with the fits of the 4POT sample is considered. The TSP and GSTSP have the smaller median MSE, being so the distributions that can represent the entropy of the observed hydrograph the best. The six bell shaped distributions have worse performance, whereas the Weibull and the Beta have the largest median MSE and the Inverse Gamma and the Fréchet have the smallest one.

In Tab. 4.2 the Root Mean Squared Error (RMSE) between observed and fitted entropies for the time intervals before and after the occurrence of the flood peak is given. For each catchment the average RMSE for each season (winter and summer) are calculated for the fits of the hydrographs from the 4POT sample. The median, the maximum and the minimum of the average catchment RMSE are given in Tab. 4.2. Only four distributions are included, the two sharp distributions and the two bell shaped distributions, since the trend in the behavior over the bell shaped distributions is similar. It is observed that for all PDFs the entropy of the hydrograph after the peak is better represented than the entropy before the peak (smaller RMSE). This can be attributed to smaller variations present on the recession limb of the hydrograph between two time intervals. The same applies for the entropies of the winter months, which are closer to the observed entropies than in the case of the summer months.

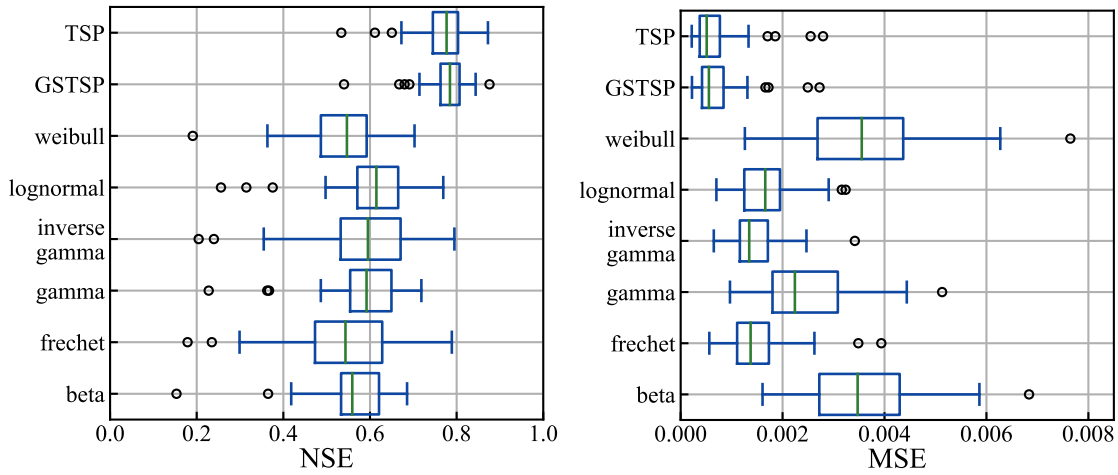

Figure 4.6: Goodness of fit for the eight PDFs to represent the design floods hydrograph. Left panel: average NSE per catchment over all 4POT samples. Right panel: average MSE per catchment over all 4POT samples.

For both the winter and summer events, the TSP distribution represents the entropies of the increasing and decreasing limbs better. It is observed that although the lognormal distribution has larger errors the performance can be comparable to those of the sharp distributions, especially when looking at the entropies after the peak.

Table 4.2: Median, minimum and maximum RMSE between the observed and fitted entropies for the intervals before and after the peak. The bold values indicate the lowest values, i.e. the best performance. The seasons 1 and 2 differentiate the winter and summer seasons, corresponding to the months April to September and October to March respectively.

		RMSE of entropy before the peak			**RMSE of entropy after the peak**		
PDF	**Season**	**Median**	**Min**	**Max**	**Median**	**Min**	**Max**
Beta	1	0.07	0.03	0.25	0.08	0.05	0.12
	2	0.17	0.08	0.48	0.10	0.07	0.18
Lognormal	1	0.08	0.05	0.21	0.04	0.02	0.07
	2	0.15	0.07	0.37	0.05	0.03	**0.12**
GSTSP	1	**0.04**	**0.02**	**0.16**	0.04	**0.01**	0.07
	2	0.11	**0.06**	0.34	0.04	**0.02**	0.13
TSP	1	**0.04**	**0.02**	**0.16**	**0.02**	**0.01**	**0.05**
	2	**0.10**	**0.06**	0.32	**0.03**	**0.02**	0.14

Additionally, it is noticed that the six bell shaped distributions tend to underestimate the

entropy after the peak and overestimate the entropy before the peak. This indicates that the errors for the case of the whole hydrograph (see right panel of Fig. 4.6) are low as a result of the compensation between the over and underestimation of the two separate entropies. The actual hydrograph representation is worse as what evaluated with the entropy of the whole hydrograph. This effect is also observed in Fig. 4.2, where the recession limbs of the bell shaped PDFs underestimate the duration and volume of the observed flood.

In Fig. 4.7 the average NSE of the fits from a TSP distribution for the 4POT samples is plotted in space. The size of the scatter points is representative of the catchment sizes, the blue-green color map gives the scale of the NSE. There is no observed pattern of the distribution of the errors in space or catchment sizes, the same is noted for the case of the entropies MSE over all PDFs. This is an advantage for the regionalization of the flood hydrographs, since no bias will be introduced to certain catchment groups due to the chosen PDF distribution for constructing the DFH.

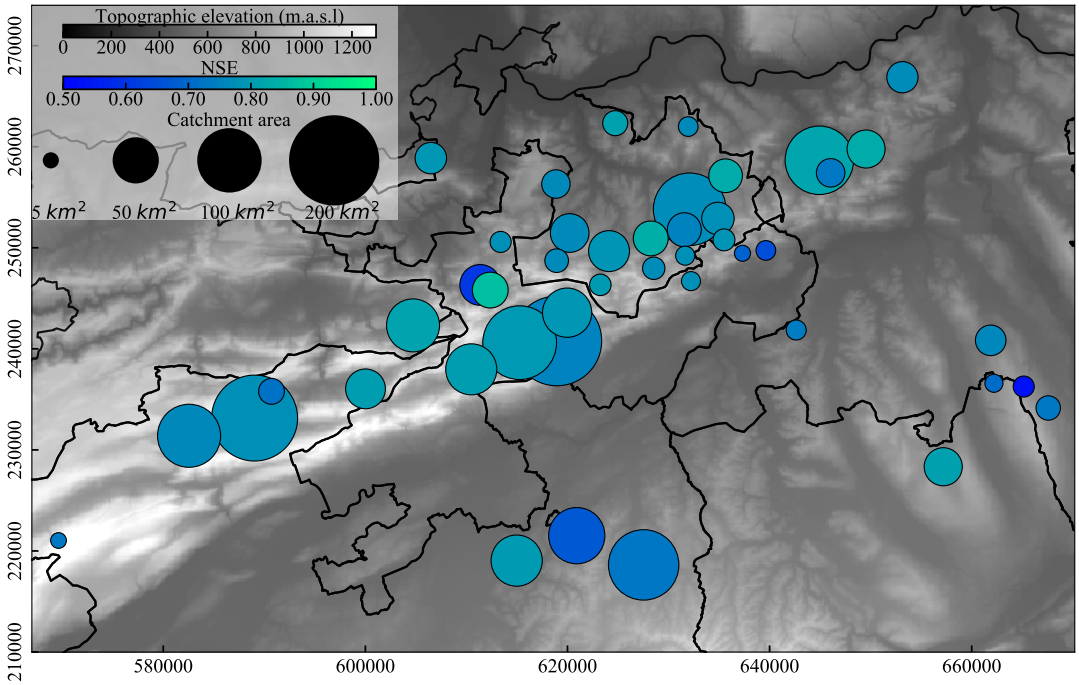

Figure 4.7: Spatial distribution of the average NSE per catchment when fitting the TSP distribution to the 4POT. The blue-green color map gives the scale of the NSE.

According to the flood estimation purposes one could choose a different PDF to fit to the flood hydrograph. When looking at both the NSE and the entropies MSE, the TSP is the one with the best overall performance. However, the TSP is a sharp distribution and might seem unrealistic for modeling the winter floods with longer durations. From the bell shaped distributions, it is observed that although with larger errors, the Lognormal has comparable performance as the obtained with TSP. In further stages of this study, both the TSP and the Lognormal will be considered.

Chapter 5

Meteorological Forcing Causing the Floods

The purpose of this chapter is to analyze the meteorological forcing event causing extreme discharges. Precipitation data with high temporal resolution is used to explore the relationship of flood drivers and catchment reactions. Temperature data is also included for evaluating the impact of snow processes. Finally, the soil moisture at the occurrence of the floods is evaluated using precipitation data aggregated within days.

For assessing the precipitation triggering the floods and the temperature change before the occurrence of the flood, the data of the geographical nearest neighbor is used. An overview on these available data is given in Chap. 3. The time periods of the precipitation and discharge measurements do not always match and are sometimes short. A tradeoff between maximizing the length of the measurements and the spatial coverage on the study area is needed to select the stations to be included. Depending on the objective of the analysis, different time periods will be selected. For example, when looking at the meteorological event triggering the floods, a minimum of 7 years is selected: discharge, precipitation and temperature neighbors are included if they had at least 7 years of consecutive measurements. Since consecutive consecutive beginning and end of the records is of importance in the case of precipitation analysis, the following time periods are selected: 1984-2017, 2001-2017 and 2010-2017. Different periods are considered to identify if the observed patterns are a matter of the data scarcity in space and time or patterns of the actual weather. In Chap. 3 Fig. 3.2 the available data for precipitation measurements with 10 minutes resolution are plotted. It shows that long records, are available only at few stations, resulting in a scarce spatial resolution. However, the spatial coverage increases as the observation period is shortened. Records of a couple of years are not enough for analyzing extremes, thus a compromise between spatial coverage and length must be taken.

5.1 Characterization of Precipitation Causing the Floods

To characterize the precipitation event triggering the floods the following parameters are used: (1) the total precipitation, (2) the duration, (3) the intensity, (4) the temporal entropy and (5) the precipitation association. Their definition is described in the following sections.

Total precipitation. This quantity corresponds to the total amount of rainfall triggering the flood, if not mentioned otherwise. Sometimes it corresponds to the total amount of liquid water triggering a flood, meaning that melted snow is included as part of the precipitation event, the method used for including snowmelt water equivalent is explained later in this chapter. The beginning and end of a precipitation event is determined by the duration of the flood wave plus the amount of precipitation falling before the rising of the flood curve. The start of the precipitation event is determined by the point at which at least two consecutive hours of no precipitation are recorded.

From the total of 4816 4POT samples, 59 floods had precipitation records of 0 mm and 1568 had data sets containing NaN. Those events are tagged as unreliable and are not included in the analysis. Events with 0 mm precipitation at the occurrence of a flood are not physically possible. These records are found to be mainly flood events exceeding in 75% of the cases the median peak to volume ratio (PVR) of the catchment. As mentioned in Chap. 4 large PVR values represent steeper hydrographs with fast increasing and decreasing limbs, which is a typical catchment respond to convective precipitation cells, with high intensities and short durations, that could have been missed at the neighboring station. The high number of NaN values corresponds to precipitation stations with no records, in some cases precipitation measurements with high temporal resolutions (10 min.) had shorter data series than the discharge station. As already mentioned, a compromise between data series length and proximity to catchment had to be taken.

Duration. It is considered as the number of wet intervals within a fixed period of time, defined as

$$D_{j,N} = \sum_{i=1}^{N} k_i, \quad \text{with} \quad k_i = \begin{cases} 1.0 & P_i > 0 \\ 0.0 & P_i = 0 \end{cases}, \tag{5.1}$$

where N is the number of intervals calculated with a data aggregation j and k_i equals 0 or 1 depending on the precipitation P_i measured within the i-th interval. For example, $D_{h,24h}$ is a duration calculated with an hourly aggregation in a 24 hour period. In this study durations are always given in hours, if not calculated with hourly aggregations, they are converted to hours.

In Fig. 5.1 the observed durations, within the flood-day ($D_{10min,24h}$), versus the PVR of the floods are plotted. A flood-day is considered as the interval between 12 hours before and 12 hours after the peak. In Fig. 5.1a and Fig. 5.1b all flood events of two example catchments are included. In Fig. 5.1c the mean PVR and $D_{10min,24h}$ over each season are given for each catchment. Additionally, in Tab. A.3 a summary with the mean characteristics of the meteorological event triggering the floods for each catchment is included.

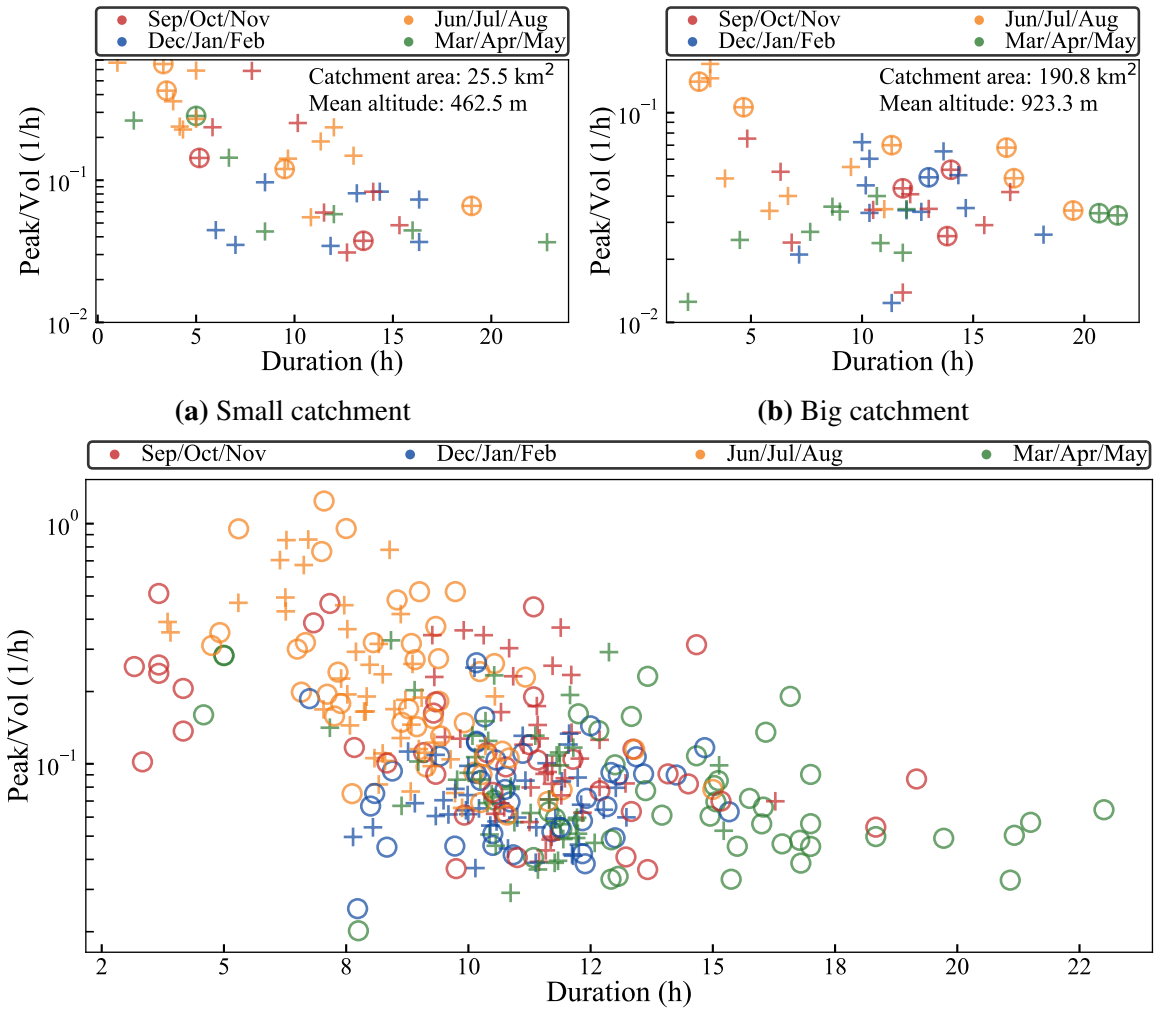

(a) Small catchment

(b) Big catchment

(c) Mean per season for each catchment

Figure 5.1: Scatter plots of the duration of the precipitation event ($D_{10min,24h}$) versus the PVR of flood events. The colors represent the different seasons and the markers are used for identification between 1POT (circles) and 4POT (crosses) samples. (a) and (b) give examples of all floods for two different catchment areas. (c) shows the seasonal mean for all catchments.

As expected, events with lower PVR, shallow increasing and decreasing hydrographs, tend to have longer durations and are more common in winter. Most of floods occurring in summer have smaller durations than the winter events. Convective precipitation is known

for having short durations and high intensities and trigger flash floods. On the other hand, longer durations in winter can be associated to other flood mechanisms as snowmelt or rain over snow. A difference in durations depending on the catchment size (see Tab. A.3) is also observed. As it is well known, bigger catchments have longer concentration times, and thus, longer precipitation durations are triggering their floods. Figure 5.1c suggests that extremer events (1POT) have longer durations in spring than 4POT events, highlighting the importance of the sample selection according to the purpose of the flood estimation. If more events are included the duration of the extremer ones can be underestimated. The duration of the precipitation event gives the number of wet hours but does not reveal the temporal distribution of precipitation. The use of temporal precipitation entropy for identifying the influence of the temporal variation of precipitation on the hydrograph shape is going to be analyzed later in this chapter.

Intensity. Precipitation intensity is the amount of precipitation falling per unit time. In this study, intensity refers to the mean rainfall rate, as described by Dunkerley (2008). It is defined as

$$I = \frac{P}{D}\,, \tag{5.2}$$

where I is the intensity or rainfall rate, is the accumulated precipitation depth in the considered duration D. Here, intensity depends on the definition of duration. It can be ambiguous, since two precipitation events can have similar intensities but a different temporal distribution. For example, if the precipitation intensity is calculated over one hour, two events that have the same amount of precipitation accumulated in the hour. However, in one event all precipitation came within 10 minutes and in the other it came equally distributed over the hour.

Fig. 5.2 shows the mean intensity triggering both 1POT and 4POT for all catchments. The mean of the intensities is calculated per season. The intensities considered for these plots are computed using the precipitation accumulated within $D_{10min,24h}$. Even though, there is a tendency that summer events have bigger intensities, the same value can trigger different hydrograph shapes, represented by the PVR. The flood-day intensity (Fig. 5.2) does not help to separate the flood mechanisms. The same is observed for the case of the maximum ten minutes intensity. As Fig. 5.2 suggests there is a wide range of $PVRs$ having the same intensities, especially for events in spring, fall and winter. In the next section a method to resolve this problem is introduced.

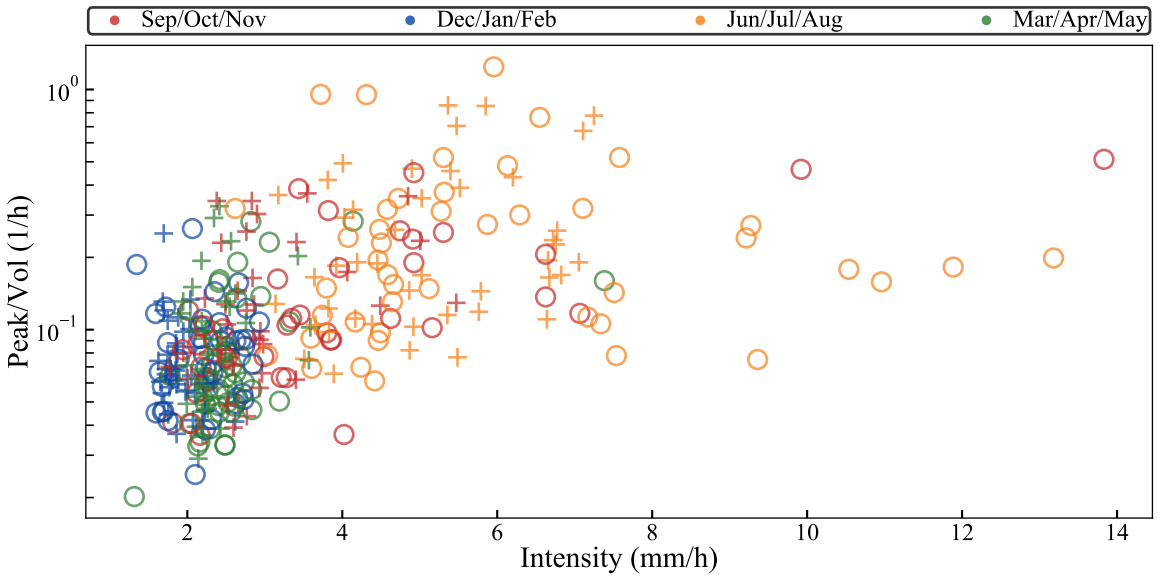

Figure 5.2: Scatter plot of intensity versus the PVR of the flood events. The intensity is calculated using a $D_{10min,24h}$. The different seasons are represented by the colors and the markers are used to identify floods belonging to 1POT (circles) and 4POT (crosses) samples.

5.2 Entropy for Evaluating Precipitation Temporal Distribution

Entropy is used to characterize the temporal variability of precipitation. Entropy H is a measure of information, uncertainty and chaos. Its discrete form as defined by Shannon (1948) is given by

$$H(P) = -\sum_{i=1}^{N} p_i \log p_i, \tag{5.3}$$

where $H(P)$ is the entropy of the discrete set of probabilities of the random variable P, N the number of outcomes and p_i the probability of occurrence of each possible event. The base of the logarithm defines the unit of the entropy. Here, the base of the logarithm is two, which defines the units of entropy to be bits. The entropy function is bounded on the minimum and maximum values it can assume and is always positive. If there is only one possible outcome, the entropy is at its lower limit $H(P) = 0$, implying absolute certainty. In contrast, $H(P)$ suggests maximum uncertainty when all outcomes are equally likely to occur, which corresponds to the case of a uniform distribution. Additional properties of the entropy are: **(1)** the value of $H(P)$ is not altered by the order of the outcomes, **(2)**

it is continuous, meaning that small changes of p_i have a small effect on $H(P)$, **(3)** it is monotonous suggesting that with an increase of N the uncertainty also increases and **(4)** by the presence of impossible events $H(P)$ does not change (Singh, 2013).

For calculating the temporal variability of precipitation, the concept of apportionment entropy introduced by Mishra et al. (2009) is used. In this study it is applied for measuring temporal variability over one precipitation event and not the variability of monthly precipitation over a year, which is defined as

$$H_t = -\sum_{i=1}^{N} r_i \log r_i \,, \tag{5.4}$$

where H_t is the temporal entropy of precipitation, N the number of intervals subdividing the domain of H_t and r_i the weighted precipitation of the given time step, expressed as

$$r_i = \frac{P_i}{\sum_{i=1}^{N} P_i} \,, \tag{5.5}$$

where P_i is the aggregated precipitation for each interval. In order to get an intuitive picture, one could think of temporal entropy as an N number of empty rain buckets. If each bucket has a lid that only opens during an interval i, H_t measures the distribution of water in these buckets. In case of a small H_t (low uncertainty event, see Fig. 5.3a) the precipitation event is highly intense, which is a typical characteristic of convective precipitation, in which the total precipitation measured lies between a couple of intervals (only a few buckets contained water). On the contrary, a large H_t (high uncertainty event, Fig. 5.3b) represents a longer and more uniform precipitation event, typical of a frontal event, orographic precipitation or rain over snow, in which the amount of precipitation measured over the event is more equally distributed in all intervals (all buckets are almost evenly filled with water).

Figure 5.3 shows two flood events for the same catchment for which the intensity is calculated with a $D_{10min,24h}$. It can be observed that both events, although having diverse temporal structure result in comparable intensities (2.8 and 2.6 mm/h). If the intensities of the same events are calculated using a $D_{h,24h}$, values of 1.3 mm/h for Fig. 5.3a and 2 mm/h for Fig. 5.3b are obtained, which are still very similar between each other. Even if one looks at the maximum intensity within 10 minutes intervals, both events have around 4 mm/10min (maximum of the blue line). Yet, both events have different values of H_t, which indicates a better potential of its use as an indicator of the temporal variation of precipitation and of its influence on the hydrograph shape.

Special care must be taken, when comparing records with diverse resolutions or events with a different number of aggregated precipitation intervals. Entropy measures randomness relative to the coordinate system considering an equal weight for each interval, if the coordinate system changes, the value of entropy is altered (Shannon, 1948). Here, the coordinate

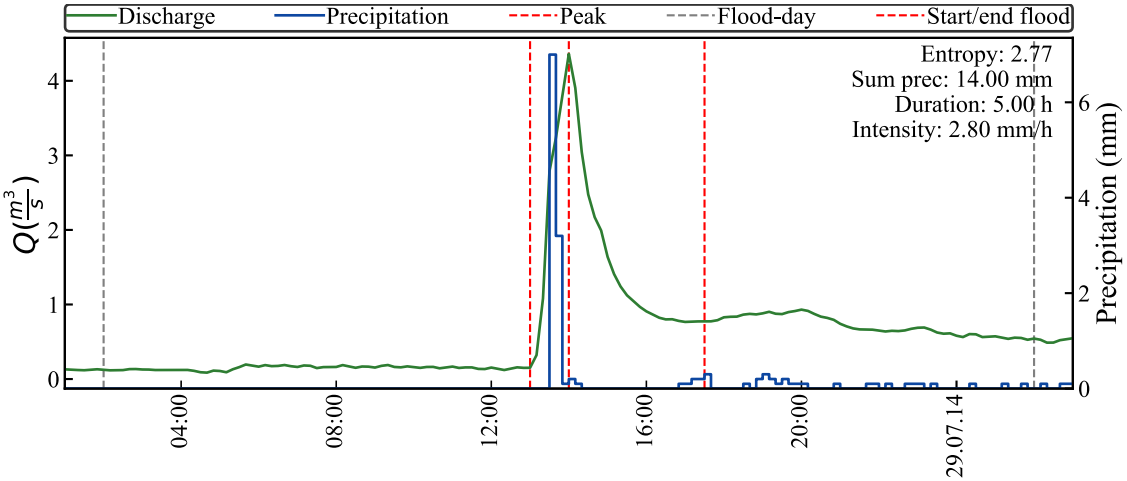

(a) Low entropy event

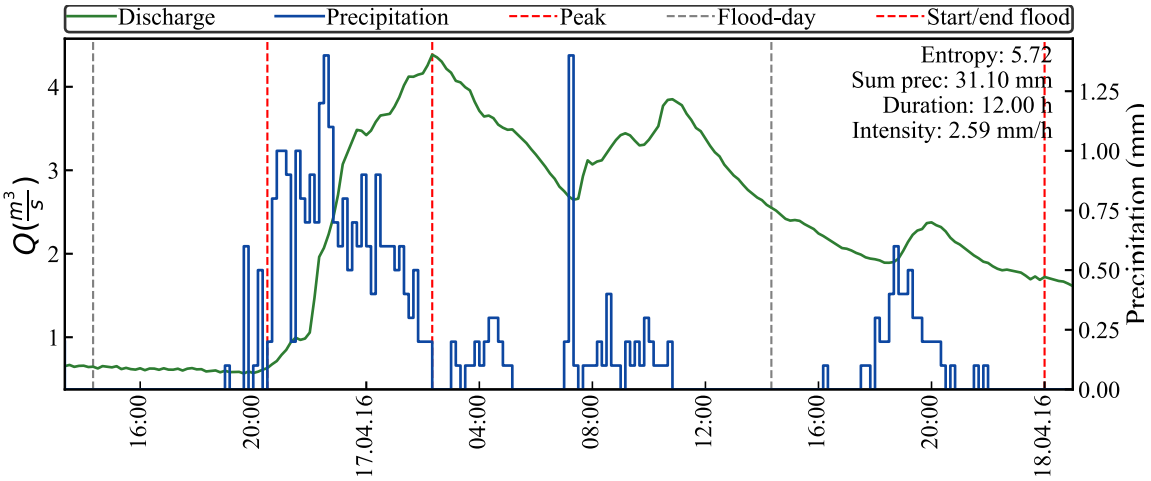

(b) High entropy event

Figure 5.3: Example of temporal precipitation entropy. The precipitation observations are given in blue and its corresponding triggered hydrograph reaction in green. The plot shows two different catchment reactions due to different temporal distribution of precipitation. The parameters of the meteorological events for the flood-day are displayed in each subplot.

system corresponds to time and can be either in days, hours or minutes. To be able to compare values of entropy coming from different coordinate system definitions, the concept of relative entropy or dimensionless entropy must be used. Relative entropy H_R is defined as the ratio of entropy to maximum entropy. It is given as (Singh, 2013)

$$H_R = \frac{H(P)}{H_{max}(P)} = \frac{H(P)}{\log N}, \tag{5.6}$$

where $H(P)$ is the entropy of the considered coordinate system, H_{max} the upper bound of the entropy, which depends on the sample size N, i.e. the number of aggregated precipitation intervals. The proof of $H_{max} = \log N$ can be found in example 2.10 of Singh (2013). In this study H_R is used when the coordinate system changes and for those cases it will be mentioned. Otherwise H_t will be used within a fixed period using observations with 10 minutes resolutions.

5.2.1 Statistics of Precipitation Sums and Temporal Entropy

An overview of the precipitation sums and the temporal precipitation entropies H_t are given in this section, with the intention of having a general picture of the precipitation regime in the study area. The empirical distribution function (EDF) for the precipitation sums and the temporal entropy for the study period of 1984 to 2017 are shown in Fig. 5.4. Observations with a resolution of 10 minutes are considered, only including those stations that measured the whole study period. For both precipitation and H_t a moving window is used, for which every 10 minutes the data of the preceding 24 hours is either aggregated or used for calculating H_t. Given that H_t is calculated within 24 hours using observations every 10 minutes, the minimum and maximum values that H_t can take are 0 to 7.17.

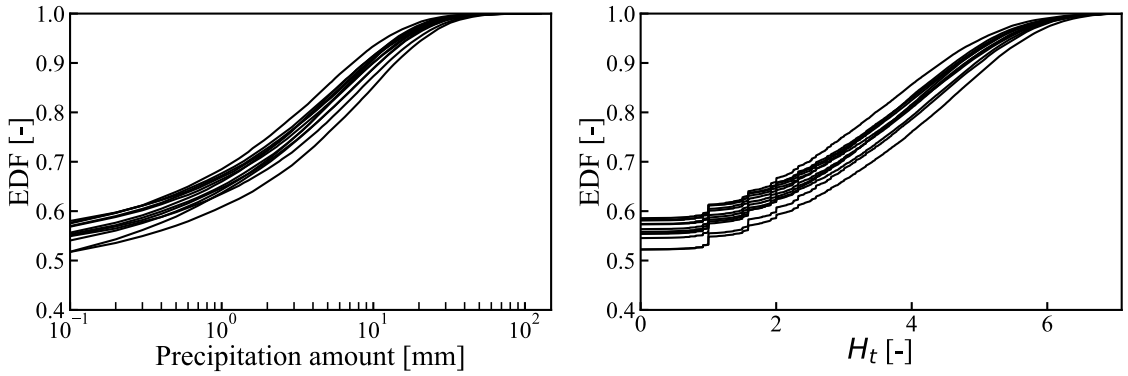

(a) Daily precipitation **(b)** Temporal precipitation entropy

Figure 5.4: The empirical distribution function (EDF) of daily precipitation (left) and temporal entropies calculated over a day with observations every 10 minutes (right).

As an orientation on the meaning of the different quantiles, a summary of the observed quantiles is included in Table 5.1 for the different study periods. Typical values for the probabilities of observing a given precipitation sum or having a determines H_t are given. In this table the mean over all stations that had measurements in a period is included. Also, the minimum and maximum observed values are given. In the study area, the probability of having a dry or a wet day has a range from around 0.5 to 0.6. It can also be observed that around a value of H_t equal to 6, some of the stations have the maximum observed quantile and this does not correspond with the maximum possible H_t of $\log_2(144) = 7.17$. This is expected due to the random nature of precipitation, which makes it unlikely that within a day

all 144 intervals of 10 minutes observations will have the exact same amount of precipitation per interval. Further, it can be observed that the probabilities of having 0 mm of precipitation are lower than those of having $H_t = 0$. This occurs due to those 24 hours periods with only one interval measuring precipitation. From Eq. 5.4 it can be observed that when r_i equals to 1 H_t is zero.

Table 5.1: Selected summary statistics of precipitation sums and H_t for different study periods, all ending in 2017. px are the probabilities of observing x mm in a day and Hx are the probabilities of not exceeding a H_t of x.

		Precipitation					Entropy					
Start year		**p0**	**p5**	**p10**	**p20**	**mean (mm)**	**H0**	**H3**	**H4**	**H5**	**H6**	**mean H_t**
1984	**min**	0.48	0.76	0.85	0.94	2.27	0.52	0.66	0.76	0.88	0.97	1.42
	max	0.55	0.85	0.93	0.98	4.10	0.59	0.75	0.86	0.95	0.99	1.82
	mean	0.52	0.81	0.90	0.97	3.04	0.56	0.71	0.81	0.92	0.98	1.59
2001	**min**	0.48	0.75	0.84	0.94	2.27	0.51	0.66	0.76	0.87	0.97	1.31
	max	0.58	0.86	0.93	0.98	4.10	0.62	0.76	0.86	0.95	0.99	1.82
	mean	0.53	0.82	0.90	0.97	2.87	0.57	0.72	0.82	0.92	0.98	1.53
2010	**min**	0.45	0.75	0.84	0.94	2.09	0.51	0.65	0.75	0.87	0.97	1.24
	max	0.58	0.86	0.93	0.98	4.10	0.74	0.82	0.88	0.95	1.00	1.82
	mean	0.53	0.83	0.91	0.97	2.81	0.57	0.73	0.82	0.92	0.99	1.52

5.2.2 Temporal Entropy of Precipitation Triggering the Floods

The precipitation temporal entropy H_t of the flood-day (considered as previously mentioned plus/minus 12 hours from the peak) is calculated using stations with a resolution of 10 minutes. Figure 5.5 displays the temporal entropy of the precipitation event causing the flood against the PVR of the flood wave, for all flood events of two example catchments (Fig. 5.5a and Fig. 5.5b) and for the seasonal mean of each catchment (Fig. 5.5c). On the graphs the seasons are identified with different colors and the sampled POT with different markers. All catchments show decreasing trend of the PVR with increasing H_t, meaning that the flood waves with faster rise and decay are triggered by precipitation events with smaller H_t. These types of events are more frequent during summer, which can be associated with the occurrence of convective precipitation. Figure 5.5 suggests that the mean temporal entropy of the different seasons can be underestimated depending on how many POT are sampled, since it is observed that the 4POT sample has smaller H_t values than the 1POT sample.

Comparing H_t (Fig. 5.5) with the duration (Fig. 5.1) and the intensity (Fig. 5.2) it seems that the information capture with H_t might be more useful for separating flood mechanisms and hydrograph shapes. The spread of scatter plots is smaller for H_t (Fig. 5.5c) as for $D_{10min,24h}$ (Fig. 5.1c). If one looks for example at a value of PVR of 0.2, it suggests that

every precipitation duration can cause the same hydrograph shape. In fact, a better separation might be achieved with H_t as observed in Fig. 5.1c. This will be further investigated in Chap. 6.

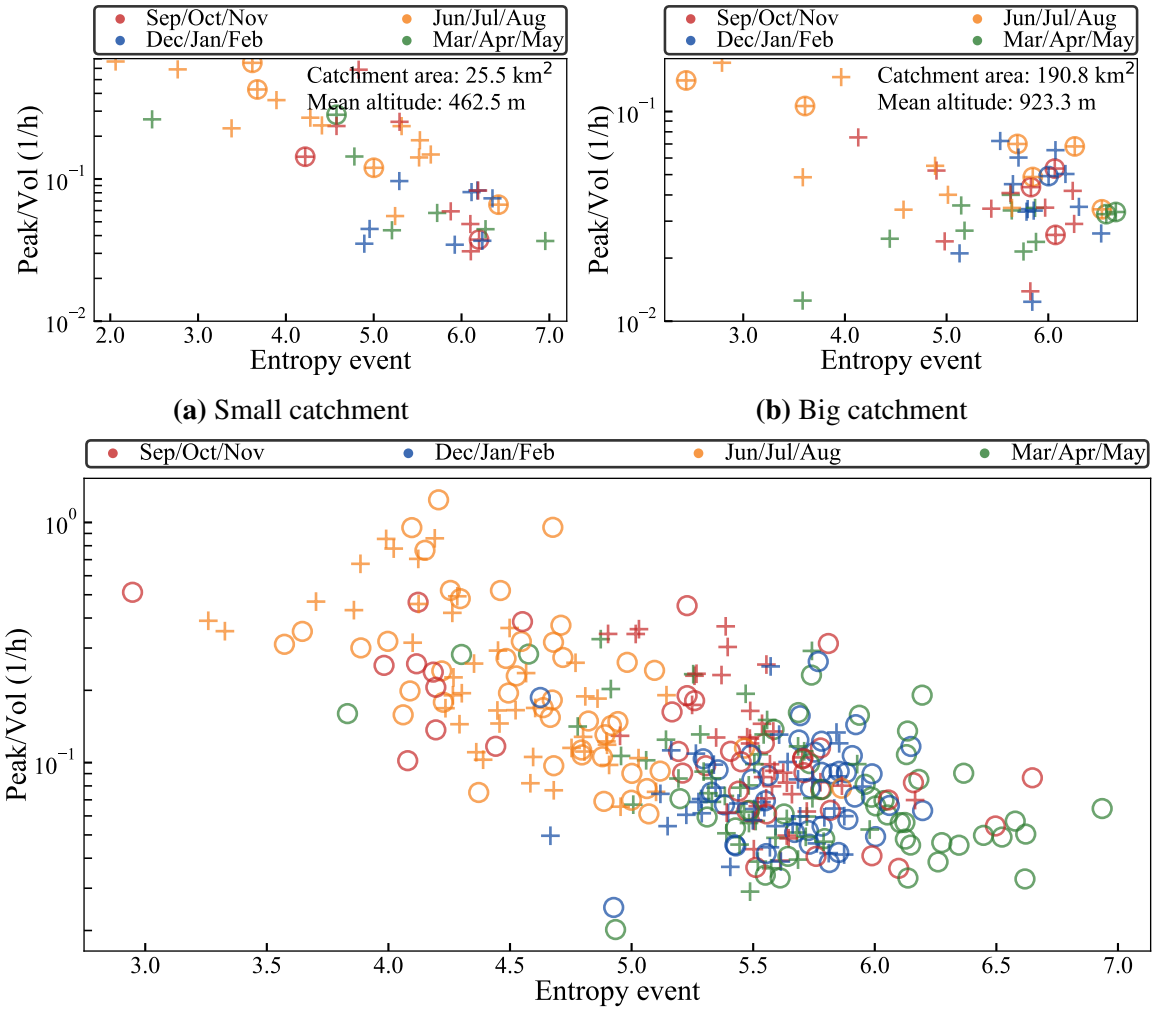

(a) Small catchment

(b) Big catchment

(c) mean per season for each catchment

Figure 5.5: Temporal entropy of precipitation versus the PVR of flood events. The colors represent the different seasons and the markers are used for identification between 1POT (circles) and 4POT (crosses) samples.

The maximum value that H_t can take is constrained by the duration of the precipitation event, which is defined as $-\log_2 \frac{1}{k}$, where k is the number of wet intervals adding information to the entropy calculation, i.e. the duration of the event. Figure 5.6 shows the entropy and duration of the meteorological event triggering the 1POT floods. The entropy and the duration are included for the case of considering only precipitation measurements (left panel) and when snow melt is included as water equivalent. The calculation of the snow water equivalent is given further in this chapter. As expected, the longer precipitation durations result in higher entropies, converging towards the limit of $-\log_2 \frac{1}{k}$. Figure 5.6 suggests that by

not considering snow accumulation and snowmelt into the meteorological event triggering the floods (Fig. 5.6a), the duration and entropy of the winter events will be underestimated. The winter events with significantly smaller H_t as the maximum entropy limit (red line in Fig. 5.6) are accounted to meteorological events with durations much longer than a day, suggesting that 24 hours around the peak are not long enough to characterize them. Different time periods can be used for calculating the temporal entropy of precipitation triggering the floods, but in this case the relative entropy (H_R) must be used. It is observed in Fig. 5.6b that summer events tend to have lower H_T and winter events are closer to the H_t maximum limit.

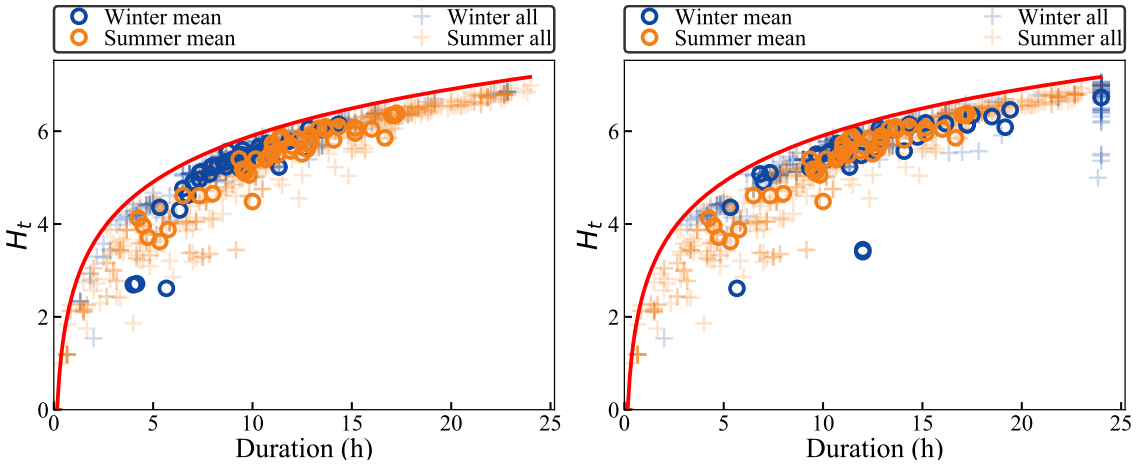

(a) without snow **(b)** with snow

Figure 5.6: Temporal entropy of precipitation H_t versus duration ($D_{10min,24h}$) of the meteorological event triggering the floods. Solely extremer events are considered (1POT), the mean of the winter and the summer events are plotted in top of all events with circles. The red line represents the limit of the maximum entropy defined as $-\log_2 \frac{1}{k}$.

5.3 Spatial Analysis of Precipitation

Entropy can also be used as a measure of association of precipitation in space. As suggested by Bárdossy and Pegram (2009) the spatial dependence of stations can be determined using entropy of the binary probabilities of three stations being jointly over or under a threshold with

$$H_s = -\sum_{i,j,k=0}^{1,1,1} p(i,j,k) \log_2 p(i,j,k)\,, \tag{5.7}$$

where H_s is the level of association of precipitation triplets located at the vertices of equilat-

eral triangles. Here, with the subscript s to avoid confusion with other entropies introduced before. The value $p(i, j, k)$ corresponds to the binary probabilities, defined by stations triples being below or above a given precipitation quantile threshold, when $i, j, k = 0$ or $i, j, k = 1$ respectively. This gives a total of the eight possible patterns (combinations of i, j, k). The partition threshold considered determines the maximum value that H_s can take. A station can only exceed a threshold with a probability of one minus the quantile. With this in mind, it is possible to compute the limits of H_s. The minimum H_s is achieved when the tree stations are complete dependent. On the contrary, the maximum is reached when they are complete independent. The independent limits for various thresholds are given in Tab. 5.2. Therefore, it is to be expected that the further H_s is from this independent value, the more associated the triples are.

Table 5.2: H_s limits of complete interdependence and independence and the maximum probability of jointly exceeding the threshold for complete independent stations.

	Complete interdependence	**Complete independence**	
Threshold	**Entropy**	**Entropy**	$p(1,1,1)$
0.5	1.00	3.00	0.125000
0.6	0.97	2.91	0.064000
0.7	0.88	2.64	0.027000
0.8	0.72	2.17	0.008000
0.9	0.47	1.41	0.001000
0.95	0.29	0.86	0.000125
0.975	0.17	0.51	0.000016
0.99	0.08	0.24	0.000001

As pointed out by Bárdossy and Pegram (2009) it is important that the triangles are nearly equilateral, to avoid ambiguities of stations being too close to each other and triples describing the spatial dependence of only two stations. They are nearly equilateral since precipitation stations are randomly positioned in space and it is, therefore, not possible to get exact equilateral triangles. The limit for accepting the triples depends on the difference of triangles sides, which is chosen to be less than 10% of the perimeter.

To evaluate the spatial dependence H_s of stations, the three dimensional two state probabilities of precipitation aggregated daily and H_t of the triples in the study area are calculated. By evaluating precipitation sums, one can determine if stations are being jointly wet or dry. Moreover, when considering H_t it is possible to establish the spatial association of the temporal entropy of precipitation, meaning that stations are jointly having an irregular event (small H_t) or uniform event (large H_t). These probabilities are obtained by counting how often each of the eight possible patterns appear. First the empirical distribution function (EDF)s of daily precipitation and H_t are obtained for all accepted stations (Fig. 5.4 and Tab. 5.1). The occurrences of triples exceeding or not exceeding the studied partition quantiles

are determined, using the EDFs to calculate the trivariate two state probabilities $p(i, j, k)$ and finally obtain H_s.

The studied thresholds for daily precipitation sums are chosen to be 0.6, 0.9, 0.975 and 0.99. The quantile of 0.6 is selected as the partition of stations being either wet or dry (Fig. 5.4a). The higher thresholds are included for later use to compare precipitation triggering the floods. The chosen quantiles for H_t are 0.7, 0.8, 0.9 and 0,99. A value of H_t of 0.7 is found to be more representative than 0.6, since some stations have values for the lower quantile ($H_t = 0$) larger than 0.6. Additionally, it is observed in Fig. 5.5 that most of the precipitation events triggering the floods have H_t values between 4 and 6, which correspond to mean quantiles of around 0.8 to 0.99 (Fig. 5.4 and Tab. 5.1).

To compare the H_s obtained for different thresholds, H_s is divided by the independent maximum, given in Tab. 5.2. In this manner, triples are more independent the closer they get to one and more independent if they tend to zero. Figure 5.7 shows the results of H_s divided by the independent limit versus the natural logarithm of the triangle area. It refers to all precipitation triples over the periods between 2001 to 2017 and 2010 to 2017. It is observed that the level of association of precipitation sums drops as the distance between stations increases, i.e. larger triangles (Fig. 5.7a and Fig. 5.7c). This agrees with the observation of Bárdossy and Pegram (2009) and Bárdossy and Pegram (2012). The same occurs for H_t (Fig. 5.7b and Fig. 5.7d), where the larger triangles have smaller association of the temporal distribution of precipitation in space.

In the case of daily precipitation aggregation (Fig. 5.7c and Fig. 5.7a) it is observed that for increasing partition quantiles the triples become more independent. For the case of daily entropy, the trend is similar, but the changes in dependence within the quantiles is smaller. The blue crosses located way below the main group in Fig. 5.7d can be explained by one station having a probability of $H_t = 0$ higher than 0.7. Figure 5.7 suggest that H_t has a higher association in space over all thresholds than the daily precipitation sums.

The two periods (2001 to 2017 and 2010 to 2017) are included for a comparison of trends as the number of triangles increases. For example, in Fig. 5.7c looking at the smaller triangles, there is first an increase of daily precipitation association followed by a decrease. There is a larger spread on the association bounds per threshold for the period 2010-2017, since there is less data to calculate the binary probabilities resulting in larger variations of the resulting H_s. It can also be accounted to the number of triangles considered in each period. Less triangles result in less spread of the association at each threshold.

Fig. 5.7c and Fig. 5.7d show that around a value of 20 of the natural logarithm of the triangle area there is a change in the spatial dependence structure of precipitation and H_t. This is defined by the change in the slope at which the association is dropping. In the following section the spatial dependence of precipitation at the occurrence of a flood is going to be analyzed. Analyzing spatial dependence of precipitation records is important since these are used as input to rainfall runoff models and predictions in ungauged catchments. Later in this chapter, these spatial distributions of precipitation are going to be compared to the

subsamples of the spatial dependence of precipitation triggering the floods.

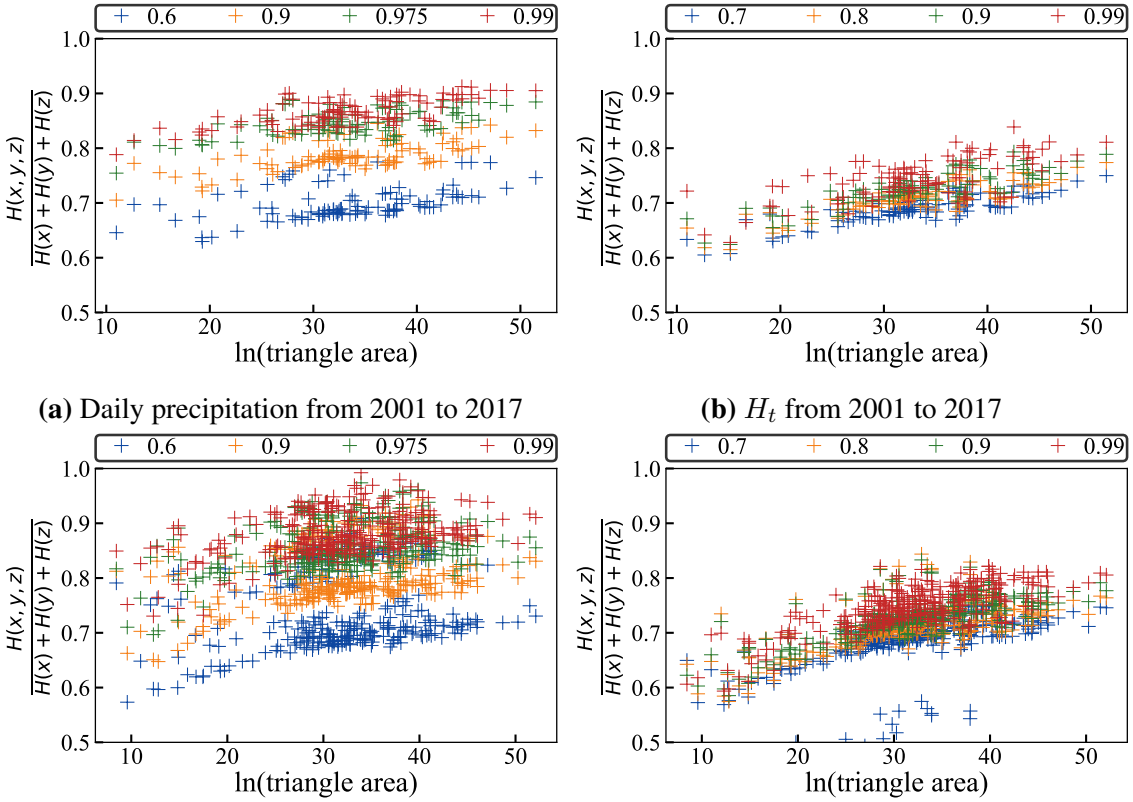

(a) Daily precipitation from 2001 to 2017

(b) H_t from 2001 to 2017

(c) Daily precipitation from 2010 to 2017

(d) H_t from 2010 to 2017

Figure 5.7: The entropy of the two state probabilities of precipitation triples is plotted versus the natural logarithm of the triangle area. The different colors represent the selected evaluation thresholds for determining if stations are mutually dry or wet, i.e. precipitation sum (a) and (c), or have an irregular or uniform temporal distribution, i.e. H_t (b) and (d).

5.3.1 Association of Precipitation Sum and Temporal Precipitation Entropy Triggering the Floods

The concept of association previously mentioned is also used to analyze the sub samples of precipitation events causing a flood. For this purpose, the probabilities of precipitation sums and temporal precipitation entropy of station triples jointly exceeding a threshold are conditioned on the occurrence of a POT. This are recoginized as $p(i, j, k|POT)$.

In this case the precipitation triples considered do not only need to satisfy the condition of nearly equilateral triangles, but they also should be representative of the catchment. Triangles are going to be accepted only if they have a given positioning with respect to a

catchment. This is intended to ensure that the results represent the actual spatial dependence and are not driven by the catchment being closer to only one of the precipitation stations. Due to the random location of stations, a unique positioning of precipitation triples with respect to the catchments cannot be achieved. To keep consistency over all catchments, the triangles fulfilling the following cases are considered. C1: the whole catchment is contained in the precipitation triangle (see Fig. 5.8a). C2: the catchment centroid is contained in the precipitation triangle (see Fig. 5.8b). C3: the catchment centroid is contained in an enclosed triangle, whose vertices are at the medians of the precipitation triangle (see Fig. 5.8c). C4: a percentage difference of the distances between the triangle vertices and the closest catchment point is achieved, meaning that the following is fulfilled $\left\{|l_1 - l_2| / \frac{l_1+l_2}{2}, |l_1 - l_3| / \frac{l_1+l_3}{2}, |l_2 - l_3| / \frac{l_2+l_3}{2}\right\} \leq x$, where l_1, l_2 and l_3 are the distances and x is the allowed percentage difference (see Fig. 5.8d). C5: like case C4 but using distances from the vertices to the centroid of the catchment (see Fig. 5.8e). C6: a percentage of the catchment is contained in the enclosed triangle formed by the precipitation triangle medians, $A_2 \geq x(A_1 + A_2 + A_3)$, where x is the selected allowed percentage (see Fig. 5.8f).

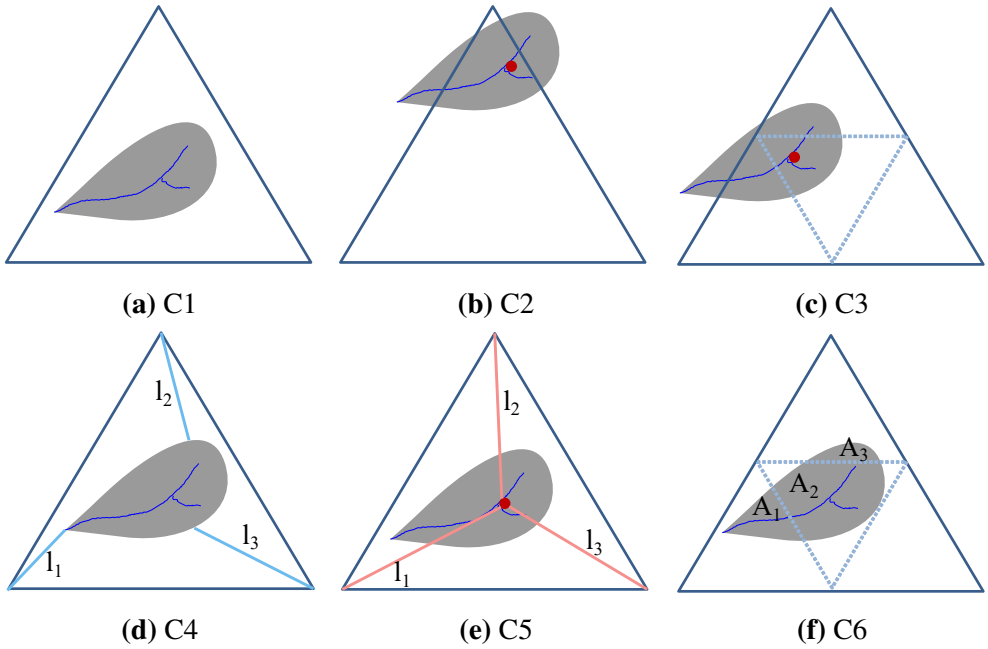

(a) C1 **(b)** C2 **(c)** C3

(d) C4 **(e)** C5 **(f)** C6

Figure 5.8: Positioning of precipitation triples and catchments for the various cases of accepting the precipitation triple. The dark blue triangle is formed by precipitation triples. The red dot represents the catchment centroid. The light blue dotted triangle corresponds to a enclosed triangle, whose vertices are at the medians of the precipitation triangle.

The eight binary probabilities of the precipitation stations jointly exceeding a threshold are used to evaluate the spatial dependence of precipitation at the occurrence of a flood. These probabilities are calculated for the sub sample of precipitation events when a POT occurred $p(i, j, k|POT)$. The $p(i, j, k|POT)$ probabilities are divided into three groups to represent flood events triggered by a precipitation event with local, total or partial coverage.

By this reasoning, if precipitation sums are considered, $p(0,0,0|POT)$ corresponds to the binary probabilities of no station exceeding the threshold and it represents a precipitation event with local coverage. Similarly, $p(1,1,1|POT)$ gives the case of all stations jointly exceeding the threshold and it indicates a precipitation event with total coverage. Finally, the remaining 6 possible probabilities describe the case of one or two stations jointly exceeding the threshold, which means a precipitation event of partial coverage triggered the flood. Likewise, if H_t is been analyzed, the probability groups $p(0,0,0|POT)$, $p(1,1,1|POT)$ and $1-p(0,0,0|POT)-p(1,1,1|POT)$ represent the cases of having locally, totally or partially the same temporal precipitation distribution, when the flood occurred. One must be aware that these probabilities depend on the partition threshold selected. If for instance, for one catchment a 0.9 threshold is chosen and the obtained $p(1,1,1|POT)$ are 0.1, 0.7 and 0.2, the catchment has a 10% , 70% and 20% likelihood of having a flood triggered by a precipitation event with local, total and partial coverage according to this threshold. This in no way means that if $p(1,1,1|POT)$ is really small, there is no precipitation measured.

Table 5.3 gives a summary of the three probability groups of precipitation sum triggering 1POT floods, according to a precipitation quantile threshold of 0.9. Two measurement periods are included, 1984-2017 and 2001-2017. The values given correspond to the average of the probabilities calculated over three groups of catchment sizes, i.e. $A \leq 20$ km^2, $20 > A \leq 40$ km^2 and $A > 40$ km^2. For each observed catchment, triples are included if they follow the cases in Fig. 5.8, for some cases there is no triangle to satisfy the positioning of the catchment with respect to the precipitation triples, those are, therefore, left blank. Comparing the exact number of the probabilities over the periods, cases and catchments sizes is not viable, since the number of triangles, catchments and data items differ and as a result the probabilities will change. Nevertheless, it is useful determine if the tendencies are similar when more records are included or more triangles are considered.

One can observe in Table 5.3 that the trends of the probabilities over all periods and cases are similar for a given threshold. For example, for the case of having a 0.9 threshold the probability of the event being of local coverage is higher than the probabilities of total or partial coverage. As the catchment size increases the probability of a 1POT flood being triggered by a precipitation with local coverage is higher than the probabilities of being of total or partial coverage, according to the 0.9 threshold. Although this effect is observed along various thresholds, it is only valid when looking at the mean over all catchments in a size group. This behavior is explained by the randomness of the locations of the stations, by the difference in triangle sizes and by the number of selected triangles, rather than being a trend over the catchment sizes. Since the catchment size groups selected for averaging the results are assigned with no objective reason, they are chosen with the intention of analyzing variations in the tendency and not with the intention of taking conclusions over the assigned group.

Table 5.3: Probabilities of a flood triggered by an event with local, total or partial coverage according to a 0.9 quantile threshold, for the periods 1984-2017 and 2001-2017. For C1-C6 the mean of the probabilities for groups of catchment sizes are calculated using the triples (see Fig. 5.8). The number of catchments (No. cat.) gives the number of catchments that have at least one triangle fulfilling the case. The symbol $\bar{\triangle}$ represents the mean number of triangles selected per catchment for the given case.

		1984-2017					**2001-2017**				
				$p(i,j,k\|POT)$					$p(i,j,k\|POT)$		
Cat. Area	**Case**	**No. cat.**	$\bar{\triangle}$	**local**	**total**	**partial**	**No. cat.**	$\bar{\triangle}$	**local**	**total**	**partial**
	C1	4	3.3	0.64	0.08	0.27	9	11.4	0.63	0.07	0.29
	C2	6	4.2	0.61	0.11	0.28	9	16.7	0.64	0.07	0.29
$\leq$ **20**	C3	-					6	3.5	0.70	0.03	0.27
km²	C4	-					3	2.7	0.61	0.02	0.37
	C5	-					3	2.0	0.61	0.02	0.37
	C6	-					5	3.4	0.68	0.02	0.30
	C1	5	2.8	0.61	0.10	0.28	9	9.1	0.69	0.09	0.21
20 $>$	C2	7	4.3	0.62	0.08	0.29	10	15.4	0.69	0.08	0.23
x $\leq$	C3	-					6	5.7	0.72	0.06	0.23
40	C4	-					2	11.0	0.68	0.10	0.22
km²	C5	-					2	10.5	0.68	0.10	0.22
	C6	-					6	4.7	0.72	0.06	0.23
	C1	2	2.5	0.69	0.06	0.25	8	7.6	0.74	0.04	0.22
	C2	5	3.2	0.67	0.04	0.28	10	16.3	0.73	0.04	0.23
$>$ **40**	C3	1	2.0	0.84	0.03	0.13	6	5.0	0.77	0.03	0.20
km²	C4	1	2.0	0.84	0.03	0.13	3	4.0	0.80	0.04	0.16
	C5	1	2.0	0.84	0.03	0.13	2	5.5	0.79	0.06	0.15
	C6	-					4	2.8	0.81	0.04	0.15

The different positioning of the catchments with respect to the triangles in Fig. 5.8 show small variations on the trends, reflecting the actual spatial dependence of the observations rather than an effect due to the selection of the stations. For the following analysis merely case C2 is going to be considered, in which the centroid of the catchment is inside the triangle (Fig. 5.8b), since the behavior for all cases is similar. Case C2 maximizes the number of selected triangles per catchment and has the most equal number of mean selected triangles and catchments within the different catchment size groups, with an average of 16.1 selected triangles for describing a catchment and 9.6 catchments for each of the three size groups. When looking at the cases in Fig. 5.8, it seems that case C2 has more chances of reflecting

the spatial dependence of only one or a pair of stations, since it is the less conservative case when it comes to the selection of the precipitation triple regarding the position of the catchment. If this were so, one would expect that the probabilities of the event being of local coverage will be higher for case C2 than for the other cases, but this effect is not observed. Therefore, case C2 will be further on used because it maximizes the available information.

With longer precipitation and discharge measurements the trends of the probabilities versus the size of the triangle are observed to be more pronounced (period 1984 to 2017). This is expected since considering more data reduces the uncertainties. For this period, only 18 catchments with areas between 10.5 and 196.0 km^2 are found in the study area. These catchments have on average four nearly equilateral triangles with consecutive 10 minutes precipitation measurements that satisfy case C2. The areas of the triangles vary between 1047.7 and 2051.6 km^2 and it is observed that these areas are large compared to the catchment areas. For the period between 2001 and 2017, 29 catchments (6.1 and 196.0 km^2) are measured and on average 16.1 triangles fulfilled case C2, with areas between 277.9 and 2650.7 km^2. The number of catchments and triangles following case C2 increases when looking at the period from 2010 to 2017. However, the period of 2001 to 2017 is selected for the following analysis, because having more years of measurements results in a more confident analysis.

Figure 5.9 shows box plots for each of the three probability groups of precipitation triggering 1POT and 4POT according to 0.6, 0.9, 0.975 and 0.99 precipitation thresholds. The data points used for constructing the box plot are the average coverage probabilities according to a given threshold for all events of a catchment, using all triangles fulfilling case C2. This means that each single box is constructed out of 29 data points (the number of catchments). As general trend it is observed that as the threshold increases the likelihood of a local coverage event increases, the likelihood of a total coverage event decreases and there is a parabolic trend for the case of partial coverage, i.e. a rising likelihood until it reaches a maximum and then it drops. Figure 5.9b indicates that as more POT are sampled on average per year, the probability of having an event with total coverage decreases according to the majority of the precipitation quantile thresholds. On the other hand, the probability that the triggering event is local increases with an increasing number of POT (see Fig. 5.9a). This implies that as fewer POT are considered, the extremer the sampled flood events are, and thus the likelihood of this event being triggered by triples jointly exceeding a given quantile raises.

Within the study area a given spatial dependence is needed for triggering a flood. On average with a 70% likelihood, triples will have spatially equal precipitation exceeding a 0.9 threshold when a 1POT takes place. This means that stations measured at least $\sim$10 mm of precipitation within the flood-day (see Fig. 5.4). It can be observed in Fig. 5.9c that even at a 0.975 quantile, which is around having 20 mm of precipitation (see Fig. 5.4 and Tab. 5.1), there is a mean probability of 50% that at least one station (partial coverage) will exceed the threshold. This is the case for both 1POT samples and 4POT samples. These effects are also observed in the other studied periods, with the difference that with a decreasing number of years the spread of the probability of a flood driver increases, whereby it can be either a local event, or an event with total or partial coverage. This is expected since the uncertainties

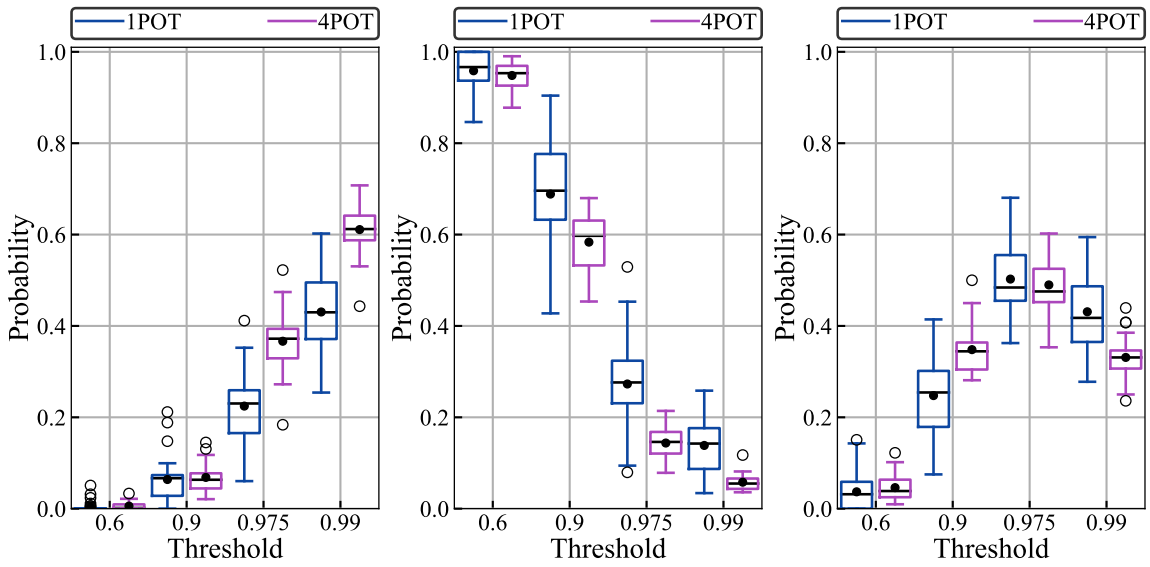

(a) Local **(b)** Total **(c)** Partial

Figure 5.9: Probabilities of a precipitation event triggering the floods being of (a) local, (b) total or (c) partial coverage according to various thresholds. One blue and one violet box plot belong to each threshold, corresponding to 1POT and 4POT respectively. 29 catchments with triangles selected using case C2 are considered, for the period from 2001 to 2017. The full black dots correspond to the mean.

increase with less information, making the previous statements about the spatial behavior of $p(i, j, k|POT)$ less reliable.

The plots in Fig. 5.10 and Fig. 5.11 can be viewed as a detailed representation of a box plot from Fig. 5.9 for the 0.9 and 0.975 thresholds. In these cases, a variation of the probabilities due to the distance between the triples can be noticed. Additionally, the catchments are separated into three groups according to their sizes. i.e. $A \leq 20$ km^2, $20 > A \leq 40$ km^2 and $A > 40$ km^2. The probabilities are identified using different markers ($\times$, $+$ and $\circ$). Every triangle size must contain at least one time all of the three markers, which represents the joint probabilities of a triangle for a given catchment. Having more than three markers per triangle size means that the same triangle is considered for more than one catchment. For example, in Fig. 5.10a the six points at the smallest triangle size represent two catchments that are being separately described by the same triple, but the probabilities of floods being triggered by precipitation with local, total or partial coverage are different.

Both Fig. 5.10 and Fig. 5.11 show a slightly decreasing trend on the triples interdependence as the triangle area increases, no matter the threshold and the catchment group considered. It is more significant when looking at the 4POT samples. This effect is observed in the decay of total coverage, i.e. blue $\times$, and the rise of partial coverage, i.e. red $+$, as the triangles are bigger. Stations are more independent since the probability of jointly exceeding a threshold decreases and the probability of partially exceeding a threshold increases. There

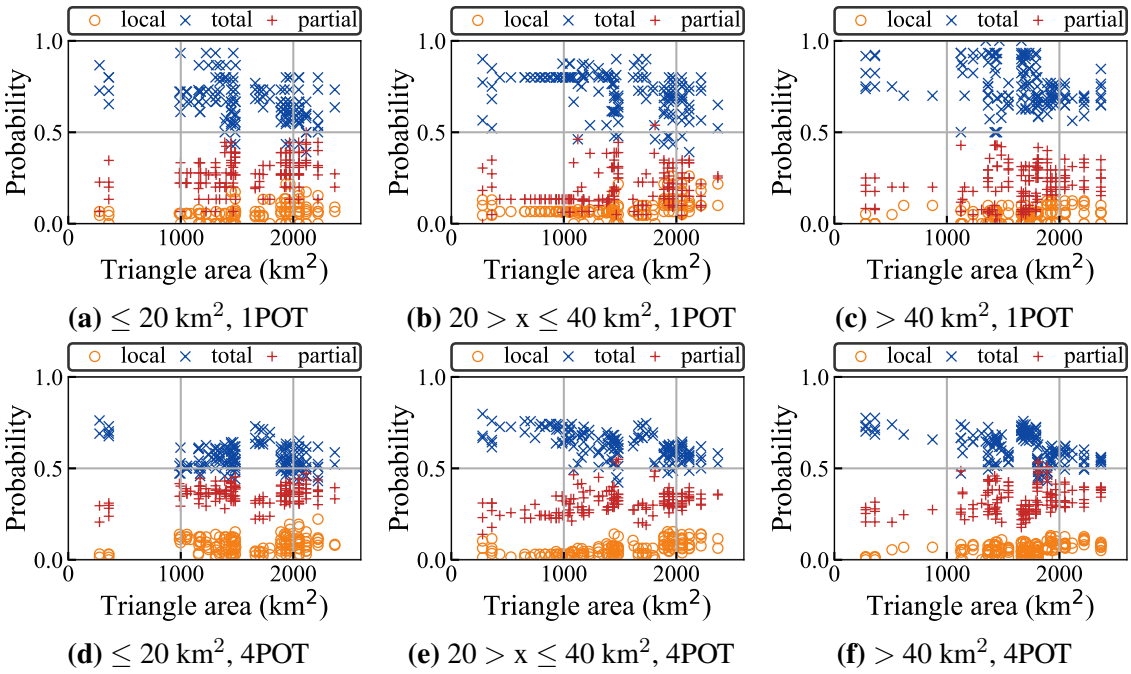

(a) ≤ 20 km^2, 1POT **(b)** $20 > x \leq 40$ km^2, 1POT **(c)** > 40 km^2, 1POT

(d) ≤ 20 km^2, 4POT **(e)** $20 > x \leq 40$ km^2, 4POT **(f)** > 40 km^2, 4POT

Figure 5.10: Binary probabilities of precipitation triggering the floods for a 0.9 threshold. First row (a, b and c): 1POT sample. Second row (d, e and f): 4POT sample. At each panel the catchment sizes vary from left to right.

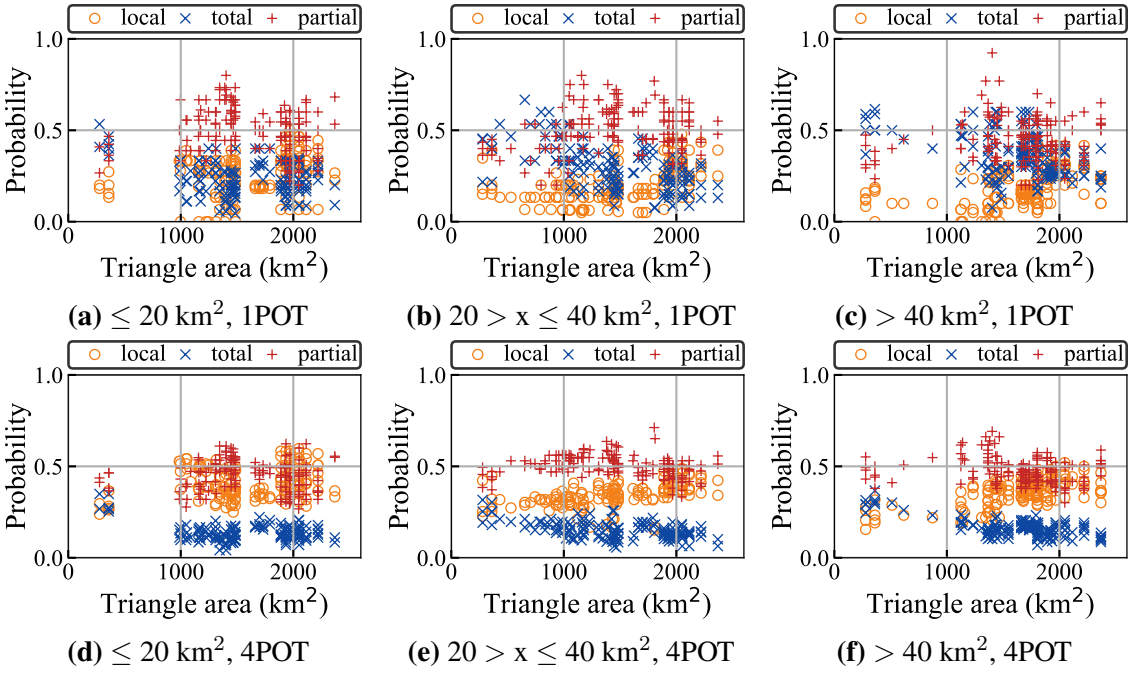

(a) ≤ 20 km^2, 1POT **(b)** $20 > x \leq 40$ km^2, 1POT **(c)** > 40 km^2, 1POT

(d) ≤ 20 km^2, 4POT **(e)** $20 > x \leq 40$ km^2, 4POT **(f)** > 40 km^2, 4POT

Figure 5.11: Binary probabilities of precipitation triggering the floods for a 0.975 threshold. First row (a, b and c): 1POT sample. Second row (d, e and f): 4POT sample. At each panel the catchment sizes vary from left to right.

is no observed difference of the spatial dependence of precipitation between the catchment sizes according to threshold 0.9. For the case of a higher quantile 0.975, a light tendency of smaller catchments (see Fig. 5.11) having higher probabilities of floods being triggered by a local precipitation event is observed, whereas bigger catchments are more likely to be triggered by a total precipitation event. When looking at the top panel of Fig. 5.11 there is a smaller separation between total and partial (blue $\times$ and red$+$) events as the catchment sizes increase. This behavior is expected, since smaller catchments are more sensitive to convective precipitation events, which are less spatially distributed, and floods in bigger catchments take place more frequently when precipitation is present across the whole catchment.

As observed in Fig. 5.10 and Fig. 5.11 there is a high variability over the values of each probability group. These variations can be explained due to: the records length, the fact that there is no constant number of triangles per catchment, the randomness in the position of the stations, the more uniform distribution of triangle sizes and the occurrence of different flood mechanisms.

The binary probabilities of temporal precipitation entropy H_t are studied to get a further insight on the spatial dependence of precipitation at the occurrence of a flood. In Fig. 5.12 the probabilities of a precipitation event triggering the floods, which has locally, totally or partially the same temporal distribution, are given. There is an observed trend of a decrease on the spatial dependence, i.e. event with total coverage, as the threshold increases. Samples with less POT have on average higher probabilities of triples jointly exceeding the H_t threshold. Figure 5.12c shows likelihoods of partial coverage from 0 to 40 % through the thresholds while in Fig. 5.9c it varies from 0 to 70%. This is also reflected in Fig. 5.7 where the entire observations of precipitation are used, without sampling according to the occurrence of POT. In this case, the entropy of the binary triples is further away from the value of 1.0 over all thresholds, i.e. complete independence.

In Fig. 5.12 the probabilities of jointly not exceeding or partially exceeding a quantile of around 0.7 are lower than 2%. As it is shown previously on this chapter in Fig. 5.4 and Tab. 5.1 a quantile value of 0.7 of the temporal entropy of precipitation corresponds to a $H_t \approx 3$, which indicates there is a minimum temporal entropy required for triggering a flood. The value of $H_t = 3$ is consistent with the previous minimum mean H_t observed over all catchments (see Fig. 5.5). In Fig. 5.12 it is observed that around a threshold of 0.9 the variability of the probability groups is at its maximum, with a median likelihood of 18, 70 and 22% of events H_t being locally, totally or partially equal distributed in space if looking at the 1POT samples. This larger variability agrees with the uncertainty of the flood mechanisms being triggered by a given H_t and the apparent mean H_t boundary between summer and winter events observed in Fig. 5.5, which occur around a value of $H_t = 5$ which is close to the 0.9 quantile (see Tab. 5.1).

In a box plot, those values marked as individual points correspond to outliers. Nevertheless, in this case a box plot is only considered to facilitate the visualization of the results, and, therefore, the empty dots in Fig. 5.12 should not be considered outliers. They represent catchments, which are more responsive to a given meteorological event. For example,

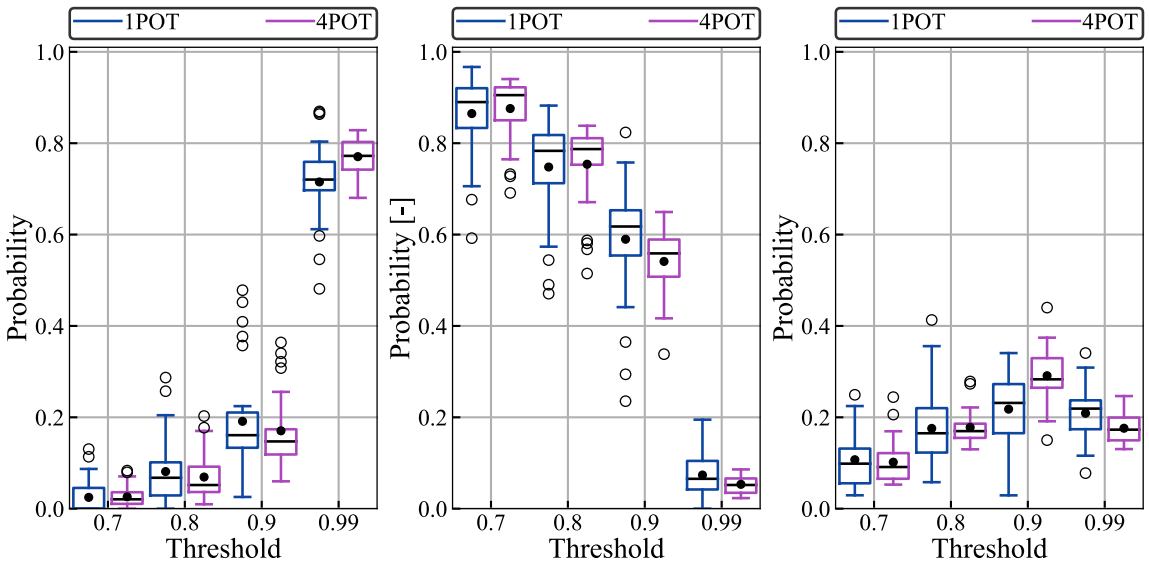

(a) Local **(b)** Total **(c)** Partial

Figure 5.12: Probabilities of a precipitation event triggering the floods having in space (a) locally, (b) totally or (c) partially the same temporal distribution over the flood day according to the threshold. One blue and one violet box plot belong to each threshold, corresponding to 1POT and 4POT respectively. 29 catchments with selected triangles using case C2 are considered, for the period from 2001 to 2017. The full black dots correspond to the mean.

looking at the partition quantile of 0.9, there are some catchments located around the 40% likelihood of having a local H_t. These catchments are more prone to react to isolated events, like thunderstorms. I one looks at the H_t from the neighboring station of these five catchments marked as outliers, it is observed that the summer events present a $H_t = 3.8$ in average, this in contrast to a $H_t = 5.1$ of the summer events of all catchments.

For the case of the binary probabilities of H_t also scatter plots of the probabilities versus the triangle area are shown (Fig. 5.13 and Fig. 5.14). Analogous to the plot shown before for the case of precipitation sums, they are a detailed representation of the box plots in Fig. 5.12 for H_t thresholds of 0.9 and 0.975 respectively. Similar to the precipitation sum (see Fig. 5.10 and Fig. 5.11), the spatial dependence of H_t slightly drops as the triangle area increases especially for the case of considering 4POT. There is no significant trend observed within the chosen catchment groups, apart from small catchments having in some cases higher probabilities of local H_t, when one compares Fig. 5.14a with Fig. 5.14c. This uniformity over the catchment sizes, exposes the variability of flood mechanisms and the hydrological cycle, and it shows that the catchment area is not enough to identify changing patterns of the meteorological input triggering the floods. There are other factors as soil moisture, slope, land use, soil, etc. that influence the catchment respond.

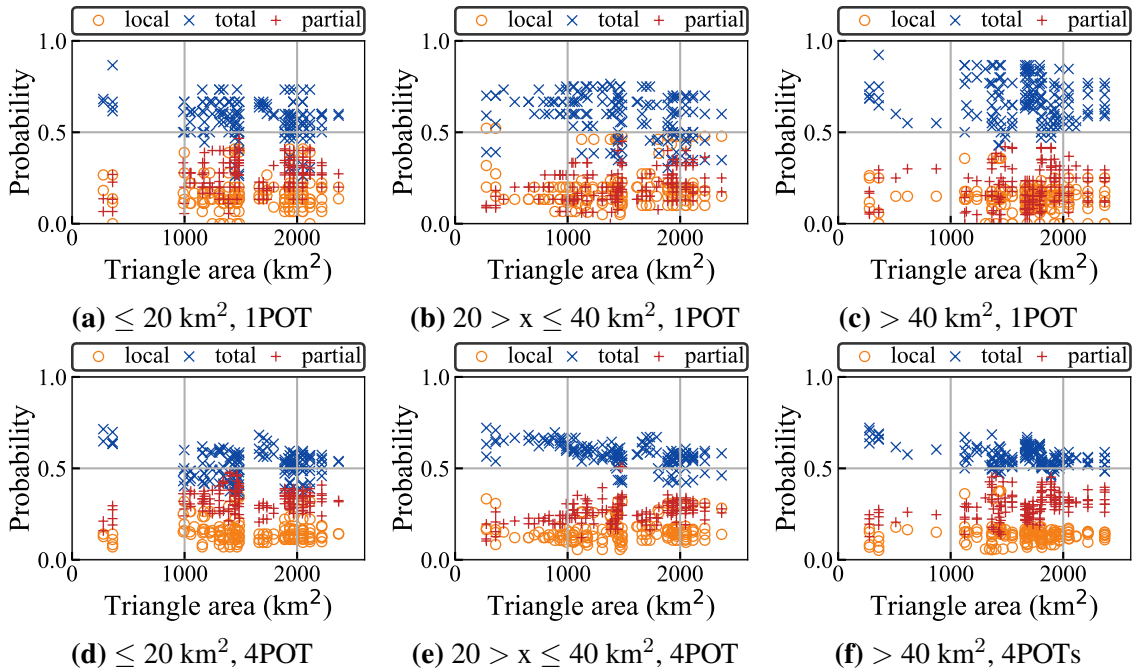

Figure 5.13: Binary probabilities of temporal precipitation entropy triggering the floods for a 0.9 threshold. First row (a, b and c): 1POT sample. Second row (d, e and f): 4POT sample. At each panel the catchment sizes vary from left to right.

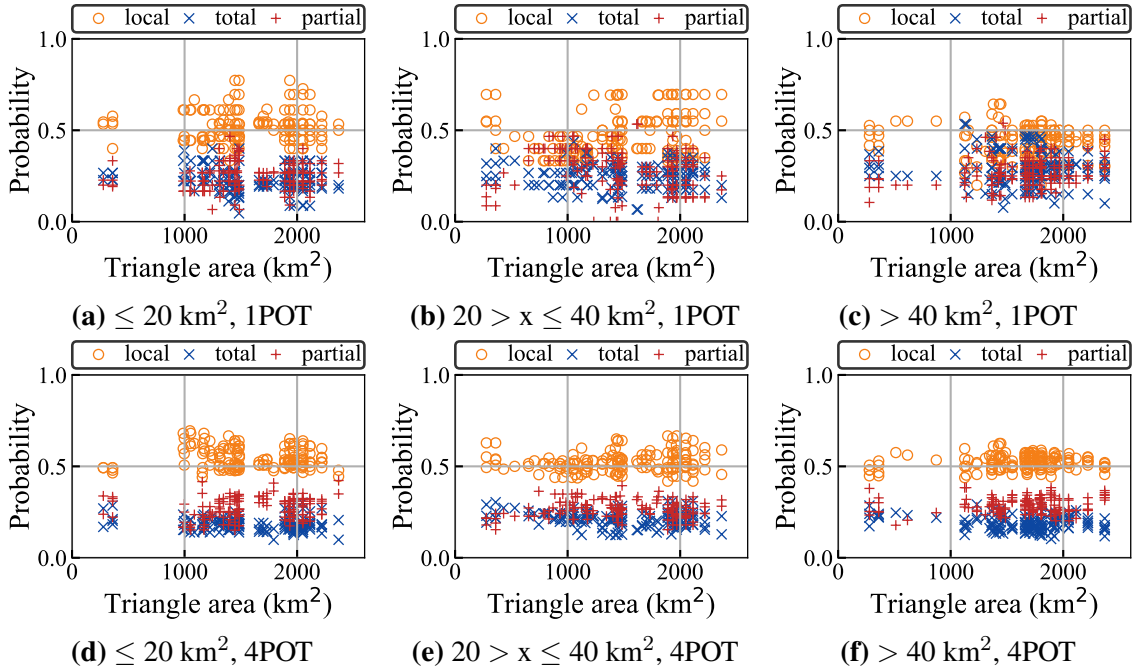

Figure 5.14: Binary probabilities of temporal precipitation entropy triggering the floods for a 0.975 threshold. First row (a, b and c): 1POT sample. Second row (d, e and f): 4POT sample. At each panel the catchment sizes varies from left to right.

One can conclude that in the study area 1POT flood samples are likely (with a median of 70%) triggered by precipitation sums with total spatial coverage exceeding the 0.9 quantile (see Fig. 5.9). As the quantile increases, the probability of observing joint occurrence in space decreases. If more POT are considered, the probability of observing a total event, according to the larger quantiles, i.e. values greater than 0.9, decreases and flood events are more likely to be triggered either by a local precipitation event or by a partial precipitation event. The selection of the POT sample is important to assess the spatial dependence of the extremes, since triples have a larger spatial dependence at the occurrence of extremer flood events. As for the temporal distribution of precipitation within the flood day a homogeneous spatial H_t is required, but it does not imply that this temporal distribution must be uniform, on the contrary it changes due to the different flood mechanisms, which is shown in Fig. 5.3, Fig. 5.6, Fig. 5.13 and Fig. 5.14. Both, the spatial dependence of the entire precipitation records and the observations of precipitation conditioned by the occurrence of a flood have previously been studied. In the following chapter, a comparison between this two is included, evaluating the potential of describing precipitation triggering the floods out of precipitation observations.

5.3.2 Divergence between Precipitation Observations and Precipitation Triggering the Floods

Rainfall-runoff methods for estimating floods, typically use extreme precipitation observations to calculate an expected runoff at ungauged catchments. Some studies have shown that the spatial distribution of precipitation affects the model performance and hydrograph shapes (Sivapalan et al., 2005; Bárdossy and Das, 2008; Zehe et al., 2005). In this section, the uncertainty introduced to the modeling of floods due to the representation of the spatial dependence of precipitation sums and the temporal precipitation entropy H_t are analyzed. This is done by comparing the distribution of binary triples of precipitation stations $p(i, j, k)$ and the conditional distribution of precipitation triples at the occurrence of a flood $p(i, j, k|POT)$. The concept of divergence from information theory is used.

Kullback and Leibler (1951) defined a measure of divergence for comparing two distributions as

$$D_{kl} = \sum_{i=1}^{N} P(x_i) \log \frac{P(x_i)}{Q(x_i)}\,, \tag{5.8}$$

where D_{kl} is the Kullback-Leibler divergence and P and Q are two distribution functions. In information theory, it is defined as the expected code length for a language written in two different encodings. If $P(x)$ is the original language, D_{kl} measures the information cost of using another language $Q(x)$ to transmit a message. This cost can be interpreted as the divergence D_{kl} and tells how much longer the code will be or how much it will differ from

the original. It measures the uncertainty around the random variable X when a probability distribution function $Q(x)$ is used instead of the true one $P(x)$. It is not a distance but a divergence, since it is not symmetrical and it thus depends on which distribution is considered as the true one (Weijs et al., 2010).

The divergence D_{kl} requires absolute continuity of $P(x)$ with respect to $Q(x)$, meaning that for each $P(x) > 0$ there must be a $Q(x) \neq 0$. Otherwise, D_{kl} is going to be undefined when $Q(x) = 0$ (Lin, 1991). Here, the objective is to assess how much uncertainty is introduced, when using the precipitation distribution with no information about the occurrences of floods $p(i, j, k)$ as the transmitting language $Q(x)$, given that the original language or the true distribution $P(x)$ is considered to be $p(i, j, k|POT)$. Under this assumption, it is true that for each $P(x) > 0$ the case $Q(x) \neq 0$ is given. However, for every catchment and threshold, it is not necessarily that $P(x) \neq 0$ for all $Q(x) > 0$. This means that all binary probabilities $p(i, j, k)$ that exist in a given precipitation triple do not need to exist in the subset of probabilities conditioned on the occurrence of the floods $p(i, j, k|POT)$. Further, D_{kl} is always positive such that $D_{kl}\,[0, \infty]$ can take values between 0, $+\infty$. The divergence has a minimum $D_{kl} = 0$ if $P = Q$ for every x. For these values of x that have low probabilities (very improbable to occur) according to Q, but exist with high probabilities in P, D_{kl} increases rapidly. It can even go to $+\infty$, if $Q(x) = 0$ (Singh, 2013).

The studied probabilities $p(i, j, k)$, not conditioned on the occurrence of the floods, are bounded by the selected threshold. As the threshold increases, the probabilities of the stations to have precipitations above the threshold decrease, regardless of whether the stations are totally dependent or independent. This implies that as the threshold increases a larger penalty is considered, if the stations are not jointly above the threshold. This means that D_{kl} is going to be larger for $(i, j, k) = (1, 1, 1)$, given that for larger thresholds $p(1, 1, 1)$ is less probable to occur.

Lin (1991) proposed a divergence based on the Kullback-Leibler divergence, which resolves some of the difficulties mentioned above. The Lin divergence K between two distributions P and Q is defined as

$$K = \sum_{i=1}^{N} P(x_i) \log \frac{P(x_i)}{\frac{1}{2}P(x_i) + \frac{1}{2}Q(x_i)}\,, \tag{5.9}$$

K is a divergence measure that does not require P and Q to be absolutely continuous. It is defined for all x, no matter if $P(x) = 0$ or $Q(x) = 0$, thus $K\,[0, 1]$. If $P = Q$ for every x then $K = 0$.

Here, the K is calculated using the precipitation distributions from the whole observation period $p(i, j, k)$ as $Q(x)$, the transmitting language. This distribution is compared with the case of having $p(i, j, k|POT)$ as $P(x)$, the original or true language. For this purpose, the probabilities $p(i, j, k)$ and $p(i, j, k|POT)$ calculated in the previous sections are used.

Here, also the precipitation triples are selected according to condition C2 of Fig. 5.8. In Fig. 5.15 the results of the obtained K are shown. Both, the case of precipitation sums and precipitation temporal entropy are considered (see left and right panels of Fig. 5.15). The various thresholds used for calculating the association of the triples are given in the horizontal axis. Additionally, the blue box plots correspond to the 1POT case and the violet ones to the 4POT case. Both, the precipitation sums and the temporal precipitation entropy, show a decrease in K as the threshold increases. This indicates that choosing the right spatial distribution of precipitation can have an effect on modeling the floods, as a constant K is not observed across the thresholds. As expected, the divergences decrease as more POT are considered. When the number of POT is larger more observations are sampled from the $p(i, j, k)$ distribution to build $p(i, j, k|POT)$ and, therefore, the penalty of encoding P with Q is smaller.

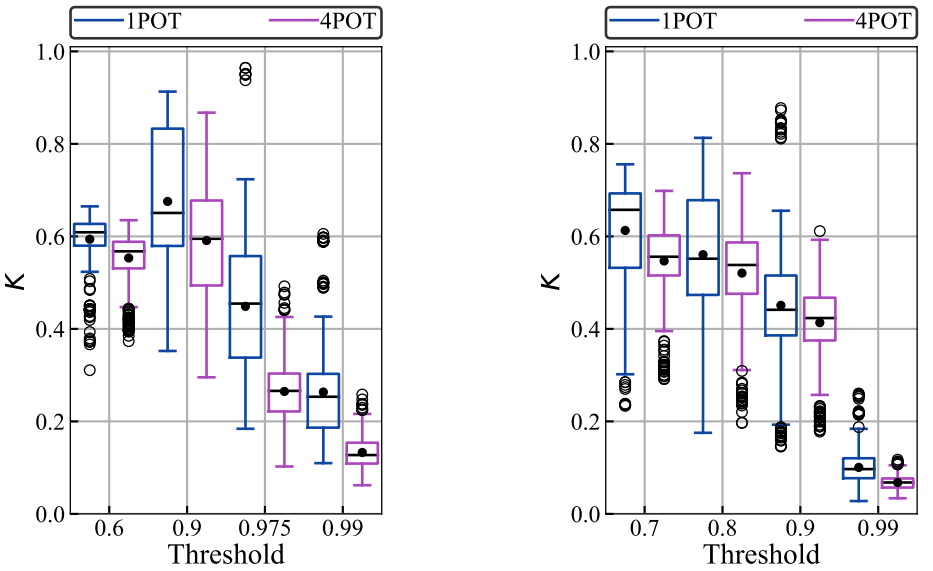

(a) Precipitation sums

(b) Temporal precipitation entropy

Figure 5.15: Divergence between the association of precipitation triples conditioned on the occurrence of flood events $p(i, j, k|POT)$ and precipitation triples for the whole observation period $p(i, j, k)$. In (a) the association for the case of precipitation sums are given and in (b) those for the temporal precipitation entropy. One blue and one violet box plot belong to each threshold, corresponding to 1POT and 4POT respectively. 29 catchments with triangles selected using case C2 are considered, for the period from 2001 to 2017. The full black dots correspond to the mean.

There is an added uncertainty when the distribution of precipitation records is used to describe the spatial dependence of precipitation causing a given POT. Further research to understand the sources of this uncertainty is required. It might be explained by the effects of precipitation and soil moisture seasonality, as for the case in the UK (Ledingham et al., 2019) or Austria (Sivapalan et al., 2005). Moreover, the binary probabilities $p(i, j, k)$ are obtained within a duration of one day. An analysis to understand the spatial behavior under

longer and shorter durations could be useful for understanding the spatial association of precipitation triggering different flood mechanisms, ex. convective precipitation triggering flash floods. Further, no snow water equivalents are considered until this stage. This might be a relevant factor influencing the observed association of the winter events. Additionally, a seasonal analysis is not carried out for the divergence within this study. Further research can consider the season of the year in which the events occurred, to get further insight on the spatial distribution of precipitation triggering the floods.

5.4 Temperature and Snow

At the presence of winter floods, temperature is an important parameter to determine snow accumulation and snowmelt. If snow is not considered, the meteorological event is underestimated, as already suggested in Fig. 5.6. From the 3189 4POT, 1604 took place in winter, i.e. October, November, December, January, February and March. The temperature change between the flood day and the mean temperature over two days before the flood showed that around 70% of these events had on average 2 °C positive temperature differences, indicating that there is a temperature increase at the occurrence of the floods. Additionally, the temperature standard score at the occurrence of a flood is calculated, to determine how unusual the temperature at the flood-day is. The standard score Z_{flood} is calculated as follows

$$Z_{flood} = \frac{T_{flood} - E\left(T\right)}{\sigma\left(T\right)}\,, \tag{5.10}$$

where T_{flood} is the temperature at the day the event occurred, $E\left(T\right)$ is the expected temperature and $\sigma\left(T\right)$ is the variance of the temperature. Both, $E\left(T\right)$ and $\sigma\left(T\right)$ are calculated using the temperature records of 30 days before the flood event. From the winter 72% of the floods have a positive Z_{flood}, i.e. these floods presented an increase in temperature. In 38% percent of the cases, Z_{flood} is greater or equal to one, with an average of 1.8 standard deviations away from the mean over the previous 30 days. These larger increases of temperature are observed more frequently in December, January, February and March, months that will most likely present snow melt floods in the study area.

Figure 5.16 shows the runoff coefficient of winter floods for all catchments when no snow is considered. This means that the runoff coefficient is computed as the runoff divided by the sum of the precipitation triggering the flood event, without considering any snow water equivalent. In total, 53 winter floods have runoff coefficients greater than one, which means that the volume of water measured at the discharge station is bigger than the precipitation observed. There is a possibility, that the neighboring precipitation station does not capture the volume measured at the discharge station, due to the spatial heterogeneity of rainfall and cloud formation. Nevertheless, this is less expected in winter, when events are spread in space, in contrast to summer where convective precipitation events occur frequently and

could have been missed by a given station. The high runoff coefficients in winter are explained by missing the discharge volume coming from snowmelt and will be included using the degree-day method.

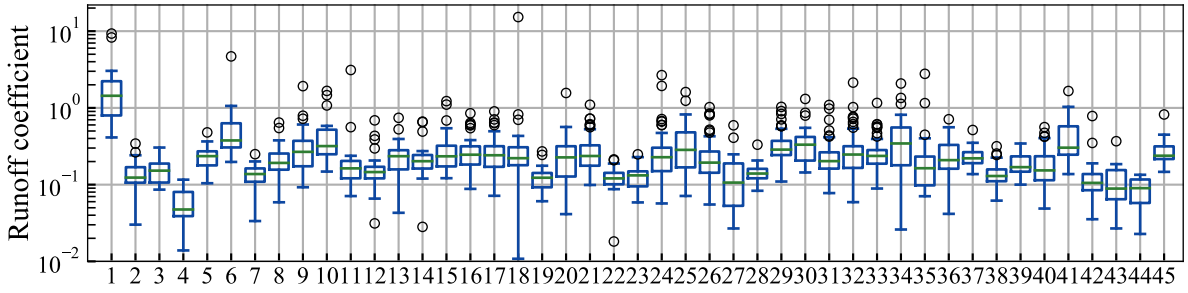

Figure 5.16: Runoff coefficient of winter floods without considering snow. All 4POT that occurred in winter, i.e. October, November, December, January, February and March, are used for generating the plot.

The degree-day method is a simple method for including snowmelt into the meteorological event. It is used in this study and included in a snow routine composed of two steps: snow accumulation SP_d and snowmelt SM_d. Precipitation accumulates as snow with a ratio η in mm per °C per day, when the mean daily temperature T_d is below the specified temperature threshold T_t, giving

$$SP_d = \eta(T_t - T_d)\,. \tag{5.11}$$

On the contrary when T_d exceeds the chosen threshold T_t snow will melt, if there is available snow accumulated. This results in

$$SM_d = \eta(T_d - T_t)\,. \tag{5.12}$$

No optimization of the snow routine is done since it is out of the scope of the study. The value η, at which snow accumulates and melts, is considered to be 2.5 mm/°C and the T_t is fixed at 0 °C. Refreezing is not taken into account, since the focus here is on independent flood hydrographs and not on the whole discharge time series. Within the duration of the flood, the accumulated liquid water equivalent SM_d is assumed to add to the precipitation event with no restriction of snowpack retention or refreezing in contrast to Bergström et al. (1992) and Staudinger et al. (2014).

When including snow into the calculation of the precipitation volume, 20 from the 53 flood waves with runoff coefficients greater than one, resulted in runoff coefficients smaller than one. The average runoff coefficient decreases from 0.32 to 0.27 when snow is considered. This means that the amount of precipitation triggering the floods is underestimated by not

considering snow. Fig. 5.17 shows the total precipitation sums when considering snow versus the sums without snow for the winter flood events. If snow is included, 15% of the winter floods presented changes in the amount of precipitation. The maximum change in volume is 29.4 mm. As it is shown, the total volume is underestimated if snow is not considered. Nine events resulted in a reduction of the volume when snow is included. One reason for this can be the chosen T_t used for accumulating snow. For these events, precipitation is accumulated as snow, since the temperature is below T_t. Nevertheless, it could be that precipitation did not fall as snow even though the temperature is below the threshold.

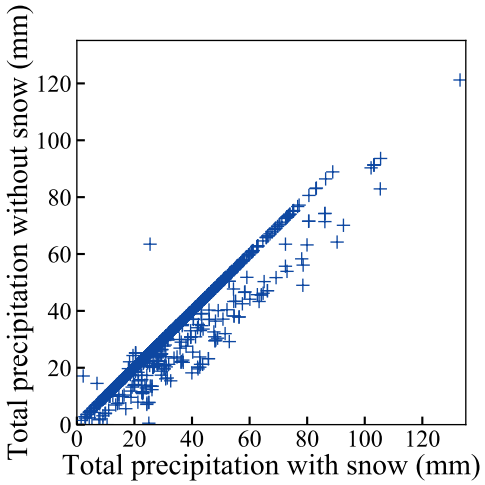

Figure 5.17: The total water equivalent, taking snow into account, is plotted against the observed precipitation for the winter events.

5.5 Antecedent Precipitation Index

Tarasova et al. (2019) highlighted the importance of the inclusion of antecedent moisture condition to identify causation of floods. One of the goals of this research is to estimate flood events considering different flood mechanisms. The antecedent precipitation index API is an indicator of the catchment soil moisture and is commonly used when no soil moisture records are available, as it is in the case of the studied catchments. It is defined as

$$API = \sum_{i=1}^{N} P_d(t_{0-i}) \cdot \alpha^i \,, \tag{5.13}$$

where P_d is the precipitation aggregated daily for the t_{0-i} day over N total of days. The number N of antecedent days varies normally between 5 to 30 days. With the value of α it is assumed that the recession of soil moisture after a precipitation event is exponential. The larger the chosen parameter α, the smaller the assumed precipitation losses due to infiltration

and evapotranspiration. A value of $\alpha = 0.9$ is commonly used in literature. Nevertheless, this value can variate according to the region and characteristics of the catchments. As shown before the inclusion of snow matters and, therefore, for the calculation of the API, the snow routine explained Chap. 5.4 is also considered. Thus, the API is calculated with the liquid water equivalent.

In Figure 5.18 the mean seasonal API versus the PVR is plotted for both the 1POT and 4POT samples. The API is calculated for the period of 30 days previous to the flood event with $\alpha = 0.9$. As revealed by Scherrer et al. (2007) there is a high variability in the processes influencing runoff formation in Switzerland, which is also observed here with API values between 2 and 101 mm for the 1POT samples. The authors found out that depending on the dominant runoff process the effect of soil moisture on the runoff generation varies. This results in some catchments not being sensitive to antecedent rainfall conditions, due to high infiltration capacities and deep percolation, and other catchments with a strong relationship between the soil moisture and the runoff coefficient.

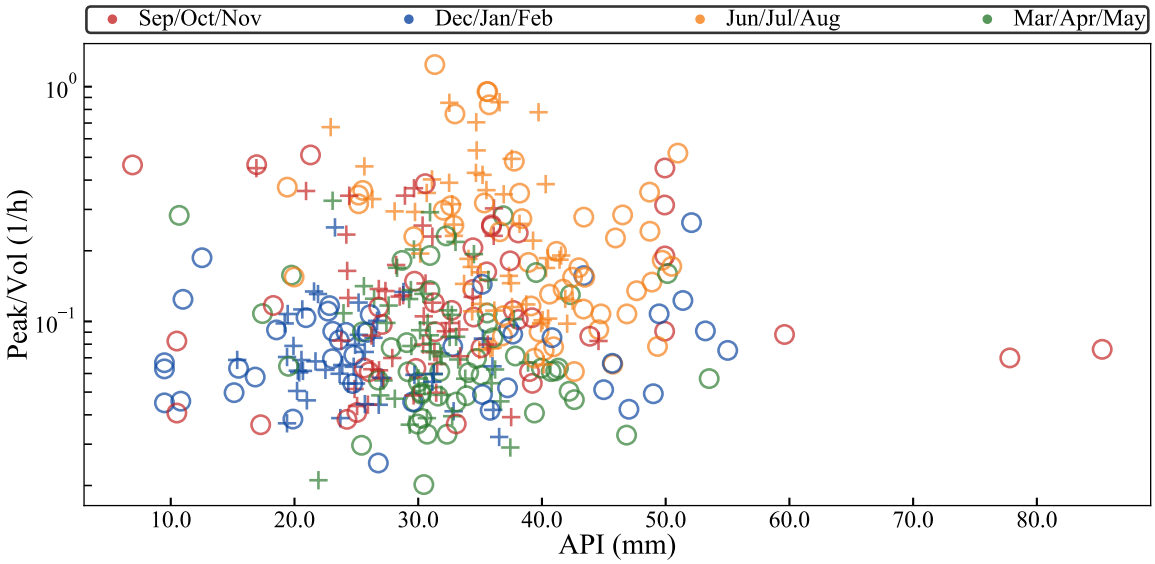

Figure 5.18: API versus the PVR of flood events. The colors represent the different seasons and the markers are used for identification between 1POT (circles) and 4POT (crosses) samples.

Although the relationship between API and the PVR is weak resulting in high variability in both the PVR and the API, some tendencies can be observed in Fig. 5.18 and Tab. 5.4. In Tab. 5.4 the mean seasonal API over all catchments for the 1POT and 4POT samples are given. The values indicate that summer events have on average larger APIs as winter events. This is consistent with the occurrence of higher temperatures in summer resulting in larger precipitation losses and, as consequence, larger precipitation amounts are required to achieve wet soil conditions, which favor larger runoff generation. Figure 5.18 suggest a decreasing trend of the PVR as the API increases for the summer flood (plotted in yellow). This is also consistent with larger precipitation losses, due to larger evaporation rates in summer. The

weak dependency between the PVR and the API, suggest that the same API value can have a different meaning in winter as in summer, given the difference in the evapotranspiration potential.

Table 5.4: Mean seasonal API [mm] triggering the floods. The mean API of each season is calculated for the 1POT and the 4POT samples.

	winter	spring	summer	fall
1POT	27.8	34.6	39.7	33.6
4POT	23.7	31.3	35.8	29.6

Further, it is important to identify, if the information contained in the API series is useful to differentiate between a random meteorological event and a meteorological event triggering a flood. The idea is to distinguish whether or not, the empirical distribution function (EDF) of the API triggering a POT can be sampled from the EDF of an API sample that is independent of the flood event. For this evaluation two non parametric statistical tests are chosen, the Wilcoxon rank-sum test and the Kolmogorov-Smirnov test.

The Wilcoxon rank-sum test is equivalent to the Mann-Whitney U test (Kottegoda and Rosso, 2008). The Wilcoxon rank-sum test uses the ranks of the observations to quantify if two samples, assumed to have the same distribution, have the same location against a shift of the distributions. The Wilcoxon rank-sum statistic W_n is defined as

$$W_n = \sum_{i=1}^{n} iZ_i \,, \tag{5.14}$$

where i is the rank of the observation assigned joined to all observations in both samples. This means that if $X = X_1, X_2 \ldots X_{n_1}$ and $Y = Y_1, Y_2 \ldots Y_{n_2}$ are the two samples studied, the ranks are assigned to all observations in X and Y. The observations are ordered and the ranks are allocated until $n = n_1 + n_2$ is reached. Here, Z_i is the indicator function, which has a value of 1 if the i^{th} observation belongs to sample X and 0 if it belongs to Y (Gibbons and Chakraborti, 2003; Kvam and Vidakovic, 2007). The W_i statistic is proportional to the size of the samples tested. For this reason, to compare between different EDFs it is decided to use the standardized form of W_n, defined as:

$$Z_W = \frac{W_n - E(W_n)}{VAR(W_n)} \,, \tag{5.15}$$

where Z_W is the standardized rank-sum statistic and $E(W_n)$ and $VAR(W_n)$ are the mean and the variance of W_n, given as

$$E(W_n) = \frac{n_1(n_1 + n_2 + 1)}{2}\,,$$
$$VAR(W_n) = \sqrt{\frac{n_1 n_2 * (n_1 + n_2 + 1)}{12}}\,. \tag{5.16}$$

The Kolmogorov-Smirnov test measures the largest distance between two EDFs. The Kolmogorov-Smirnov maximum absolute distance $D_{m,n}$ is defined as

$$D_{m,n} = \sup_x |F_m(x) - G_n(x)|\,, \tag{5.17}$$

where $F_m(x)$ and $G_n(x)$ are two EDFs of two samples with sizes n and m respectively (Kottegoda and Rosso, 2008). Here the supremum may be considered as the maximum deviation between two EDFs.

For both tests the EDF of the API triggering 1POT flood events are compared to the EDF of various API samples, which are not conditioned on the occurrence of the flood events. The daily series of API used for the tests are calculated using various recession coefficients α. This gives additional information about the memory of the catchment and it indicates whether the long or the short memory is more relevant for triggering a flood in the study area. In all cases the liquid water equivalent is considered to include the effect of snow. In this study, the following API samples are considered:

1. *Daily*: daily API series, calculated with a moving window of 30 days and a step of one day.
2. *MMean*: daily API series aggregated by the monthly mean.
3. *MMax*: the monthly maximum of the daily API series.
4. *4AMax*: the four largest daily APIs per year.
5. *AMax*: the largest daily API per year.

The Wilcoxon test analyzes if one distribution is shifted from the other. Moreover, assuming that the two distributions are equal, it tests if the median of a random variable is stochastically larger than the median of another random variable. If Z_W equals to 0, there is no expected shift in the distributions. In this study, a negative Z_W indicates that the EDF of the API triggering 1POT floods is shifted to the left of the EDF of API not conditioned on the occurrence of the floods. On the contrary, a positive Z_W indicates a shift to the right.

Figure 5.19 gives the median Z_W obtained from the Z_W of each catchment. This statistic is calculated between the EDF of the API triggering 1POT floods and the EDFs of API samples not conditioned on the floods. The EDFs not conditioned on the floods are given with different markers and colors. The used value of α is given in the horizontal axis. The two panels differentiate between summer and winter events. In general, it can be observed that the *MMax* is the sample that shows larger variations of the median Z_W as α changes and *MMax* is the sample that gets closer to Z_W equal to zero (achieved when $\alpha = 1$). There are no major differences between the results obtained for summer and winter, yet the median Z_W is smaller for winter than for summer. For the summer events, if $\alpha = 0.2$, comparable results are obtained for the *MMean* sample as those obtained for the *MMax* with larger αs. This gives a first insight, that for estimating purposes the longer memory of the catchment is more informative of the flood event. Otherwise, the API of a flood event will resemble a typical value expected to occur at any time during the month, without being able to differentiate between extraordinary events, such as flooding.

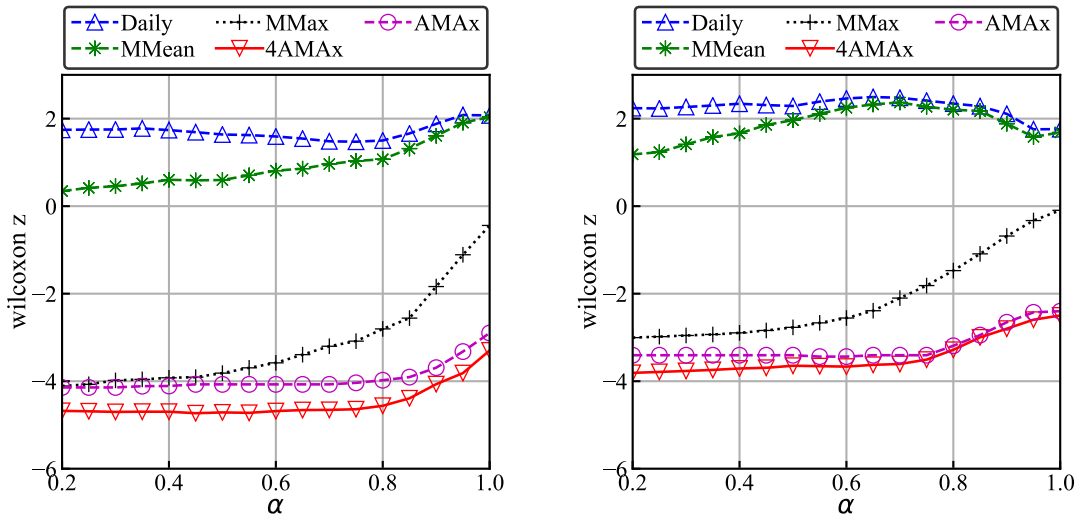

(a) summer events **(b)** winter events

Figure 5.19: Wilcoxon test statistic Z_W comparing the EDF of API triggering 1POT floods and the EDF of API samples not conditioned by the occurrence of floods. The figures give the median of the Z_W obtained for each catchment.

Some summary statistics of Z_W are given in Tab. 5.5. The results are given for $\alpha = 1$, since it resulted in the smallest expected shift. The trends from Figure 5.19 are maintained in most of the catchments. This is recognized on the inter-quartile range, which is smaller for *MMax* sample. In Fig. 5.19 it is observed that the median Z_W gets really close to zero, when the *MMAx* sample is considered and α equals to 1, in particular for the winter events. This indicates that the median of the EDF of the API triggering 1POT floods and the EDF of API samples not conditioned by occurrence of floods are similar. However, for some catchments, the API triggering the floods might be better represented if another EDF is chosen (see Tab. 5.5). The Wilcoxon rank-sum statistic is not sensitive to the shape of

the distributions, meaning that differences at the tails of the distributions are not represented. The Kolmogorov-Smirnov test is sensitive to both, the location and the shape; it is, therefore, also studied here.

Table 5.5: Summary statistics for the obtained values of Z_W comparing the EDF of API triggering 1POT floods and the EDF of API samples not conditioned by the occurrence of floods. For this table $\alpha = 1$.

	summer events					winter events				
	Daily	*MMean*	*MMax*	*4AMax*	*AMax*	*Daily*	*MMean*	*MMax*	*4AMax*	*AMax*
mean	1.9	1.9	-0.4	-3.3	-2.9	1.6	1.5	-0.2	-2.5	-2.4
std	0.9	0.9	1.0	1.1	1.0	0.9	1.0	0.9	1.1	1.0
min	-0.6	-0.7	-2.1	-5.4	-4.7	-1.2	-1.4	-2.3	-4.6	-4.2
25%	1.3	1.3	-1.2	-4.0	-3.5	1.0	0.9	-0.8	-3.3	-3.1
50%	2.1	2.0	-0.4	-3.3	-2.9	1.8	1.7	-0.1	-2.5	-2.4
75%	2.5	2.6	0.3	-2.6	-2.4	2.3	2.2	0.6	-1.6	-1.6
max	3.3	3.4	1.4	-0.4	-0.7	3.0	3.0	1.5	-0.7	-0.7

The median Kolmogorov-Smirnov distance ($D_{m,n}$) over all catchments is given in Fig. 5.20. These distances are calculated between the EDF of the API triggering 1POT floods and the EDF of API samples not conditioned on the occurrence of floods. As in the figure before, the EDFs not conditioned on the floods are given with different markers and colors and α changes on the horizontal axis. The two panels differentiate between summer and winter events. As a general trend for both seasons, it is observed that the median $D_{m,n}$ shows little variation as α changes for the *Daily* sample and the *MMean* sample. This might be explained by the aggregation effect of the median, given that the median $D_{m,n}$ over all catchments is plotted. However, independent catchments can be affected by changes in α. Yet, changing α has no effect on the majority of the study area, at least none that can be represented with the median $D_{m,n}$. On the contrary, if samples *MMax*, *4AMax* and *AMax* are considered, there is a decreasing trend observed, the median $D_{m,n}$ decreases significantly as α increases. The global minimum of the median $D_{m,n}$ is achieved with $\alpha = 1$, when the sample *MMax* is considered. The minimum achieved $D_{m,n}$ for samples *4AMax* and *AMax* is larger than those obtained for the *Daily*, the *MMean* and the *MMax* samples. This means that to trigger a flood in the study area an extreme soil moisture condition is not required; the API does not have to be an annual extreme. It also does not correspond to the soil moisture of any randomly selected day, but rather resembles the monthly maximum of the API. This is due to the fact that, for large αs, the median $D_{m,n}$ is smaller for the *MMax* sample as for the *Daily*, which indicates that the EDF of the API triggering the floods is closer to the EDF of the *MMax* than to the EDFs of the *Daily* or the *MMean*. As for the case of Z_W, this indicates that the long memory of the catchment contains more information to identify the API triggering a flood from the API of a random day.

Comparing the results for both seasons small differences are observed. In summer $D_{m,n}$ is smaller than in winter, if the *Daily* sample and the *MMean* sample are considered. This

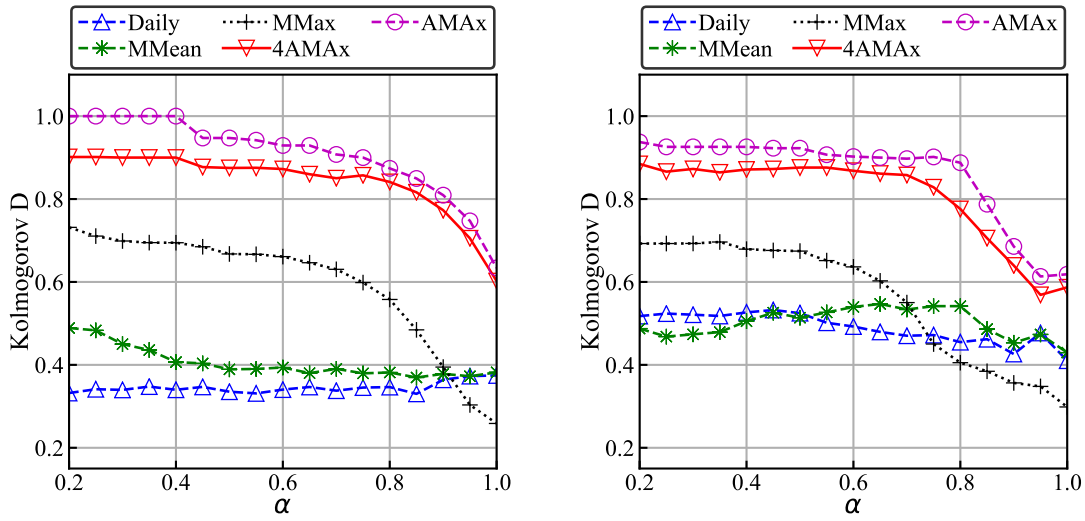

(a) summer events **(b)** winter events

Figure 5.20: Kolmogorov-Smirnov distance between the EDF of API triggering 1POT floods and the EDF of API samples not conditioned by the occurrence of floods. The figures give the median of the $D_{m,n}$ obtained for each catchment.

suggests that the API triggering the summer floods could be closer to that of a random day than those triggering the winter events. The summer floods are more influenced by the characteristics of the precipitation event than by the soil moisture. Even if events are separated in seasons, there is the possibility that various flood mechanisms occurred in a catchment and the separation in two seasons is not enough to identify all flood processes. For example, in summer a flood can be triggered by a convective precipitation as the main driver and having the soil moisture as a secondary factor. Whereas, it can also be triggered by a precipitation front, normally less intense but of longer duration, which can have both precipitation and soil moisture as factors of comparable importance. Nonetheless, the median $D_{m,n}$ of both seasons are still smaller for the *MMax* as for any other sample, if a larger α is considered.

In Tab. 5.6 summary statistics of the computed $D_{m,n}$ are given for $\alpha = 1$. It can be observed that not only the median $D_{m,n}$ is smaller if *MMax* is considered, but also it is the one with the smallest inter quantile range. This suggests, as in Tab. 5.5, that the EDF of the API causing the floods is closer for most of the catchments to the EDF of the *MMax* sample. As already pointed out, the fact that other samples achieve comparable $D_{m,n}$ indicate that some catchments can have an extremer and others a more ordinary API at the occurrence of a flood. The results for all catchments and samples are not included here. Nonetheless, it is observed that for the summer floods, the EDF of those catchments less represented by the *MMax* sample is moving to the left towards the EDFs of the *Daily* sample and the *MMean* sample. On the contrary, in the case of the winter events, it is moving towards the EDF of the *4AMax* sample.

Table 5.6: Summary statistics for the obtained values of $D_{m,n}$ comparing the EDF of API triggering 1POT floods and the EDF of API samples not conditioned by the occurrence of floods. For this table $\alpha = 1$.

	summer events					winter events				
	Daily	*MMean*	*MMax*	*4AMax*	*AMax*	*Daily*	*MMean*	*MMax*	*4AMax*	*AMax*
mean	0.39	0.40	0.29	0.61	0.65	0.42	0.44	0.32	0.58	0.62
std	0.13	0.13	0.11	0.15	0.15	0.14	0.14	0.12	0.13	0.14
min	0.17	0.19	0.13	0.28	0.31	0.23	0.25	0.17	0.30	0.30
25%	0.29	0.31	0.20	0.52	0.55	0.31	0.35	0.23	0.49	0.55
50%	0.37	0.38	0.26	0.60	0.63	0.41	0.43	0.30	0.59	0.62
75%	0.49	0.49	0.36	0.72	0.74	0.53	0.52	0.40	0.66	0.67
max	0.67	0.71	0.56	1.00	1.00	0.76	0.78	0.72	0.85	0.95

Figure 5.19 shows that the EDF of the API at the occurrence of the floods is closer to the *MMean* sample than to the *Daily* sample. However, in Fig. 5.20 the results are the other way around, which means that even though the medians of the distributions are closer together (measured with Z_W), there are some parts of the distributions that are further apart (measured with $D_{m,n}$).

The EDF of the various API samples not conditioned on the occurrence of the floods are, however, not truthful to the concept of the antecedent moisture responsible for the occurrence of the floods, given that they can contain the extreme precipitation event triggering the flood wave. By sampling the API by their annual maximum or the monthly maximum it is implied that the flood causing precipitation is included. Further, the extreme precipitation event is not considered in the API sample conditioned by the occurrence of the flood. The concept of one day lag will be studied on the following, to get API values that are more representative of the antecedent moisture, and do not include the precipitation triggering the floods. The EDFs of the API series considering -1 day lag from the day the extreme API occurred are extracted. This is done to simulate the soil moisture preceding an extreme precipitation event, which can trigger a flood.

In Fig. 5.21 the Z_W and $D_{m,n}$ are presented in the top and bottom panel respectively. In this case, the API values used are those corresponding to a day preceding one of the API samples considered before (*Daily*, *MMean*, *MMax*, *4AMax* and *AMax*). Note that for *Daily* no changes are expected from the results presented before. The resulting EDF of a day preceding each value of the *Daily* sample results in the same *Daily* sample. Analogous to the previous plots, the two horizontal panels differentiate between summer and winter events; and the various markers and colors give the API sample considered.

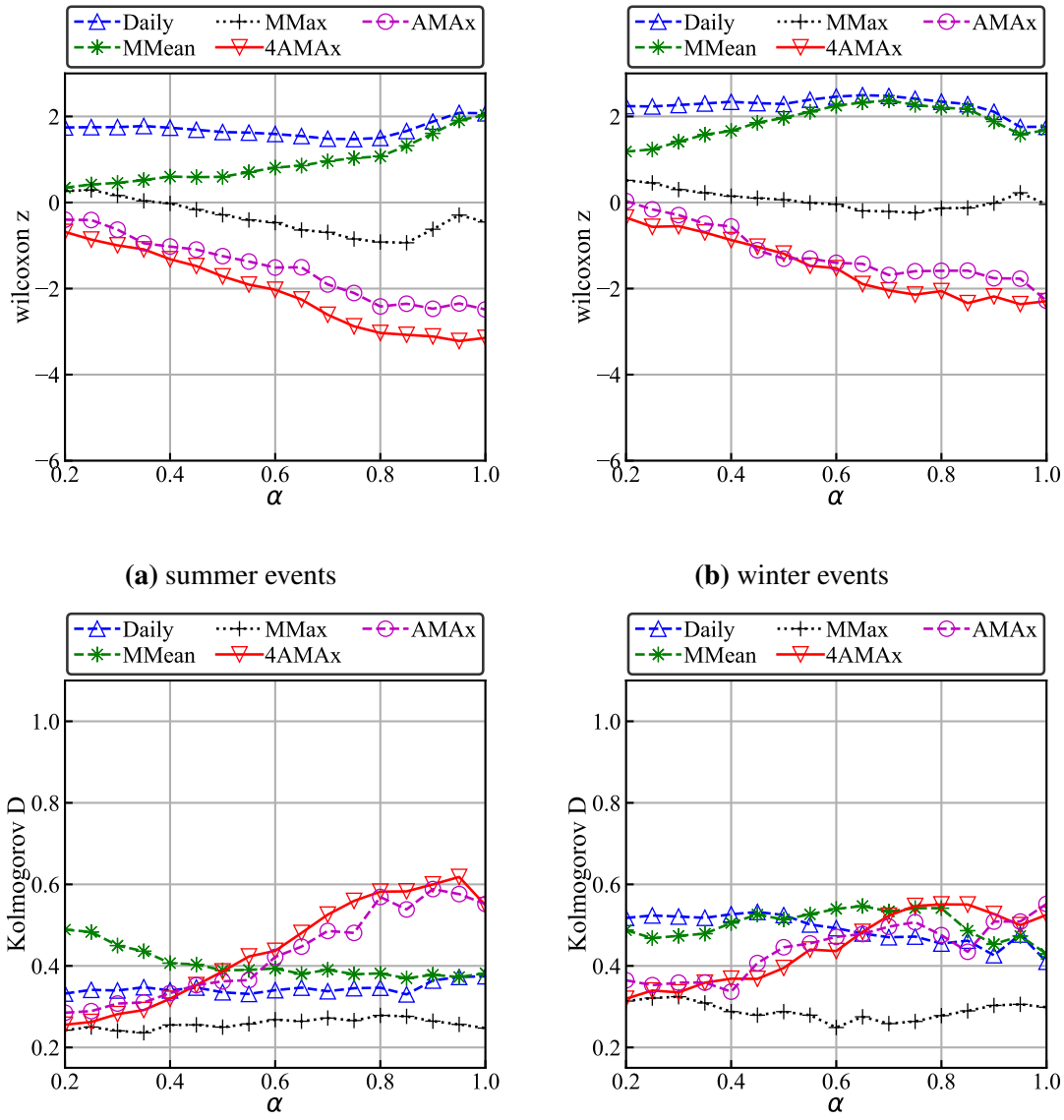

(a) summer events

(b) winter events

(c) summer events

(d) winter events

Figure 5.21: Wilcoxon test statistic and Kolmogorov-Smirnov distance between the EDF of API triggering 1POT floods and the EDF of API samples not conditioned by the occurrence of floods considering a lag of -1. The figures give the median of the Z_W (top) or the $D_{m,n}$ (bottom) obtained for each catchment.

If one looks at both the median Z_W and $D_{m,n}$ at small values of α, it is observed that the API preceding a *MMax*, a *4AMax* or an *AMax* achieve comparable values. Looking into detail, it is observed that for $\alpha = 0.2$ half of the catchments have Z_W and $D_{m,n}$ indicating that the EDF of the API conditioned on the occurrence of a flood are closer to that of the API preceding a *MMax* and the remaining catchments are distributed between the API

preceding either a *4AMax* or an *AMax*. Further, it is observed that catchments closer to the API preceding a *MMax* tend to have smaller temporal precipitation entropies, which corresponds to intense convective precipitation events, where precipitation intensity might exceed the infiltration capacity of the soil. Additionally, it is observed that these catchments tend to have larger slopes, which can be an indicator of a faster catchment response with a runoff generating process less dependent on the soil moisture content.

Figure 5.21 shows that as α increases, it is less common that a flood can be triggered by an API preceding a *4AMax* or an *AMax*, i.e. Z_W is moving away from zero and $D_{m,n}$ is increasing. If one would select a small α the API preceding either *MMax*, *4AMax* or *AMax* could be representative of the API causing the floods. However, by selecting larger αs, the API preceding a *MMax* can describe almost the entire studied region. Thus, the longer memory of the catchments contains more information to differentiate the floods. There is little variation of the API preceding a *MMax* as the value of α changes. Further studies should try to explain this. Nevertheless, it might be an effect of changes in the number of catchments getting closer to *MMax* as the value of α increases.

The results presented here, suggest that a flood event is more frequently taking place when the accumulated precipitation of 30 days is close to the monthly maximum. One would rather expect that *4AMax* or *AMax* should be responsible for the runoff generation of floods. Nevertheless, it is important to point out that these extremes are samples of the accumulation of precipitation aggregated daily. For the size of the catchments considered sub-daily aggregations of precipitations might be more representative. Further studies should include the sampling of the extremes with smaller precipitation aggregations and use their occurrence of extremes to extract the API samples taking place on a day (or a time lag) preceding those extremes. More specifically, the results should be studied by considering precipitation directly to sample the critical days where a flood might have occurred, and not its accumulation as it is in the case of the API.

Further, the importance of the water content of the soils for the generation of runoff can be different in the studied catchments. Froidevaux et al. (2015) found out that from different regions of Switzerland the API had an influence on the occurrence of floods only for some catchments located on the Jura Mountains (area of most of the catchments of this study). As already mentioned, the field experiments of Scherrer et al. (2007) led them to the conclusion that the antecedent soil moisture is not of equal importance for all runoff processes. For example, catchments that normally have a rapid respond, showed that the soil moisture has little or no effect on the formation of runoff, i.e. the runoff builds up fast no matter if the soil is dry or wet. This study indicates that in the study area, the longer memory of the catchment is of importance to the flood process. Yet, this is not observed in all catchments, it is only true when looking at the whole study area. Overall, the results suggest that the EDF of the API triggering the floods is closer to the EDF of *MMax*, if larger values of α are used for calculating the API.

Chapter 6

Regionalization of Catchment Reactions

To regionalize the reactions of the catchments, when a flood occurs, a model that can capture the complex hydrological interactions is needed. A random forest algorithm is chosen, to evaluate the similarity of flood mechanisms. The flood distances in the random forest space are used to transfer hydrograph shapes from gauged to ungauged catchments. This chapter contains an overview of the random forest algorithm and it explores how this algorithm is used to represent the dynamics of flood mechanisms and the regionalization of the hydrograph shape for a known meteorological event.

6.1 Random Forest Theory

A Random Forest (RF) algorithm consists of many single decision trees, where each decision tree is trained on a subsample of the entire data. A single decision tree is trained using the Classification and Regression Tree (CART) algorithm from Breiman et al. (1984). The CART algorithm can be used for either regression or classification problems, meaning that it can estimate either continuous or categorical data. For building a single decision tree, the observations are repeatedly split into two subsets at each node, using a decision based on one predictor. The predictor of a given node is determined by the one that minimizes the variability on the target quantity. This variability is typically evaluated using either the Mean Squared Error (MSE), when growing regression trees, or the Gini index or entropy for classification trees. In Fig. 6.1 an example of a decision tree is given, which is built to estimate the PVR of the floods as its target. The estimation involves a chain of if-then decisions, which depend on the predictors, in this example chosen to be precipitation temporal entropy (H_R), the API, the catchment area (C. Area) and the drainage density (D.D) (see Chap. 3, Chap. 4 and Chap. 5). Given a decision, i.e $H_R \leq 0.4$ in the first node in Fig. 6.1, a subset of the observations is passed to the left node and the remaining observations are passed to the right, forming two child nodes. At these two new nodes the observations are

split again with a new decision, as it was done in the first node. This procedure is repeated up to the terminal node. Within this iterative process at each node the remaining data sets become smaller and smaller, until either purity is achieved or a certain condition is fulfilled, i.e. no variability over the target variable, tree reaches a given depth or the terminal node has a determined number of observations. In such a way, one obtains an estimation of the target in the form of a decision tree, a tree-based estimator. The advantage of this algorithm is that it is fast and works well with the training data. However, the estimator is too specific to the training data with a poor performance on test data, meaning that it cannot generalize to unseen samples. To overcome this problem, Breiman (2001) introduced Random Forest (RF), a bootstrap aggregation algorithm (*bagging*) of tree-based estimators.

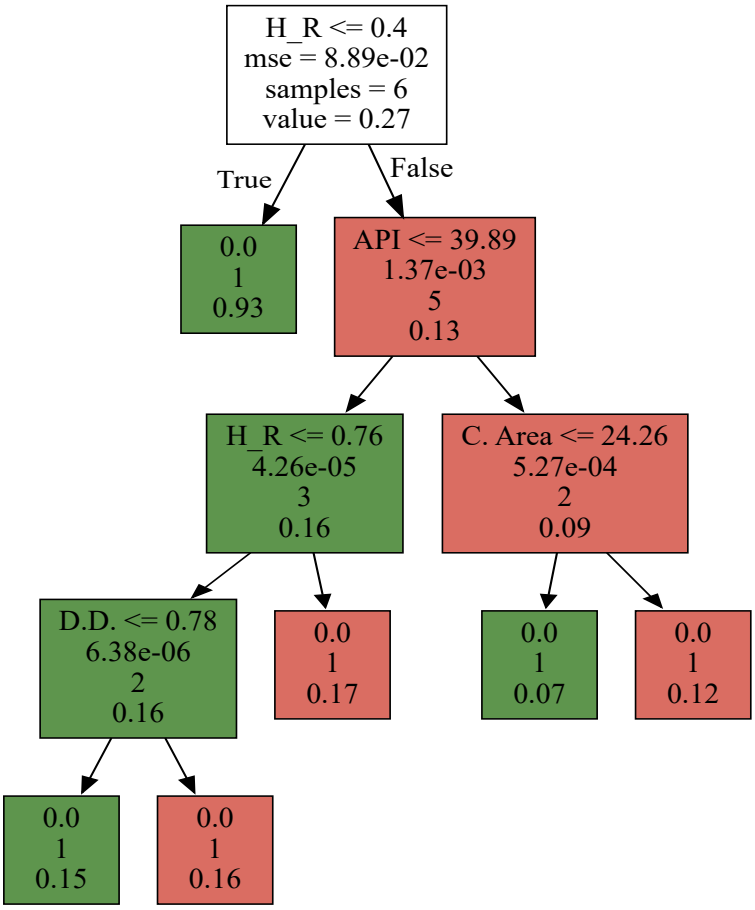

Figure 6.1: A decision tree trained to estimate PVR with 6 observations randomly selected from the floods database. The predictors are: the precipitation temporal entropy H_R, the API, the catchment area (C.Area) and the drainage density (D.D.). Each node contains the predictor that makes the best binary split of the data according to the target (except for the terminal nodes), the MSE, the number of observations and the average target value. Note: the tree is used as an example and should not be considered to draw conclusions about the floods.

A RF is an ensemble of N decision trees. The main difference to a single decision tree

algorithm comes from the *bagging* for sampling the observations to train each tree and the parameter m. The parameter m controls the number of randomly selected variables (predictors) at each split. These are the only predictors considered when evaluating the split. *Bagging* is proven to have a better performance, since it reduces the high variance of a single tree and keeps the low bias character of deep trees (Gregorutti et al., 2017). Since the trees are independent from each other, it allows for parallel computing, keeping the computational times short. Each tree T_i in a RF is trained with a bootstrap sample of the observations $\boldsymbol{x_i}$, resulting in a series of split rules θ_i that minimizes the variance of the random target vector $\boldsymbol{y_i}$ on the child nodes. The vector θ_i contains the information of the predictor that optimizes the binary split at each node and its size equals the number of splits in a tree. Thus, a random forest estimator $\hat{f}(\boldsymbol{x})$ can be formally written as

$$\hat{f}(\boldsymbol{x}) = \frac{1}{N} \sum_{i=1}^{N} T_i(\boldsymbol{x}; \theta_i)\,, \tag{6.1}$$

where $\boldsymbol{x}$ is a given input vector, N the number of trees, $T_i(\boldsymbol{x}; \theta_i)$ the $i - th$ decision tree with the random vector $\theta_i = (\theta_{i,1}, \ldots, \theta_{i,K})$. Originally Breiman (2001) proposed RF trees to be fully grown. A fully grown tree means that the observations in the terminal node either belong to only one class (i.e. in case of classification RF) or the variance of the observed target variable in the terminal node is zero (i.e. in case of a regression RF). However, there are some approaches, in which the trees are pruned, although the purity condition is not satisfied, resulting in an extra parameter n, which defines the allowed number of observations in a terminal node. There are some recommended values for m and n according to the type of RF. For a classification RF $n = 1$ and $m = \sqrt{p}$, where p is the total number of predictors. For a regression RF $n = 5$ and $m = p/3$ (Hastie et al., 2017). Depending on the structure of the data and the amount of noise it contains, these values do not necessarily achieve the best performance over all data sets. Therefore, n and m must be considered as tuning parameters and should be studied with each data set.

In Fig. 6.2 an illustration of the RF algorithm is given. For this example, 15 observations are randomly selected from the floods database and the same four predictors are considered, as in the case of the single tree in Fig. 6.1. These are used to train a RF with 10 trees $N = 10$ for estimating the PVR. The RF is chosen to have fully grown trees $n = 1$ and 2 random predictors per split $m = 2$. As it is observed on the first node of each tree, to grow each tree from the 15 observations just 7 samples are randomly chosen with replacement. One can be observed that the resulting trees are different form each other, given that at each tree a new bootstrap sample is used and at each split not all predictors are considered ($m \leq 4$ the total number of predictors). Those terminal nodes that are close to each other have a similar PVR. i.e. the target variable. At the stage of the model estimation appears the aggregation part of the *bagging* term, where the estimations of each tree are aggregated to give the final estimation.

The Out of Bag (OOB) observations can be used to estimate the performance of the RF algorithm. The OOB samples are the observations that are not randomly selected for growing

a tree, those not included in the bootstrap sample. The use of the OOB observations allows to include more data to train the RF. Nevertheless, in this study the prediction error of $\hat{f}(\boldsymbol{x})$ will be estimated using test observations, since it has been observed that the OOB prediction error leads to an overestimation of the actual test error. This overestimation has already been studied by other authors and is, therefore, not further analyzed here (see Janitza and Hornung (2018)).

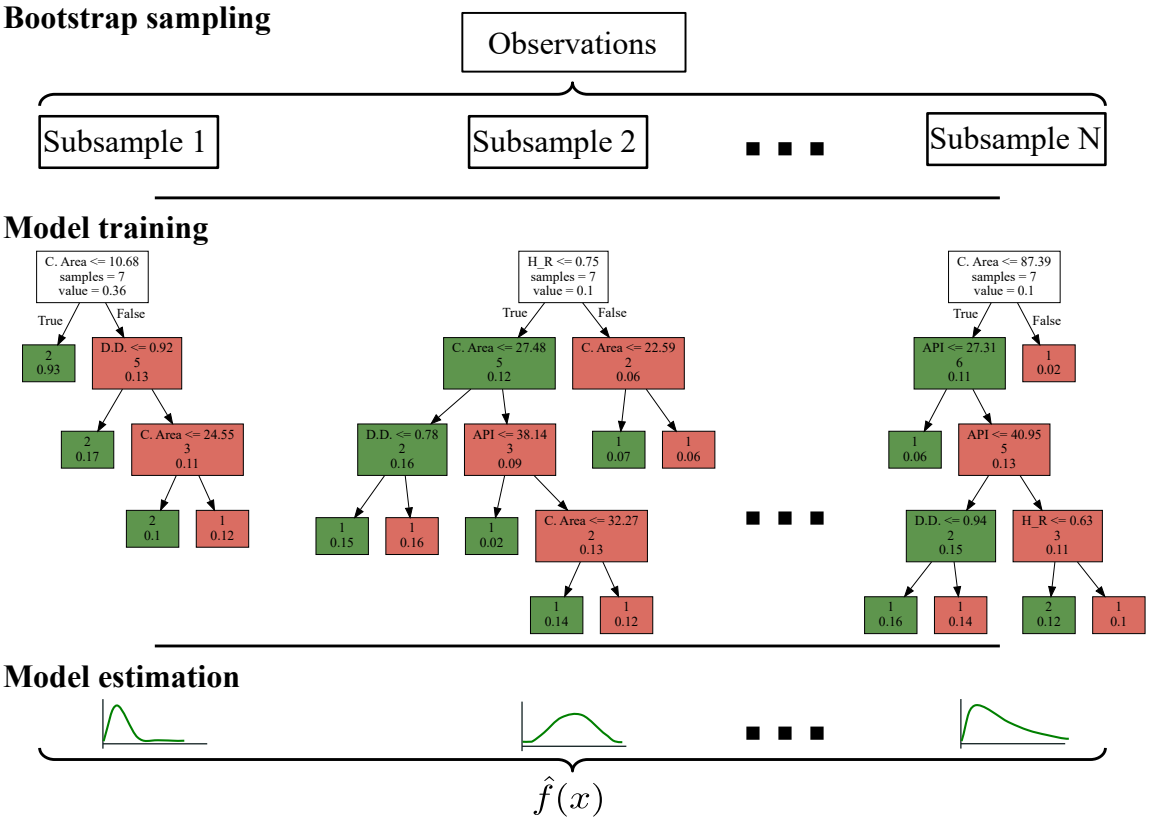

Figure 6.2: Illustration of the random forest algorithm. To grow each tree the training observations are sampled with replacement. Each tree is grown by adding an extra randomness at each node, limiting the number of predictors evaluated. An estimation is made by aggregating the single estimations of each tree. Note: the trees on the RF are used to represent how the algorithm works and should not be considered to draw conclusions about the floods.

The OOB observations are also used for estimating the predictors' importance in the RF space. The importance is used to identify main players of the predictors' space, causing the different reactions of the catchments. For calculating the predictors' importance in the RF, the prediction error $\hat{R}(\hat{f}, \theta_i^{OOB})$ of the OOB observations is calculated. For this purpose, the OOB observations are passed through those trees, whose bootstrapped sample did not contain them. Additionally, for each predictor an error $\hat{R}(\hat{f}, \theta_i^{OOB_j})$ is calculated. In this case, the vector with the observations corresponding to the $j-th$ predictor are permuted

before passed down the trees to make the estimation. The predictors' importance is obtained by comparing both prediction errors as:

$$\hat{I}(X_j) = \frac{1}{N}\sum_{n=1}^{N} \hat{R}(\hat{f}, \theta_n^{OOB_j}) - \hat{R}(\hat{f}, \theta_n^{OOB})\,. \tag{6.2}$$

One disadvantage of random forest is that it cannot extrapolate, the estimations are contained in the space of the observations. Nonetheless, RF is used in this study to regionalize catchment reactions, i.e. hydrograph shape, by evaluating the similarities of floods in the RF space. It is not used to estimate a peak or a volume corresponding to a return period. It is, therefore, assumed that even if flood events occur with larger peaks and/or volumes as the observed ones, the dimensionless reaction of the catchment will be similar to an observed one considering that all flood mechanisms are included in the RF.

6.1.1 Random Forest Measure of Similarity

One feature of the RF algorithm is the possibility to generate a similarity matrix. It measures the similarity of the observations by counting the occurrence of observations in the same terminal node. The similarity matrix is defined as:

$$\boldsymbol{S} = \begin{pmatrix} s_{11} & s_{12} & \cdots & s_{1j} & \cdots & s_{1k} \\ s_{21} & s_{22} & \cdots & s_{2j} & \cdots & s_{2k} \\ \vdots & \vdots & \ddots & \vdots & \ddots & \vdots \\ s_{i1} & s_{i2} & \cdots & s_{ij} & \cdots & s_{ik} \\ \vdots & \vdots & \ddots & \vdots & \ddots & \vdots \\ s_{k1} & s_{k2} & \cdots & s_{kj} & \cdots & s_{kk} \end{pmatrix}, \tag{6.3}$$

$$s_{ij} = \frac{1}{N}\sum_{n=1}^{N} x_{ij_n}, \quad \text{with} \quad x_{ij_n} = \{1, 0\}\ ,$$

where $\boldsymbol{S}$ is the similarity matrix, N is the number of trees in the RF, s_{ij} are the elements of the matrix, which give the similarity of two observations in the RF space. The similarity matrix is of size $k \times k$, where k is the number of observations used for training the RF. x_{ij_n} is equal to one at those trees where observation i ends in the same terminal node as observation j, otherwise it is equal to zero. These occurrences are added through all N trees and they are normalized by the number of trees in the forest, resulting in the similarity values in matrix $\boldsymbol{S}$ from zero to one, where zero means no similarity and one total similarity (equality). It can be observed that the elements of the main diagonal of $\boldsymbol{S}$, i.e. where $i = j$, must be equal to

one since it represents the similarity between an observation and itself. Furthermore, S is a square matrix and it is symmetric since $s_{i,j} = s_{j,i}$.

The similarity matrix can be used to test hypothesis about the structure of the data and to understand which observations are close in the RF space. It can be given as input to a Multidimensional Scaling (MDS) algorithm. MDS is a method that represents distances in a lower dimensional space with the aim of visualizing and exploring high dimensional problems (Borg and Groenen, 2005). In MDS, a dissimilarity matrix is used rather than a similarity matrix, which can be obtained by subtracting S to the scalar 1, given that it is a representation of distance where zero indicates close observations. The transformation of the high-dimensional space obtained with the MDS, gives a representation of the distances in an Euclidean space and it allows for visualizing the data using the coordinates obtained. Those points that are close in a representation of the MDS space represent the similarity evaluated through the similarity matrix of the RF. It is useful for understanding the RF space.

6.1.2 Random Forest for Clustering

Another possibility for identifying similar observations are clustering algorithms. When dealing with unlabeled data, RF offers an application to cluster the observations. Using an unsupervised RF algorithm, a similarity matrix is obtained to distinguish between observed and synthetic data (Shi and Horvath, 2012). To generate the synthetic data, individuals are drawn from the empirical distribution of each of the observed variables, getting independent random vectors, which for each variable follow the same distribution as the observed one, but the dependence structure of the variables is removed (Alhusain and Hafez, 2017). The RF algorithm is run as a classification problem with two classes, labeling the observed data as class one and the synthetics data as class two. The similarity matrix reveals how close observations are when compared to synthetic data. This similarity matrix can be given as input to an algorithm for clustering the observations. Either an algorithm that is based on the distances between points, as is the case of an agglomerative hierarchical clustering or k-medoids, or an algorithm based on coordinates, for which the representation of the similarity matrix obtained with MDS can be used.

This concept of using the similarity matrix for clustering the data can also be used in a supervised manner, as mentioned by Xiao and Segal (2009) as a “guided” clustering to identify patterns and relationships between variables given a certain signature or response. In this case, the RF is trained to predict a given response, it can be either classification or regression. The obtained similarity matrix is used for clustering, as in the case of the unsupervised RF. The logic behind this approach is that the RF structure captures the nonlinear representation of the observations with respect to a given training variable. In this study, it is used to identify similar catchment reactions at the occurrence of a flood.

Another approach for using RF for clustering is by means of a clustering ensemble. It allows combining different clusters of the same dataset, resulting in a more robust measure

than any individual clustering. It is composed of the "base clusterings" which by means of a consensus function (function for aggregating the results of each clustering) give the final clusters of the observations. There are different proposed approaches for determining the consensus function to merge the clusters from different ensemble members into one (Alhusain and Hafez, 2017). In this study, a pair-wise approach will be used, which represents the information of the base clusterings by looking at the co-occurrences of observations belonging to the same cluster. The co-association matrix $\boldsymbol{CO}$ is calculated with this information as:

$$\boldsymbol{CO} = \begin{pmatrix} co_{11} & co_{12} & \cdots & co_{1j} & \cdots & co_{1k} \\ co_{21} & co_{22} & \cdots & co_{2j} & \cdots & co_{2k} \\ \vdots & \vdots & \ddots & \vdots & \ddots & \vdots \\ co_{i1} & co_{i2} & \cdots & co_{ij} & \cdots & co_{ik} \\ \vdots & \vdots & \ddots & \vdots & \ddots & \vdots \\ co_{k1} & co_{k2} & \cdots & co_{kj} & \cdots & co_{kk} \end{pmatrix}, \tag{6.4}$$

$$co_{ij} = \frac{1}{Z} \sum_{z=1}^{Z} x_{ij_z}, \quad \text{with} \quad x_{ij_z} = \{1, 0\} \ ,$$

where co_{ij} denotes the proportion of observation i and j belonging to the same cluster over the Z number of base clusterings, given a k number of observations. When observations i and j have the same cluster label then co_{ij_z} equals to one on the contrary it is zero. The cluster labels for the $z - th$ member of the ensemble are obtained by using a clustering algorithm whose input is a similarity matrix S from a supervised RF according to Eq. 6.3.

In summary it can be said that the potential of using a supervised RF for selecting the flood donors and estimate a Design Flood Hydrograph (DFH) by differentiating between flood mechanisms can be assess using the RF similarity matrix, MDS and a clustering algorithm. Few applications were found in literature that use supervised RF for clustering and evaluating similarity in the observations (see Segal and Xiao (2011); Xiao and Segal (2009)). These are applications of the biostatistics, none was found in hydrological applications. Although the RF model has been used for estimations in hydrological problems, the approach of a "guided" similarity measure is applied here for the first time. In the next section a summary of the use of the previous concepts in this study is given and afterward the results are presented.

6.2 The Proposed Method

RF is chosen in this study because it can capture complex interaction structures present in the data, shows a good performance with high dimensional problems, handles categorical and

ordered variables and can be used also for multivariate problems (Hastie et al., 2017; Gregorutti et al., 2017; Shi and Horvath, 2012). The RF algorithm is used for the regionalization of the dimensionless Design Flood Hydrograph (DFH), given a known meteorological event. As mentioned in Chap. 2 there are regionalization strategies that are based on the similarity of the catchments. Here, these similarities are quantified by the RF using the similarity matrix as the "measurement tape" of the flood distances over the complexity of the hydrological players and responses. It is used to quantify the relationship between catchment characteristics and the nature of the meteorological event triggering a flood hydrograph (i.e. a flash flood caused by a convective precipitation in an impermeable catchment or a snow melt event in the same catchment).

The similarity matrix infers the underlying structure from the floods database and is used as the space that defines the hydrograph donors to the ungauged catchment. For this purpose, a supervised RF is trained to capture the structure when pointing at a specific target variable, which describes the response of the catchment when a flood event occurs. Three methods for obtaining the similarity matrix are used in this study, which are briefly introduced here and explained in more detail later in this chapter. The first is the direct similarity obtained from the random forest, the second is an average similarity over a RF ensemble and the third is the co-association matrix of a clustering RF ensemble, which measures the co-occurrence of observations belonging to the same cluster. Due to the random nature of RF the resulting similarity matrix is different at each run (Alhusain and Hafez, 2017), which motivates the usage of an average similarity of a RF ensemble and the co-association matrix of a clustering ensemble, to test if they deliver more robust results. The chosen approach of using the floods' space as donors avoids having fixed number of catchment donors allowing for catchments to be donors only for a given flood mechanism. As observed by Fischer (2018) and Fischer and Schumann (2019) catchments can have different dominating mechanisms depending on the season and on the catchment characteristics. The regionalization is done at the flood level, allowing for catchments to be donors if they react similarly.

The studied target variables and predictors used for training the RF are going to be explained in the following sections. A tuning of the RF global parameters is done to optimize the performance with the floods database. It is done by varying the number of trees, the observations in terminal node and the random variables at each split and comparing the performance of the estimations. The use of different target variables is studied, looking at the estimation performance of the peak discharge and the time of the occurrence of the peak. Further, the physical relationships interpreted by the RF are analyzed using the RF similarity space through MDS and clustering. This allows to recognize whether the relationships captured by the model agree with the understanding of the hydrological cycle and the catchment physical processes. For example, whether sharp hydrograph curves, i.e. high PVR, are mainly caused by convective precipitation. It is important to determine if the model can capture the underlying processes, because it makes the estimations more reliable. A comparison of an unsupervised RF with a supervised RF for evaluating the similarity of the floods mechanisms is included. These two methods are evaluated according to their ability to recognize similar catchment reactions by looking at their estimation performance.

6.3 Selected Training Variables

In this section the floods database set used for training the RF model is described, looking at the definition of the predictors and the target variable. Throughout this study, different predictor groups are used and different target variables are included to describe the response of the catchment.

6.3.1 Random Forest Response Variables

The response variables, also known as target or training variables, are the values that $\hat{f}(x)$ in Eq. 6.1 can take, which is the variable or class that is going to be estimated with the RF. The goal of this study is to have a model that can estimate the peak, the volume and shape of the hydrograph, considering the different catchment reactions to meteorological critical events. Specifically, in this chapter a method for translating the hydrograph shape to an ungauged catchment given a meteorological event and some hydrological characteristics is studied. With this in mind, various response variables, that describe the catchment response, are considered to train the RF model. These variables are summarized in Tab. 6.1 and can be divided in three groups:

1. Target variables associated to the fit of the probability density function (PDF) to the hydrograph flood wave.
2. Target variables that explain the shape of the original hydrograph.
3. Target variables that define the magnitude of the flood.

For those cases in Tab. 6.1 where the response variable is multivariate, the RF is trained to estimate the co-dependence of the variables by looking jointly at both target variables at each split and tree of the RF. In this chapter only the Lognormal and the TSP distributions are considered. In the analysis of Chap. 4 it was shown that the PDFs, which represented the hydrograph shape more accurate are the Lognormal from the bell shaped distributions and the TSP from the sharp distributions. In Tab. 6.1, α and β are chosen as reference when referring to the parameters of the PDF. The entropy of the hydrograph curve, is referred in an analog manner as it was used for the case of temporal precipitation entropy, described by Eq. 5.6. Here it represents the relative entropy of the flood waves. Using the relative entropy allows to eliminate the effect of different hydrograph durations, i.e. number of time intervals, from the entropy result. The skewness and kurtosis of the hydrograph are calculated assuming the hydrograph observations as a PDF.

Training the RF as multivariate to predict the relative peak and volume of the flood is different than training it to the PVR. Even though the PVR is defined by the peak and

volume, for the first case the co-dependence of the magnitudes peak and volume is targeted, whereas for the PVR ratio the shape of the hydrograph is addressed.

Table 6.1: Response variables used for training the RF.

Group	Target	Notation	Description
Shape of fitted hydrograph	Entropy of PDF	H_{PDF}	Temporal entropy of the PDF fitted to the hydrograph.
	Parameters of PDF	α , β	RF trained as multivariate to estimate the co-dependence of the parameters obtained with thePDF fit to the hydrograph flood wave.
	Entropy and parameters of PDF	H_{PDF}, α, β	Multivariate RF trained to estimate the co-dependence of the entropy and the PDF parameters.
Shape of original hydrograph	Entropy of measured hydrograph	H_{hy}	Relative temporal entropy of the original discharge measurements using Eq. 5.6 and Eq. 5.5.
	Peak to volume ratio	PVR	A measure of the duration of a flood as defined with Eq. 4.2.
	Entropy and PVR	H_{hy}, PVR	Multivariate RF trained to estimate the co-dependence of the entropy and PVR.
	Hydrograph statistics	Sk, Ku	Skewness and kurtosis of the flood wave, which represent the symmetry and shape of the curve.
	Hydrograph statistics and PVR	PVR, Sk, Ku	Multivariate RF trained to estimate the co-dependence of hydrograph statistics and peak to volume ratio.
Hydrograph magnitudes	Relative peak	Q_p/A	Flood peak divided by catchment area.
	Relative volume	V/A	Flood volume divided by catchment area.
	Relative peak and volume	Q_p/A, V/A	Multivariate RF trained to estimate the co-dependence of the relative flood peak and volume.

6.3.2 Random Forest Predictors

The RF predictors, also known as covariates, are used for estimating the response. A total of 34 predictors were considered to estimate the catchment reaction at the occurrence of a flood. They are described in Chap. 3, Chap. 4, Chap. 5 and in the appendix (see Tab. A.2

and Tab. A.3). These predictors are roughly classify into the following groups:

1. Precipitation: duration, intensity, precipitation total and precipitation temporal entropy.
2. Temperature: standard score.
3. Soil moisture: as estimated using the antecedent precipitation index (API).
4. Time: indicating the time of the year when the flood occurred.
5. Climate: The amplitude and phase of the sin-cos fit to daily precipitation data and some precipitation quantiles.
6. Catchment characteristics: long term catchment descriptors as area, shape, orientation, drainage density, land use, soil, etc.

From these variables some are flood specific, meaning that they can vary at the occurrence of each flood, as for example the precipitation and API. Other variables are catchment specific, and thus they remain constant for each catchment as for example the catchment area, land use, climate, etc. If not mention otherwise, as standard all predictors are included when training a RF.

Having the predictors and target variables defined it is possible to train a RF to obtain a measure of similarity between floods. Nonetheless, a study of the changes in performance of the RF when changing the global parameters of the RF is first carried.

6.4 Tuning Random Forest Global Parameters

The performance of the RF depends on the chosen tuning parameters. If the number of predictors is large but only few of them are relevant to the target variable and the rest are noise, sa small number of random variables m at each split will most likely give a poor performance, since the probability of randomly selecting one of the relevant variables is lower (Hastie et al., 2017). A sensitivity analysis of the RF parameters is carried out, to avoid that a target variable results in a better performance because the default parameters of the RF favor the prediction in one target more than another. Three parameters are tuned independently, the number of trees N, the randomness applied at each split m and the number of floods in a terminal node n. For each case, the tuning parameter is varied while the other two are kept constant, for determining the performance of the RF. It is assumed that if the performance of the RF to predict the target variable increases also does the ability of the RF to discover the structure of the data. Thus, enabling differentiation between flood mechanisms, giving a more reliable similarity matrix.

The performance of the RF is evaluated using the coefficient of determination R^2 defined as

$$R^2 = 1 - \frac{\sum_{i=1}^{t}(y_i - \hat{y}_i)^2}{\sum_{i=1}^{t}(y_i - \overline{y})^2}\,, \tag{6.5}$$

where y_i is the observed response, $\hat{y}_i$ the RF estimation, $\overline{y}$ the mean over the observations in the test sample and t is the size of the test sample. The R^2 is a measure of goodness-of-fit which basically compares the difference in performance between an estimation from the random forest versus the estimation using the observations mean. The closer R^2 is to one the better the performance. The separation between train and test samples is done with the k-fold method, where k equals to 10, which means that per target variable and tuning parameter 10 RF are trained. For tuning purposes, all 11 target variables (see Tab. 6.1) are used to independently train the RF with the 37 predictors (see Tab. A.2 and Tab. A.3). In Fig. 6.3, Fig. 6.4 and Fig. 6.5 the change in performance due to the change in the tuning parameters is plotted. In all cases, the observations used belong to the 1POT samples. The 11 target variables can be identified by the marker and are colored according to the response group in Tab. 6.1. Note that for the tuning of the global parameters, only the TSP function is considered, and, therefore, H_{PDF} is the entropy of the fitted TSP. When referred to α and β it is meant the fitted parameters of the TSP.

Number of trees. In Fig. 6.3 the performance of the RF with an increasing number of trees per forest is plotted. The forest size ranged between $N = 5$ and $N = 300$ trees. Given that 10 folds were considered for the cross-validation, this resulted in training 2950 RF for each target variable. For tuning the number of trees, the variables considered at each split and the number of floods in the terminal node are kept constant as $m = 12$ and $n = 2$, respectively. It is observed, that independent of the target chosen to train the RF, as the number of trees increases the performance increases up to a point where it converges asymptotically and the benefit on increasing the size of the RF is low. This is reasonable, since by increasing the number of trees the ability of the model to generalize to unseen data increases, when a new tree is trained a new perspective of the space is included. Even though Probst and Boulesteix (2018) argue that the number of trees should not be considered as a tuning parameter since an increase on the number of trees can not result in the overfitting of the model. It is studied here to be confident that the RF performance converges with the selected number of trees for all target variables. A large RF will guarantee stability, but influences the computational time. The number of trees must be kept samll, to reduce the computational time of the similarity matrix, since for its calculation each observation goes down each tree. The number of trees is chosen to be 100 for all RF in this study, to ensure that the change in performance is due to the difference in the chosen target variables and predictors and not due to a small number of trees that give unstable results.

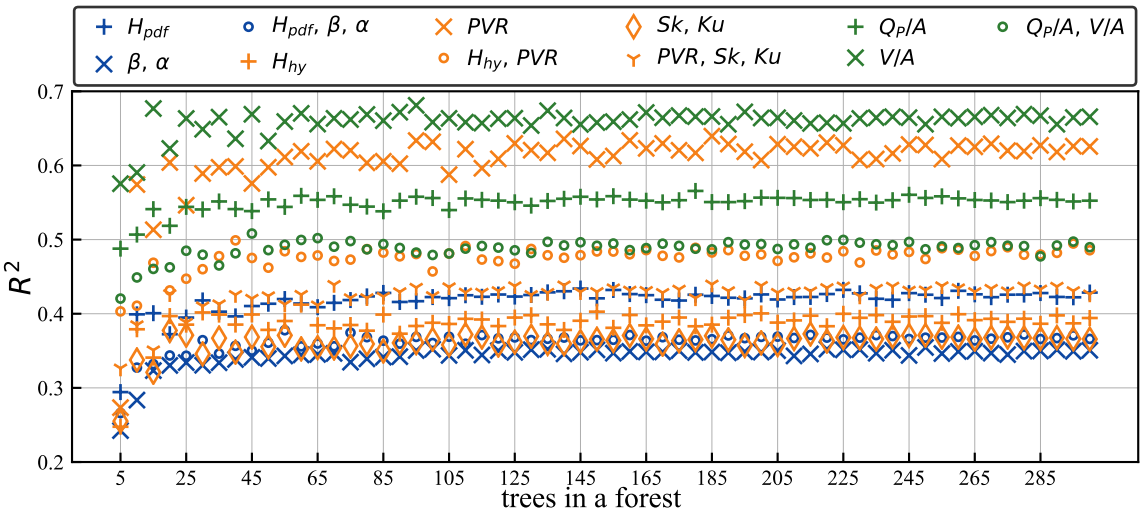

Figure 6.3: Mean RF performance over 10 folds for all target variables, trained with the observations of the 1POT sample. The number of trees N varies, while $m = 12$ and $n = 2$ are set constant.

Number of random predictors. In Fig. 6.4 the change in performance due to the variation of the number of random predictors at each split of a tree is plotted. The number of trees per forest is kept at 300 and the trees are grown until the terminal node reaches purity or had only 2 floods. It is observed that overall, a low value of m results in a lower performance. A lower performance indicates that not all predictors are equally important for the estimation, and thus with a smaller m the chances of selecting one of the relevant predictors decreases. There is no universal value of m, which achieves the largest performances over all target variables. For example, for H_{hy} the largest performance is achieved with $m = 18$, but for H_{PDF} with $m = 12$. Nevertheless, it is observed that for values of m larger than 12 the increase of performance is smaller than for $m < 12$. From a total of 37 predictors, 12 correspond to the recommend value of m, previously mentioned as $p/3$. The value of m will be chosen to be 12 for training the RF and estimating the similarity of floods, for $m > 12$ the gain in performance can be neglected. As m increases, the correlation between trees is expected to increase, since the probability of selecting one of the relevant predictors is larger. This reduces the advantage of using a large number of trees, since the trees are more correlated by having a large m, which is not desired since it can hamper the recognition of less frequent mechanisms or overlapping flood processes.

Number of floods in a terminal node. The depth of a tree can be modified either by defining a given number of splits or a given number of observations to end up together in a terminal node. In this study, the second approach is used, which is achieved by setting n and keeping the number of splits larger than the number of observations. This ensures that a tree is pruned only by satisfying the purity condition or by reaching a given number of observations. In the bottom panel of Fig. 6.5 the performance of estimating a target variable

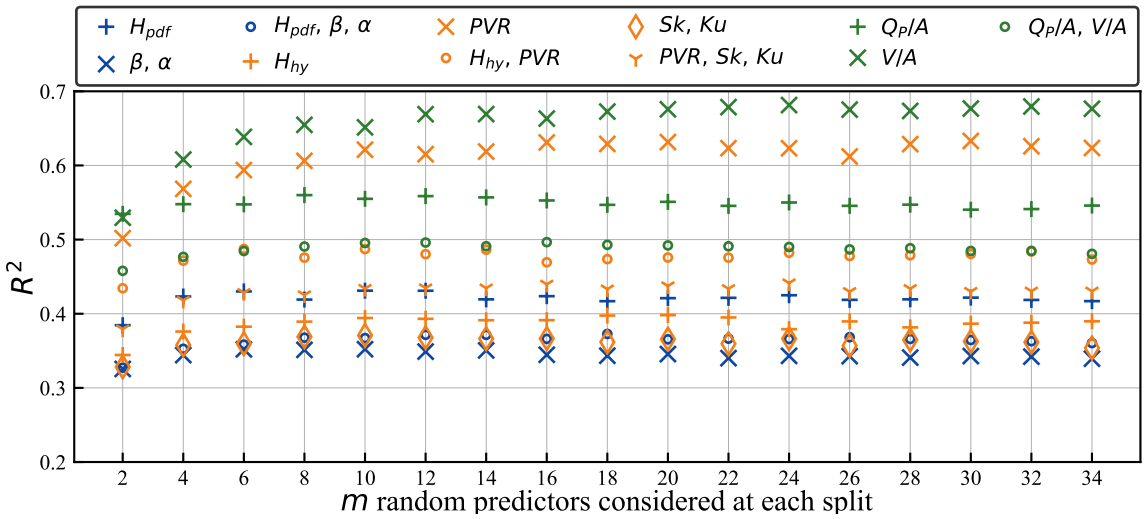

Figure 6.4: Mean RF performance over 10 folds for all target variables, trained with the observations of the 1POT sample. The number of randomly selected predictors at each split m varies, while $N = 100$ and $n = 2$ are set constant.

for different sizes of the terminal node is plotted. The RF are trained to have 300 trees and allowing 12 random predictors at each split. It can be observed that the effect of changing the number of floods at the terminal node is different depending on the target variable used for training the RF. For most target variables, the performance of the RF is continuously decreasing as the number of observations in the terminal node increases, e.g. PVR, V/A and α, β. In other cases, the performance of the RF increases until n reaches a maximum, but then it decreases, e.g. H_{hy}, H_{PDF} and Q_p/A. Only two of the target variables have the maximum performance at the recommended value for regression RF of $n = 5$, the H_{hy} and H_{pdf}. There is no single value for the terminal node size that maximizes the performance of the RF over all target variables. Given that the observed decrease in performance is larger than the gain in performance when increasing n, it is decided that the RF will be trained until they reach purity or a maximum of two floods in the terminal node. By increasing the number of observations ending together in the terminal node, the model is smoothed meaning that it is less sensitive to rare events, since the average of the samples is considered as the prediction.

If the number of observations increases, by considering more POT on average per year, no matter which target variable is analyzed the overall model performance increases (see Fig. A.1). With more observations the performance is expected to increase since more information is used for training the RF. The target variables that have the highest performance according to the R^2 are V/A and H_{hy}, implying that these variables can be directly estimated with more confidence. This does not necessarily mean that those are also going to be the best variables for identifying flood donors with similar mechanisms. The entropy of the PDF fit can be more accurately represented by the RF than the entropy of the hydrograph. One explanation for that is that the actual data of the hydrograph can strongly vary within the

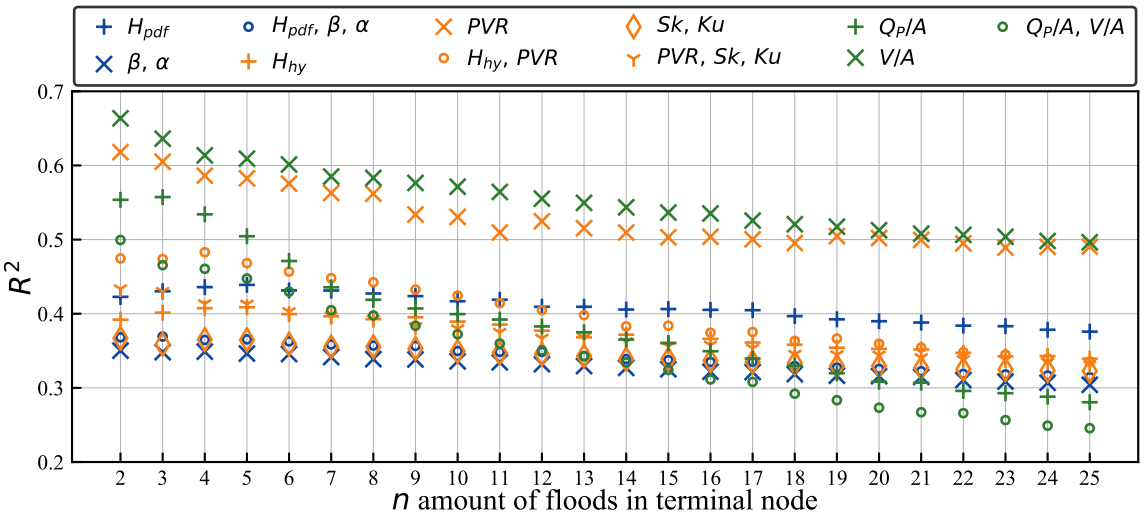

Figure 6.5: Mean RF performance over 10 folds for all target variables, trained with the observations of the 1POT sample. The number of floods in the terminal node n varies, while $m = 12$ and $N = 100$ are set constant.

measured intervals, while the PDF smooths out the hydrograph resulting in less variability.

In conclusion the RF parameters will be kept constant for the following analysis. Although there are some target variables that will not have the optimal performance, the overall effect is small and can, therefore, be neglected for simplifying the analysis. Each RF will be trained to have 100 trees, with a random selection m of 12 predictors per split and each tree will be allowed to grow until it reaches purity or there are only 2 observations, i.e. floods, at the terminal node.

6.5 Estimation of Peaks and Hydrographs

As mentioned before, the peak and the hydrograph shape will be estimated by means of a similarity matrix. The focus of this study lies on the estimation of floods recognizing different catchment responses to various meteorological inputs. The RF algorithm is used to evaluate the similarity between the floods and select the flood donors for the estimation. For this purpose, a "guided" approach for recognizing similar floods is applied, for which a supervised RF is used. As mentioned in Chap. 6.2, three methods for determining the similarity between catchment responses are used:

1. Random forest similarity matrix $\boldsymbol{S}$: The similarity of the floods is determined according to Eq. 6.3.

2. Random forest ensemble average similarity matrix $\bar{\boldsymbol{S}}$: The similarity of the floods

as the average of the $\boldsymbol{S}$ similarity matrices obtained with Eq. 6.3 for each RF in an ensemble.

3. Clustering ensemble co-association matrix $\boldsymbol{CO}$: The similarity of floods is determined as the co-association matrix of a clustering ensemble; the members are obtained by clustering the similarity matrix $\boldsymbol{S}$ of supervised RFs. The clusters co-occurrences gives the co-association matrix $\boldsymbol{CO}$ according to Eq. 6.4 .

Independent of the similarity matrix used, the procedure for estimating the flood hydrographs is as follows:

1. Determine the similarity matrix of the floods, either as $\boldsymbol{S}$, $\bar{\boldsymbol{S}}$ or $\boldsymbol{CO}$.
2. Set a similarity threshold to get the flood donors.
3. Estimate the dimensionless hydrograph shape as the PDF function, whose parameters correspond to the weighted mean or median of the flood donors.
4. Denormalize the estimated dimensionless hydrograph using Eq. 4.3 with V and D.
5. Determine the maximum discharge of the hydrograph Q_p and the time to peak t_p.

For the three methods of generating the similarity matrix, the RFs are trained to have $k = 100$ trees, $m = 12$ predictors at each split and $n = 2$ observations at the terminal node. The RFs are trained using one of the 11 variables as target (see Tab. 6.1) and all 34 predictors (see Tab. A.2 and Tab. A.3). For evaluating the quality of the estimations various similarity thresholds are considered, to be able to analyze the change in performance as more donors are included. For the estimation of the hydrograph, both, the TSP and the Lognormal distributions are used. The parameters of the resulting hydrograph are either the weighted mean or median of the PDF parameters of the corresponding flood donors. The values of the similarity are used as the weights of the donors for calculating the estimated parameters. Using the value of the similarity itself as the weight is chosen. Nevertheless, other methods for weighting were studied, but there was no significant effect observed.

One example of the estimated flood hydrographs and the corresponding flood donors is given in Fig. 6.6. On the left panel the estimations using the TSP distribution are given and on the right panel the case of using the Lognormal distribution. These are obtained using the similarity matrix $\boldsymbol{S}$ of one RF, which is trained using the fit parameters of each distribution and its entropy (α, β, H_{PDF}) as target variable. The PDF fitted to the observations is given in red, the PDFs from the flood donors are given in gray and the estimations using the mean or the median of the parameters are given in blue and orange respectively. For this specific example taking the mean of the PDF's parameters gives a better estimation of Q_p and t_p for the case of the TSP function. For the case of the Lognormal distribution, t_p can be estimated better by using the median of the donors, this, however, overestimates Q_p.

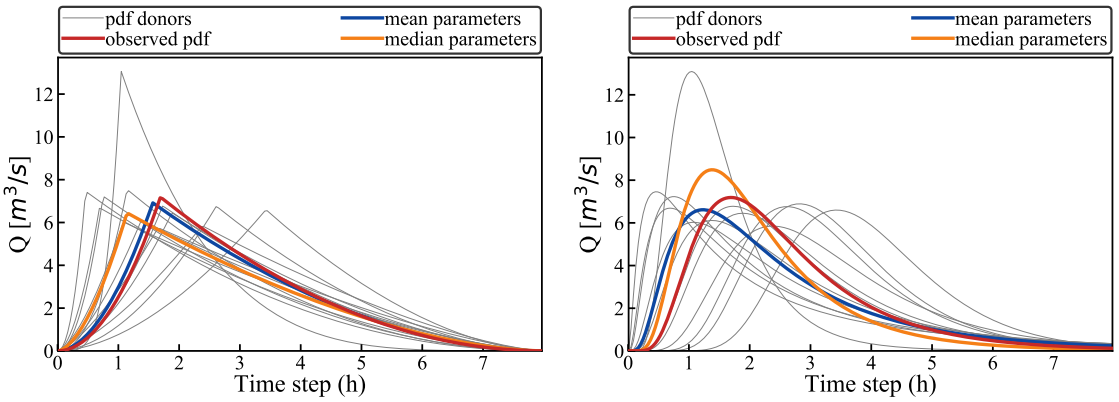

(a) TSP **(b)** Lognormal

Figure 6.6: Flood hydrograph estimated with the similarity matrix S of a RF trained with H_{PDF}, α, β as target. The donors are selected with a threshold of 0.1. On the left panel the TSP distribution is used and, on the right, the Lognormal. In red the PDF fitted to the observed hydrograph and in blue and orange the corresponding estimated hydrographs using the mean and the median of the donors are given. Flood donors are plotted on the background with light gray lines.

The example shown in Fig. 6.6 corresponds to one hydrograph out of 1064 1POT observations, for using one target variable and one similarity measure. In this study, different target variables to train the RF are chosen, various types of similarity matrix ($\boldsymbol{S}$, $\bar{\boldsymbol{S}}$ or $\boldsymbol{CO}$) are studied and the number of donors selected for the estimations are varied, by means of setting a similarity threshold. Here, the quality of these choices is going to be evaluated using Q_p and t_p as performance indicators. As in the example, Q_p and t_p are determined either from the mean or the median of the donors. For comparison, these estimations are then averaged for each catchment as

$$\varepsilon_R = \frac{1}{N} \sum_{i=1}^{N} \frac{\hat{y}_i - y_i}{y_i}, \tag{6.6}$$

where N is the number of observations in the catchment, $\hat{y}$ is the estimated value of Q_p or t_p and y the corresponding observation. For this purpose, observations are separated in train and test samples using a 10-folds strategy, resulting in 10% of the observations being left out for validation. Since no absolute value of the error is considered, it is possible to identify if there is a bias to over- or underestimate, when $\varepsilon_R > 0$ or $\varepsilon_R < 0$, respectively.

First, as an example, the results of using $\boldsymbol{S}$ as a similarity matrix are going to be described, where observations are donors if they have a similarity ≥ 0.1 to a test event. In Fig. 6.7 the average of ε_R over all 45 catchments (see Fig. 3.1) is plotted, for the estimation of the 1POT floods. The error bars correspond to the standard deviation. The horizontal axis gives the target variable used for training the RF. On the top panel the estimation error for Q_p is given and on the bottom panel the error for t_p. Both using the mean and the median of the TSP

parameters from the selected donors are included in blue and orange respectively. Only the RF where a given observation is not used for training the model is considered for assessing the similarity of a test observation.

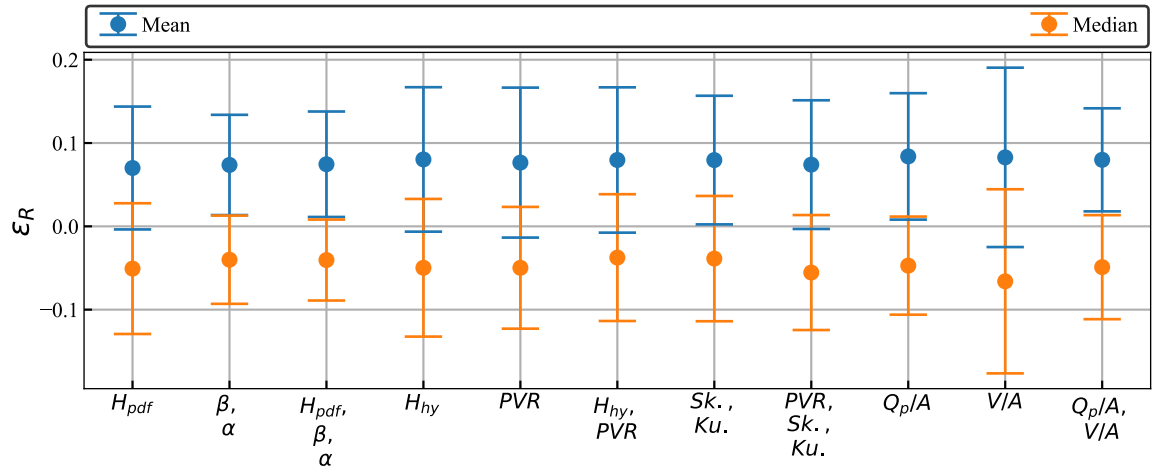

(a) Q_p

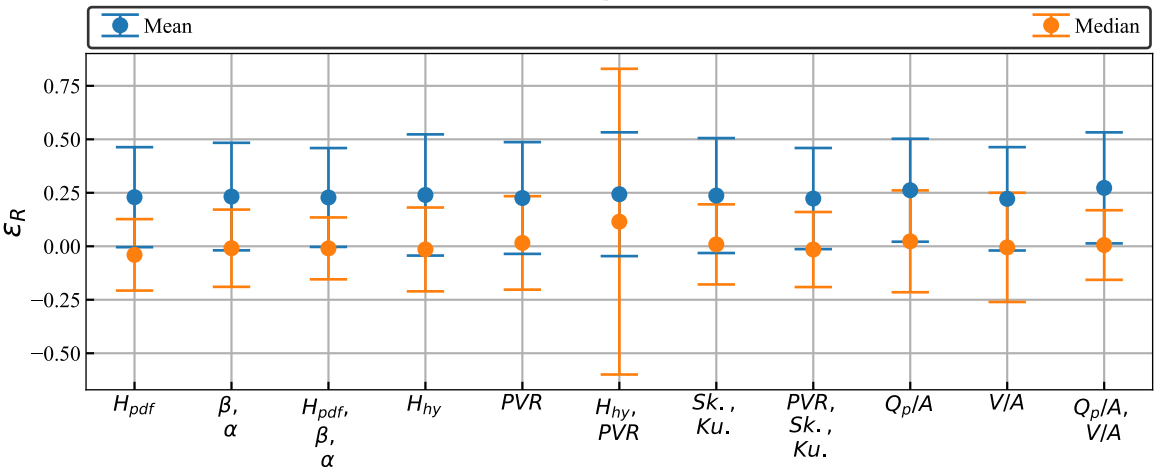

(b) t_p

Figure 6.7: Summary of the average relative error for the estimation of Q_p **(a)** and t_p **(b)** obtained for each catchment. The horizontal axis, gives the target parameter used for training the RF. The flood donors are selected for a similarity value of 0.1 using $\boldsymbol{S}$ as the similarity measure of the floods and a TSP distribution for the estimation of the hydrograph.

Figure 6.7 shows that by using the mean of the parameters, independent on the target used for training the RF, Q_p and t_p are overestimated, i.e. their relative error ε_R is positive. If the median is used Q_p is underestimated but t_p is very close to zero and its error bars are significantly smaller, compared to when using the mean. The overall best estimation for Q_p and t_p is achieved for the target variables (α, β, H_{PDF}) of a TSP distribution, where the standard deviation and relative error is smallest for both parameters. Using V/A as the target

variable results in the largest standard deviation of Q_p. The largest standard deviation for the estimation of the median t_p occurs when (H_{hy}, PVR) are used as target variables of the RF. Interestingly, such a large standard deviation is not observed for the mean of t_p. The median t_p and Q_p will be used in the subsequent analysis, due to the smaller standard deviation of the relative error for Q_p and t_p for almost all target variables. As already pointed out the standard deviation of ε_R on t_p for H_{hy}, PVR as target variable is significantly larger than for the other target variables. A possible explanation is the randomness when sampling the train and test data (with k-folds) and the random nature of RF. Each time a RF is constructed, even if it is trained with the same observations and target variable, the similarity obtained is different. With the idea of obtaining more robust results, which are less sensitive to the randomness of one RF, using the similarity matrices $\boldsymbol{S}$, $\bar{\boldsymbol{S}}$ and $\boldsymbol{CO}$ for the estimation is explored in the next subsections.

6.5.1 Similarity Matrix $\boldsymbol{S}$

In Fig. 6.8 a representation of the average catchment ε_R for the estimations of Q_p (top panel) and t_p (bottom panel) is given for various similarity thresholds, which are identified in the horizontal axis. The data shown in Fig. 6.7 corresponds to a similarity of 0.1 in Fig. 6.8. The colored bars are given for visualization purposes and they represent the mean of the average catchment ε_R. The three colors blue, orange and green, correspond to the three target groups mentioned in Tab. 6.1. The gray lines give the standard deviation of ε_R for the 45 catchments.

On the top panel of Fig. 6.8 a decrease of the ε_R for all target variables is observed, as the similarity threshold decreases. A decrease of the similarity value implies that more floods are accepted as donors. For a similarity value from 0.05 on, no significant change is observed and ε_R no longer improves. However, by including more flood donors the estimations start to worsen, which can be seen by the slightly larger error bars. Looking at the bottom panel, the estimations of t_p, the same trend can be observed. For a similarity smaller than 0.1 the error transitions into an overestimation and ε_R starts increasing as the similarity keeps decreasing. For the similarity thresholds, where the mean of ε_R is closer to zero, for both the estimation of Q_p and t_p, there is an observed variability of the standard deviation of these errors (especially for t_p), when choosing a different target for the RF. The standard deviation of ε_R is smallest for the similarities obtained when training the RF using as target either α , β or H_{PDF}, α , β (see Tab. A.4). Although there is no single combination of similarity value and target variable that minimizes ε_R on both Q_p and t_p, a similarity threshold between 0.1 and 0.05 could be chosen depending on the flood estimation purposes, i.e. whether it is more important catching the peak or its temporal occurrence. This will result in an estimated hydrograph with an expected error of $\pm 10\%$ for Q_p and $\pm 15\%$ for t_p. If the mean of the TSP parameters is used instead of the median, an overall bias to overestimate both, Q_p and t_p, is observed, independent of the similarity threshold used (see Tab. A.4). If a Lognormal distribution is considered, using the mean of the fitted parameters yielded no better performance (see Tab. A.4 and Tab. A.5). The results obtained by estimating Q_p

with the median of the TSP parameters had similar performances to those of using the mean of the Lognormal parameters. The best performance for estimating Q_p can be found for a similarity threshold between 0.1-0.2 for the Lognormal distribution and for a similarity threshold of 0.05-0.1 for the TSP distribution. The estimation of t_p, using the Lognormal distribution, results in overall larger ε_R as compared to the TSP distribution.

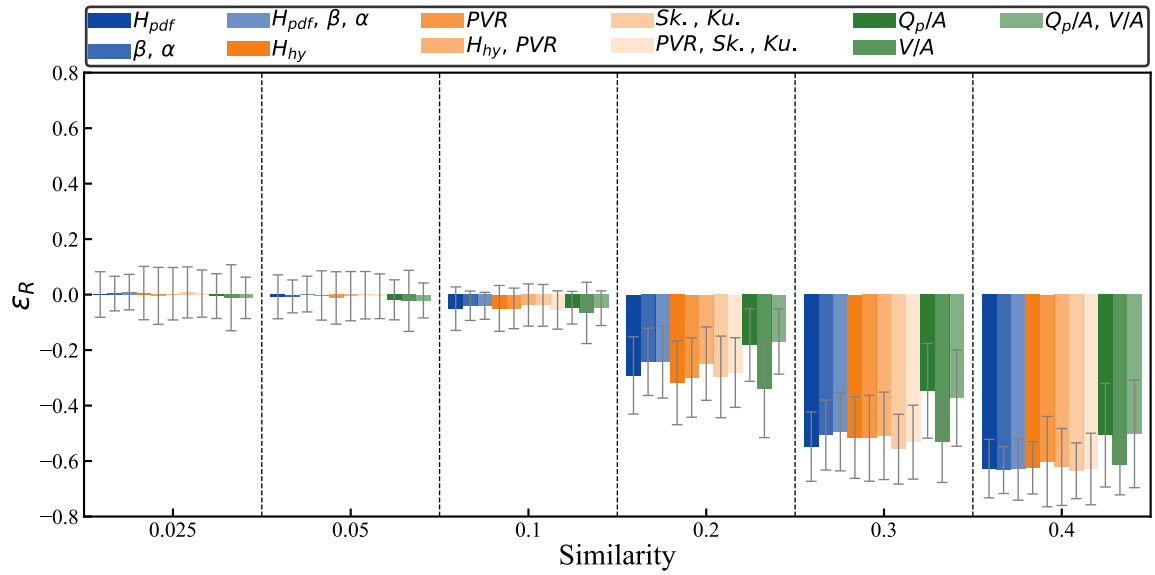

(a) Q_p

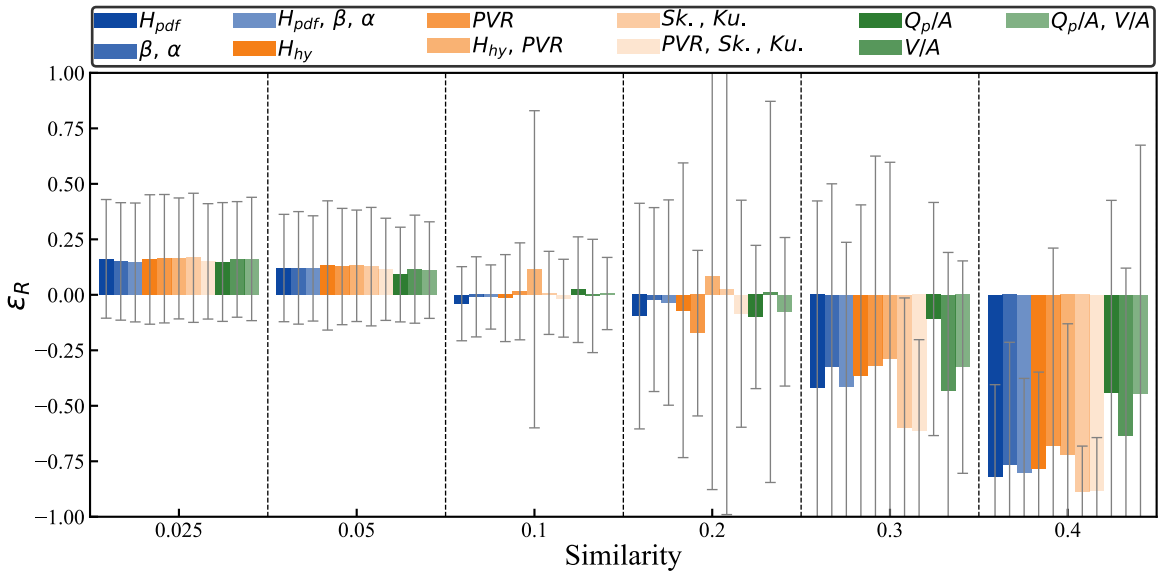

(b) t_p

Figure 6.8: Distribution of the average relative error for the estimation of Q_p **(a)** and t_p **(b)** obtained for each catchment. The similarity threshold considered are identified on the the horizontal axis. The flood donors are selected using $\boldsymbol{S}$ as the similarity measure of the floods according to a given threshold. The median of the TSP parameters from the donors are used for the estimations.

In Fig. 6.8, when looking at the similarity thresholds of 0.4 and 0.3, a larger decrease on ε_R is observed if using Q_p/A as target in comparison to the other target variables. This is attributed to more flood donors being selected for those similarity thresholds. It is important to point out that the similarity matrix $\boldsymbol{S}$ captures the non linear representation of the observations with respect to the chosen training variable. Thus, the resulting similarity values depend on the target variable, given that the RF is built with a different guidance. This leads to having different numbers of donors selected for the same similarity threshold, depending on the target variable considered. In Fig. 6.9 the number of donors selected for different thresholds are given.

Here, the three colors blue, orange and green, also represent the three target groups mentioned in Tab. 6.1. As expected, the number of flood donors increases with decreasing similarity, since the donors are allowed to be more distant from the flood to be estimated. The number of average donors selected per catchment is almost constant for each similarity threshold, independent on the target variable used for training the RF. However, it is observed that using Q_p/A or $Q_p/A, V/A$ as targets, results in less donors for the smaller similarity thresholds and more donors for the larger similarities. This can explain the differences in performance between Q_p/A or $Q_p/A, V/A$ with respect to the other targets (see Fig. 6.8).

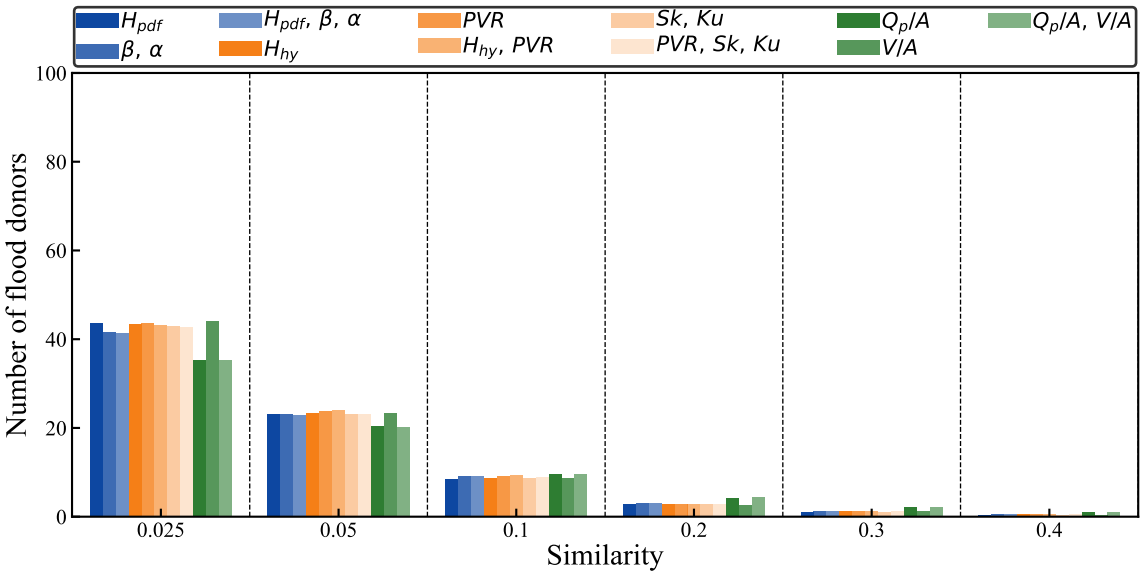

Figure 6.9: Number of flood donors selected according to different similarity thresholds using $\boldsymbol{S}$ as the similarity matrix.

6.5.2 Similarity Matrix $\bar{S}$

In Fig. 6.10 the values of ε_R for the estimation of Q_p and t_p are given, when considering the similarity of the floods as $\bar{\boldsymbol{S}}$ in the same format as in Fig. 6.8.

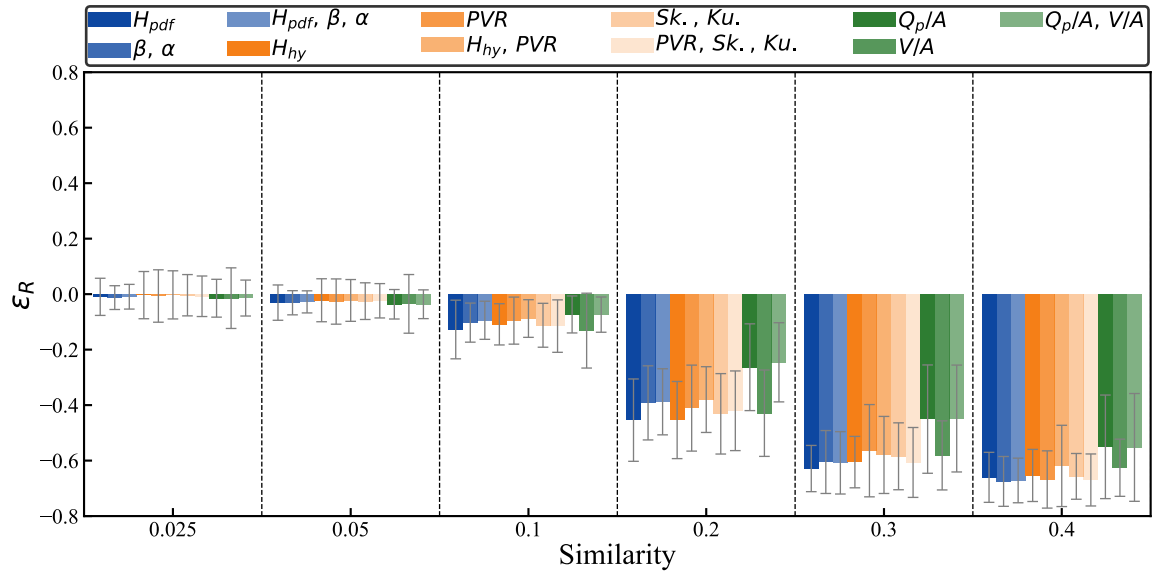

(a) Q_p

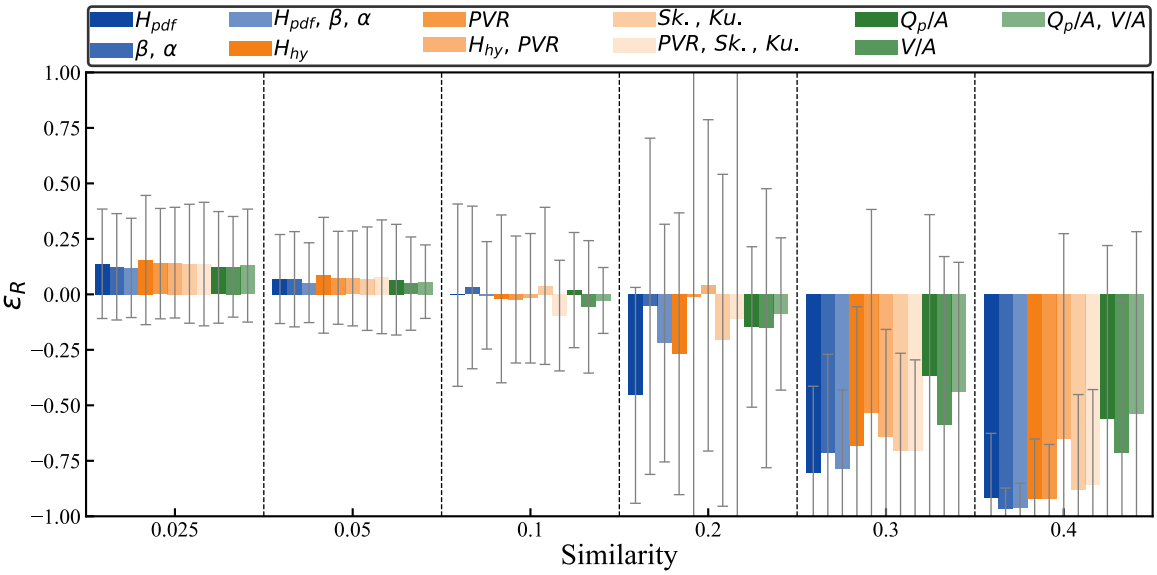

(b) t_p

Figure 6.10: Distribution of the average relative error for the estimation of Q_p **(a)** and t_p **(b)** obtained for each catchment. The similarity threshold considered are identified on the the horizontal axis. The flood donors are selected using $\bar{S}$ as the similarity measure of the floods according to a given threshold. The median of the TSP parameters from the donors are used for the estimations.

For Q_p, a decrease of ε_R with decreasing similarity can be observed, as well as an underestimation as a general trend over all target variables. At a similarity of 0.025 the mean of ε_R is closest to zero. Nonetheless, the overall standard deviation of ε_R is slightly larger than for a similarity of 0.05. In particular, for a similarity of 0.025, the standard deviation is $\pm$0.074,

compared to ± 0.065 when a similarity of 0.05 is chosen (see Tab. A.6). REgarding the estimations of Q_p, a reduction in the mean and the standard deviation of ε_R is obtained with $\bar{\boldsymbol{S}}$ compared to those when using $\boldsymbol{S}$. Independent of the target variable chosen for training the RF, the overall trend of the estimations of t_p (bottom panel Fig. 6.10) is similar when using $\boldsymbol{S}$ as a similarity matrix (bottom panel Fig. 6.8). For the larger similarity values, there is an underestimation on t_p. At a similarity of 0.1 there seems to be an optimum on the performance (i.e. minimum ε_R). However, by including more donors ε_R increases again, leading to an overestimation of t_p. It is also observed that the very large standard deviation in Fig. 6.8, when using H_{hy}, PVR as the target variable and for a similarity of 0.1 of $\boldsymbol{S}$, is no longer present when using $\bar{\boldsymbol{S}}$. There is also an improvement for the estimation of t_pv, if considering $\bar{\boldsymbol{S}}$ instead of $\boldsymbol{S}$ ε_R decreases by ≈ 0.025 (see Tab. A.4 and Tab. A.6). For the case of the Lognormal distribution with the similarity matrix $\bar{\boldsymbol{S}}$, the mean of the parameters instead of the median also resulted in an overall smaller ε_R. Using a more robust similarity showed a more significant reduction of the standard deviation of ε_R (see Tab. A.5 and Tab. A.7). Even though the observed differences in ε_R when considering $\bar{\boldsymbol{S}}$ instead of $\boldsymbol{S}$ are small, choosing $\bar{\boldsymbol{S}}$ as the similarity deals with the random nature of the RF algorithm. This is observed on the smaller variability of the standard deviations of ε_R. Thus, there is a better performance of the hydrograph estimation if a more robust similarity measured is considered.

6.5.3 Similarity Matrix CO

In analogous representation as in Fig. 6.8 and Fig. 6.10, the estimation errors for Q_p and t_p are given in Fig. 6.11, considering the similarity between the observations with the $\boldsymbol{CO}$ matrix.

At first, it is important to point out that the similarity thresholds chosen here are different compared to the case of $\boldsymbol{S}$ and $\bar{\boldsymbol{S}}$. This is due to the fact that for calculating the $\boldsymbol{CO}$ matrix, the similarity between the cluster labels of 9 "base clusterings" are compared. This results in the set of possible similarities of $\left\{\frac{0}{Z}, \frac{1}{Z}, \ldots, \frac{Z}{Z}\right\}$, where Z is the number of "base clusterings". Thus, there are less similarity thresholds considered and, therefore, less variation between the number of selected donors. A value of 10 clusters per "base clustering" is chosen, based on the findings from (Brunner et al., 2018d) of three reactivity regions, each with three possible catchment reactions.

If the similarities are considered as the $\boldsymbol{CO}$ matrix the median of the TSP also showed to have a better performance over taking the mean, for both the estimation of Q_p and t_p. It is observed that both, Q_p and t_p, undergo a transition from underestimation to overestimation with decreasing similarity. Nonetheless, this occurs at different similarity thresholds, between 0.6 and 0.5 for Q_p and between 0.8 (or larger) and 0.7 for t_p. For the case of estimating Qp, it is observed that for some targets a larger similarity value reduces the bias, given that ε_R is closer to zero. The standard deviations are smaller when less donors are considered (see also Tab. A.8). For the estimation of t_p a tendency on the overestimation is observed for all targets and similarities as well as a significantly larger standard deviation (see Tab. A.9).

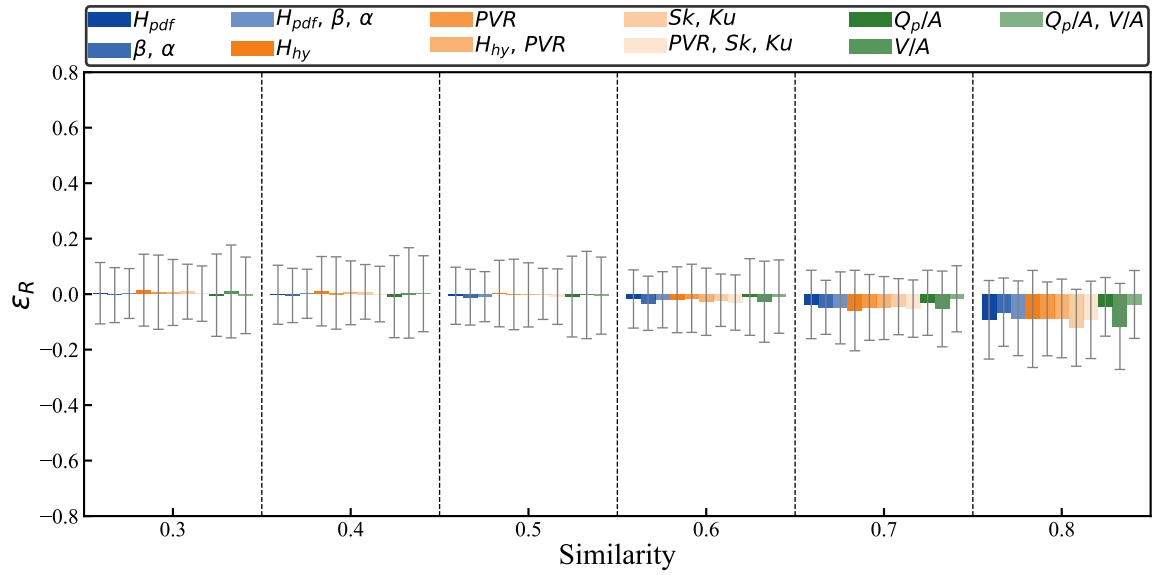

(a) Q_p

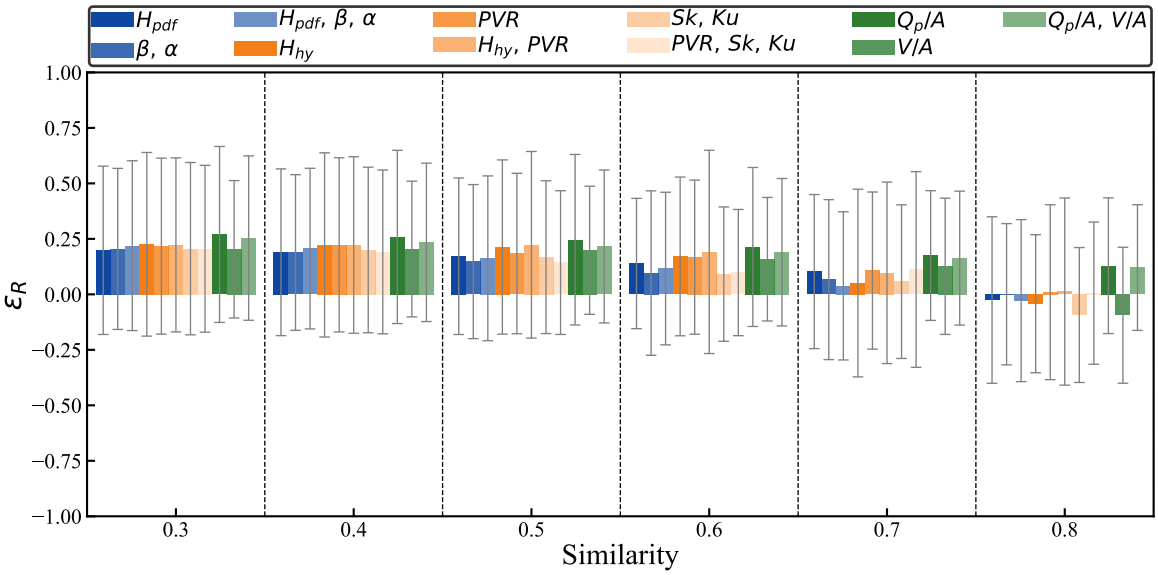

(b) t_p

Figure 6.11: Distribution of the average relative error for the estimation of Q_p **(a)** and t_p **(b)** obtained for each catchment. The similarity threshold considered are identified on the the horizontal axis. The flood donors are selected using $\boldsymbol{CO}$ as the similarity measure of the floods according to a given threshold. The median of the TSP parameters from the donors are used for the estimations.

6.5.4 Concluding Remarks on Similarity

Given that a similarity value has a different meaning, depending on the matrix used. For the three similarity matrices considered, the thresholds of similarity of 0.8, 0.05 and 0.05 are chosen for $\boldsymbol{CO}$, $\boldsymbol{S}$ and $\bar{\boldsymbol{S}}$ respectively. This assures a similar number of selected donors within the three similarity matrices (see Fig. 6.9, Fig. A.2, Fig. A.3). In all three cases, for most of the targets, the same tendencies are observed: an overestimation of Q_p and an underestimation of t_p, independent on the PDF distribution. For almost all targets, this bias is observed to be smallest for $\bar{\boldsymbol{S}}$ and largest for $\boldsymbol{S}$, no matter if the median of the TSP parameters or the mean of the Lognormal parameters is considered. However, the standard deviations of ε_R, for both the estimation of Q_p and t_p, showed to be largest for $\boldsymbol{CO}$ than for $\boldsymbol{S}$ and smallest when using $\bar{\boldsymbol{S}}$.

The extra model complexity when using $\boldsymbol{CO}$ seems to worsen the estimations. Nonetheless, it can be that the representation of the observations space is simplified by the use of 10 clusters, which can result in a worse estimation of the distances between the floods. An ensemble of a larger size (more "base clusterings") and/or a larger number of clusters might lead to better results. Nevertheless, this was not further pursued.

Given that various target variables showed small variation on the performances of the estimations of Q_p and t_p, one could think that an unsupervised RF could satisfy the same purpose. To evaluate if there is an advantage of using the guided RF approach, the performance of a similarity matrix obtained when instead an unsupervised RF is considered, are going to be studied next.

6.6 Supervised versus Unsupervised Random Forest

The similarity matrix of an unsupervised RF reveals how close observations are when compared to synthetic data. This means that an unsupervised RF is not trained to estimate a given target but to differentiate between two classes, the true and the synthetic. An unsupervised RF is considered in this study, to evaluate whether its similarity space represents the distance of the floods through the complexity of the flood reactions as done by the supervised RF. This determines if there is an advantage of using a supervised RF. In this case, the similarity matrix $\bar{\boldsymbol{S}}$ is used for both the supervised and unsupervised RF, given that $\bar{\boldsymbol{S}}$ is the one that resulted in the better performances for the estimation of Q_p and t_p in the previous chapter.

The first difference between the supervised and unsupervised RF is the number of flood donors selected according to the similarity thresholds. In Fig. 6.12 the number of donors when choosing different similarity thresholds are given. It can be observed that the number of donors increases as the similarity threshold decreases as it was for the case of the supervised RF. However, this increase is larger than the observed with the supervised RF (Fig. A.2). For the unsupervised RF the floods seem to be closer to each other than for the

supervised RF, where a larger separation is observed, i.e. less donors for the same similarity threshold. One explanation for this is that with the unsupervised RF, the similarities between the observations are more driven by the catchment characteristics than by the meteorological event causing the floods. This results in flood donors being selected only if they belong to a similar catchment without distinguishing between different flood mechanisms. To visualize this, the importance of the predictors in the case of the supervised and the unsupervised RF are given in the top and bottom panel of Fig. 6.13. The importance of each predictor is calculated with Eq. 6.2.

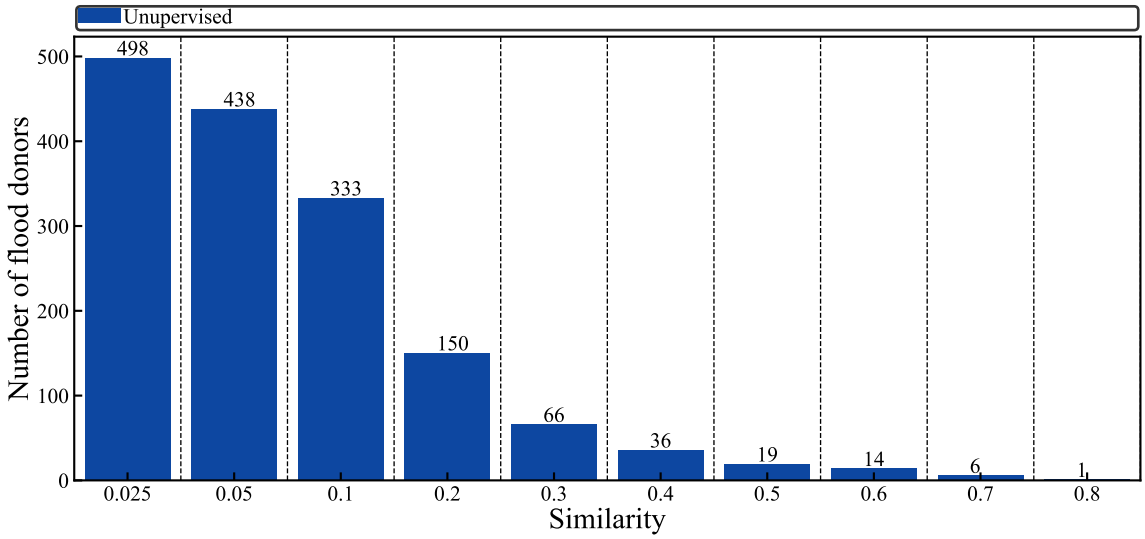

Figure 6.12: Number of flood donors selected according to different similarity thresholds using $\bar{\boldsymbol{S}}$ as the similarity matrix, obtained from an unsupervised RF.

On the bottom panel of Fig. 6.13 it can be observed that predictors belonging to the constant catchment descriptors (groups marked in green, yellow, purple and gray) are the most important predictors when considering an unsupervised RF. These predictors contain information that is repeated for the flood events belonging to a given catchment. It shows that the relationships found with the unsupervised RF are driven by the similarities between the catchments rather by the meteorological forcing causing each event. On the contrary, when considering a supervised RF the most important predictors belong to the characteristics of the precipitation event causing the floods (H_R, API, etc.). The meteorological event is the main driver of floods and it is, therefore, responsible of different flood processes. For example, an intense precipitation event as a result of convective precipitation will typically trigger a flash flood with a sharp hydrograph. It is, therefore, expected that a RF, which gives more importance to the meteorological forcing, results in a similarity matrix that is a better representation of the flood mechanisms space. Nonetheless, it is also important to determine whether an unsupervised RF possesses an advantage for obtaining more accurate estimations.

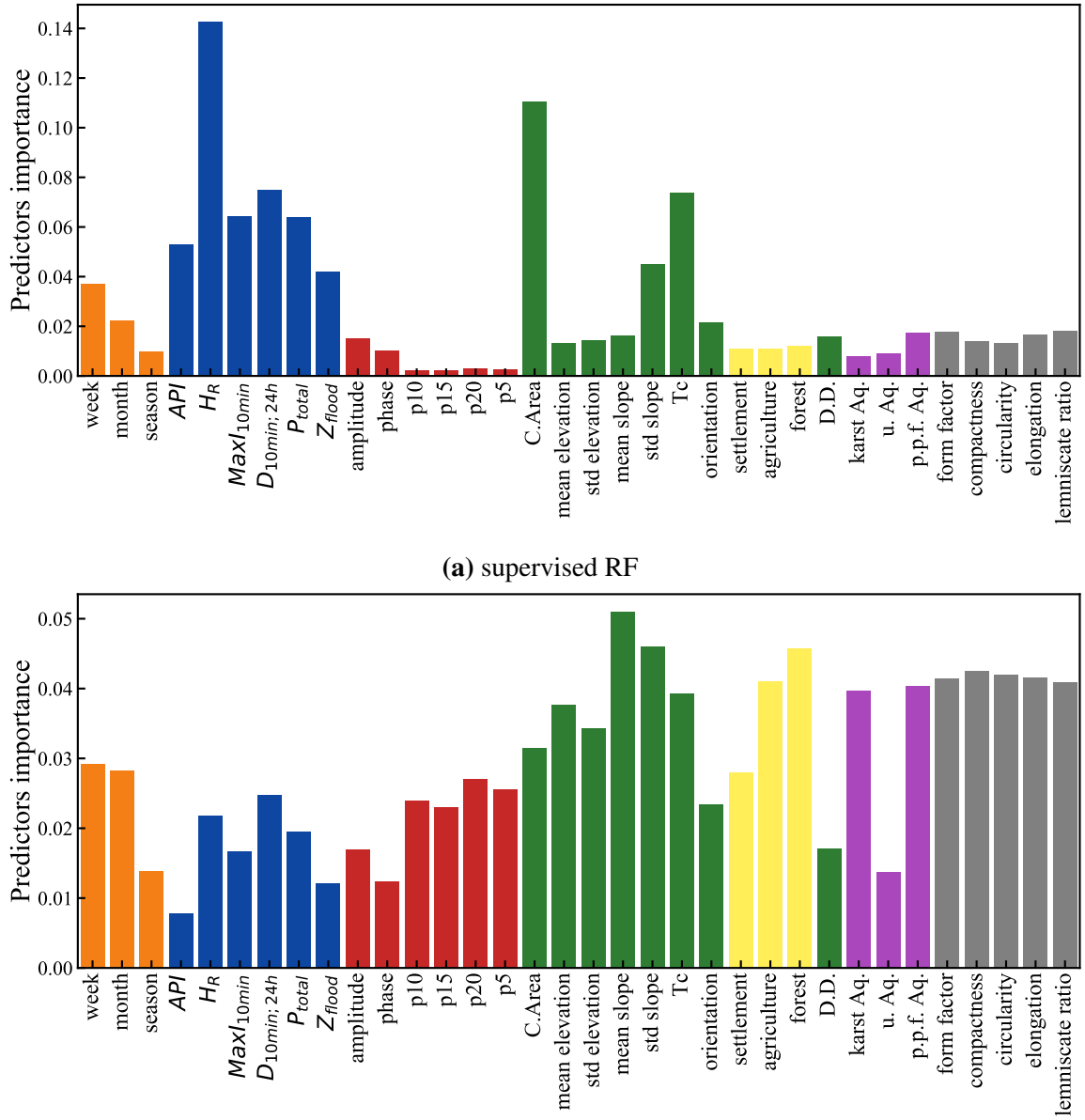

(a) supervised RF

(b) unsupervised RF

Figure 6.13: Predictors importance for a supervised and unsupervised RF

Figure 6.14 shows the performance for the estimation of Q_p and t_p when using the similarity matrix $\bar{\boldsymbol{S}}$ of an ensemble of unsupervised RF models to select the flood donors. In this case, the median of the parameters of a TSP distribution is used for the estimation of the flood hydrographs. On the top panel of Fig. 6.14 it is observed that for the case of Q_p the mean ε_R gets closer to zero as the similarity threshold decreases and thus the bias becomes smaller. However, this is not observed for the standard deviation of ε_R, which has a minimum at a similarity value 0.5 and not at the lowest similarity value considered. At this similarity threshold the performance over all catchments is the best, with a small underesti-

mation of Q_p. If the results are compared with those of the supervised RF in Fig. 6.10, there is no similarity threshold that achieves the same performance as the one obtained with a supervised RF. Nevertheless, the difference in the minimum standard deviation of ε_R between the supervised and the unsupervised RF is only around 0.02.

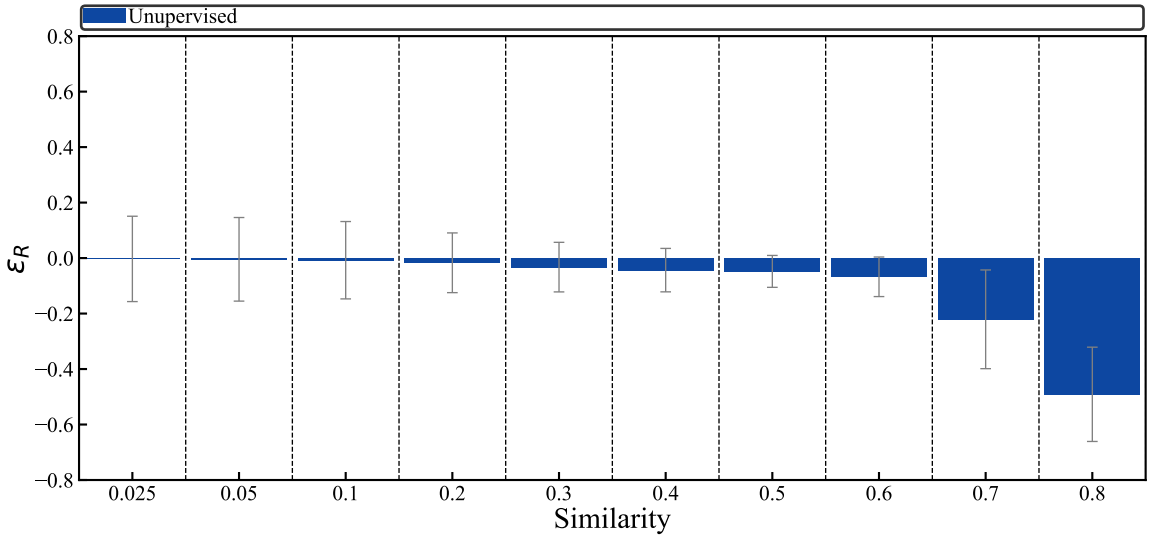

(a) Q_p

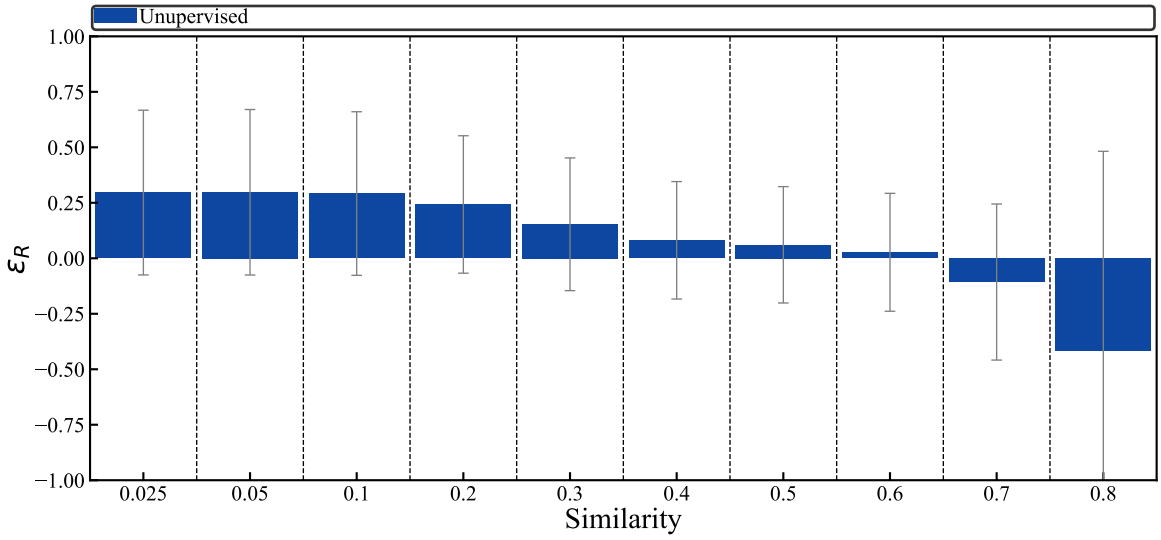

(b) t_p

Figure 6.14: Distribution of the average relative error for the estimation of Q_p **(a)** and t_p **(b)** obtained for each catchment. The similarity threshold considered are identified on the the horizontal axis. The flood donors are selected using $\bar{S}$ from an ensemble of RF as the similarity measure of the floods according to a given threshold. The median of the TSP parameters from the donors are used for the estimations.

On the bottom panel of Fig. 6.14 the summary of the estimation performance of t_p is given. It can be observed that at a similarity threshold of 0.6 the best performance is obtained, with both the smallest bias and the smallest ε_R. For larger similarity values, there is a tendency to underestimate t_p and for smaller values this changes to the overestimation. Comparing these results to the ones obtained with the supervised RF (see Fig. 6.10), it is also observed that when considering an unsupervised RF the estimations of t_p is worse. The difference in the minimum standard deviations of ε_R obtained for the case of the supervised and the unsupervised RF is 0.09, which is larger as the value obtained for the case of Q_p.

It is shown that a supervised approach gives better estimations than an unsupervised one, which leads to conclude that by adding the guidance with a given target variable, the interrelationships causing different flood responses can be captured better. Additionally, it is important to understand whether the physical interpretations obtained with the RF agree with the known hydrological responses, to assure a consistent and reasonable regionalization model. Therefore, in the next chapter an analysis of the RF space is going to be carried out, to identify what do the flood events that are close to each other according to the RF have in common.

6.7 Floods Similarity According to Random Forest

The evaluation of the similarity representation is challenging since the true similarity of the observations space is not known. One can evaluate the similarity space with a plot of the first dimensions obtained with MDS, by looking at the common characteristics of observations that are close to each other. However, with many observations this is not feasible. For simplicity, one can cluster the similarities obtained by the RF to identify patterns in the data and to understand the representation of what are considered to be similar observations. This helps to understand if the known physical interactions are rightfully represented by the model. It helps peeking inside the black box of the algorithm to reveal how the algorithm interprets the interrelationships.

For clustering purposes $1 - \bar{\boldsymbol{S}}$ is used, because clustering algorithms are based on the representation of data in an Euclidean space, meaning that small "distances" represent close observations and larger "distances" more distant observations. This results in a matrix with values between 0 and 1, where 0 indicates the most similar floods and 1 the most dissimilar floods. This matrix is used as input to a clustering algorithm. Three clusters are chosen here, to facilitate the interpretation of the results. Note that this should not imply that the optimal classification number of the floods mechanisms is three. At this stage, the clusters are considered just for representation and understanding purposes. Finding the true number of clusters in the data is not the main goal, since only the similarity of the floods is needed for the regionalization. Merely the similarity matrix obtained from a supervised RF trained having as target parameter H_{PDF}, α, β is going to be considered here.

The distribution of the PVR for each of the obtained clusters is given on the left panel of Fig. 6.15. The distributions are given as a box plot, where the green line indicates the median and the orange triangle the mean. This plot helps to identify which catchment reaction occurs more frequent at each of the three clusters. The clusters are sorted from the one with the smallest mean PVR (A) to the one with the largest mean PVR (C). On the right panel of Fig. 6.15 an example of the hydrographs from one catchment are plotted. These are colored according to the cluster they belong to. It can be observed that cluster C, yellow hydrograph, has a sharp curve with a fast occurring Q_p and that cluster A and B have slower reactions. In this sense, cluster A, B, C correspond to hydrographs with slow, intermediate and quick reactions respectively. A classification of the flood mechanisms could be achieved by means of a supervised RF. However, further research is required to identify the optimal number of clusters. This is not further pursued, since it is considered out of the scope of this study.

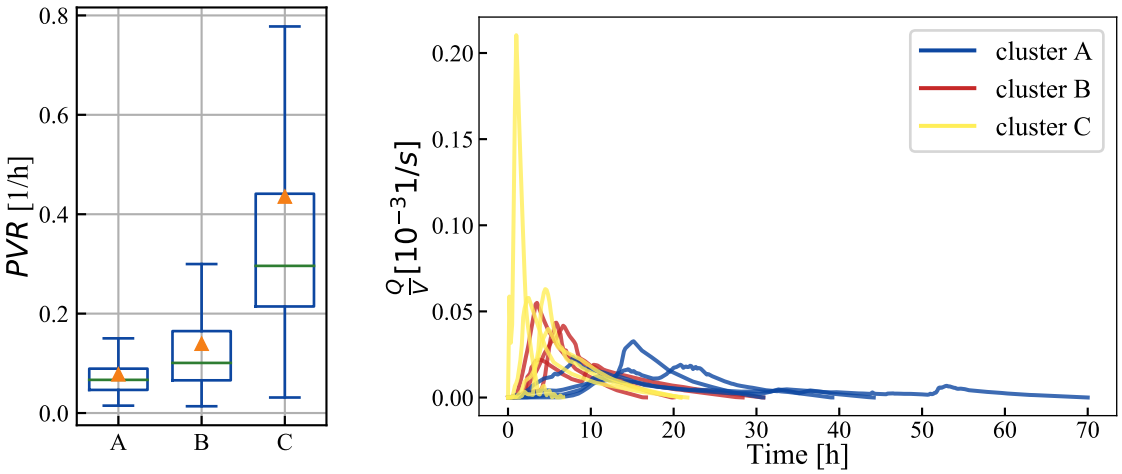

Figure 6.15: Similarity of hydrographs according to a supervised RF trained with the 1POT to estimate the parameters of the fitted PDF (H_{PDF}, α, β). Left panel: shows the distribution of the PVR for the three catchments obtained using the similarity matrix of the RF. Right panel: Example of the hydrographs belonging to one catchment, the hydrographs are colored according to the cluster.

In Fig. 6.16 the distribution of some characteristics of the meteorological events triggering the floods are given, as a box plot representation. It can be observed in Fig. 6.16a that the precipitation temporal entropy (H_R), is the variable that shows a larger separation between the clusters. This agrees with the observation on the top panel of Fig. 6.13, where it is shown that the temporal distribution of precipitation, measured by H_R, is the most important predictor for the supervised RF, it is the predictor that gives more information for estimating different reactions. The predictor H_R is the one that allows a better binary split of the observations through the nodes of the trees in the RF. In Fig. 6.16 it can be observed that the physical understanding of the processes is represented properly. The quickly reactive events (cluster C) have mainly precipitation events that are concentrated within a few time intervals, with small H_R, high intensities and lower durations (see also Fig. 6.16b and Fig. 6.16c). The

slow and intermediate catchments reactions (cluster A and B) are rather triggered by longer precipitation events with lower intensities and larger H_R. These events can be the result to orographic effects or frontal systems.

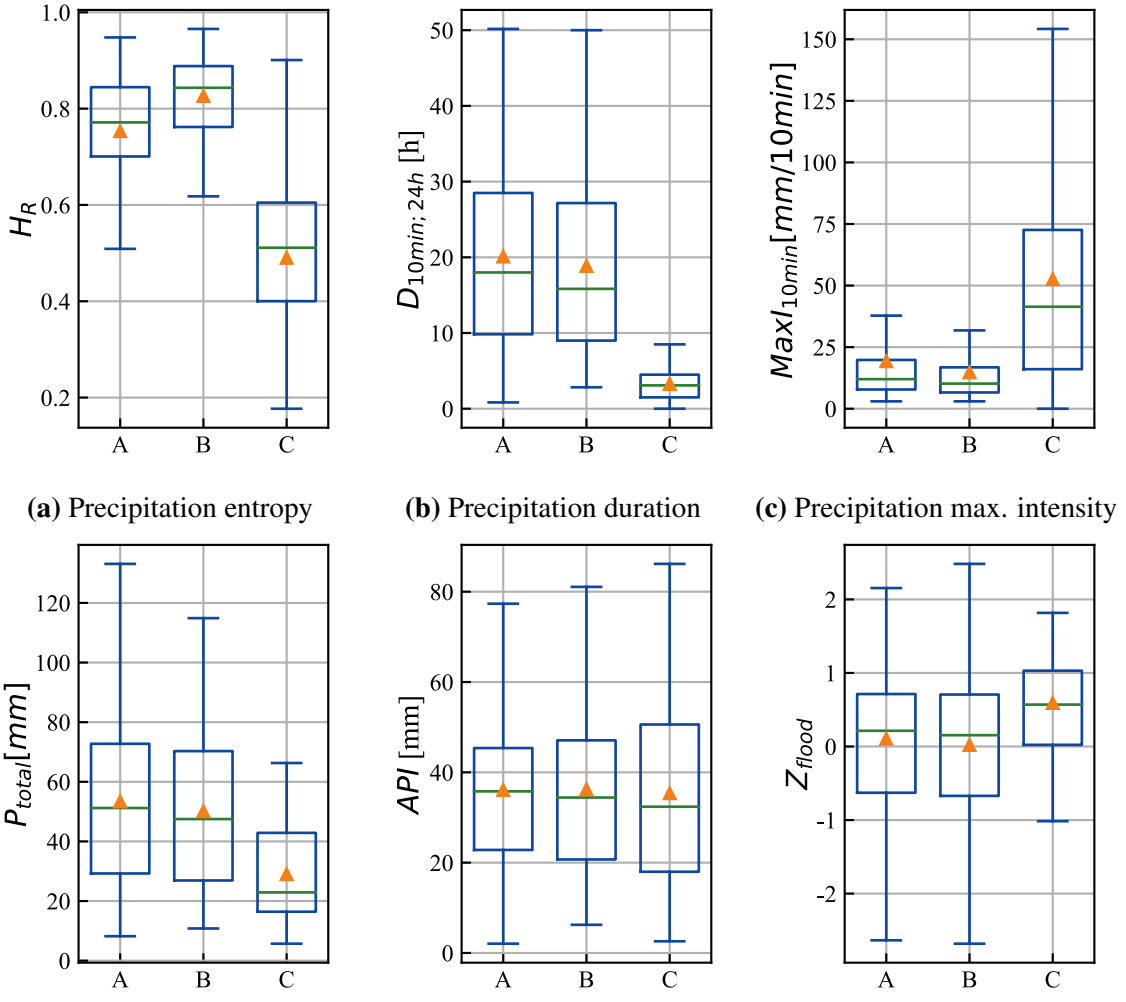

(a) Precipitation entropy **(b)** Precipitation duration **(c)** Precipitation max. intensity

(d) Precipitation sum **(e)** API **(f)** Temperature standard score

Figure 6.16: Similarity of the characteristics of the meteorological event triggering a 1POT according to a supervised RF trained to estimate the parameters of the fitted PDF (H_{PDF}, α, β). On the subplots the distribution of various meteorological characteristics is given, each box constructed from the events belonging to one cluster.

Regarding the total amount of precipitation triggering the 1POT events (see Fig. 6.16d), it can be observed that both cluster A and B have larger volumes of precipitation. This larger precipitation volumes distributed in longer periods of time explain the fact that clusters A and B have smaller PVR. Concerning the API triggering the 1POT events (see Fig. 6.16e), it is observed that there is almost no difference within the three clusters. However, if the API of each cluster is further separated by the season the flood event occurred, some patterns of

the API triggering a flood through the seasons can be identified (see Fig. A.4). The equal ranges of API observed within the clusters can be explained by the fact that for a given catchment, the same API value indicates different soil moisture depending on the time of the year the event occurred. For instance, the same value of API in winter and in summer is expected to indicate a drier soil for the case of the summer event since larger evaporation takes place. One can conclude that the relationship between the API and the floods is more complex as the one explained only by the three clusters considered here.

In Fig. 6.17 the seasonal frequency of occurrence of the flood events are given. Each of the panels represents a cluster. Additionally, the bars are colored for differentiating the season in which each event occurred. It can be observed that for the case of the quick hydrographs (cluster C), most of the floods took place in summer. This agrees with the fact that flash-floods is a typical mechanism taking place in summer. Moreover, the temperature's standard score at the occurrence of a flood (Z_{flood}) has a stronger tendency of being larger than zero than for the case of the other two clusters (see Fig. 6.16f). This is an indicator of having more temperature increases, which results in convective precipitation. Slow and intermediate events (clusters A and B) are observed to be more evenly distributed within the year. This type of reactions are known to be caused by meteorological fronts or orographic effects that take place over the whole year.

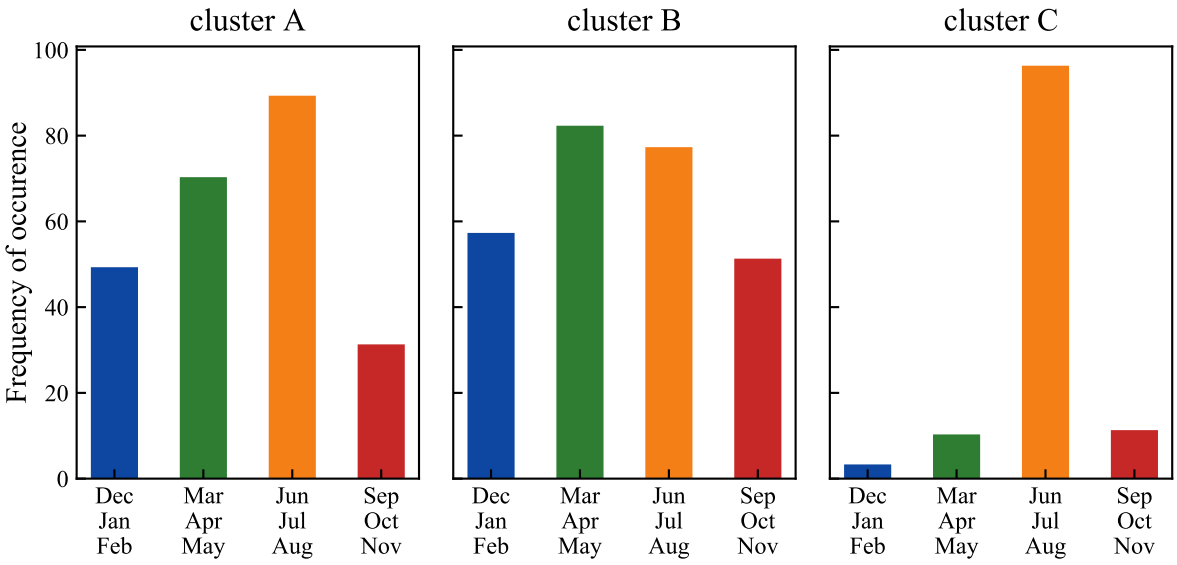

Figure 6.17: Seasonal frequency of occurrence of various hydrograph reactions clustered according to similarities obtained a supervised RF. Each subplot is constructed with the events belonging to each cluster.

In Fig. 6.18 the distribution of the land use of the events belonging to the three clusters is given. The low variations are explained by the possibility of the same catchment being able to have a slow, intermediate or quick reaction. Given that various meteorological events can take place over a catchment. Nevertheless, the differences show that there is a slight tendency for catchments with larger percentages of agriculture and settlement and smaller

percentages of forest to generate more quick reactions (cluster C).

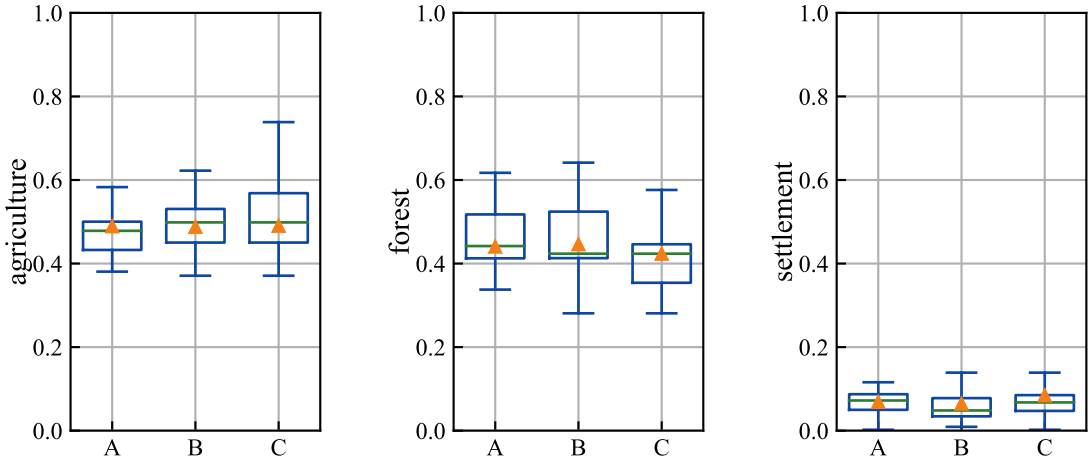

(a) Agriculture **(b)** Forest **(c)** Settlement

Figure 6.18: Similarity of the land use of 1POT events belonging to three clustered reactions, according to a supervised RF trained to estimate the parameters of the fitted PDF (H_{PDF}, α, β).

Last, in Fig. 6.19 catchment area, concentration time and the percentage of karst aquifer are included. It can be observed that a quick reaction (cluster C) is a more typical reaction of smaller catchments, with lower concentration times. Larger catchments, as expected have a rather slow reaction (cluster A), given that the runoff is the result of the added reactions of the sub-basins. The precipitation temporal entropy H_R showed to be smaller in the slow hydrograph reactions (cluster C) than for the intermediate reaction (cluster B) and the corresponding PVR where larger for cluster B than for cluster A. This means that the precipitation events that are more uniformly distributed in space tend to produce more sharp hydrographs. This is not an expected catchment reaction to the characteristics of the precipitation event. Nevertheless, it might be explained by the ratio of karstic rocks. There is a larger tendency of catchments with larger ratios of a karst aquifer, to generate a intermediate reaction (cluster B). Water can travel faster through the karstic rock and be reconnected to the surface flow (Bonacci et al., 2006). Brunner et al. (2018a) also found out that to include information about the karst aquifer is important for the estimation of the hydrograph shape.

On the previous plots some of the similarities of the floods were highlighted. The complexity of the floods space and how the hydrograph curve might change according to differences in the meteorological input or the characteristics of the catchments were shown. There is a large quantity of variables influencing the flood processes. However, it was shown that H_R is a key parameter for differentiating flood mechanisms. To get a fixed number of clusters, which can explain the relationships that led to a given catchment reaction is difficult. The number of possibilities is large. The use of the similarity of the floods and not a fixed number of clusters, gives flexibility to the selection of the floods donors and enables to find donors, when the flood is a result of mixed processes.

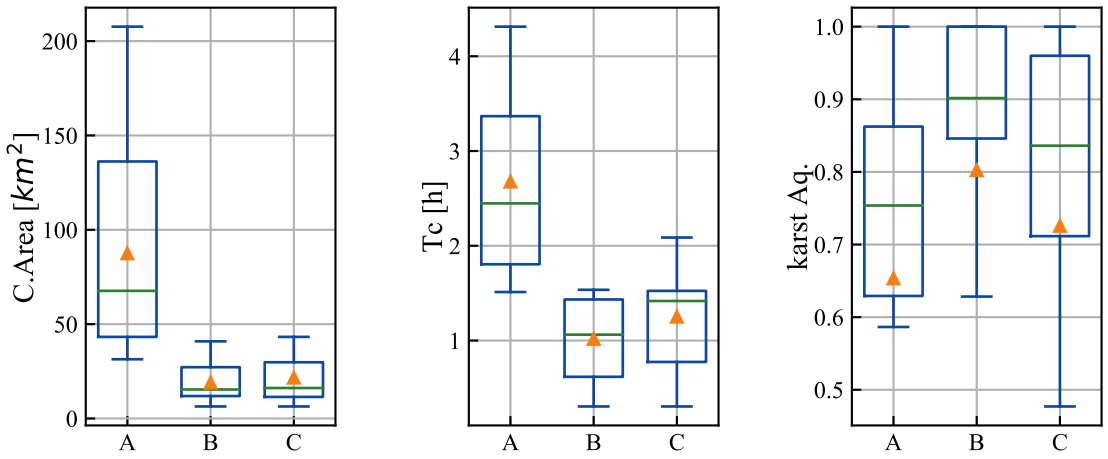

(a) Catchment area **(b)** Concentration time **(c)** Proportion of karst

Figure 6.19: Similarity of the catchment areas, concentration times and karstic aquifer of 1POT events belonging to three clustered reactions, according to a supervised RF trained to estimate the parameters of the fitted PDF (H_{PDF}, α, β).

Chapter 7

Estimation of Flood Volume and Flood Duration

In the previous chapters, an analysis of the mechanisms causing the floods was conducted to understand the dynamics of flood generation. A random forest regionalization framework was applied for transferring hydrograph shapes to ungauged or partially gauged catchments. This chapter focuses on modifying a rainfall-runoff model to estimate discharge volumes in the studied region. Thus, meteorological events identified as critical can be used as the input to the rainfall-runoff model to estimate plausible discharge volumes in ungauged catchments. Further, the whole hydrograph wave can be derived applying the Random Forest (RF) regionalization from Chap. 6.

7.1 Assumptions and Considerations of the Chosen Rainfall-Runoff Model

Estimating flood volumes using precipitation measurements has the advantage that longer records are available and that they have a greater spatial coverage and are measured with a high temporal resolution. A rainfall-runoff model can be used, which takes the meteorological event as input and generates a corresponding runoff volume considering the characteristics of the catchment. In a first step, the SCS rainfall-runoff model was used for estimating the discharge volumes. Nevertheless, it was recognized on an early stage that the observations were not represented satisfactorily. The results showed a structure, which suggested that the SCS must be modified to capture the soil moisture of the catchments. In this document, the results of the SCS model are not included since they were not further investigated. Instead, a modification of the SCS is used, the methodology suggested by Shaperly and Williams (1990), which is implemented in the EPIC calculator (Chap. 2). The EPIC is a modification of the SCS model to account for the soil moisture and the topography of the

catchments.

Since no measured data about the soil moisture are available, the soil moisture is estimated with the antecedent precipitation index (API). At first, its value was assumed to be equal to the API of the 5 days previous to the flood event. However, this value led to having many meteorological events estimated to cause zero runoff. Additionally, the estimation errors of the events generating a runoff were large. This was observed regardless of the chosen value of the recession (α) considered for the calculation of the API (Eq. 5.13), or the chosen value for the regional constant (λ). These results agree with the observations in Chap. 5, which showed that the longer memory of the studied catchments is more representative of a flood day as compared to the API of any other random day. Therefore, it is decided to use the API of the previous 30 days as an estimation of the soil moisture. When referring to API in this study, it indicates that 30 days are considered for its calculation if nothing else is specified.

As shown in Chap. 5 the precipitation amounts of the winter floods will be underestimated if no information of snow melt is included. Therefore, the snow routine in Chap. 5 is considered, to take into account the snow water equivalent for the calculation of the precipitation and the API causing a flood event. Further, an API-soil moisture transformation is applied and an equivalent dimensionless curve number CN is used in the rainfall-runoff model, as described in the following section.

7.1.1 Soil Moisture Transformation

The soil moisture (SW) of the catchments previous to the occurrence of a flood, is estimated by means of the API. However, the API is an indicator of the amount of water in the soil, though there are other processes affecting the water content of the soil, as for example the evapotranspiration, the interception, the soil properties, the slope, etc. For this reason, the value of API is not considered directly as the soil moisture (SW). Instead, the API is transformed using the field capacity and wilting point of each catchment. A linear relationship between the SW and the API is assumed. To account for seasonality, the transformation is done for summer and winter events separately. The API has a different meaning according to the seasons. In summer evapotranspiration is larger than in winter; therefore, the same API is an indicator of a smaller SW in summer than in winter. The transformation is done as follows

$$SW = WP + API \cdot \frac{FC - WP}{API^{FC} - API^{WP}} \tag{7.1}$$

where SW is the soil water content, WP and FC are the wilting point and the field capacity of the catchment respectively. API^{FC} is the value of API corresponding to SW equal to the field capacity FC. Likewise, API^{WP} is the value of API corresponding to SW

equal to the wilting point WP. API^{WP} is assumed to be zero, given that, even with no antecedent precipitation a minimum soil moisture is expected to be found in the soil, which corresponds to the wilting point. The optimal values of API^{FC} for each catchment depend on the parameters selected for the rainfall-runoff model. Specifically for this case, the values considered for the API recession α (Eq. 5.13) and the regional constant λ (Eq. 2.3). As mentioned before, to account for the effects of seasonality, summer and winter events are studied separately; therefore, two optimal values of API^{FC} would be obtained for each catchment, one for summer and one for winter. These results are included in later sections of this chapter.

7.1.2 Equivalent CN

The EPIC model takes the dimensionless curve number CN from the SCS model to estimate the initial average soil moisture condition. This value is modified according to the slope of the catchment as explained in Chap. 2. Typically, the estimation of the runoff in a catchment is done by aggregating the runoff generated by each of the land uses of a catchment, i.e. each land use has a corresponding CN value that generates a certain amount of runoff. This practice should be preferred over the one that considers a unique runoff, which is calculated using a single area weighted CN, given that the relationship between precipitation and discharge is not linear, nor should the CN be assumed as linear. An area weighted CN is calculated as a function of the land use areas. This can lead to an underestimation of the effect of precipitation in some areas of the catchment. For instance, precipitation falling over an impermeable surface will always generate a runoff, whereas precipitation falling over forest has a larger retention.

However, if the rainfall-runoff model is applied for each land use separately, more parameters must be estimated for the ungauged catchments. A value of API^{FC} would be needed per season and per land use. It is therefore decided to estimate the runoff volume using an equivalent curve number CN_{eq}. The CN_{eq} is an equivalency to account for a better representation of the runoff generation of the independent land uses, than the one obtained by considering an area weighted CN. The CN_{eq} is defined as

$$CN_{eq} = \frac{1}{A_{total}} \left(A_s \cdot s \cdot CN_s + A_a \cdot a \cdot CN_a + A_f \cdot f \cdot CN_f \right) \tag{7.2}$$

where CN_s, CN_a and CN_f are the curve numbers for settlement (s), agriculture (a) and forest(f). The equivalency coefficients a, s and f are the weights given to each CN (CN_s, CN_a and CN_f). The land use areas are A_s, A_a and A_f, corresponding to settlement, agriculture and forest. Finally, A_{total} is the entire catchment area.

The coefficients a, s and f are found by means of an optimization over the flood events of all catchments. For this purpose, the optimal values for a, s and f are searched to minimize

the Mean Squared Error (MSE) in the following equality

$$Q(CN_s, P, \lambda) + Q(CN_a, P, \lambda) + Q(CN_f, P, \lambda) = Q(CN_{eq}, P, \lambda) \tag{7.3}$$

Q is the runoff volume. It is calculated using Eq. 2.4 of the EPIC model. It is a function of the precipitation triggering the flood event P and CN corresponding to a given land use. Thus, Eq. 7.3 compares the runoff obtained as an aggregation of the runoff of each land use to the runoff of having only one CN, the CN_{eq}. The results obtained for the coefficients a, s and f are included in the following section.

7.2 Calibrating the Rainfall-Runoff Model

According to the considerations mentioned above, there are some parameters of the model that must be calibrated to represent the study area. On the one hand, optimal values for the API recession α and the regional constant λ of the model are studied. On the other hand, a resulting API^{FC} for each catchment is obtained, for each combination in the space of α and λ. Additionally, the coefficients a, s and f for considering a CN_{eq} are calculated.

7.2.1 The Space of α and λ

In the EPIC model, the initial abstraction I_a of the catchment is proportional to the storage S (Eq. 2.3), where λ is the proportionality factor. In practice a value λ equal to 0.2 is typically used. A value of λ smaller than 0.2 implies that the initial abstraction of the catchment is smaller than 20% of potential storage capacity of the catchment. However, this value comes from the application of the SCS model, which was developed for catchments in the United States. Maniak (2016) suggests that for European catchments λ should be smaller, a value of around 0.05. For the case of Austrian catchments, Merz and Blöschl (2009) concluded that a similar value was more representative for the studied catchments. The parameter α is the recession considered for the calculation of the API (Eq. 5.13). As the value of α decreases less importance is given to the long memory of the catchment. This means that only the precipitation that falls a few days before the flood event control the soil moisture at the occurrence of the flood. On the contrary the larger the α is the more importance is given to the long memory of the catchment.

As mentioned before, the optimal value of API^{FC} for each catchment depends on the considered α and λ. Thus, the error in the estimation of runoff volume is affected by the values of these parameters. If α and λ change, so do the values of API^{FC} and the estimation error. At each point in the α and λ space an optimization is done for each catchment, to obtain the optimal value of API^{FC} for each catchment. This means that for each catchment

a value of API^{FC} is found, which minimizes the MSE of the observed and the estimated flood volumes. The MSE is calculated as in Eq. 4.5. This is iteratively repeated for each combination of α and λ considered. The parameters λ and α are looped to find the combination that can better represent the study area, where λ is looped from 0.05 to 0.2 in steps of 0.01 and α is looped from 0.2 to 1.0 in steps of 0.01 as well.

In this chapter, the floods are considered as the sample of the 1POT events. To calculate the MSE between the observed and estimated flood volumes, the effective precipitation (P_e) is considered. P_e is the amount of precipitation that directly contributes to the runoff and is not intercepted, evaporated or infiltrated and it is used to omit the effects of different catchment sizes in the volume calculation. To calculate the flood volume, one must multiply P_e with the catchment area. Additionally, for getting an estimation of the bias the Mean Error (ME) is calculated as

$$ME = \frac{1}{N}\sum_{i=1}^{N}(\hat{y}_i - y_i) \tag{7.4}$$

where $\hat{y}_i$ is the estimated value P_e, y_i is the observed P_e and N is the number of observed flood events in each catchment. In this case, ME has units of mm given that it computes the error of P_e. If ME is larger than zero it means, there is a tendency to overestimate. On the other hand, when ME is smaller than zero, the tendency is to underestimate. The estimations of P_e are obtained using the optimal API^{FC} for each catchment and set of λ and α.

In Fig. 7.1 the mean over the values of the MSE and the ME obtained for the catchments is plotted in the space of α and λ. These are plotted on the left and right panel respectively. The plots give the results when considering only the summer events for the optimization. The values of the mean MSE and ME are given by the color bars on top of each plot. For the case of the MSE (left panel), a dark blue value represents the minimum MSE as an average over all catchments. It can be observed that the smaller MSE are achieved for λs between 0.07 and 0.15 in combination with αs between 0.85 and 0.95. As already pointed out in Chap. 5, it can be observed that the long memory of the catchment is more representative for estimating a flood event, i.e. smaller estimation errors are obtained when a larger α is considered. This is observed as a general tendency, regardless of the chosen λ.

For the case of ME (right panel of Fig. 7.1) the lighter colors, colors close to white, are the values for which less bias in the estimations can be expected. Thus, selecting a λ of around 0.04 results in the smaller bias. This means that there might be some overestimation and underestimation, but it is compensated on average. If one considers $\lambda = 0.2$, as the one suggested in the SCS model, there is a bias to underestimate the discharge volume, regardless of the value of α chosen. In conclusion, the summer events could be estimated with a value of λ of around 0.07 to reduce the bias and the estimation error and a value of α between 0.85 and 0.95 to reduce the estimation error.

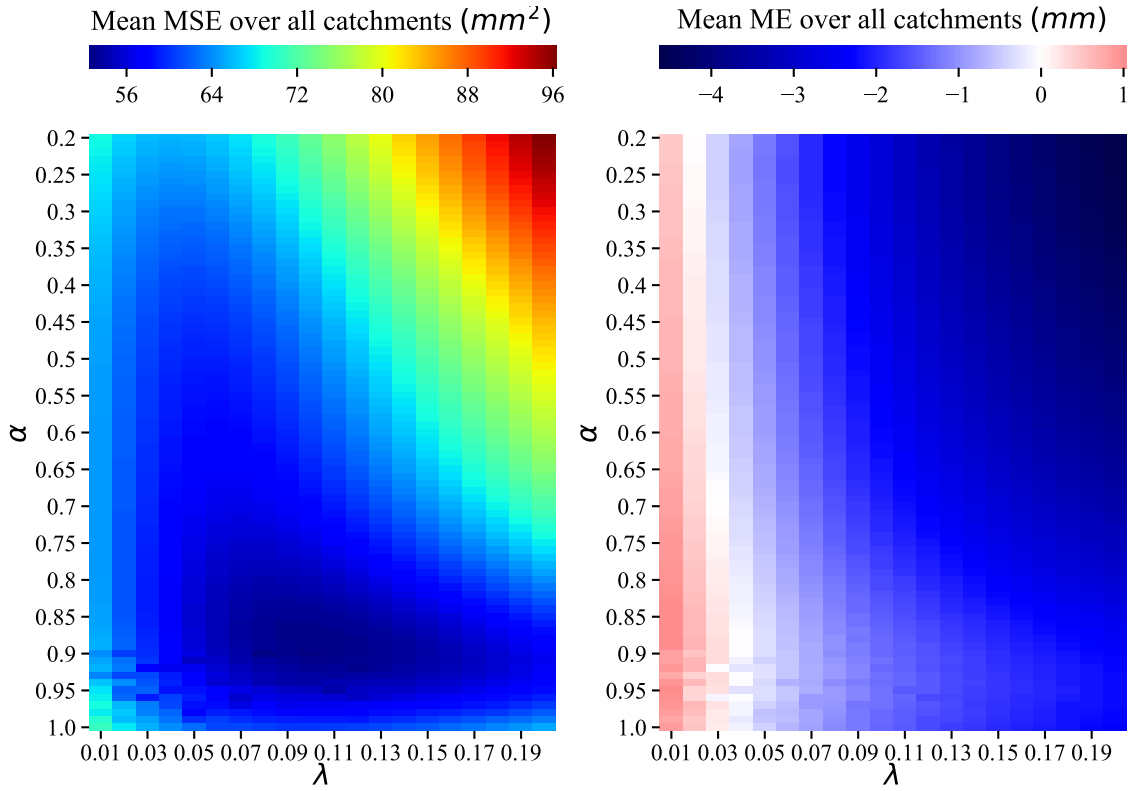

Figure 7.1: MSE and ME in the α-λ space for the estimation of the summer flood volumes. The color maps display the resulting mean MSE (left) and mean ME (right) obtained over all study catchments.

Figure 7.2 gives the results of the optimization for the winter events, in the same format as for the summer events. The first observation that can be made is that MSE does not change smoothly in the space of λ versus α, as is the case in the summer events. Rather, a striped structure in the results is present for the case of the winter events. This structure can be attributed to few catchments resulting in much larger MSE values than those obtained for most of the catchments. One example is catchment 1. This is the smallest catchment of the studied ones. It is located on the west corner of the Jura mountains (see Fig. 3.1). It is the catchment with the highest elevations and the largest variability in elevations within the catchment (see mean and standard deviation of the elevation in Tab. A.2). The MSE for this catchment is large regardless of the combination of α and λ. There is no value of API^{FC} found to reduce this error. Catchment 1 exhibits runoff coefficients larger than one, even after including the snow routine (see Chap. 5.4 and Tab. A.3). Meaning that the observed discharge is larger than the precipitation event, which is physically not plausible. The temperature station assigned to characterize this catchment is located in the uppermost part of the catchment. Therefore, the temperature records might be lower than the representative temperature for the catchment as a whole. In some cases, there may be greater accumulation of precipitation as snow or less snow melting, depending on the temperature recorded. If one looks at the characteristics of the winter floods, it is observed that not all events are

affected by having low temperatures. When the snow routine is applied some events have large precipitation equivalents, others have small precipitation equivalents. Nevertheless, the problem encountered is not the lack of precipitation, there is precipitation recorded when the flood occurred. The error is rather attributed to the fact that for some events the temperature recorded is lower than the accumulation threshold (see Chap. 5.4). Therefore, the falling precipitation is accumulating as snow and it does not contribute to the runoff. Flood events in winter are expected to take place at the borderline between positive and negative °C temperatures, which is around the freezing threshold. In this range, as highlighted by Bárdossy and Pegram (2011), the hydrological balance can be affected by small biases, impacting the whole catchment regime.

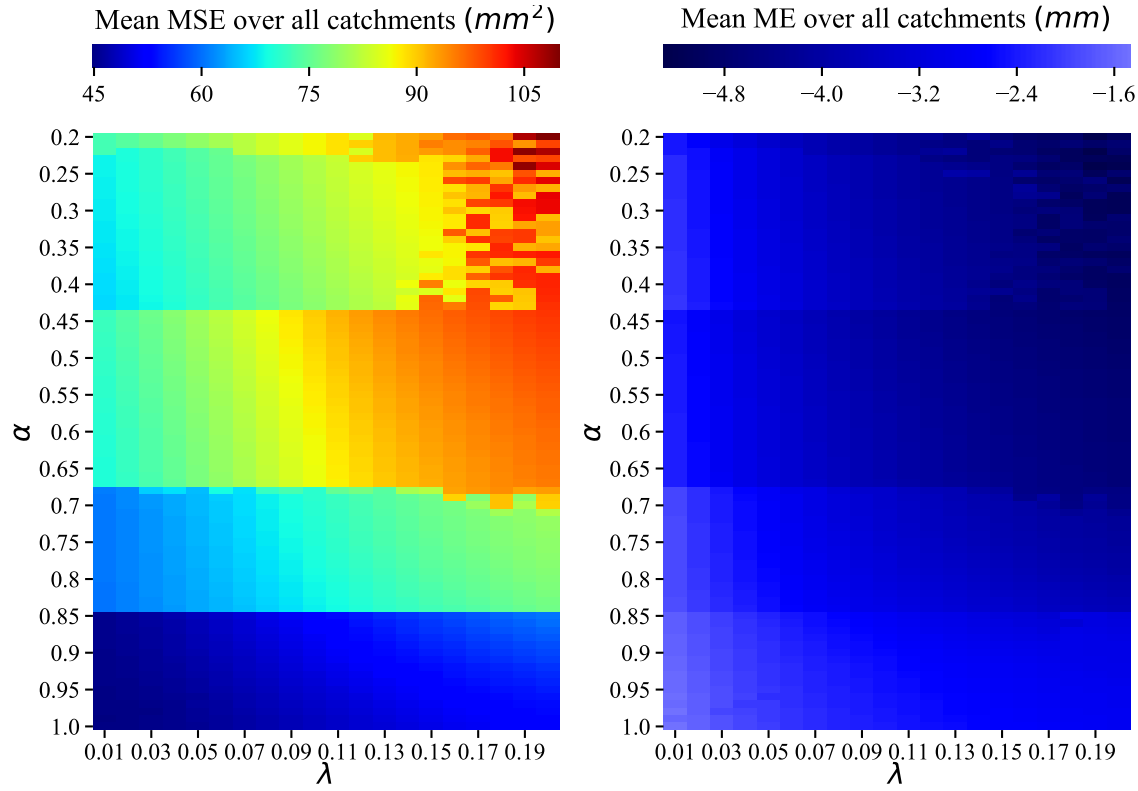

(a) MSE **(b)** ME

Figure 7.2: MSE and ME in the α-λ space for the estimation of the winter flood volumes. The color maps display the resulting mean MSE (left) and mean ME (right) obtained over all study catchments.

Moreover, only daily mean precipitation measurements are used for the estimation of the snow accumulation and snow melt. It might be worth analyzing if by assuming a temperature change over the day, the results for catchment 1 will improve. Another option could be a correction of the observed temperature considering the altitude. In addition, it is possible that not all flood events are generated by the same mechanism; some may be the result of snow melt and others the result of rain on snow. Therefore, in some events the observed amounts of rainfall and temperature may be sufficient to generate runoff and in others they

may not.

If one removes station 1 and calculates the mean MSE, without this catchment, the striped structure from Figure 7.2 reduces and a smoother plot is observed. On the left panel of Fig. 7.3, the mean MSE for the estimations without taking catchment 1 into consideration is given. By looking at the color bar of Fig. 7.2a and Fig. 7.3a it can be recognized that the mean MSE is reduced, which is expected since catchment 1 is the catchment that presented the largest MSE. Nonetheless, the overall tendency remains that large mean MSE are on the top right corner (for large λs and small αs) and small mean MSE are on the bottom left corner (for small λs and large αs).

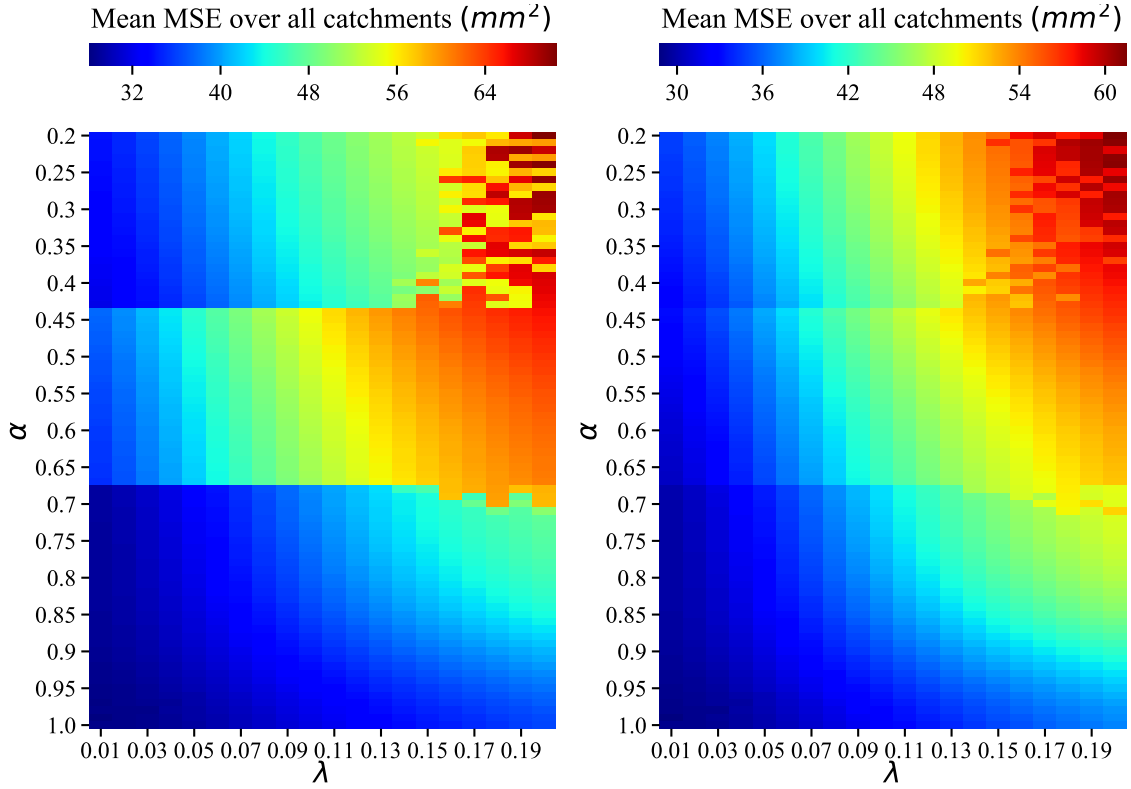

(a) without station 1

(b) without station 1 and 10

Figure 7.3: MSE in the α-λ space for the estimation of the winter flood volumes. The color maps display the resulting mean MSE obtained over the study catchments, without including station 1 (left) or station 1 and 10 (right).

The behavior of the estimation errors in the α and λ space can become even smoother when catchment 10 is also removed from the analysis. However, it can be observed that for those α and λ where the MSE achieves its minimum (large αs and small λs) the benefit is small, i.e. there is a small reduction in the mean MSE. For the case of catchment 10, there might also be a bias in the temperature measurements selected to represent the catchments. It is observed that the temperature station is located on the valley behind the catchment. If one looks at Fig. 3.1 the catchment is facing to the north-west, but the temperature station for

this catchment is located on the valley facing to the south-east. This is important given that the direction of the mountains is affecting the sunshine and thus the recorded temperature. Especially in the case of the winter floods, given that temperature is an important triggering factor of floods. A slight change in temperature can impact the snow accumulation and snow melt. In this study the selection of the nearest neighbors was automatized with a code that searched the closest station from the available ones. To account for the position of the mountains, the nearest neighbor approach can be extended, constraining the selection of the neighboring station with the topography.

Overall, the estimations obtained for the winter floods have a smaller mean MSE than the ones obtained for the summer floods. This can be quickly identified by looking at the colored bars, which for the summer events ranged from around 50 to 96 and for the winter events from 30 to 60 (see left panel of Fig. 7.1 and right panel of Fig. 7.3). A possible reason may be the occurrence of connective rainfall in the summer. The maximum precipitation might be missed by the station, what randomly changes the amount of precipitation recorded. Regarding the bias of the estimation, it can be said that for the summer floods, there is the possibility to choose α and λ to achieve a value close to zero mean ME (see right panel of Fig. 7.1). Whereas, in the case of the winter events there will always exist a tendency to underestimate, for the values of α and λ studied here (see right panel of Fig. 7.2). The results of the mean ME when leaving out catchments 1 and 10 are not included, given that they resemble those obtained for all the catchments and only little variations are observed.

7.2.2 Coefficients for the Calculation of the CN_{eq}

As explained before, CN_{eq} is used to represent the aggregated behavior of different land uses instead of an area weighted CN. For this purpose, the optimal equivalency coefficients a, s and f must be found. In this case, λ is chosen as 0.07 and α as 0.9, given that minimum mean MSE of the estimations lies around these values.

In Fig. 7.1 the resulting coefficients for calculating the CN_{eq} are given. The optimization considers the flood events of the 1POT sample. Three optimization scenarios are considered, one for all 1POT, one only for the summer events and one for the winter events. It can be observed that the equivalency coefficient is mostly greater than one. This implies that a compensation is needed for the nonlinear behavior of CN. This means that a larger runoff volume results from considering the runoff of each land use separately than for the case of using an area weighted CN.

Additionally, in Fig. 7.4 the runoff volumes obtained by using the CN_{eq} or the area weighted CN are plotted versus the aggregated runoff of each land use area. As a general trend, it can be observed that including the equivalency coefficients for the calculation of the runoff volumes, generates results closer to those obtained by aggregating the runoffs of each land use when calculated separately. This can be observed by the fact that the CN_{eq} lies closer to the 1:1 line. This happens regardless of considering summer or winter events

Table 7.1: The optimal equivalency coefficients for calculating CN_{eq} for the three scenarios considered: all 1POT events, only the summer events and only the winter events. Results for considering $\lambda = 0.07$ and $\alpha = 0.9$

	s	a	f
All 1POT	1.00	1.01	1.05
summer 1POT	0.99	1.01	1.05
winter 1POT	1.04	0.99	1.07

(left and right panel of Fig. 7.4 respectively). However, the correction is larger in winter than in summer, as observed in the larger values of the equivalency coefficients (a, s and f) for summer than for winter (see Tab. 7.1). A possible explanation of this correction is the presence of frozen ground in winter. Infiltration and soil moisture can be affected when the temperatures of the ground drop below 0°C (Dingman, 1975).

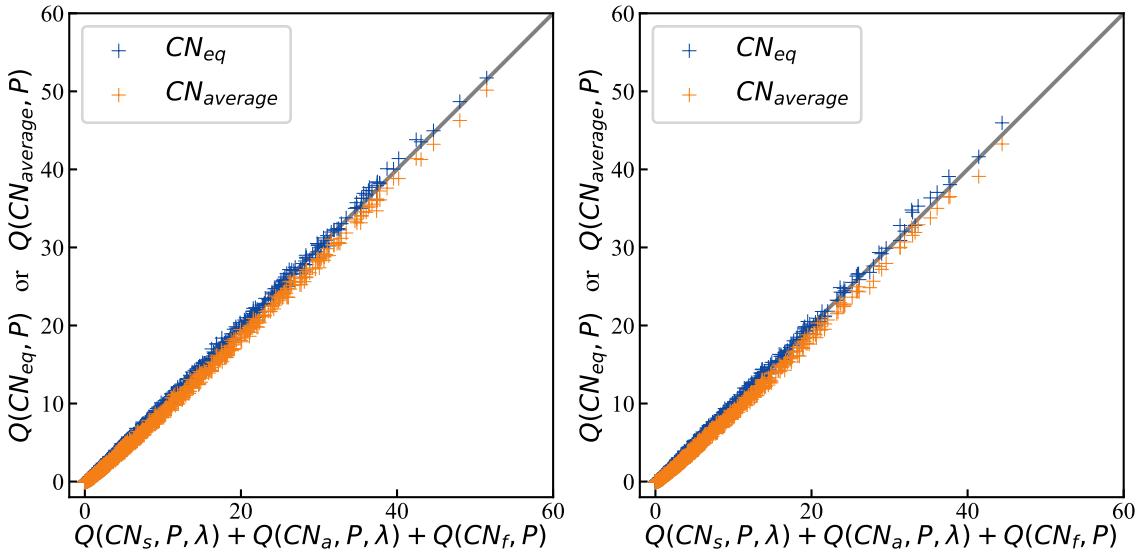

(a) summer events

(b) winter events

Figure 7.4: Comparison of the runoff volumes for different CN values. In blue and orange respectively, both the the CN_{eq} and the average CN are plotted versus the aggregated runoff obtained for each land use area. The diagonal line is the 1:1 line, given as orientation.

To verify the variability of the equivalency coefficients (a, s and f) for the study region, these coefficients are also estimated by iteratively leaving one catchment out. In Tab. 7.2 a summary of the obtained values is given. All three optimizations' scenarios (all events, summer or winter events) are included. The maximum, the minimum, the mean and the standard deviation of the equivalency coefficients obtained are given. It can be observed that there is small to no variation on the optimal values found for a, s and f, when one catchment is left out of the analysis. The variations are observed when all events are considered jointly;

however, when separated in winter and summer these variations can be neglected. This indicates that if new study catchments are to be considered, the same coefficients can be used to calculate CN_{eq}.

To sum up, it can be inferred from Tab. 7.2 that to calculate the runoff of the summer events the CN value of forest and agriculture should be increased by 5% and 1% respectively. This takes in to account the effects of taking only one CN value to estimate the runoff volumes. Additionally, CN value of settlement should be reduced by 1%. For the case of the winter events, the CN values of settlement and forest should be increased by 4 and 7% to account for the underestimation of considering only one CN and the CN of agriculture should be decreased by 1%. Looking at Fig. 3.5 it is observed that most of the catchments have similar areas of agriculture and forest, and small areas of settlement. This means that as a general regional trend, the obtained values of the equivalency coefficients (a, s and f) imply an increase of CN and thus of the estimated runoff, even if some of the coefficients reduce the value of CN.

Table 7.2: Summary of the optimal equivalency coefficients obtained by iteratively leaving one catchment out. For these calculations a $\alpha = 0.9$ and a $\lambda = 0.07$ are used.

	All 1POT			summer 1POT			winter 1POT		
	s	a	f	s	a	f	s	a	f
max	1.01	1.01	1.06	0.99	1.01	1.05	1.04	0.99	1.07
min	0.98	1.00	1.05	0.99	1.01	1.05	1.04	0.99	1.07
mean	1.00	1.01	1.05	0.99	1.01	1.05	1.04	0.99	1.07
std	6.1×10^{-3}	1.4×10^{-3}	1.6×10^{-3}	8.5×10^{-8}	1.3×10^{-8}	1.1×10^{-8}	9.0×10^{-8}	2.4×10^{-8}	3.4×10^{-8}

The optimization of the CN_{eq} was also evaluated with different α and λ. Nevertheless, the variations of the equivalency coefficients a, s and f are small. These results are therefore not included in this document. An overall trend is observed of having larger a, s and f, when larger λs are considered. This can be attributed to larger compensations of the model needed if the initial abstraction I_a is larger.

7.3 Analysis of Flood Duration

In this section an analysis of the flood duration is carried out. In hydrology, the flood duration has been explained for practical applications as a function of the catchment's concentration time and the duration of the precipitation event. As mentioned in Chap. 3, the concentration time T_c is an indicator of the time that is needed for the entire catchment to contribute to the runoff. In the concentration time there are some catchment characteristics involved, such as the length of the catchment and the slope, which are parameters controlling how fast water can move through the catchment. Additionally, the precipitation is the principal trigger of

runoff, and thus is the most important factor, responsible for the changes of the hydrograph.

In Fig. 7.5 scatter plots of the characteristics of the precipitation event triggering the floods versus the flood duration are given. In the left panel, the duration of the precipitation event plus the T_c versus the flood duration are plotted. For the plot, the events of each catchment are divided in winter and summer, and the mean for each season and catchment are used. In the right panel, analogous to the left panel, the temporal entropy of the precipitation versus the flood duration are plotted.

As expected, the duration of the flood event relates to the duration of the precipitation event, as the precipitation duration increases, so does the duration of flooding (see left panel of Fig. 7.5). Additionally, it can be observed (see right panel of Fig. 7.5) that the summer events have lower precipitation entropies as the winter events. This is explained by a more frequent occurrence of convective precipitation in summer. Moreover, if precipitation is peaky (small entropy, see Chap. 5) it is not a flood with a long lasting duration. This is represented by the dots in the lower left corner of Fig. 7.5 (right panel).

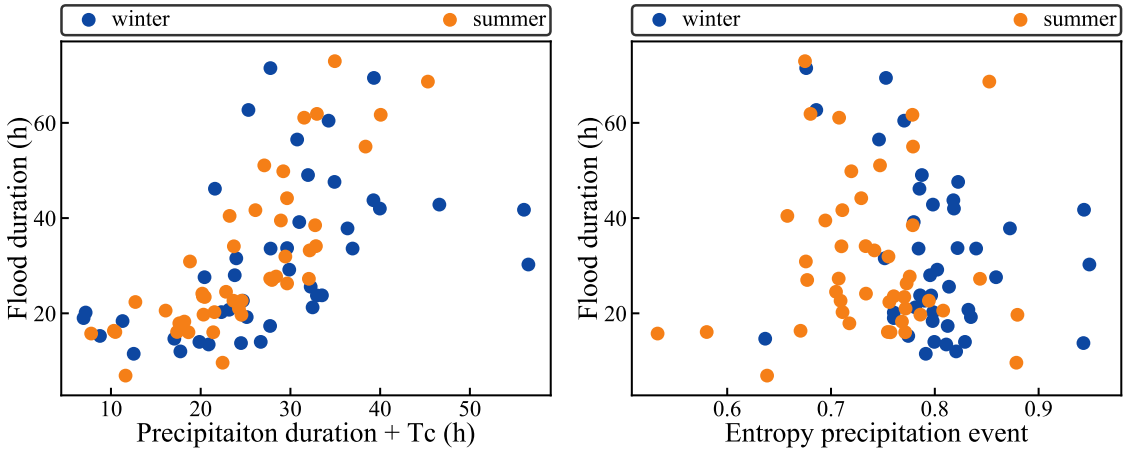

Figure 7.5: Scatter plots of the duration of the precipitation event plus the T_c and the precipitation temporal entropy versus the duration of the flood event. The seasonal means are given.

Given the relationship observed between the precipitation duration and the flood duration, it is decided in this study to use a simple linear model to estimate the flood duration. In the next chapter, where a validation of the flood estimation models is carried out, the linear model for the estimation of the flood duration is going to be studied.

Chapter 8

Validation of the Flood Estimation

In this chapter, a validation of the models previously proposed to estimate the floods in small sized catchments in Northwestern Switzerland is carried out. For this purpose, a leave-one-out cross-validation is chosen. For which, iteratively one catchment is treated as ungauged, using its observations to test the models, whereas the remaining catchments are considered for training the models. The relative error and the absolute relative error are chosen to quantify the performance of the estimations. In this chapter only the 1POT sample is considered for the validation, since these are the most extreme events. In the following sections the results of the validation are presented for the estimation of the flood volume, the duration and the hydrograph.

8.1 Flood Volume

As explained in Chap. 7 the runoff volume is estimated using the EPIC model. For simplicity in this validation, only one λ and one α are considered, as the initial abstraction and the recession of the API respectively. However, selecting unique values for each season might result in better estimations. Further, the value of API^{FC} needs to be estimated for the validation catchment, as it is one parameter of the model, which is used to transform the API to soil moisture (see Chap. 7). In this chapter, the API^{FC} of the "ungauged" catchment is estimated as the value of API^{FC} from the nearest neighbor catchment.

Table 8.1 presents some statistics of the relative error for the estimation of the flood volume. The median of the relative errors shows that there is a bias to underestimate the winter events and to overestimate the summer events, which jointly results in an underestimation bias. The median is preferred to avoid drawing conclusions influenced by few large errors. If one looks at the flood events in detail, it is observed that the largest errors take place when the observed precipitation sum is smaller. These events are more common in summer when intense convective precipitation occurs. The spatial distribution of convective precipitation

events has a large uncertainty in space, given that the spatial association is lower. As a result, it is more probable to underestimate the rainfall of such events, if the precipitation of the nearest neighbor station is considered as the event precipitation.

Table 8.1: Statistics of the relative error for the estimation of the flood volume. The rows of 25%, 50% and 75% give the values of the corresponding quantiles.

	all	winter	summer
mean	0.18	-0.13	0.33
std	1.28	0.70	1.45
25%	-0.57	-0.67	-0.48
50%	-0.10	-0.31	0.00
75%	0.46	0.20	0.62

Additionally, in Fig. 8.1 the median absolute relative errors of each catchment are plotted in space. The color bar is given to represent the error and the size of the markers indicates the catchment sizes.

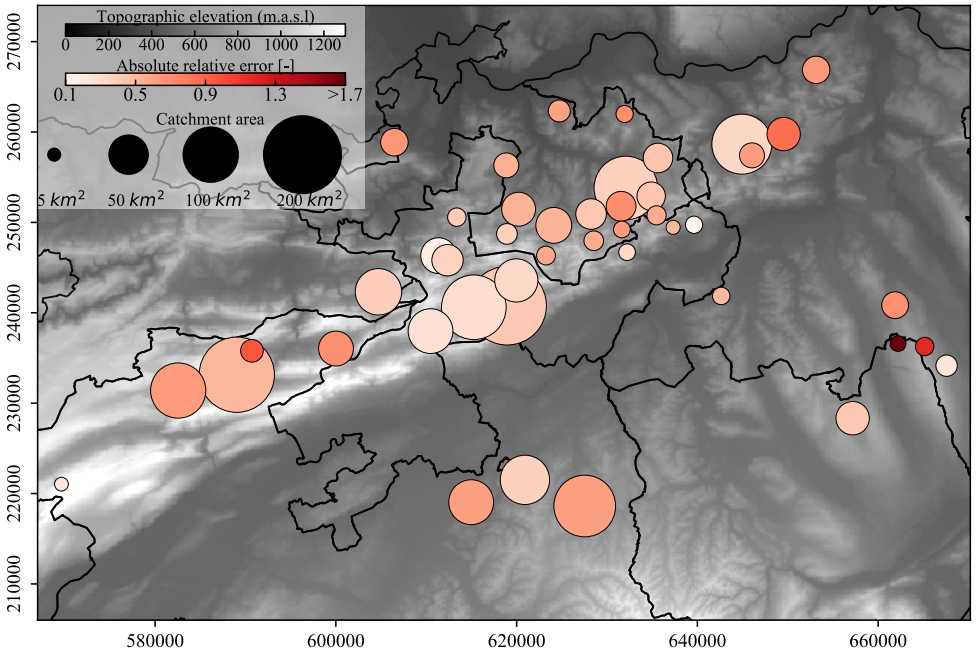

Figure 8.1: Median absolute relative error per catchment for the estimation of the flood volume. The color bar gives the values of the error and the size of the marker indicates the catchment size.

It can be observed in Fig. 8.1 that catchments 43 and 44 (catchments located on the south east of the study area, see Fig. 3.1) have the largest estimation errors. If one would exclude

those two catchments, there would not be a regional bias, nor a bias to have better estimates according to different catchments sizes. Looking at catchments 43 and 44 in detail, it is observed that the large estimation errors are driven by summer events. As suggested before, the occurrence of convective precipitation can result in the underestimation of precipitation sums. Further studies are needed in which other precipitation estimations are considered. Having better precipitation estimates, with less uncertainties, results in a better performance of the estimation of the flood volume.

8.2 Flood Duration

As it was shown in Chap. 7.3, it is reasonable to assume a linear relationship between the flood duration and the sum of the precipitation duration and the concentration time of the catchments. For the estimation of the duration a linear regression model is trained, leaving each time the validation catchment outside for finding the parameters of the linear fit.

Table 8.2 contains a summary of the leave-one-out cross-validation, i.e. statistics of the relative error for the estimation of the flood duration. One can see that, both in summer and in winter, a bias to overestimate the flood duration is present. The large mean estimation errors are a result of some errors being much larger than the rest, i.e. larger means but smaller medians. A visual assessment of the hydrograph separation for the flood events with the larger estimation errors is carried out to identify possible error sources. It is observed that the precipitation duration of these events is overestimated due to the method used for the selection of the duration of the precipitation event. In this study, the start of the event is determined as the point previous to the flood rise, which is preceded by at least two consecutive hours of no precipitation. This leads in some particular cases to the overestimation of the precipitation duration, that is contributing to the analyzed peak.

Table 8.2: Statistics of the relative error for the estimation of the flood duration. The rows of 25%, 50% and 75% give the values of the corresponding quantiles.

	all	winter	summer
mean	1.52	1.72	1.42
std	8.53	6.97	9.22
25%	-0.50	-0.46	-0.53
50%	0.11	0.15	0.11
75%	0.88	1.16	0.85

In Fig. 8.2 the median absolute relative errors are plotted in space for the estimations of the flood duration. The color bar is given to represent the error and the size of the markers indicates the catchment sizes. No regional bias can be recognized, as for the case of the volume. However, the estimation of the flood duration in smaller catchments results in larger errors than those obtained for bigger catchments, smaller markers are darker.

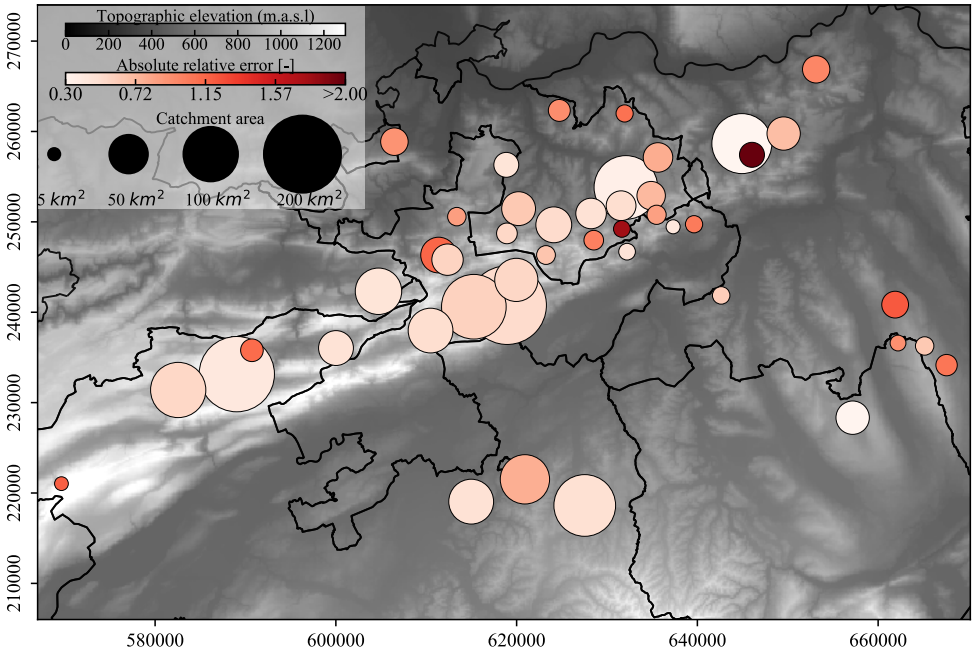

Figure 8.2: Median absolute relative error per catchment for the estimation of the flood duration. The color bar gives the values of the error and the size of the marker indicates the catchment size.

The linear regression model estimates the expected flood duration; however, the real duration can be different, not all observations lie on the estimated line. More robust estimates can be achieved by simulating the linear regression, accounting for the variability of the observations, and thus resulting in a stronger linear regression. The linear regression is simulated to get an ensemble of possible flood durations. For this purpose, a number N of errors are sampled random taking into account the quality of the linear regression trained, i.e. residuals. The ensemble of errors when added to the estimated expected duration give the ensemble of possible durations. The aggregation of this durations by the mean or the median results in the new estimation of the duration. From now on, this last explained method will be called "strong linear regression", while the former one will be called "weak linear regression".

Figure 8.3 gives the results of the strong linear regression obtained for different ensemble sizes. In blue the median absolute relative errors of the flood duration estimation are given for the results of the strong linear regression. As a reference the value obtained for the weak linear regression is given by the orange dashed line. As it can be observed, the estimation errors are lower for the case of the strong linear regression than the one of the weak linear regression. At the beginning, for small ensemble sizes, a fast decay of the estimation error is observed as the ensemble size increases until it reaches a point where no further gain in performance is achieved no matter the size of the ensemble chosen.

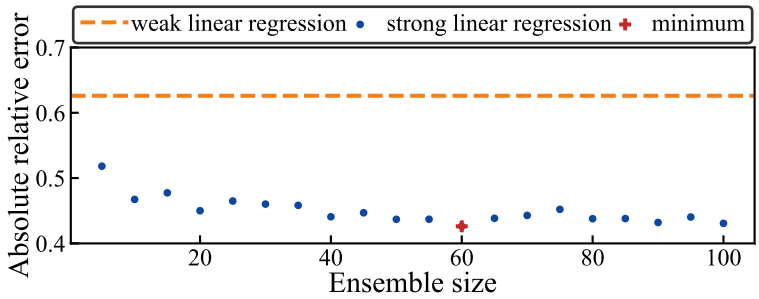

Figure 8.3: Median absolute relative error for the estimation of the flood durations with the strong linear model for different ensemble sizes (blue). The dashed orange line gives the median absolute error obtained for the weak linear regression

In Fig. 8.4 the distributions of the absolute relative error are presented as box plots for the different catchments. The catchments are ordered by their area on the horizontal axis. On the top and bottom panels, the results for the weak and the strong linear regressions are plotted respectively. An overall improvement of the estimations is observed, especially for those catchments that had lower variability of the estimation errors, i.e. shorter box plots. However, for both linear regression methods large errors are observed. Nonetheless, in most of the distributions a skewed behavior is observed, showing that if larger errors are to be expected these do not occur with the same frequency as the smaller ones.

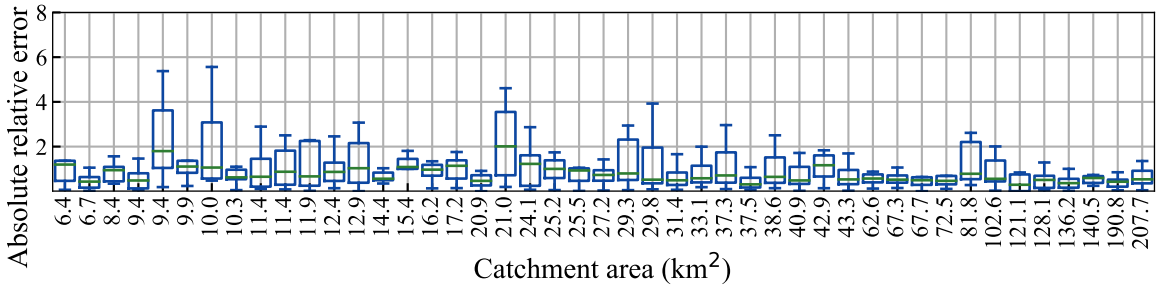

(a) Weak linear regression

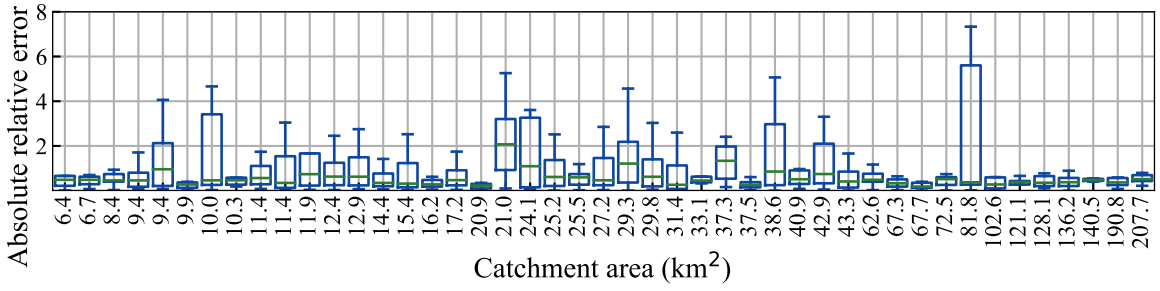

(b) Strong linear regression

Figure 8.4: Absolute relative error distribution for the estimation of the flood duration. On the horizontal axis the size of the catchments is give.

As it can be observed from Fig. 8.3 and Fig. 8.4 better estimates are achieved when the strong linear regression is considered. Nevertheless, there are still some large estimation errors for the study catchments, specially expected for catchments ranging between 20 km^2 and 40 km^2. As already suggested, the largest estimation errors are explained by errors of the precipitation event duration. However, if one removes those events, there are some events that present large estimation errors. This indicates that the errors are not only a result of precipitation duration, but also a result of the estimation model. The flood duration is more complex as simply described by the precipitation duration and the concentration time of the catchment. There are other processes affecting the duration of the floods. As shown in Chap. 7 the duration of the flood can also be influenced by the temporal distribution of the precipitation event, precipitation events with small entropies are triggering short duration floods. A multiple linear regression model that also includes the precipitation entropy was also studied. Nevertheless, it is not included here because no significant improvement on the performance was achieved.

Moreover, there are uncertainties in the flood duration and precipitation duration, which are explained in this paragraph. The duration of the flood event depends on the flood wave separation method. It is worth considering other separation techniques to quantify the uncertainty due to the separation method chosen. Regarding the precipitation duration, the determination of the inter event time could be further studied, a sensibility analysis on the influence of the selected threshold can give an insight on the expected changes. Additionally, the observations themselves have uncertainties. As for the case of the precipitation volume, these uncertainties can also vary according to the type of precipitation causing the floods.

8.3 Flood Hydrograph

In Chap. 6 a regionalization model for the estimation of the catchment reaction was proposed. For the estimation of the Design Flood Hydrograph (DFH) the similarities of a Random Forest (RF) model are used to select the flood donors. In this chapter, the similarity matrix $\bar{\boldsymbol{S}}$ of a RF ensemble is used for the estimations. The threshold of similarity for selecting the donors is set to 0.06. The TSP distribution is used to represent the hydrograph shape. The RF are trained as supervised having $H_{PDF}, \alpha\,,\, \beta$ as target variables. The performance is evaluated using the errors of the peak (Q_p) and the time to peak (t_p) from the estimated DFH. It is important to mention that the DFH is a dimensionless hydrograph. The real final estimations of Q_p and t_p depend on the previous estimated volume and duration, which are used to denormalize the DFH.

In Table 8.3 the statistics of the relative error for the estimation of the dimensionless Q_p and t_p are given. The estimations errors of t_p are larger than the ones obtained for Q_p. It can be observed that there is a slight bias to overestimate both Q_p and t_p, which is larger for the case of the summer events. The mean and the medians are similar to those obtained in Chap. 6 (see Fig. 6.10 and Tab. A.6). However, there is a larger spread of errors in the

case of this validation, which means that there are more events that result in larger errors. These differences can be explained by the randomness of the RF algorithm and the chosen cross-validation strategy. In Chap. 6 the problem of the partially gauged catchment (k-folds cross-validation) was assessed, rather than the case of the totally ungauged catchment, as is the case here (leave-one-out cross-validation). The k-folds cross-validation method allows for the training data set to contain events from a catchment that is also present in the train set. Nevertheless, the same floods event is never present in the train and test data sets.

Table 8.3: Statistics of the relative error for the estimation of the dimensionless hydrograph. The rows of 25%, 50% and 75% give the values of the corresponding quantiles.

	Dimensionless Q_p			Dimensionless t_p		
	all	winter	summer	all	winter	summer
mean	0.05	0.03	0.06	0.25	0.14	0.30
std	0.25	0.23	0.25	0.74	0.56	0.80
25%	-0.10	-0.12	-0.10	-0.20	-0.22	-0.19
50%	0.05	0.03	0.05	0.05	0.00	0.08
75%	0.19	0.16	0.20	0.45	0.30	0.52

In Fig. 8.5 the median absolute relative errors are plotted in space for the estimations of Q_p and t_p (on the top and bottom panels respectively). The color bar is given to represent the error and the size of the markers indicates the catchment sizes. For comparison reasons, the same color bar limits are used for both maps.

As already mentioned, a better performance is achieved for the estimation of Q_p than of t_p, noted by the darker colors of t_p. It can be observed that the regional pattern of the obtained errors for the estimation of Q_p and t_p do not match. This means that an improvement of the estimation of Q_p does not guarantee an improve of the estimation of t_p. Additionally, there is no regional bias or bias regarding the size of the catchments, for neither of the two cases, Q_p and t_p.

Further, the performances of the estimations of Q_p and t_p are better than the one obtained for the models of the flood volume and flood duration. Possibly, as it was observed in Chap. 6, because the hydrograph shape can be better explained by means of the temporal precipitation entropy, which is more homogeneous in space (see Chap. 5). If observations are more associated in space, the uncertainty of using the value of the precipitation station of the nearest neighbor is reduced. On the other hand, the precipitation sum is more heterogeneous in space, thus the observed precipitation on the neighbor station has larger uncertainties. This results in larger errors for the estimation of the volume.

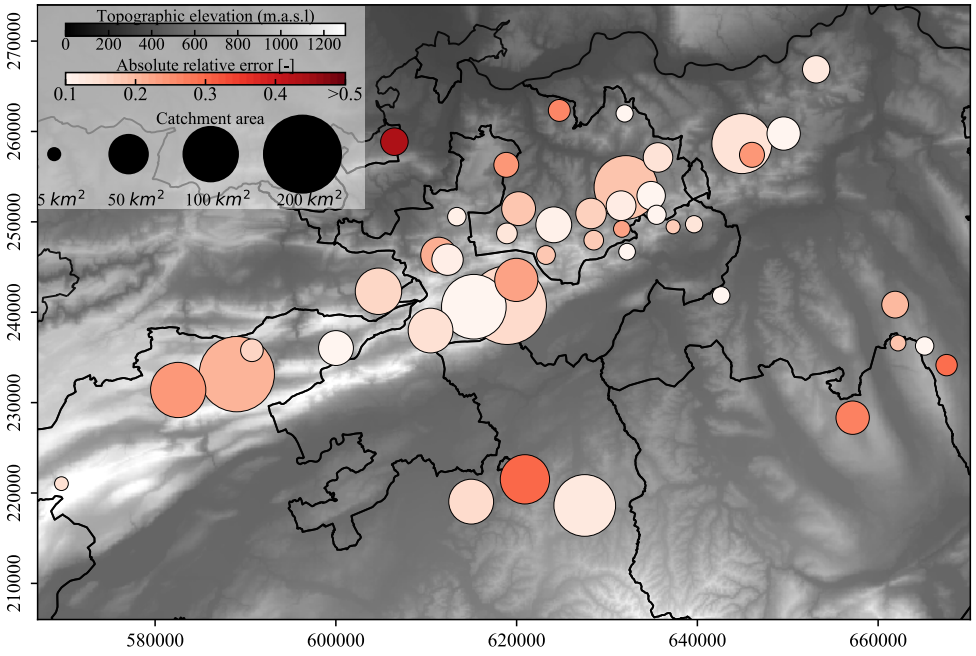

(a) Q_p

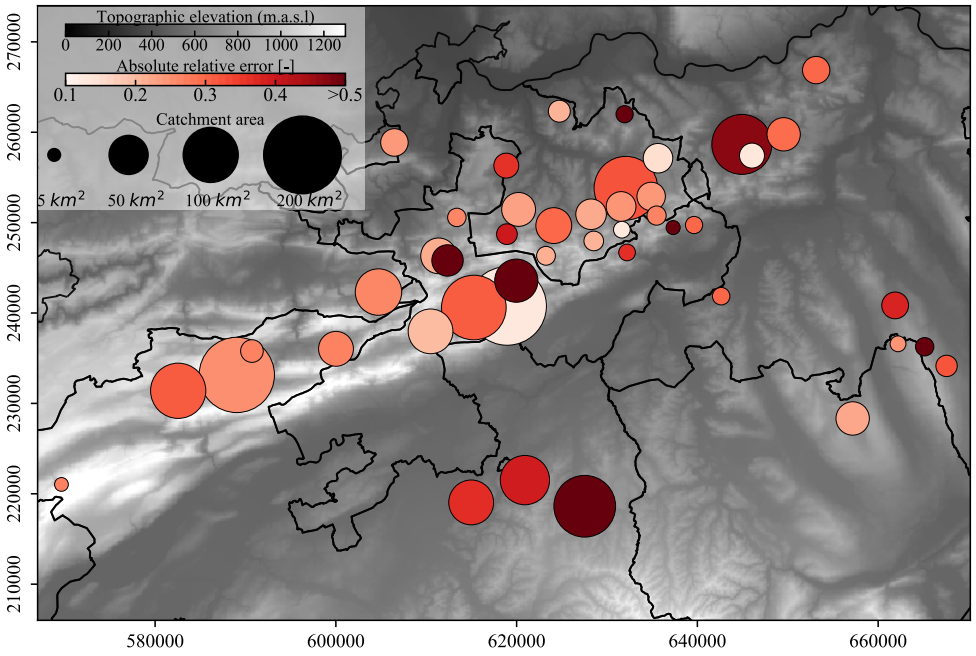

(b) t_p

Figure 8.5: Median absolute relative error per catchment for the estimation of the dimensionless Q_p and t_p. The color bar gives the values of the error and the size of the marker indicates the catchment size.

8.4 Denormalized Hydrograph

As suggested before, with the estimated duration and flood volume, it is possible to denormalize the dimensionless DFH (see Eq. 4.3). The denormalized hydrograph gives the expected cumulative error if floods were to be estimated using the three models explained before: the EPIC model for the estimation of the flood volume, the strong linear regression for the estimation of the duration and the similarity of the RF ensemble for the estimation of the hydrograph shape. Table 8.4 presents statistics of the relative error for the estimation of the denormalized DFH, specifically the estimation of the denormalized Q_p and t_p.

Table 8.4: Statistics of the relative error for the estimation of the dimensionless hydrograph. The rows of 25%, 50% and 75% give the values of the corresponding quantiles.

	Denormalized Q_p			Denormalized t_p		
	all	winter	summer	all	winter	summer
mean	0.23	-0.21	0.44	0.85	0.54	0.99
std	6.59	0.66	7.94	1.79	1.07	2.03
25%	-0.69	-0.71	-0.64	-0.10	-0.15	-0.07
50%	-0.26	-0.41	-0.19	0.29	0.17	0.35
75%	0.28	0.11	0.42	1.16	1.06	1.27

It can be observed in Tab. 8.4 that after the DFH is denormalized, a bias to underestimate Q_p and overestimate t_p is present. The underestimation of the flood volume and overestimation of the flood duration, observed in the previous validations, results in an underestimation of the denormalized Q_p, given that Q_p is directly proportional to the volume and inversely proportional to the duration (see Eq. 4.3). The Spearman's rank correlation coefficient are calculated, to have an idea of which of the errors has a larger influence on the estimation of Q_p. The Spearman's coefficient is chosen to minimize the effect of single large errors. The Spearman's rank correlation coefficient between the relative error of the denormalized Q_p and the relative error of the volume, the duration and the dimensionless Q_p are 0.77, -0.11 and 0.16 respectively. This indicates that the errors in the volume estimation are more correlated to the errors of the estimation of the denormalized Q_p. The denormalized t_p is the multiplication of the estimated flood duration and the dimensionless t_p. The Spearman's rank correlation coefficient between the relative error of the denormalized t_p and the relative error of the duration and the dimensionless t_p are 0.30 and 0.52 respectively. The small correlations could be explained by the fact that for some events one of the variables is overestimated and the other one is underestimated, which results in a compensation of the errors of the denormalized t_p.

Additionally, in Fig. 8.6 the median absolute relative errors are plotted in space for the estimations of the denormalized Q_p and t_p (on the top and bottom panels respectively). The color bar is given to represent the error and the size of the markers indicates the catchment sizes. For comparison reasons, the same color bar limits are used for both maps.

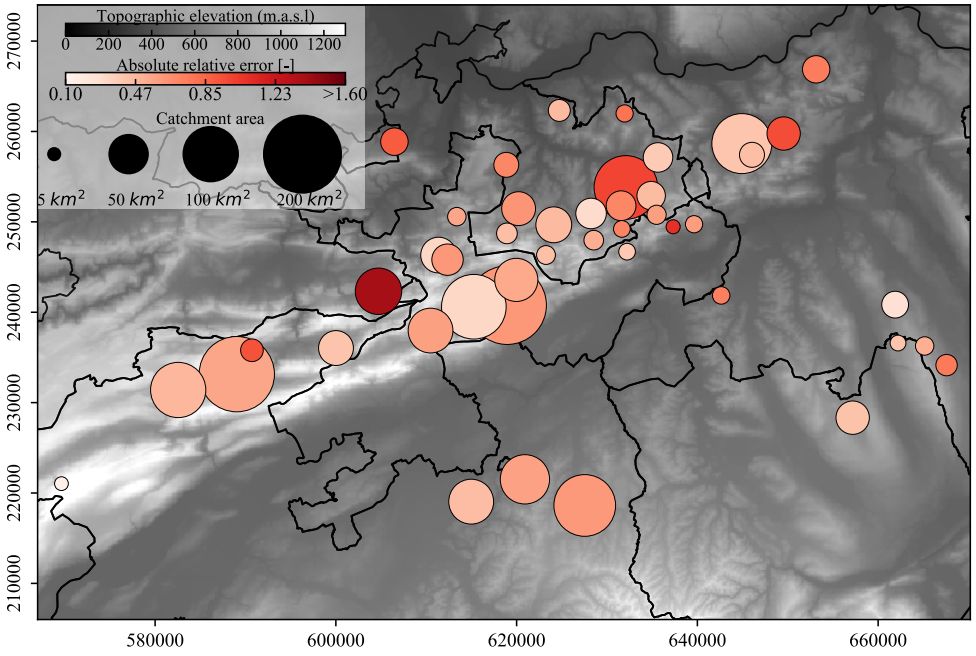

(a) Q_p

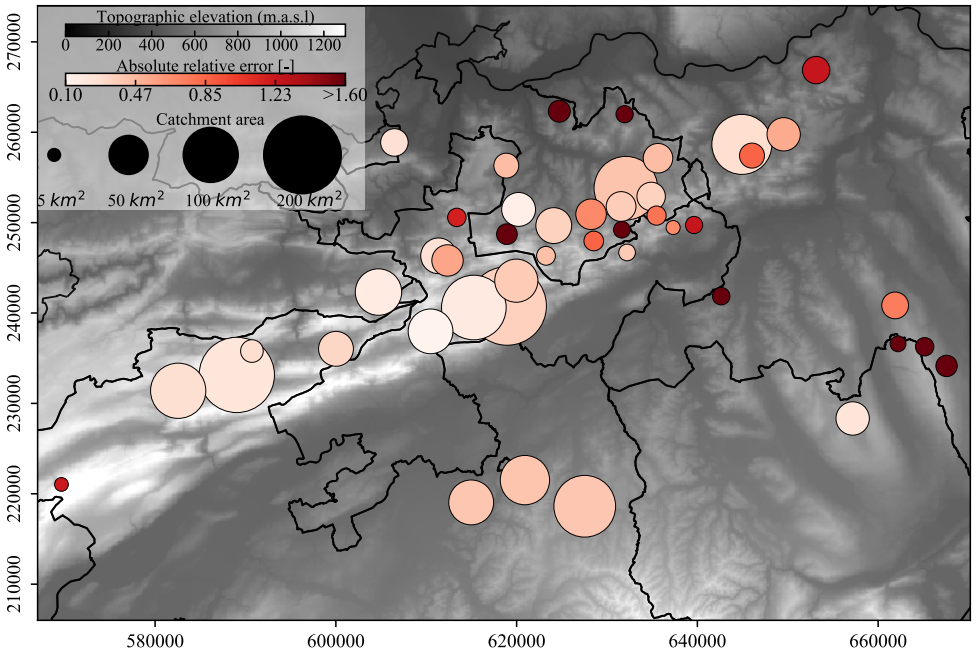

(b) t_p

Figure 8.6: Median absolute relative error per catchment for the estimation of the denormalized Q_p and t_p. The color bar gives the values of the error and the size of the marker indicates the catchment size.

It can be observed on the top panel that there is no regional bias present on the estimation of the denormalized Q_p and there is no pattern recognized for different catchment sizes. Nonetheless, on the bottom panel the four catchments located on the east of the study area (catchments 42, 43, 44 and 45, see Fig. 3.1) have darker red colors, which indicates larger estimation errors of t_p for that region. This regional pattern is, however, not observed as strong in the errors of the duration and the dimensionless t_p separately (see Fig. 8.2 and bottom panel of Fig. 8.5), the joint result of the two models results in a distinct regional pattern. Also, as it was the case of the duration, the t_p gives better estimates on bigger catchments.

To sum up there are no clear spatial patterns observed for the estimation errors, apart from some exceptions, but those are regions not larger than a couple of catchments. However, for the case of the duration and the denormalized t_p, it is observed that bigger catchments achieve better estimates. Also, it can be pointed out that some of the variables have lower errors depending on the season the flood event occurred. For example, the denormalized Q_p have smaller bias in summer than in winter. Yet, for the denormalized t_p it is the other way around, the summer events have larger bias than the winter events.

Overall, it is observed that the smaller errors are achieved for the estimation of the dimensionless DFH. The obtained errors can be considered acceptable if one considers that hydrological data are subject to uncertainties (Blöschl et al., 2013; Sauer and Meyer). Particularly, in the case of extreme discharges, where the rating curves are extrapolated beyond their calibrated discharge stages (Coxon et al., 2015). As a general conclusion the methods can estimate relatively well how the flood will be develop (dimensionless DFH) but improvement is needed for the estimation of the magnitude of the flood.

Chapter 9

Conclusion and Outlook

The objective of this study, to develop an estimation framework taking advantage of precipitation series with a high temporal resolution, is achieved. Including more precipitation observations and more catchments can improve the estimation further. The results obtained are plausible and produce satisfactory estimation errors, given the complexity of the floods space.

An analysis of the meteorological event triggering the floods showed that the precipitation temporal entropy is a better indicator of hydrograph shape than the duration or the intensity. Further it was observed, through the analysis of the association of precipitation triples, that floods are more likely triggered by precipitation events of total coverage exceeding the 0.9 quantile. However, as the quantile increases, the probability of observing joint occurrence in space decreases. As the number of POT increases, i.e. more floods that are less extreme are considered, the probability of observing a total event decreases and flood events are more likely to be triggered either by a local precipitation event or by a partial precipitation event. Given that triples showed a greater geographical dependency at the occurrence of extremer flood events, one can conclude that the floods sample selection is critical for assessing the spatial dependence of the precipitation generating the runoff. These findings reinforce the need of models that can better represent the rainfall field. The dependence structure of precipitation is more complex than the one described by a multivariate normal, models using a multivariate copula showed better representation (Bárdossy and Pegram, 2009). However, the spatial association of a precipitation event is still one of the challenges in hydrology. The temporal distribution of precipitation H_t within the flood day showed that homogeneous spatial H_t takes place. However, this does not mean that the temporal distribution must be uniform; rather, it varies owing to the many flood processes. Additionally, it was found that a precipitation model that does not represent the temporal and spatial distribution of the subsamples of meteorological events triggering the floods will result in an added uncertainty.

Further, it was observed that at the occurrence of the floods, the soil moisture does not need to be an annual extreme, rather a value close to the monthly maximum API is sufficient to

generate a 1POT flood. This was recognized by the fact that the empirical distribution function (EDF) of the API triggering the floods is closer to the EDF of the monthly maximum API than to any other of the EDFs tested.

The meteorological input responsible for the different flood mechanisms is normally not considered in the estimation of Design Flood Hydrograph (DFH). Usually, catchment and climate characteristics are used, to transfer the flood estimates from gauged to ungauged catchments. In this study, the similarity of the flood space is determined using a Random Forest (RF) algorithm, which takes as predictors not only catchment characteristics and climate descriptors, but also event-based parameters, such as temporal precipitation entropy, duration and intensity, antecedent moisture, etc., that are responsible for the occurrence of the floods. From all the predictors those related to the precipitation event triggering the floods were the ones that showed the greatest significance in the supervised RF. Specifically the entropy of the precipitation event, which describes the temporal variability of the precipitation event, showed to be important for recognizing different hydrograph responses. Precipitation is known to be the main driver of the reactions of the catchments, yet it is frequently left out from regionalization approaches.

A supervised regionalization approach proved to generate better estimates as an unsupervised approach. The added information by means of a supervised RF had advantages, especially for the estimation of the occurrence of the hydrograph peak (t_p), a parameter strongly associated with the hydrograph shape. The estimation errors of the hydrograph peak (Q_p) were comparable to those obtained with the unsupervised RF, although slightly smaller if a supervised RF is considered. Comparable estimation errors were observed when different target variables were selected to train the RF. This is not a surprise, given that all of the target variables used, describe the hydrograph to a given extent. This represents the equifinality problem, often encountered in hydrology: different sets of parameters or model structures can generate the same quality of estimates, given that the models are an approximation of the reality (Beven, 1993).

As mentioned in Chap. 6 it is possible to assess which predictors are the most important for the model and take a look at the similarities of the observations being close together in the RF space. This enables to determine if the found relationships agree with the understanding of the physical hydrological processes, making the model more robust. For example, it was found that rapid hydrographs were mainly a result of intense and short precipitation, probably a flash-flood as a result of convective precipitation. The selected approach of a similarity matrix has the benefit that it allows the superposition of flood mechanisms, as opposed to the approach of having a fixed number of clusters, which represents the flood mechanisms.

The estimations of the RF, for the case of using the relative volume (V/A) as the target variable, had a R^2 of around 0.7 (see Fig. 6.3, Fig. 6.4 and Fig. 6.5). This value represents a good model performance, indicating that a RF would be sufficient to estimate the flood volume and no rainfall-runoff model has to be considered. However, the RF cannot extrapolate outside the space of the observations, meaning that predicting a flood volume with a return

period longer than the records is not possible.

For the estimation of the flood volume, the EPIC model was studied. The floods volume is crucial to denormalize the DFH obtained from the RF regionalization and estimate the peak discharge. Through an analysis of the model parameters, it was possible to identify those that minimize the error in the flood volume estimation. An important finding for the study area was that smaller values of the regional constant λ can better represent the runoff generation of the studied catchments. These findings agree with studies of other European catchments (Maniak, 2016; Merz and Blöschl, 2009). It was recognized that the long memory of the catchments has more information to estimate the floods, i.e. the antecedent precipitation index (API) calculated with larger recession α had lower estimation errors. Further, it was showed that the duration of the precipitation event relates strongly to the flood duration and it was, therefore, considered that the duration of the flood event can be estimated with a simple linear model.

A leave-one-out cross-validation was carried out to evaluate the performance of the models investigated here for the estimation of the floods. On the one hand, it showed that little bias is present in the results. Estimates showed no regions with outstanding performance, nor was the case for floods events taking place in winter or in summer. However, it was observed that for the estimation of the flood duration and the denormalized t_p, better results were achieved for larger catchments than for smaller ones. The best performance was achieved for the estimation of the dimensionless flood hydrograph. Nonetheless, when the hydrograph is denormalized, the errors in the resulting Q_p and t_p become larger. This due to the estimation errors of the flood volume and the flood duration.

There is room for improvement of the regionalization model and topics that can be further investigated. For example, to incorporate the uncertainties of the flood mechanisms described by the nearest precipitation station. If the station is further away from the catchment, it is less representative or if the catchment is very large, it might be representative merely for a given area but not for the whole. This uncertainty could be added to the RF. One way to include this uncertainty would be to consider a weight to determine the observations that should be included more often, when randomly selecting the observations to train each tree.

In Chap. 4 only one hydrograph separation technique was introduced. However, there are other approaches in the field of hydrology, that can be grouped in graphical methods and digital filters (Blume et al., 2007). To test the model with other hydrograph separation methods could yield different results, impacting the hydrograph shape, and thus the observed flood volume. Comparing the results by changing the floods database to match other hydrograph separation techniques allows to quantify the introduced uncertainties, due to the hydrograph separation approach used. Another possibility to assess the uncertainty introduced by thy hydrograph separation technique would be to randomly alter the parameters used in this study for the separation. This would allow to analyze, if the influence on a more inclusive or exclusive selection of the start and end of the hydrograph, improves or worsens the estimates.

In this study, the use of the EPIC rainfall-runoff model was proposed for the estimation

of the floods volume. However, there is a possibility to use a different model. It was chosen here for its simplicity. Given that no soil moisture information was available, the API was used for describing the moisture conditions before the flood. Some adjustments had to be made to transfer the information obtained with the API to a representative soil moisture. It was proven that a seasonal modification of the soil moisture was needed. This is reasonable, knowing that in summer the potential evapotranspiration is larger, which makes a given value of API to have a different corresponding soil moisture condition in winter than in summer.

Although not investigated here, the model allows for the evaluation of climate scenarios. Adjusting the meteorological forcing to account for future climate scenarios, as investigated by Köplin et al. (2014) the inter-annual variability of floods in Switzerland is expected to change with climate projections. Even some synthetic generated hydrographs could be included in the RF to account for expected hydrograph changes. This allows to understand whether it is to be expected that some types of reactions are more common than others.

The measure of the spatial association of precipitation at the occurrence of a flood, studied in Chap. 5, was not considered as a predictor for the RF. A new tool was introduced, which quantifies the uncertainty derived by the use of precipitation observations to represent the temporal and spatial distribution of the sub sample of meteorological events triggering the flood. For this purpose, the Kullback-Leibler divergence was used, to compare the probabilities of precipitations triples jointly exceeding a threshold in or in the absence of a flood. The advantages of including the spatial variation of the meteorological event in the RF should be studied further as it can enhance the estimations by characterizing the distribution of precipitation in space. This allows to differentiate between those events less associated in space, as for example convective precipitation, and those more associated, as those caused by global atmospheric mechanisms.

Bibliography

Alhusain, L. and Hafez, A. M.: Cluster ensemble based on Random Forests for genetic data, BioData mining, 10, 37, doi:10.1186/s13040-017-0156-2, 2017.

Bárdossy, A. and Das, T.: Influence of rainfall observation network on model calibration and application, Hydrology and Earth System Sciences, 12, 77–89, doi:10.5194/hess-12-77-2008, 2008.

Bárdossy, A. and Filiz, F.: Identification of flood producing atmospheric circulation patterns, Journal of Hydrology, 313, 48–57, doi:10.1016/j.jhydrol.2005.02.006, 2005.

Bárdossy, A. and Pegram, G.: Downscaling precipitation using regional climate models and circulation patterns toward hydrology, Water Resources Research, 47, doi:10.1029/2010WR009689, 2011.

Bárdossy, A. and Pegram, G. G. S.: Copula based multisite model for daily precipitation simulation, Hydrology and Earth System Sciences, 13, 2299–2314, doi:10.5194/hess-13-2299-2009, 2009.

Bárdossy, A. and Pegram, G. G. S.: Multiscale spatial recorrelation of RCM precipitation to produce unbiased climate change scenarios over large areas and small, Water Resources Research, 48, 498, doi:10.1029/2011WR011524, 2012.

Bárdossy, A. and Schmidt, F.: GIS approach to sclae issues of perimeter-based shape indices for drainage basins, Hydrological Sciences Journal, 2002.

Bergström, S., Harlin, J., and Lindström, G.: Spillway design floods in Sweden: I. New guidelines, Hydrological Sciences Journal, 37, 505–519, doi:10.1080/02626669209492615, 1992.

Beven, K.: Prophecy, reality and uncertainty in distributed hydrological modelling, Advances in Water Resources, 16, 41–51, doi:10.1016/0309-1708(93)90028-E, 1993.

Beven, K. J.: Rainfall-runoff modelling: The primer, Wiley-Blackwell, Chichester, West Sussex and Hoboken, NJ, 2nd ed. edn., 2012.

Blöschl, G., Sivapalan, M., Wagener, T., Viglione, A., and Savenije, H., eds.: Runoff Prediction in Ungauged Basins: Synthesis Across Processes, Places and Scales, Cambridge University Press, Cambridge, doi:10.1017/CBO9781139235761, 2013.

Blume, T., Zehe, E., and Bronstert, A.: Rainfall—runoff response, event-based runoff coefficients and hydrograph separation, Hydrological Sciences Journal, 52, 843–862, doi:10.1623/hysj.52.5.843, 2007.

Bonacci, O., Ljubenkov, I., and Roje-Bonacci, T.: Karst flash floods: An example from the Dinaric karst (Croatia), Natural Hazards and Earth System Science, 6, 195–203, doi:10.5194/nhess-6-195-2006, 2006.

Bonacci, O., Pipan, T., and Culver, D. C.: A framework for karst ecohydrology, Environmental Geology, 56, 891–900, doi:10.1007/s00254-008-1189-0, 2009.

Borg, I. and Groenen, P. J. F.: Modern Multidimensional Scaling: Theory and Applications, Springer Series in Statistics, Springer Science+Business Media Inc, New York, NY, second edition edn., doi:10.1007/0-387-28981-X, 2005.

Breiman, L.: Random Forests, Machine Learning, 45, 5–32, doi:10.1023/A:1010933404324, 2001.

Breiman, L., Friedman, J. H., Stone, C. J., and Olshen, R. A.: Classification and regression trees Charles J. Stone, R.A. Olshen, Chapman & Hall/CRC, USA, 1984.

Brunner, M. I., Viviroli, D., Sikorska, A. E., Vannier, O., Favre, A.-C., and Seibert, J.: Flood type specific construction of synthetic design hydrographs, Water Resources Research, 53, 1390–1406, doi:10.1002/2016WR019535, 2017.

Brunner, M. I., Furrer, R., Sikorska, A. E., Viviroli, D., Seibert, J., and Favre, A.-C.: Synthetic design hydrographs for ungauged catchments: A comparison of regionalization methods, Stochastic Environmental Research and Risk Assessment, 32, 1993–2023, doi:10.1007/s00477-018-1523-3, 2018a.

Brunner, M. I., Seibert, J., and Favre, A.-C.: Representative sets of design hydrographs for ungauged catchments: A regional approach using probabilistic region memberships, Advances in Water Resources, 112, 235–244, doi:10.1016/j.advwatres.2017.12.018, 2018b.

Brunner, M. I., Sikorska, A. E., Furrer, R., and Favre, A.-C.: Uncertainty Assessment of Synthetic Design Hydrographs for Gauged and Ungauged Catchments, Water Resources Research, 54, 1493–1512, doi:10.1002/2017WR021129, 2018c.

Brunner, M. I., Viviroli, D., Furrer, R., Seibert, J., and Favre, A.-C.: Identification of Flood Reactivity Regions via the Functional Clustering of Hydrographs, Water Resources Research, 54, 1852–1867, doi:10.1002/2017WR021650, 2018d.

BWG: Hochwasserabschätzung in schweizerischen Einzugsgebieten: Praxishilfe, Bundestamt für Wasser und Geologie (BWG), Bern, 2003.

Chow, V. T., Maidment, D. R., and Mays, L. W.: Applied hydrology, McGraw-Hill, Inc., United States of America, 1988.

Coles, S.: An Introduction to Statistical Modeling of Extreme Values, Springer Series in Statistics, Springer London, London, doi:10.1007/978-1-4471-3675-0, 2001.

Coxon, G., Freer, J., Westerberg, I. K., Wagener, T., Woods, R., and Smith, P. J.: A novel framework for discharge uncertainty quantification applied to 500 UK gauging stations, Water Resources Research, 51, 5531–5546, doi:10.1002/2014WR016532, 2015.

Dingman, S. L.: Hydrologic effects of frozen ground—literature review and synthesis: Special Report 218, U.S. Army Corps of Engineers Cold Regions Research and Engineering Laboratory, Hannover, 1975.

Dunkerley, D.: Rain event properties in nature and in rainfall simulation experiments: A comparative review with recommendations for increasingly systematic study and reporting, Hydrological Processes, 22, 4415–4435, doi:10.1002/hyp.7045, 2008.

Field, C. B., Barros, V., Stocker, T. F., and Dahe, Q.: Managing the Risks of Extreme Events and Disasters to Advance Climate Change Adaptation: Special Report of the Intergovernmental Panel on Climate Change, Cambridge University Press, New York, 1st ed. edn., `https://ebookcentral.proquest.com/lib/gbv/detail.action?docID=907179`, 2012.

Fischer, S.: A seasonal mixed-POT model to estimate high flood quantiles from different event types and seasons, Journal of Applied Statistics, 45, 2831–2847, doi:10.1080/02664763.2018.1441385, 2018.

Fischer, S. and Schumann, A.: Spatio-temporal consideration of the impact of flood event types on flood statistic, Stochastic Environmental Research and Risk Assessment, 15, 3207, doi:10.1007/s00477-019-01690-2, 2019.

Fischer, S., Schumann, A., and Schulte, M.: Characterisation of seasonal flood types according to timescales in mixed probability distributions, Journal of Hydrology, 2016.

Froidevaux, P., Schwanbeck, J., Weingartner, R., Chevalier, C., and Martius, O.: Flood triggering in Switzerland: The role of daily to monthly preceding precipitation, Hydrology and Earth System Sciences, 19, 3903–3924, doi:10.5194/hess-19-3903-2015, 2015.

Gaál, L., Szolgay, J., Kohnová, S., Hlavčová, K., Parajka, J., Viglione, A., Merz, R., and Blöschl, G.: Dependence between flood peaks and volumes: A case study on climate and hydrological controls, Hydrological Sciences Journal, 60, 968–984, doi:10.1080/02626667.2014.951361, 2015.

Gibbons, J. D. and Chakraborti, S.: Nonparametric statistical inference, vol. 168 of *Statistics : textbooks and monographs*, Marcel Dekker, New York, 4th ed., rev. and expanded / jean dickinson gibbons, subhabrata chakraborti edn., 2003.

Gottschalk, L. and Weingartner, R.: Distribution of peak flow derived from a distribution of rainfall volume and runoff coefficient, and a unit hydrograph, Journal of Hydrology, 208, 148–162, doi:10.1016/S0022-1694(98)00152-8, 1998.

Gregorutti, B., Michel, B., and Saint-Pierre, P.: Correlation and variable importance in random forests, Statistics and Computing, 27, 659–678, doi:10.1007/s11222-016-9646-1, 2017.

Grimaldi, S., Petroselli, A., and Serinaldi, F.: A continuous simulation model for design-hydrograph estimation in small and ungauged watersheds, Hydrological Sciences Journal, 57, 1035–1051, doi:10.1080/02626667.2012.702214, 2012.

Hastie, T., Tibshirani, R., and Friedman, J. H.: The elements of statistical learning: Data mining, inference, and prediction, Springer Series in Statistics, Springer, New York, NY, second edition, corrected at 12th printing 2017 edn., 2017.

He, Y., Bárdossy, A., and Zehe, E.: A review of regionalisation for continuous stream-flow simulation, Hydrology and Earth System Sciences, 15, 3539–3553, doi:10.5194/hess-15-3539-2011, 2011.

Hilker, N., Badoux, A., and Hegg, C.: The Swiss flood and landslide damage database 1972–2007, Natural Hazards and Earth System Science, 9, 913–925, doi:10.5194/nhess-9-913-2009, 2009.

Horton, R. E.: Drainage-basin characteristics, Transactions, American Geophysical Union, 13, 350, doi:10.1029/TR013i001p00350, 1932.

Horton, R. E.: Erosional development of streams and their drainage basins; hydrophysical approach to quantitative morphology, Geological Society of America Bulletin, 56, 275, doi:10.1130/0016-7606(1945)56[275:edosat]2.0.co;2, 1945.

Janitza, S. and Hornung, R.: On the overestimation of random forest's out-of-bag error, PloS one, 13, e0201 904, doi:10.1371/journal.pone.0201904, 2018.

Kjeldsen, T. R.: The revitalised FSR/FEH rainfall-runoff method: Flood Estimation Handbook Supplementary Report No.1, Supplementary Report, Centre for Ecology and Hydrology, Wallingford, 2007.

Kjeldsen, T. R., Jones, D. A., and Bayliss, A. C.: Improving the FEH statistical procedures for flood frequency estimation, vol. SC050050 of *Science report*, Environment Agency, Bristol, 2008.

Klemeš, V.: Tall tales about tails of hydrological distributions. I, Journal of Hydrologic Engineering, 5, 227–231, doi:10.1061/(ASCE)1084-0699(2000)5:3(227), 2000.

Köplin, N., Schädler, B., Viviroli, D., and Weingartner, R.: Seasonality and magnitude of floods in Switzerland under future climate change, Hydrological Processes, 28, 2567–2578, doi:10.1002/hyp.9757, 2014.

Kottegoda, N. T. and Rosso, R.: Applied statistics for civil and environmental engineers, Blackwell Publishing, Oxford, 2nd ed. edn., 2008.

Kullback, S. and Leibler, R. A.: On Information and Sufficiency, The Annals of Mathematical Statistics, 22, 79–86, doi:10.1214/aoms/1177729694, 1951.

Kvam, P. H. and Vidakovic, B.: Nonparametric statistics with applications to science and engineering, Wiley series in probability and statistics, Wiley and Chichester : John Wiley [distributor], Hoboken, N.J., `http://www.loc.gov/catdir/enhancements/fy0739/2007002534-b.html`, 2007.

Lang, M., Ouarda, T., and Bobée, B.: Towards operational guidelines for over-threshold modeling, Journal of Hydrology, 225, 103–117, doi:10.1016/S0022-1694(99)00167-5, 1999.

Lebrenz, H. and Bárdossy, A.: Estimation of the Variogram Using Kendall's Tau for a Robust Geostatistical Interpolation, Journal of Hydrologic Engineering, 22, 04017 038, doi:10.1061/(ASCE)HE.1943-5584.0001568, 2017.

Ledingham, J., Archer, D., Lewis, E., Fowler, H., and Kilsby, C.: Contrasting seasonality of storm rainfall and flood runoff in the UK and some implications for rainfall-runoff methods of flood estimation, Hydrology Research, 50, 1309–1323, doi:10.2166/nh.2019.040, 2019.

Lin, J.: Divergence measures based on the Shannon entropy, IEEE Transactions on Information Theory, 37, 145–151, doi:10.1109/18.61115, 1991.

MacDonald, D. E. and Fraser, R. J.: An improved method for estimating the median annual flood for small ungauged catchments in the United Kingdom, Journal of Flood Risk Management, 7, 251–264, doi:10.1111/jfr3.12047, 2014.

Maniak, U.: Hydrologie und Wasserwirtschaft, Springer Berlin Heidelberg, Berlin, Heidelberg, doi:10.1007/978-3-662-49087-7, 2016.

Martínez-Goytre, J., House, P. K., and Baker, V. R.: Spatial variability of small-basin paleoflood magnitudes for a southeastern Arizona mountain range, Water Resources Research, 30, 1491–1501, doi:10.1029/94wr00065, 1994.

Merz, R. and Blöschl, G.: A process typology of regional floods, Water Resources Research, 39, doi:10.1029/2002WR001952, 2003.

Merz, R. and Blöschl, G.: Regionalisation of catchment model parameters, Journal of Hydrology, 287, 95–123, doi:10.1016/j.jhydrol.2003.09.028, 2004.

Merz, R. and Blöschl, G.: Flood frequency regionalisation—spatial proximity vs. catchment attributes, Journal of Hydrology, 302, 283–306, doi:10.1016/j.jhydrol.2004.07.018, 2005.

Merz, R. and Blöschl, G.: A regional analysis of event runoff coefficients with respect to climate and catchment characteristics in Austria, Water Resources Research, 45, doi:10.1029/2008WR007163, 2009.

Mishra, A. K., Özger, M., and Singh, V. P.: An entropy-based investigation into the variability of precipitation, Journal of Hydrology, 370, 139–154, doi:10.1016/j.jhydrol.2009.03.006, 2009.

Nadarajah, S.: Probability models for unit hydrograph derivation, Journal of Hydrology, 344, 185–189, doi:10.1016/j.jhydrol.2007.07.004, 2007.

Pallard, B., Castellarin, A., and Montanari, A.: A look at the links between drainage density and flood statistics, Hydrology and Earth System Sciences, 13, 1019–1029, doi:10.5194/hess-13-1019-2009, 2009.

Patil, S. R.: Regionalization of an Event Based Nash Cascade Model for Flood Predictions in Ungauged Basins, Disertation, Universität Stuttgart, Stuttgart, 2008.

Probst, P. and Boulesteix, A.-L.: To tune or not to tune the number of trees in random forest?, Journal of Machine Learning Research, 18, 1–18, 2018.

Rao, A. R. and Hamed, K. H.: Flood frequency analysis, New directions in civil engineering, CRC Press, USA, 2000.

Sauer, V. B. and Meyer, R. W.: Determination of error in individual discharge measuremnts, Open-File Report 92-144, U.S. GEOLOGICAL SURVEY, Norcross, Georgia.

Scherrer, S., Naef, F., Faeh, A. O., and Cordery, I.: Formation of runoff at the hillslope scale during intense precipitation, Hydrology and Earth System Sciences, 11, 907–922, doi:10.5194/hess-11-907-2007, 2007.

Segal, M. and Xiao, Y.: Multivariate random forests, WIREs Data Mining and Knowledge Discovery, 1, 80–87, doi:10.1002/widm.12, 2011.

Serinaldi, F. and Grimaldi, S.: Synthetic Design Hydrographs Based on Distribution Functions with Finite Support, Journal of Hydrologic Engineering, 16, 434–446, doi:10.1061/(ASCE)HE.1943-5584.0000339, 2011.

Shannon, C. E.: A Mathematical Theory of Communication, Bell System Technical Journal, 27, 623–656, doi:10.1002/j.1538-7305.1948.tb00917.x, 1948.

Shaperly, A. N. and Williams, J. R. E.: EPIC — Erosion/productivity impact calculator: 1: model documentation, U.S. Department of Agriculture Technical Bulletin 1768, Washington, D.C., 1990.

Shi, T. and Horvath, S.: Unsupervised Learning With Random Forest Predictors, Journal of Computational and Graphical Statistics, 15, 118–138, doi:10.1198/106186006X94072, 2012.

Shu, C. and Burn, D. H.: Homogeneous pooling group delineation for flood frequency analysis using a fuzzy expert system with genetic enhancement, Journal of Hydrology, 291, 132–149, doi:10.1016/j.jhydrol.2003.12.011, 2004.

Shu, C. and Ouarda, T. B. M. J.: Flood frequency analysis at ungauged sites using artificial neural networks in canonical correlation analysis physiographic space, Water Resources Research, 43, 903, doi:10.1029/2006WR005142, 2007.

Sikorska, A. E., Viviroli, D., and Seibert, J.: Flood–type classification in mountainous catchments using crisp and fuzzy decision trees, Water Resources Research, 51, 7959–7976, doi:10.1002/2015WR017326, 2015.

Singh, V. P.: Entropy theory and its application in environmental and water engineering, Wiley-Blackwell, New York, 2013.

Singh, V. P. and Mishra, S. K.: Soil Conservation Service Curve Number (SCS-CN) Methodology, vol. 42, Springer Netherlands, Dordrecht, doi:10.1007/978-94-017-0147-1, 2003.

Sinreich, M., Kozel, R., Lützenkirchen, V., Matousek, F., Jeannin, P.-Y., Loew, S., and Stauffer, F.: Grundwasserressourcen der Schweiz - Abschätzung von Kennwerten, AQUA & GAS, 9, 16–28, 2012.

Sivapalan, M.: Prediction in ungauged basins: a grand challenge for theoretical hydrology, Hydrological Processes, 17, 3163–3170, doi:10.1002/hyp.5155, 2003.

Sivapalan, M., Blöschl, G., Merz, R., and Gutknecht, D.: Linking flood frequency to long-term water balance: Incorporating effects of seasonality, Water Resources Research, 41, doi:10.1029/2004WR003439, 2005.

Staudinger, M., Stahl, K., and Seibert, J.: A drought index accounting for snow, Water Resources Research, 50, 7861–7872, doi:10.1002/2013WR015143, 2014.

Tarasova, L., Merz, R., Kiss, A., Basso, S., Blöschl, G., Merz, B., Viglione, A., Plötner, S., Guse, B., Schumann, A., Fischer, S., Ahrens, B., Anwar, F., Bárdossy, A., Bühler, P., Haberlandt, U., Kreibich, H., Krug, A., Lun, D., Müller-Thomy, H., Pidoto, R., Primo, C., Seidel, J., Vorogushyn, S., and Wietzke, L.: Causative classification of river flood events, WIREs. Water, 6, e1353, doi:10.1002/wat2.1353, 2019.

Viviroli, D., Mittelbach, H., Gurtz, J., and Weingartner, R.: Continuous simulation for flood estimation in ungauged mesoscale catchments of Switzerland – Part II: Parameter regionalisation and flood estimation results, Journal of Hydrology, 377, 208–225, doi:10.1016/j.jhydrol.2009.08.022, 2009a.

Viviroli, D., Zappa, M., Gurtz, J., and Weingartner, R.: An introduction to the hydrological modelling system PREVAH and its pre- and post-processing-tools, Environmental Modelling & Software, 24, 1209–1222, doi:10.1016/j.envsoft.2009.04.001, 2009b.

Viviroli, D., Zappa, M., Schwanbeck, J., Gurtz, J., and Weingartner, R.: Continuous simulation for flood estimation in ungauged mesoscale catchments of Switzerland – Part I: Modelling framework and calibration results, Journal of Hydrology, 377, 191–207, doi: 10.1016/j.jhydrol.2009.08.023, 2009c.

Wagener, T., Wheater, H., and Gupta, H. V.: Rainfall-runoff modelling in gauged and ungauged catchments, Imperial College Press, London, 2004.

Weijs, S. V., Schoups, G., and van de Giesen, N.: Why hydrological predictions should be evaluated using information theory, Hydrology and Earth System Sciences, 14, 2545–2558, doi:10.5194/hess-14-2545-2010, 2010.

Weingartner, R., Barben, M., and Spreafico, M.: Floods in mountain areas—an overview based on examples from Switzerland, Journal of Hydrology, 282, 10–24, doi:10.1016/S0022-1694(03)00249-X, 2003.

Winter, B., Schneeberger, K., Dung, N. V., Huttenlau, M., Achleitner, S., Stötter, J., Merz, B., and Vorogushyn, S.: A continuous modelling approach for design flood estimation on sub-daily time scale, Hydrological Sciences Journal, 64, 539–554, doi:10.1080/02626667.2019.1593419, 2019.

Xiao, Y. and Segal, M. R.: Identification of yeast transcriptional regulation networks using multivariate random forests, PLoS computational biology, 5, e1000 414, doi:10.1371/journal.pcbi.1000414, 2009.

Yue, S., Ouarda, T. B. M. J., Bobée, B., Legendre, P., and Bruneau, P.: Approach for Describing Statistical Properties of Flood Hydrograph, Journal of Hydrologic Engineering, 7, 147–153, doi:10.1061/(ASCE)1084-0699(2002)7:2(147), 2002.

Zehe, E., Becker, R., Bárdossy, A., and Plate, E.: Uncertainty of simulated catchment runoff response in the presence of threshold processes: Role of initial soil moisture and precipitation, Journal of Hydrology, 315, 183–202, doi:10.1016/j.jhydrol.2005.03.038, 2005.

A. Appendix

Table A.1: Overview of data

Measurement	Data Owners	Resolution
Discharge	Federal Office for the Environment (FOEN)	10 min
	Amt für Umwelt, Kanton Solothurn	10 min, 15 min
	Departement Bau, Verkehr und Umwelt, Kanton Aargau	10 min, 15 min
	Amt für Umweltschutz und Energie (AUE), Kanton Basel landschaft	10 min
	Bau- und Verkehrsdirektion, Kanton Bern	10 min
Precipitation	Meteoschweiz	10 min
	Amt für Umwelt, Kanton Solothurn	10 min
	Departement Bau, Verkehr und Umwelt, Kanton Aargau	10 min
	Universität Basel	10 min
	Basellandschaftliche Gebäudeversicherung	5 min
	Meteocentrale	10 min
	Meteofrance	6 min
Temperature	Meteoschweiz	1 day

Table A.2: Static catchment characteristics.

						Elevation		Slope		Centroid					Landuse				Aquifer			Morphometric charact.				
Id	River	Site	Owner	Peri.	Area	Mean	Std.	Mean	Std.	X	Y	L	T_c	Ori.	Settl.	Agri.	Forest	D.D.	karst	U. A.	p.p.f.	F	C	c	E	K
	[-]	[-]	[-]	[km]	[km^2]	[m]	[m]	[°]	[°]	[-]	[-]	[km]	[h]	[°]	[-]	[-]	[-]	[1/m]	[-]	[-]	[-]	[-]	[-]	[-]	[-]	[-]
1	Suze	Villeret	BE	16.5	6.4	1250	227	14.2	8.0	569637	221035	3.0	0.26	286	0.01	0.12	0.87	0.49	0.97	0.00	0.03	0.37	1.85	0.29	0.68	2.14
2	Birs	Court	BE	71.9	102.6	941	155	9.9	7.3	582555	231398	14.0	0.99	192	0.07	0.48	0.45	0.46	0.59	0.00	0.41	0.19	2.00	0.25	0.49	4.11
3	Birs	Moutier	FOEN	104.6	190.8	923	184	16.6	12.1	589039	233150	20.5	1.08	200	0.06	0.42	0.52	0.54	0.67	0.00	0.33	0.26	2.14	0.22	0.58	2.99
4	Chaliecre	Chaliecre	BE	20.0	17.2	902	151	14.7	7.5	590713	235793	5.1	0.39	181	0.02	0.37	0.61	0.46	0.84	0.00	0.16	0.48	1.36	0.54	0.78	1.63
5	Rauss	Moutier	BE	31.8	40.9	896	217	15.2	8.9	600014	236038	8.7	0.58	336	0.03	0.39	0.57	0.74	0.71	0.00	0.29	0.58	1.40	0.51	0.86	1.36
6	Scheulte	Vicques	FOEN	45.2	72.5	789	191	13.3	7.7	604717	242320	13.5	0.85	354	0.02	0.45	0.54	0.88	1.00	0.00	0.00	0.52	1.50	0.45	0.81	1.51
7	Marchbach	Oberwil	BL	31.0	25.5	463	137	6.9	6.0	606478	258871	5.0	0.52	224	0.22	0.41	0.37	0.75	0.63	0.05	0.32	0.29	1.73	0.33	0.61	2.72
8	Duennern	Laupersdorf	SO	47.6	67.3	832	208	14.8	8.2	610476	237971	15.0	0.89	204	0.04	0.40	0.57	0.87	0.63	0.00	0.37	0.28	1.64	0.37	0.60	2.80
9	Luessel	Breitenbach	SO	42.7	42.9	746	173	14.2	6.7	611367	246326	17.3	1.01	340	0.04	0.38	0.58	0.96	0.95	0.00	0.05	0.31	1.84	0.30	0.63	2.51
10	Luessel	Erschwill	SO	35.7	33.1	799	148	15.0	6.7	612355	245817	13.0	0.80	0	0.00	0.38	0.62	1.02	1.00	0.00	0.00	0.27	1.75	0.33	0.59	2.87
11	Chastelbach	Himmelried	SO	18.6	11.4	694	69	9.9	4.7	613385	250579	6.3	0.53	317	0.13	0.39	0.49	0.81	0.97	0.00	0.03	0.33	1.56	0.41	0.65	2.36
12	Oesch	Kriegstetten	SO	58.2	67.7	530	62	3.6	2.9	614973	219045	15.5	1.59	302	0.09	0.57	0.34	0.88	0.00	0.15	0.85	0.39	2.00	0.25	0.71	2.00
13	Duennern	Bahlstahl	SO	79.6	140.5	807	187	19.2	11.8	615268	240608	18.3	0.93	197	0.05	0.43	0.52	0.92	0.77	0.00	0.23	0.45	1.89	0.28	0.76	1.74
14	Orisbach	Liestal	BL	28.4	20.9	511	97	8.4	5.2	618856	256308	8.5	0.71	236	0.10	0.42	0.48	0.70	1.00	0.00	0.00	0.31	1.75	0.33	0.63	2.51
15	Hintere Frenke	Reigoldswil	BL	18.8	14.4	735	155	13.4	6.4	618927	248723	4.0	0.34	287	0.05	0.47	0.48	1.01	1.00	0.00	0.00	0.85	1.40	0.51	1.04	0.93
16	Duennern	Olten	FOEN	102.3	207.7	734	208	17.3	12.3	618950	240782	36.0	1.64	199	0.11	0.39	0.50	0.83	0.73	0.12	0.15	0.19	2.00	0.25	0.49	4.20
17	Augstbach	Bahlstahl	SO	58.8	62.6	809	147	13.1	6.1	619965	243579	11.1	0.74	39	0.04	0.49	0.47	1.02	0.97	0.00	0.03	0.57	2.10	0.23	0.85	1.38
18	Hintere Frenke	Bubendorf	BL	35.8	38.6	602	156	9.9	5.7	620219	251462	12.5	0.90	240	0.07	0.47	0.46	1.02	0.96	0.00	0.04	0.33	1.63	0.38	0.65	2.36
19	Oenz	Heimenhausen	BE	67.3	81.8	588	96	5.4	3.6	620918	221513	21.3	1.73	279	0.06	0.58	0.35	0.92	0.00	0.28	0.72	0.35	2.10	0.23	0.67	2.24
20	Vordere Frenke	Waldenburg	BL	18.8	11.9	818	127	13.8	5.7	623250	246331	5.4	0.42	267	0.03	0.41	0.57	1.17	1.00	0.00	0.00	0.58	1.54	0.42	0.86	1.36
21	Vordere Frenke	Bubendorf	BL	40.3	43.3	650	158	10.7	5.6	624111	249672	14.8	1.00	269	0.08	0.47	0.44	1.07	0.75	0.00	0.25	0.30	1.73	0.33	0.62	2.58
22	Violenbach	Augst	BL	25.4	16.2	427	77	7.3	4.0	624725	262329	7.0	0.65	313	0.09	0.57	0.35	0.85	0.75	0.25	0.00	0.29	1.78	0.31	0.61	2.72
23	Langete	Roggwil	BE	79.6	128.1	691	106	5.4	3.0	627538	218622	27.9	2.13	282	0.08	0.70	0.23	1.00	0.00	0.11	0.89	0.29	1.98	0.25	0.61	2.72
24	Diegterbach	Sissach	BL	36.7	31.4	619	132	9.9	5.2	628237	250927	11.9	0.87	269	0.07	0.50	0.44	0.97	0.74	0.00	0.26	0.25	1.85	0.29	0.56	3.20
25	Diegterbach	Diegten	BL	18.4	12.9	739	105	12.1	5.3	628535	247973	4.2	0.36	264	0.03	0.45	0.52	0.98	1.00	0.00	0.00	0.74	1.45	0.48	0.97	1.06
26	Homburgerbach	Thuernen	BL	32.0	29.8	610	108	9.4	4.9	631560	251785	10.5	0.81	296	0.08	0.50	0.42	0.76	0.86	0.00	0.14	0.35	1.65	0.37	0.67	2.23
27	Homburgerbach	Buckten	BL	15.1	9.4	694	90	10.6	4.2	631646	249220	3.7	0.35	321	0.07	0.52	0.41	0.69	1.00	0.00	0.00	0.64	1.39	0.52	0.90	1.22
28	Buuserbach	Maisprach	BL	16.2	9.9	530	65	8.2	4.2	631949	261994	5.1	0.49	322	0.05	0.67	0.28	0.74	1.00	0.00	0.00	0.47	1.45	0.47	0.77	1.68
29	Ergolz	Itingen	BL	68.1	136.2	596	117	14.6	10.8	632090	253808	17.8	1.02	339	0.09	0.50	0.41	0.85	0.86	0.00	0.14	0.67	1.65	0.37	0.93	1.17
30	Dorfbach	Trimbach	SO	15.5	9.4	680	112	12.0	4.7	632220	246700	4.9	0.41	177	0.02	0.50	0.48	0.85	1.00	0.00	0.00	0.41	1.43	0.49	0.72	1.92
31	Eibach	Gelterkinden	BL	35.2	27.2	635	114	8.6	5.3	634886	252900	7.1	0.62	290	0.08	0.51	0.41	0.86	0.87	0.00	0.13	0.31	1.90	0.28	0.63	2.51
32	Eibach	Zeglingen	BL	20.1	12.4	721	94	10.5	4.9	635486	250781	4.7	0.42	264	0.05	0.51	0.45	0.83	0.93	0.00	0.07	0.63	1.61	0.39	0.90	1.24
33	Ergolz	Ormalingen	BL	37.7	29.3	585	90	8.6	4.8	635644	257126	11.0	0.87	324	0.05	0.53	0.42	0.88	0.90	0.00	0.10	0.36	1.97	0.26	0.68	2.16
34	Lostorferbach	Lostorf	SO	12.8	6.7	652	127	10.3	4.7	637318	249455	3.6	0.34	150	0.13	0.23	0.64	0.77	0.95	0.05	0.00	0.48	1.40	0.51	0.79	1.62
35	Stuesslingerbach	Lostorf	SO	16.4	10.0	573	119	8.8	6.2	639632	249737	6.2	0.55	90	0.08	0.57	0.35	0.69	0.48	0.52	0.00	0.46	1.46	0.47	0.77	1.71
36	Koellikerbach	Koelliken	AG	22.7	10.3	489	47	8.8	7.9	642634	241863	7.3	0.63	225	0.35	0.24	0.41	1.05	0.00	0.07	0.93	0.27	1.99	0.25	0.59	2.91
37	Sissle	Eiken	AG	63.8	121.1	531	106	13.3	10.0	644923	258657	15.1	0.93	295	0.07	0.53	0.39	0.87	0.75	0.00	0.25	0.76	1.64	0.37	0.99	1.03
38	Staffeleggbach	Frick	AG	26.1	21.0	538	91	4.1	1.8	646041	257417	9.0	0.99	286	0.07	0.53	0.40	0.87	0.69	0.00	0.31	0.31	1.61	0.39	0.63	2.56
39	Sissle	Hornussen	AG	35.1	37.3	523	77	7.2	4.2	649547	259772	9.5	0.83	331	0.05	0.53	0.43	0.92	0.60	0.00	0.40	0.57	1.62	0.38	0.85	1.37
40	Etzgerbach	Etzgen	AG	26.2	25.2	477	68	8.6	4.1	653144	266875	8.1	0.69	327	0.04	0.62	0.34	0.86	1.00	0.00	0.00	0.51	1.47	0.46	0.81	1.53
41	Wyna	Reinach	AG	39.0	37.5	687	56	6.1	5.4	657182	228334	11.8	1.05	285	0.12	0.73	0.15	0.93	0.00	0.00	1.00	0.37	1.80	0.31	0.69	2.13
42	Holzbach	Villmergen	AG	30.6	24.1	576	76	4.9	2.9	661882	240842	9.2	0.95	287	0.14	0.53	0.33	0.97	0.00	0.21	0.79	0.28	1.76	0.32	0.60	2.77
43	Dorfbach	Meist(erschw)	AG	20.7	8.4	664	86	4.1	1.8	662201	236593	8.1	0.91	322	0.16	0.74	0.10	1.16	0.00	0.50	0.50	0.17	2.01	0.25	0.47	4.62
44	Wissenbach	Boswil	AG	22.2	11.4	686	93	5.5	2.2	665148	236268	7.6	0.78	272	0.05	0.48	0.47	1.09	0.00	0.41	0.59	0.22	1.85	0.29	0.53	3.61
45	Buenz	Muri	AG	24.5	15.4	605	115	5.0	2.6	667573	234149	6.4	0.71	256	0.15	0.70	0.15	1.20	0.00	0.14	0.86	0.28	1.76	0.32	0.60	2.80

From left to right the columns are as follow: perimeter, area, elevation (mean and standard deviation), slope (mean and standard deviation), centroid (x and y coordinates), river length , concentration time, orientation, land use (settlement, agriculture and forest), drainage density, aquifer (karst, unconsolidated, porous partially fissured) and morphometric characteristics (form factor (F), compactness (C), circularity (c), elongation(E) and lemniscate ratio (K))

Table A.3: Seasonal mean of the characteristics of the meteorological event triggering the 1POT events. The columns w and s correspond to winter and summer respectively.

	API30 $\alpha = 0.9$ [mm]		H_R [-]		I [mm]		$D_{10min,flood}$ [h]		$D_{h,flood}$ [h]		P sum [mm]		Ψ [-]		Z_{flood} [-]	
Id	w	s	w	s	w	s	w	s	w	s	w	s	w	s	w	s
1	27.2	49.5	0.80	0.68	2.1	7.3	13.5	15.3	21.0	18.5	25.9	68.2	2.76	0.45	0.06	0.14
2	36.9	44.8	0.82	0.68	1.8	3.8	23.2	18.1	32.4	24.6	49.7	65.1	0.12	0.14	-0.06	-0.14
3	42.2	37.9	0.82	0.68	1.6	3.4	24.9	21.2	35.5	29.2	55.8	65.7	0.16	0.19	0.90	-0.75
4		34.7		0.76		4.1		16.4		19.7		54.6		0.07		-0.05
5	45.7	30.6	0.87	0.71	1.5	4.3	25.2	18.2	35.0	22.3	51.4	67.1	0.22	0.21	0.81	0.02
6		33.4		0.71		2.0		21.6		29.9		53.9		0.42		0.08
7	31.4	24.1	0.78	0.76	3.6	3.8	26.3	9.2	31.0	11.3	51.5	46.6	0.14	0.15	-1.09	0.56
8	29.1	34.9	0.79	0.71	1.6	3.2	20.2	19.3	29.5	23.6	42.8	55.2	0.21	0.18	1.10	0.12
9	9.5	35.6	0.94	0.77	1.2	2.4	27.3	21.0	36.0	27.6	48.2	56.0	0.20	0.35	-0.14	0.70
10	9.5	36.8	0.95	0.73	1.5	2.2	28.2	20.0	37.0	28.1	54.6	57.6	0.38	0.44	-0.16	0.00
11	17.9	42.6	0.64	0.80	5.8	3.3	10.6	16.3	14.3	19.3	41.4	52.9	0.16	0.19	-0.85	-0.13
12	43.8	38.0	0.82	0.74	2.1	2.1	14.0	20.5	20.6	27.8	39.7	54.0	0.21	0.17	0.93	0.37
13	34.1	37.0	0.77	0.73	1.7	2.5	20.4	19.5	28.3	24.0	44.1	46.2	0.24	0.16	0.39	0.16
14	32.7	39.7	0.80	0.66	2.5	3.3	22.3	20.2	28.3	27.4	44.2	47.8	0.18	0.37	-0.10	0.34
15	22.6	47.0	0.80	0.77	3.1	3.0	17.3	15.5	24.5	20.0	46.8	53.6	0.14	0.20	0.23	-0.10
16	42.3	30.9	0.75	0.78	1.7	2.0	18.1	26.3	24.6	32.2	43.0	60.8	0.30	0.30	0.65	0.01
17	39.0	34.3	0.75	0.71	1.7	2.5	14.2	21.6	18.8	27.6	27.1	56.1	0.46	0.28	0.43	0.13
18	22.7	39.2	0.79	0.72	2.4	2.3	19.2	13.1	26.7	18.7	42.1	39.7	0.19	0.23	0.44	0.57
19	49.9	37.6	0.81	0.73	1.7	2.6	15.4	22.2	22.5	29.3	31.7	65.6	0.15	0.14	0.49	-0.52
20	40.1	32.7	0.80	0.79	1.7	2.6	12.9	19.3	17.4	23.8	27.2	49.2	0.31	0.21	0.64	-0.16
21	28.0	35.0	0.78	0.71	1.8	3.8	17.0	19.6	25.1	25.8	38.1	58.5	0.31	0.20	0.38	-0.01
22	26.0	34.3	0.83	0.53	2.4	3.3	15.5	3.6	19.3	6.4	33.8	19.5	0.11	0.26	0.51	0.91
23	35.8	42.6	0.80	0.66	1.8	2.7	17.2	13.0	29.5	19.1	33.7	53.5	0.12	0.09	0.54	-0.74
24	22.4	34.9	0.84	0.70	2.0	3.9	20.0	16.3	28.6	21.3	46.8	53.7	0.47	0.20	0.60	-0.08
25	26.8	33.5	0.83	0.74	2.1	4.1	15.0	16.4	20.8	20.9	36.5	51.4	0.30	0.23	0.69	0.16
26	32.7	35.3	0.78	0.75	1.8	3.7	17.0	21.9	24.1	28.0	36.9	59.5	0.22	0.16	0.74	-0.05
27	12.5	27.3	0.94	0.77	2.2	3.1	12.9	14.2	18.0	18.1	28.5	36.0	0.11	0.09	0.90	0.56
28	39.7	35.2	0.77	0.58	3.2	2.9	6.8	6.3	8.0	9.7	22.2	22.9	0.14	0.15	0.05	0.54
29	28.4	34.0	0.75	0.67	1.6	2.9	20.4	23.7	31.5	32.5	44.1	67.9	0.33	0.25	0.33	-0.14
30	51.0	34.7	0.82	0.84	2.5	2.1	15.8	26.4	23.2	31.4	37.5	63.6	0.45	0.30	0.56	0.15
31	31.2	44.4	0.79	0.77	2.3	3.5	14.0	21.1	19.1	27.0	36.9	56.7	0.28	0.18	0.76	-0.61
32	33.2	35.0	0.81	0.70	2.1	3.8	14.6	13.0	19.1	17.0	35.0	45.3	0.24	0.20	0.37	0.08
33	27.4	45.5	0.81	0.68	1.9	3.6	15.5	16.7	22.4	22.2	35.3	48.6	0.29	0.25	0.69	-0.25
34	31.8	31.9	0.68	0.78	1.3	2.7	14.5	29.8	25.4	39.6	28.6	70.1	0.67	0.31	1.57	0.02
35	32.7	25.6	0.80	0.88	1.2	3.1	7.3	20.3	10.5	23.8	13.4	55.2	0.66	0.20	1.99	-0.59
36		30.8		0.67		4.5		5.5		8.5		35.7		0.26		0.61
37	43.3	29.7	0.69	0.85	2.2	1.6	11.9	32.8	17.5	43.0	34.1	68.2	0.27	0.17	0.84	0.33
38	37.5	36.0	0.83	0.88	2.5	2.1	14.2	17.8	20.0	21.0	39.9	42.1	0.16	0.14	0.27	-0.17
39	49.5	32.0	0.86	0.62	2.7	5.1	9.4	7.5	13.0	10.2	35.0	48.3	0.18	0.15	0.53	0.34
40	36.9	31.7	0.82	0.71	2.1	3.3	12.7	16.3	16.5	20.3	30.6	43.0	0.16	0.17	0.95	0.12
41	32.8	39.3	0.79	0.77	1.4	2.0	12.6	23.2	19.5	30.7	25.9	53.9	0.38	0.28	0.55	-0.20
42	52.7	44.4	0.80	0.77	2.4	3.1	10.6	17.6	18.0	22.8	35.4	55.2	0.25	0.10	0.32	-0.51
43	49.9	30.4	0.76	0.77	4.2	4.3	4.5	13.3	6.0	17.0	25.1	53.5	0.18	0.06	0.36	-0.29
44	50.7	37.2	0.79	0.75	3.3	3.4	8.8	12.9	11.5	16.3	37.9	46.0	0.10	0.06	0.54	-0.48
45	49.9	34.2	0.76	0.81	4.2	2.7	4.5	11.1	6.0	15.1	25.1	35.3	0.26	0.28	-0.19	-0.42

From left to right the columns are as follow: API30 $\alpha = 0.9$, relative temporal precipitation entropy, intensity, duration calculated using a 10 min aggregation, duration using an hour aggregation, total precipitation sum, runoff coefficient, standard score of the temperature of the previous 30 days

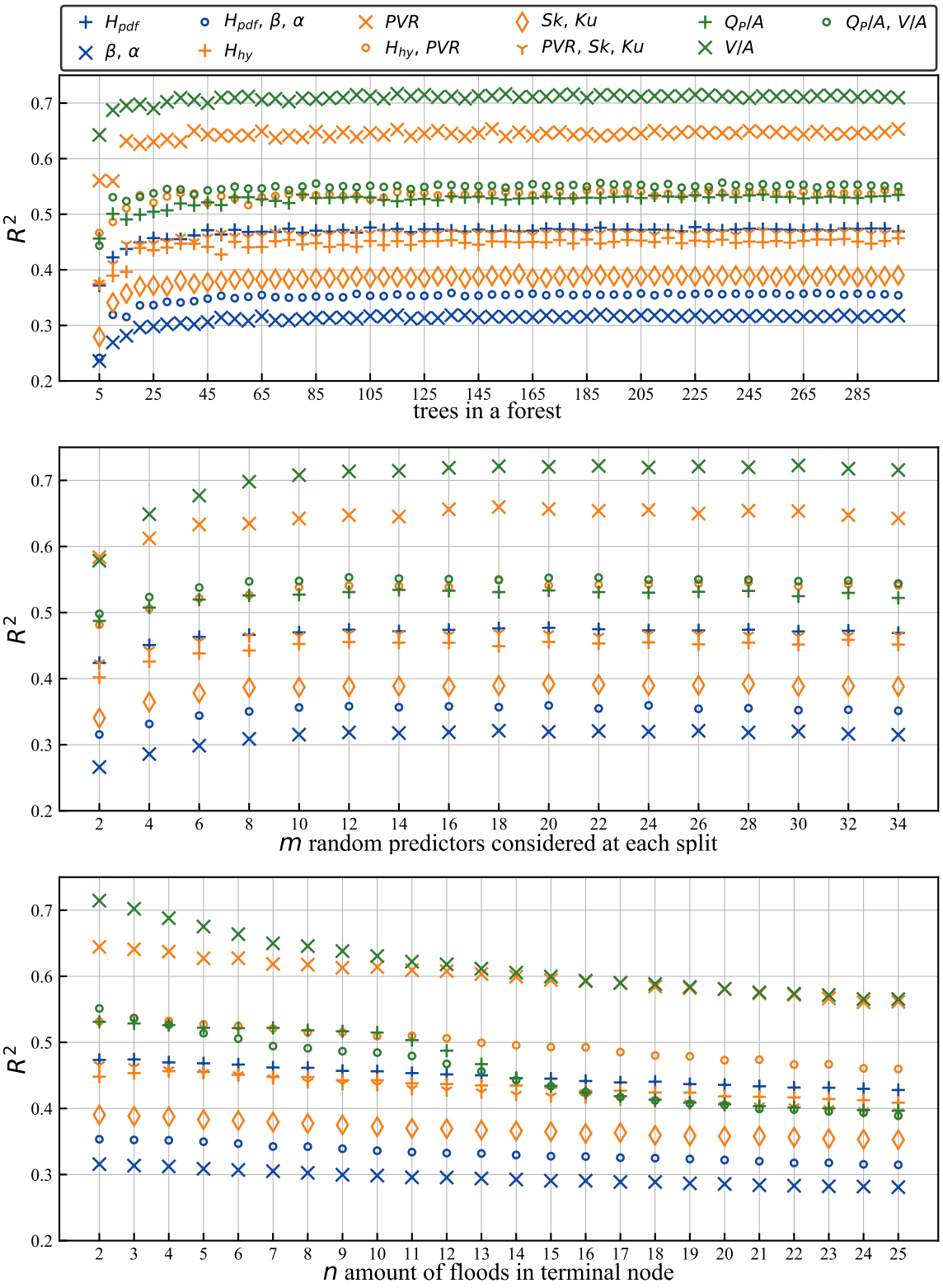

Figure A.1: Mean RF performance over 10 folds for all target variables, trained with the observations of the 4POT sample. On each panel only the evaluated RF parameter is modified while the others are set constant to $N = 300$, $m = 12$ and $n = 2$. Top: number of trees per forest. Middle: number of random variables selected at each split. Bottom: minimum number of floods in a terminal node.

Table A.4: Mean and standard deviation of catchments' ε_R for the estimations of Q_p and t_p using a similarity as S and using a TSP distribution

			mean ± std of catchments' ε_R					
			Similarity					
		Target	0.025	0.05	0.1	0.2	0.3	0.4
Estimations using the **mean** of the TSP parameters	Q_p	H_{PDF}	0.076 ± 0.089	0.072 ± 0.082	0.070 ± 0.074	**0.069 ± 0.098**	0.087 ± 0.144	0.093 ± 0.272
		α , β	0.076 ± 0.066	0.074 ± 0.062	**0.074 ± 0.060**	0.079 ± 0.099	0.080 ± 0.096	0.104 ± 0.170
		H_{PDF}, α , β	0.078 ± 0.066	0.075 ± 0.063	0.075 ± 0.063	**0.073 ± 0.087**	0.082 ± 0.118	0.076 ± 0.145
		H_{hy}	0.089 ± 0.107	0.084 ± 0.098	0.080 ± 0.087	**0.073 ± 0.088**	0.079 ± 0.134	0.159 ± 0.309
		PVR	0.081 ± 0.113	0.078 ± 0.105	0.077 ± 0.090	0.084 ± 0.111	**0.061 ± 0.118**	0.085 ± 0.133
		H_{hy} , PVR	0.084 ± 0.104	0.084 ± 0.098	**0.080 ± 0.087**	0.096 ± 0.106	0.112 ± 0.208	0.109 ± 0.243
		Sk , Ku	0.085 ± 0.094	0.083 ± 0.087	0.080 ± 0.077	0.078 ± 0.091	0.071 ± 0.122	**0.067 ± 0.144**
		PVR, Sk , Ku	0.083 ± 0.094	0.081 ± 0.088	0.074 ± 0.077	**0.072 ± 0.091**	0.073 ± 0.110	0.097 ± 0.195
		Q_p/A	0.089 ± 0.086	0.087 ± 0.078	0.084 ± 0.076	0.090 ± 0.102	0.083 ± 0.132	**0.077 ± 0.126**
		V/A	0.088 ± 0.136	0.087 ± 0.126	0.083 ± 0.108	0.073 ± 0.136	**0.064 ± 0.104**	0.102 ± 0.260
		Q_p/A , V/A	0.082 ± 0.073	0.080 ± 0.065	0.080 ± 0.062	0.076 ± 0.072	**0.075 ± 0.122**	0.101 ± 0.135
	t_p	H_{PDF}	0.266 ± 0.297	0.252 ± 0.270	0.230 ± 0.234	0.258 ± 0.413	0.215 ± 0.382	**0.173 ± 0.468**
		α , β	0.262 ± 0.292	0.251 ± 0.276	0.232 ± 0.251	0.196 ± 0.190	0.147 ± 0.196	**0.104 ± 0.324**
		H_{PDF}, α , β	0.259 ± 0.290	0.249 ± 0.275	0.228 ± 0.231	0.224 ± 0.311	0.196 ± 0.217	**0.172 ± 0.263**
		H_{hy}	0.270 ± 0.316	0.261 ± 0.308	0.240 ± 0.283	0.235 ± 0.311	0.212 ± 0.239	**0.161 ± 0.433**
		PVR	0.268 ± 0.312	0.256 ± 0.292	0.226 ± 0.261	0.161 ± 0.193	**0.117 ± 0.244**	0.162 ± 0.311
		H_{hy} , PVR	0.278 ± 0.314	0.266 ± 0.294	0.243 ± 0.289	0.188 ± 0.201	**0.150 ± 0.285**	0.176 ± 0.448
		Sk , Ku	0.267 ± 0.323	0.257 ± 0.309	0.237 ± 0.269	0.193 ± 0.236	**0.161 ± 0.249**	0.215 ± 0.365
		PVR, Sk , Ku	0.256 ± 0.297	0.243 ± 0.281	0.223 ± 0.236	0.177 ± 0.204	0.154 ± 0.201	**0.121 ± 0.337**
		Q_p/A	0.291 ± 0.270	0.284 ± 0.257	0.262 ± 0.241	0.251 ± 0.242	0.227 ± 0.168	**0.224 ± 0.257**
		V/A	0.266 ± 0.292	0.251 ± 0.278	0.222 ± 0.242	0.200 ± 0.248	0.142 ± 0.228	**0.130 ± 0.323**
		Q_p/A , V/A	0.299 ± 0.293	0.289 ± 0.273	0.273 ± 0.260	0.247 ± 0.239	**0.196 ± 0.190**	0.220 ± 0.244
Estimations using the **median** of the TSP parameters	Q_p	H_{PDF}	**0.000± 0.082**	-0.008± 0.079	-0.051± 0.078	-0.291± 0.139	-0.548± 0.125	-0.627± 0.105
		α , β	**0.004± 0.062**	-0.006± 0.059	-0.040± 0.053	-0.242± 0.121	-0.506± 0.126	-0.633± 0.084
		H_{PDF}, α , β	0.009± 0.064	**0.002± 0.064**	-0.040± 0.049	-0.243± 0.130	-0.494± 0.141	-0.630± 0.111
		H_{hy}	0.006± 0.096	**-0.003± 0.089**	-0.050± 0.083	-0.318± 0.151	-0.515± 0.147	-0.624± 0.094
		PVR	**-0.005± 0.103**	-0.012± 0.095	-0.050± 0.073	-0.299± 0.143	-0.518± 0.155	-0.602± 0.163
		H_{hy} , PVR	**0.003± 0.095**	-0.006± 0.089	-0.038± 0.076	-0.249± 0.132	-0.509± 0.158	-0.621± 0.139
		Sk , Ku	0.008± 0.092	**-0.002± 0.085**	-0.039± 0.075	-0.297± 0.147	-0.557± 0.126	-0.635± 0.101
		PVR, Sk , Ku	**0.004± 0.085**	-0.006± 0.081	-0.055± 0.069	-0.281± 0.126	-0.532± 0.133	-0.629± 0.129
		Q_p/A	**-0.005± 0.081**	-0.019± 0.072	-0.047± 0.059	-0.182± 0.131	-0.347± 0.171	-0.507± 0.187
		V/A	**-0.011± 0.119**	-0.023± 0.110	-0.066± 0.110	-0.340± 0.175	-0.530± 0.147	-0.614± 0.108
		Q_p/A , V/A	**-0.012± 0.075**	-0.021± 0.063	-0.049± 0.062	-0.169± 0.118	-0.373± 0.174	-0.502± 0.194
	t_p	H_{PDF}	0.162± 0.267	0.121± 0.242	**-0.040± 0.167**	-0.096± 0.508	-0.419± 0.842	-0.818± 0.414
		α , β	0.151± 0.265	0.121± 0.254	**-0.009± 0.181**	-0.021± 0.414	-0.322± 0.822	-0.766± 0.552
		H_{PDF}, α , β	0.146± 0.268	0.119± 0.237	**-0.010± 0.145**	-0.035± 0.463	-0.413± 0.649	-0.802± 0.425
		H_{hy}	0.159± 0.292	0.132± 0.291	**-0.015± 0.196**	-0.070± 0.664	-0.362± 0.767	-0.781± 0.433
		PVR	0.163± 0.289	0.127± 0.262	**0.016± 0.218**	-0.173± 0.373	-0.319± 0.944	-0.680± 0.891
		H_{hy} , PVR	0.164± 0.272	0.131± 0.251	0.115± 0.715	**0.085± 0.962**	-0.287± 0.885	-0.721± 0.591
		Sk , Ku	0.167± 0.291	0.127± 0.267	**0.009± 0.187**	0.024± 1.014	-0.597± 0.583	-0.889± 0.207
		PVR, Sk , Ku	0.151± 0.260	0.115± 0.230	**-0.015± 0.175**	-0.085± 0.511	-0.614± 0.412	-0.883± 0.239
		Q_p/A	0.148± 0.268	0.091± 0.213	**0.023± 0.238**	-0.100± 0.323	-0.109± 0.525	-0.441± 0.867
		V/A	0.160± 0.260	0.116± 0.243	**-0.005± 0.255**	0.013± 0.859	-0.432± 0.622	-0.633± 0.753
		Q_p/A , V/A	0.162± 0.278	0.111± 0.218	**0.006± 0.163**	-0.076± 0.335	-0.326± 0.479	-0.445± 1.120

A. Appendix

Table A.5: Mean and standard deviation of catchments' ε_R for the estimations of Q_p and t_p using a similarity as S and using a Lognormal distribution

			mean ± std of catchments' ε_R					
			Similarity					
		Target	**0.025**	**0.05**	**0.1**	**0.2**	**0.3**	**0.4**
Estimations using the **mean** of the Lognormal parameters	Q_p	H_{PDF}	-0.033 ± 0.076	-0.027 ± 0.071	**-0.017 ± 0.071**	0.018 ± 0.087	0.032 ± 0.111	0.044 ± 0.171
		α , β	-0.028 ± 0.085	-0.022 ± 0.078	**-0.012 ± 0.073**	0.046 ± 0.115	0.088 ± 0.158	0.146 ± 0.266
		H_{PDF}, α , β	-0.032 ± 0.085	-0.026 ± 0.077	**-0.016 ± 0.066**	0.028 ± 0.105	0.064 ± 0.114	0.096 ± 0.180
		H_{hy}	-0.034 ± 0.095	-0.027 ± 0.089	**-0.016 ± 0.083**	0.024 ± 0.109	0.081 ± 0.197	0.048 ± 0.203
		PVR	-0.038 ± 0.101	-0.032 ± 0.093	**-0.022 ± 0.085**	0.024 ± 0.097	0.055 ± 0.131	0.047 ± 0.165
		H_{hy} , PVR	-0.038 ± 0.088	-0.034 ± 0.081	**-0.019 ± 0.074**	0.023 ± 0.087	0.060 ± 0.133	0.102 ± 0.208
		Sk , Ku	-0.038 ± 0.082	-0.033 ± 0.077	**-0.017 ± 0.078**	0.028 ± 0.087	0.053 ± 0.126	0.086 ± 0.178
		PVR, Sk , Ku	-0.041 ± 0.081	-0.038 ± 0.075	-0.027 ± 0.070	0.024 ± 0.102	0.045 ± 0.136	**0.021 ± 0.165**
		Q_p/A	-0.043 ± 0.071	-0.041 ± 0.062	-0.033 ± 0.046	**-0.018 ± 0.056**	0.019 ± 0.084	0.033 ± 0.128
		V/A	-0.040 ± 0.114	-0.034 ± 0.104	-0.020 ± 0.095	**0.015 ± 0.098**	0.052 ± 0.108	0.032 ± 0.092
		Q_p/A , V/A	-0.042 ± 0.069	-0.040 ± 0.057	-0.031 ± 0.044	**-0.012 ± 0.042**	0.030 ± 0.104	0.026 ± 0.109
	t_p	H_{PDF}	0.166 ± 0.264	0.160 ± 0.246	**0.153 ± 0.213**	0.183 ± 0.290	0.169 ± 0.288	0.236 ± 0.332
		α , β	0.145 ± 0.234	0.130 ± 0.203	0.114 ± 0.177	0.114 ± 0.141	0.152 ± 0.255	**0.088 ± 0.349**
		H_{PDF}, α , β	0.152 ± 0.236	0.142 ± 0.221	0.132 ± 0.209	0.106 ± 0.163	0.145 ± 0.208	**0.042 ± 0.292**
		H_{hy}	0.180 ± 0.285	0.168 ± 0.268	**0.160 ± 0.250**	0.163 ± 0.184	0.168 ± 0.257	0.173 ± 0.349
		PVR	0.182 ± 0.291	0.174 ± 0.277	0.157 ± 0.261	0.136 ± 0.202	**0.100 ± 0.203**	0.188 ± 0.337
		H_{hy} , PVR	0.181 ± 0.293	0.175 ± 0.279	0.158 ± 0.241	**0.133 ± 0.196**	0.135 ± 0.221	0.159 ± 0.531
		Sk , Ku	0.179 ± 0.289	0.174 ± 0.281	0.167 ± 0.264	0.143 ± 0.206	**0.141 ± 0.218**	0.141 ± 0.222
		PVR, Sk , Ku	0.180 ± 0.288	0.174 ± 0.274	0.169 ± 0.262	**0.134 ± 0.234**	0.151 ± 0.245	0.207 ± 0.462
		Q_p/A	0.191 ± 0.264	0.190 ± 0.254	**0.189 ± 0.254**	0.206 ± 0.286	0.222 ± 0.353	0.227 ± 0.411
		V/A	0.169 ± 0.259	0.164 ± 0.250	0.148 ± 0.235	0.150 ± 0.269	**0.113 ± 0.235**	0.185 ± 0.357
		Q_p/A , V/A	0.183 ± 0.252	0.186 ± 0.247	**0.182 ± 0.235**	0.182 ± 0.287	0.184 ± 0.340	0.233 ± 0.304
Estimations using the **median** of the Lognormal parameters	Q_p	H_{PDF}	0.053 ± 0.088	0.087 ± 0.090	0.269 ± 0.127	**-0.038 ± 0.427**	-0.605 ± 0.339	-0.818 ± 0.166
		α , β	**0.044 ± 0.093**	0.083 ± 0.095	0.235 ± 0.128	-0.190 ± 0.345	-0.727 ± 0.227	-0.869 ± 0.130
		H_{PDF}, α , β	**0.043 ± 0.092**	0.081 ± 0.091	0.252 ± 0.134	-0.089 ± 0.306	-0.660 ± 0.243	-0.827 ± 0.184
		H_{hy}	0.053 ± 0.110	0.096 ± 0.106	0.272 ± 0.130	**-0.013 ± 0.382**	-0.612 ± 0.297	-0.815 ± 0.188
		PVR	0.047 ± 0.110	0.082 ± 0.105	0.227 ± 0.111	**-0.015 ± 0.345**	-0.634 ± 0.309	-0.801 ± 0.283
		H_{hy} , PVR	0.049 ± 0.097	0.084 ± 0.096	0.248 ± 0.126	**0.028 ± 0.315**	-0.591 ± 0.314	-0.790 ± 0.226
		Sk , Ku	**0.044 ± 0.093**	0.083 ± 0.084	0.275 ± 0.131	-0.070 ± 0.358	-0.624 ± 0.256	-0.858 ± 0.116
		PVR, Sk , Ku	0.042 ± 0.092	0.085 ± 0.093	0.264 ± 0.143	**-0.012 ± 0.375**	-0.642 ± 0.255	-0.845 ± 0.138
		Q_p/A	**0.056 ± 0.099**	0.108 ± 0.094	0.239 ± 0.148	0.256 ± 0.258	-0.237 ± 0.413	-0.567 ± 0.455
		V/A	**0.041 ± 0.123**	0.084 ± 0.125	0.258 ± 0.187	-0.091 ± 0.359	-0.637 ± 0.262	-0.851 ± 0.132
		Q_p/A , V/A	**0.065 ± 0.095**	0.114 ± 0.091	0.246 ± 0.130	0.235 ± 0.287	-0.221 ± 0.441	-0.550 ± 0.483
	t_p	H_{PDF}	0.205 ± 0.290	0.185 ± 0.265	**0.135 ± 0.226**	1.333 ± 1.474	2.920 ± 2.087	3.842 ± 2.326
		α , β	0.183 ± 0.241	0.156 ± 0.214	**0.154 ± 0.241**	1.634 ± 1.255	3.380 ± 1.965	4.138 ± 2.056
		H_{PDF}, α , β	0.192 ± 0.259	0.166 ± 0.248	**0.157 ± 0.289**	1.407 ± 1.203	3.164 ± 1.961	3.597 ± 2.237
		H_{hy}	0.218 ± 0.306	0.194 ± 0.285	**0.155 ± 0.287**	1.441 ± 1.304	3.188 ± 1.866	3.690 ± 2.179
		PVR	0.217 ± 0.308	0.199 ± 0.288	**0.158 ± 0.315**	1.433 ± 1.239	3.208 ± 2.256	3.917 ± 1.968
		H_{hy} , PVR	0.221 ± 0.311	0.195 ± 0.284	**0.127 ± 0.239**	1.226 ± 0.915	3.119 ± 2.120	3.621 ± 2.987
		Sk , Ku	0.217 ± 0.303	0.200 ± 0.303	**0.147 ± 0.274**	1.341 ± 1.266	2.955 ± 1.766	3.865 ± 2.426
		PVR, Sk , Ku	0.219 ± 0.305	0.194 ± 0.277	**0.181 ± 0.298**	1.358 ± 1.173	3.177 ± 1.898	3.828 ± 2.223
		Q_p/A	0.223 ± 0.298	0.190 ± 0.266	**0.145 ± 0.232**	0.649 ± 0.832	2.172 ± 1.909	3.146 ± 2.551
		V/A	0.213 ± 0.274	0.193 ± 0.269	**0.178 ± 0.332**	1.622 ± 1.468	2.827 ± 1.441	3.679 ± 2.159
		Q_p/A , V/A	0.203 ± 0.271	0.192 ± 0.268	**0.131 ± 0.217**	0.685 ± 0.817	2.070 ± 1.884	3.075 ± 2.475

Table A.6: Mean and standard deviation of catchments' ε_R for the estimations of Q_p and t_p using a similarity as $\bar{S}$ and using a TSP distribution

			mean ± std of catchments' ε_R					
			Similarity					
		Target	0.025	0.05	0.1	0.2	0.3	0.4
Estimations using the **mean** of the TSP parameters	Q_p	H_{PDF}	0.066 ± 0.074	0.059 ± 0.065	0.060 ± 0.068	0.049 ± 0.080	**0.026 ± 0.121**	0.038 ± 0.097
		α, β	0.061 ± 0.051	0.058 ± 0.046	0.059 ± 0.051	0.060 ± 0.095	**0.053 ± 0.085**	0.064 ± 0.235
		H_{PDF}, α, β	0.063 ± 0.050	0.061 ± 0.049	0.064 ± 0.063	0.057 ± 0.081	0.059 ± 0.102	**0.050 ± 0.165**
		H_{hy}	0.077 ± 0.096	0.071 ± 0.083	0.068 ± 0.074	**0.063 ± 0.109**	0.082 ± 0.146	0.085 ± 0.242
		PVR	0.081 ± 0.102	0.075 ± 0.089	0.071 ± 0.067	**0.065 ± 0.092**	0.069 ± 0.088	0.094 ± 0.154
		H_{hy}, PVR	0.077 ± 0.094	0.073 ± 0.084	0.068 ± 0.070	0.064 ± 0.089	**0.063 ± 0.129**	0.076 ± 0.229
		Sk, Ku	0.075 ± 0.080	0.071 ± 0.069	0.063 ± 0.063	0.059 ± 0.102	**0.054 ± 0.110**	0.061 ± 0.118
		PVR, Sk, Ku	0.073 ± 0.081	0.069 ± 0.071	0.065 ± 0.068	0.064 ± 0.121	**0.055 ± 0.094**	0.105 ± 0.181
		Q_p/A	0.085 ± 0.077	0.082 ± 0.075	0.079 ± 0.076	0.074 ± 0.105	**0.060 ± 0.099**	0.074 ± 0.125
		V/A	0.088 ± 0.126	0.085 ± 0.110	0.079 ± 0.109	**0.060 ± 0.093**	0.079 ± 0.134	0.098 ± 0.141
		Q_p/A, V/A	0.080 ± 0.068	0.076 ± 0.067	0.075 ± 0.071	**0.062 ± 0.078**	0.069 ± 0.106	0.073 ± 0.125
	t_p	H_{PDF}	0.253 ± 0.293	0.235 ± 0.260	0.218 ± 0.255	0.203 ± 0.229	0.233 ± 0.333	**0.090 ± 0.152**
		α, β	0.243 ± 0.274	0.233 ± 0.278	0.211 ± 0.275	0.193 ± 0.227	0.168 ± 0.191	**0.129 ± 0.267**
		H_{PDF}, α, β	0.238 ± 0.260	0.222 ± 0.252	0.211 ± 0.252	0.189 ± 0.194	0.173 ± 0.192	**0.132 ± 0.294**
		H_{hy}	0.264 ± 0.312	0.242 ± 0.276	0.232 ± 0.297	0.195 ± 0.207	0.160 ± 0.256	**0.157 ± 0.338**
		PVR	0.250 ± 0.278	0.230 ± 0.250	0.215 ± 0.264	0.179 ± 0.199	0.139 ± 0.261	**0.129 ± 0.212**
		H_{hy}, PVR	0.260 ± 0.290	0.236 ± 0.260	0.222 ± 0.264	0.173 ± 0.204	0.175 ± 0.294	**0.157 ± 0.382**
		Sk, Ku	0.249 ± 0.308	0.233 ± 0.278	0.227 ± 0.305	0.156 ± 0.170	0.154 ± 0.327	**0.106 ± 0.230**
		PVR, Sk, Ku	0.248 ± 0.316	0.233 ± 0.293	0.213 ± 0.289	0.159 ± 0.169	0.141 ± 0.255	**0.092 ± 0.176**
		Q_p/A	0.284 ± 0.260	0.275 ± 0.249	0.259 ± 0.242	0.261 ± 0.286	**0.230 ± 0.207**	0.253 ± 0.344
		V/A	0.246 ± 0.263	0.226 ± 0.248	0.192 ± 0.233	0.166 ± 0.181	0.120 ± 0.242	**0.119 ± 0.241**
		Q_p/A, V/A	0.285 ± 0.273	0.278 ± 0.254	0.258 ± 0.238	0.251 ± 0.329	**0.218 ± 0.190**	0.224 ± 0.231
Estimations using the **median** of the TSP parameters	Q_p	H_{PDF}	**-0.010 ± 0.067**	-0.031 ± 0.064	-0.127 ± 0.106	-0.454 ± 0.148	-0.629 ± 0.083	-0.660 ± 0.090
		α, β	**-0.012 ± 0.043**	-0.031 ± 0.044	-0.103 ± 0.070	-0.392 ± 0.134	-0.605 ± 0.113	-0.675 ± 0.090
		H_{PDF}, α, β	**-0.009 ± 0.045**	-0.028 ± 0.040	-0.094 ± 0.069	-0.388 ± 0.119	-0.608 ± 0.112	-0.672 ± 0.080
		H_{hy}	**-0.004 ± 0.085**	-0.022 ± 0.077	-0.109 ± 0.074	-0.454 ± 0.139	-0.605 ± 0.093	-0.654 ± 0.094
		PVR	**-0.007 ± 0.094**	-0.027 ± 0.082	-0.095 ± 0.085	-0.411 ± 0.155	-0.564 ± 0.166	-0.668 ± 0.103
		H_{hy}, PVR	**-0.003 ± 0.087**	-0.023 ± 0.075	-0.088 ± 0.068	-0.380 ± 0.119	-0.580 ± 0.139	-0.619 ± 0.146
		Sk, Ku	**-0.004 ± 0.074**	-0.025 ± 0.066	-0.112 ± 0.079	-0.431 ± 0.145	-0.585 ± 0.121	-0.657 ± 0.082
		PVR, Sk, Ku	**-0.008 ± 0.073**	-0.024 ± 0.062	-0.115 ± 0.095	-0.420 ± 0.144	-0.607 ± 0.126	-0.670 ± 0.094
		Q_p/A	**-0.015 ± 0.068**	-0.037 ± 0.053	-0.073 ± 0.067	-0.263 ± 0.156	-0.450 ± 0.195	-0.550 ± 0.187
		V/A	**-0.014 ± 0.109**	-0.035 ± 0.106	-0.132 ± 0.135	-0.429 ± 0.156	-0.581 ± 0.125	-0.626 ± 0.103
		Q_p/A, V/A	**-0.014 ± 0.065**	-0.036 ± 0.052	-0.074 ± 0.063	-0.246 ± 0.143	-0.448 ± 0.193	-0.553 ± 0.194
	t_p	H_{PDF}	0.138 ± 0.247	0.069 ± 0.201	**-0.004 ± 0.411**	-0.455 ± 0.486	-0.802 ± 0.388	-0.919 ± 0.292
		α, β	0.124 ± 0.240	0.068 ± 0.215	**0.031 ± 0.366**	-0.054 ± 0.757	-0.714 ± 0.444	-0.967 ± 0.095
		H_{PDF}, α, β	0.119 ± 0.224	0.053 ± 0.180	**-0.005 ± 0.242**	-0.220 ± 0.536	-0.787 ± 0.357	-0.960 ± 0.109
		H_{hy}	0.155 ± 0.291	0.086 ± 0.261	**-0.020 ± 0.378**	-0.268 ± 0.635	-0.683 ± 0.628	-0.921 ± 0.269
		PVR	0.138 ± 0.249	0.075 ± 0.209	-0.023 ± 0.286	**-0.013 ± 1.113**	-0.536 ± 0.918	-0.923 ± 0.247
		H_{hy}, PVR	0.143 ± 0.249	0.072 ± 0.214	**-0.018 ± 0.292**	0.040 ± 0.746	-0.643 ± 0.486	-0.652 ± 0.925
		Sk, Ku	0.138 ± 0.268	0.071 ± 0.233	**0.038 ± 0.354**	-0.207 ± 0.748	-0.704 ± 0.438	-0.882 ± 0.430
		PVR, Sk, Ku	0.136 ± 0.278	**0.079 ± 0.256**	-0.096 ± 0.249	-0.113 ± 1.112	-0.706 ± 0.411	-0.859 ± 0.430
		Q_p/A	0.122 ± 0.252	0.066 ± 0.249	**0.019 ± 0.259**	-0.147 ± 0.362	-0.365 ± 0.725	-0.559 ± 0.779
		V/A	0.124 ± 0.227	**0.048 ± 0.210**	-0.056 ± 0.298	-0.153 ± 0.629	-0.587 ± 0.757	-0.716 ± 0.690
		Q_p/A, V/A	0.130 ± 0.255	0.057 ± 0.166	**-0.028 ± 0.148**	-0.088 ± 0.343	-0.440 ± 0.584	-0.538 ± 0.820

A. Appendix

Table A.7: Mean and standard deviation of catchments' ε_R for the estimations of Q_p and t_p using a similarity as $\bar{S}$ and using a Lognormal distribution

			mean ± std of catchments' ε_R					
			Similarity					
		Target	**0.025**	**0.05**	**0.1**	**0.2**	**0.3**	**0.4**
Estimations using the **mean** of the Lognormal parameters	Q_p	H_{PDF}	-0.037 ± 0.066	-0.029 ± 0.060	**-0.005 ± 0.093**	0.033 ± 0.091	0.026 ± 0.082	0.036 ± 0.102
		α , β	-0.032 ± 0.069	-0.025 ± 0.059	**-0.005 ± 0.067**	0.036 ± 0.096	0.093 ± 0.158	0.047 ± 0.075
		H_{PDF}, α , β	-0.033 ± 0.068	-0.027 ± 0.061	**-0.008 ± 0.061**	0.036 ± 0.084	0.071 ± 0.148	0.057 ± 0.139
		H_{hy}	-0.039 ± 0.083	-0.035 ± 0.076	**-0.014 ± 0.073**	0.038 ± 0.143	0.067 ± 0.121	0.056 ± 0.131
		PVR	-0.036 ± 0.090	-0.029 ± 0.081	**-0.014 ± 0.071**	0.041 ± 0.110	0.052 ± 0.126	0.081 ± 0.162
		H_{hy} , PVR	-0.039 ± 0.082	-0.033 ± 0.073	**-0.017 ± 0.066**	0.036 ± 0.088	0.036 ± 0.069	0.050 ± 0.086
		Sk , Ku	-0.041 ± 0.070	-0.034 ± 0.065	**-0.014 ± 0.073**	0.018 ± 0.083	0.052 ± 0.113	0.081 ± 0.175
		PVR, Sk , Ku	-0.042 ± 0.070	-0.035 ± 0.063	**-0.017 ± 0.068**	0.017 ± 0.096	0.038 ± 0.112	0.082 ± 0.108
		Q_p/A	-0.041 ± 0.061	-0.037 ± 0.050	-0.027 ± 0.046	**0.002 ± 0.079**	0.019 ± 0.088	0.034 ± 0.036
		V/A	-0.037 ± 0.106	-0.027 ± 0.094	**-0.007 ± 0.090**	0.033 ± 0.087	0.080 ± 0.143	0.057 ± 0.095
		Q_p/A , V/A	-0.040 ± 0.064	-0.036 ± 0.052	-0.025 ± 0.047	**0.005 ± 0.074**	0.028 ± 0.080	0.047 ± 0.081
	t_p	H_{PDF}	0.157 ± 0.258	0.144 ± 0.225	0.149 ± 0.252	**0.142 ± 0.146**	0.189 ± 0.311	0.222 ± 0.401
		α , β	0.093 ± 0.168	0.079 ± 0.152	0.079 ± 0.161	0.080 ± 0.167	0.069 ± 0.204	**0.049 ± 0.204**
		H_{PDF}, α , β	0.097 ± 0.171	0.089 ± 0.171	0.095 ± 0.201	0.083 ± 0.163	0.054 ± 0.159	**0.012 ± 0.130**
		H_{hy}	0.174 ± 0.278	0.170 ± 0.256	0.159 ± 0.257	0.174 ± 0.207	**0.139 ± 0.291**	0.161 ± 0.440
		PVR	0.164 ± 0.265	0.151 ± 0.249	0.153 ± 0.279	0.127 ± 0.195	**0.114 ± 0.311**	0.214 ± 0.390
		H_{hy} , PVR	0.168 ± 0.262	0.157 ± 0.242	0.150 ± 0.237	**0.135 ± 0.198**	0.159 ± 0.303	0.170 ± 0.378
		Sk , Ku	0.168 ± 0.289	0.163 ± 0.277	0.162 ± 0.295	0.146 ± 0.212	0.167 ± 0.230	**0.101 ± 0.293**
		PVR, Sk , Ku	0.167 ± 0.284	0.162 ± 0.271	0.161 ± 0.314	0.128 ± 0.173	0.188 ± 0.336	**0.112 ± 0.255**
		Q_p/A	0.194 ± 0.270	0.197 ± 0.273	0.188 ± 0.264	0.201 ± 0.303	**0.185 ± 0.195**	0.217 ± 0.346
		V/A	0.159 ± 0.241	0.153 ± 0.235	0.138 ± 0.214	0.142 ± 0.202	0.119 ± 0.229	**0.113 ± 0.216**
		Q_p/A , V/A	0.181 ± 0.247	0.183 ± 0.247	**0.174 ± 0.247**	0.190 ± 0.289	0.200 ± 0.242	0.216 ± 0.355
Estimations using the **median** of the Lognormal parameters	Q_p	H_{PDF}	**0.058 ± 0.078**	0.142 ± 0.075	0.248 ± 0.231	-0.393 ± 0.394	-0.762 ± 0.240	-0.870 ± 0.122
		α , β	**0.052 ± 0.077**	0.134 ± 0.096	0.236 ± 0.208	-0.489 ± 0.311	-0.817 ± 0.131	-0.882 ± 0.102
		H_{PDF}, α , β	**0.053 ± 0.079**	0.130 ± 0.097	0.249 ± 0.201	-0.411 ± 0.298	-0.807 ± 0.129	-0.895 ± 0.104
		H_{hy}	**0.059 ± 0.102**	0.133 ± 0.098	0.303 ± 0.210	-0.388 ± 0.366	-0.799 ± 0.198	-0.888 ± 0.110
		PVR	**0.060 ± 0.100**	0.128 ± 0.088	0.271 ± 0.179	-0.326 ± 0.384	-0.719 ± 0.292	-0.879 ± 0.132
		H_{hy} , PVR	**0.061 ± 0.094**	0.134 ± 0.092	0.324 ± 0.183	-0.285 ± 0.364	-0.715 ± 0.273	-0.884 ± 0.104
		Sk , Ku	**0.053 ± 0.084**	0.127 ± 0.085	0.306 ± 0.227	-0.434 ± 0.321	-0.800 ± 0.172	-0.921 ± 0.031
		PVR, Sk , Ku	**0.054 ± 0.088**	0.132 ± 0.085	0.291 ± 0.228	-0.359 ± 0.356	-0.781 ± 0.216	-0.882 ± 0.104
		Q_p/A	**0.082 ± 0.087**	0.165 ± 0.099	0.312 ± 0.175	0.095 ± 0.316	-0.441 ± 0.445	-0.701 ± 0.377
		V/A	**0.057 ± 0.112**	0.138 ± 0.108	0.250 ± 0.220	-0.402 ± 0.343	-0.796 ± 0.167	-0.871 ± 0.158
		Q_p/A , V/A	**0.088 ± 0.096**	0.180 ± 0.121	0.351 ± 0.227	0.112 ± 0.337	-0.468 ± 0.398	-0.686 ± 0.398
	t_p	H_{PDF}	0.191 ± 0.278	**0.148 ± 0.229**	0.455 ± 0.930	2.286 ± 1.648	3.578 ± 2.137	3.695 ± 2.722
		α , β	0.122 ± 0.180	**0.087 ± 0.174**	0.358 ± 0.443	2.520 ± 1.695	3.612 ± 2.284	4.453 ± 2.062
		H_{PDF}, α , β	0.126 ± 0.192	**0.097 ± 0.177**	0.368 ± 0.577	2.273 ± 1.530	3.566 ± 2.180	3.902 ± 2.058
		H_{hy}	0.207 ± 0.302	**0.175 ± 0.266**	0.373 ± 0.778	2.453 ± 1.482	3.697 ± 2.459	4.189 ± 2.688
		PVR	0.193 ± 0.277	**0.149 ± 0.238**	0.273 ± 0.613	2.333 ± 1.692	3.346 ± 2.128	4.549 ± 2.646
		H_{hy} , PVR	0.195 ± 0.279	**0.151 ± 0.244**	0.193 ± 0.322	2.008 ± 1.514	3.405 ± 1.962	4.235 ± 2.311
		Sk , Ku	0.199 ± 0.305	**0.167 ± 0.286**	0.389 ± 0.868	2.605 ± 1.770	3.340 ± 1.939	4.201 ± 2.664
		PVR, Sk , Ku	0.197 ± 0.299	**0.166 ± 0.283**	0.432 ± 1.001	2.254 ± 1.589	3.662 ± 2.252	4.098 ± 2.619
		Q_p/A	0.205 ± 0.274	0.189 ± 0.288	**0.176 ± 0.327**	1.097 ± 1.157	2.503 ± 1.617	3.361 ± 2.378
		V/A	0.199 ± 0.255	**0.157 ± 0.243**	0.403 ± 0.665	2.461 ± 1.708	3.438 ± 2.060	3.694 ± 2.373
		Q_p/A , V/A	0.201 ± 0.283	0.153 ± 0.217	**0.105 ± 0.198**	1.036 ± 1.191	2.882 ± 2.292	3.245 ± 2.357

Table A.8: Mean and standard deviation of catchments' ε_R for the estimations of Q_p and t_p using a similarity as CO and using a TSP distribution

			mean ± std of catchments' ε_R					
			Similarity					
		Target	**0.025**	**0.05**	**0.1**	**0.2**	**0.3**	**0.4**
Estimations using the **mean** of the TSP parameters	Q_p	H_{PDF}	0.085 ± 0.121	0.079 ± 0.114	0.081 ± 0.109	0.076 ± 0.103	0.074 ± 0.104	**0.065 ± 0.097**
		α , β	0.072 ± 0.108	0.068 ± 0.106	0.068 ± 0.107	0.071 ± 0.115	0.068 ± 0.108	**0.068 ± 0.098**
		H_{PDF}, α , β	0.072 ± 0.101	0.070 ± 0.099	0.065 ± 0.097	**0.064 ± 0.099**	0.068 ± 0.098	0.067 ± 0.090
		H_{hy}	0.090 ± 0.137	0.088 ± 0.132	0.086 ± 0.128	**0.086 ± 0.123**	0.091 ± 0.125	0.086 ± 0.129
		PVR	0.101 ± 0.148	0.096 ± 0.146	0.096 ± 0.145	0.093 ± 0.138	**0.087 ± 0.128**	0.110 ± 0.150
		H_{hy} , PVR	0.091 ± 0.130	0.090 ± 0.128	0.086 ± 0.126	0.086 ± 0.121	0.080 ± 0.115	**0.078 ± 0.117**
		Sk , Ku	0.085 ± 0.108	0.083 ± 0.106	0.079 ± 0.099	0.080 ± 0.099	0.075 ± 0.094	**0.064 ± 0.088**
		PVR, Sk , Ku	0.089 ± 0.111	0.088 ± 0.109	0.085 ± 0.106	0.080 ± 0.103	0.073 ± 0.100	**0.068 ± 0.107**
		Q_p/A	0.100 ± 0.158	0.095 ± 0.160	0.095 ± 0.159	0.100 ± 0.157	0.098 ± 0.142	**0.086 ± 0.128**
		V/A	0.108 ± 0.183	0.101 ± 0.178	0.094 ± 0.173	0.090 ± 0.164	0.083 ± 0.152	**0.081 ± 0.145**
		Q_p/A , V/A	0.097 ± 0.145	0.098 ± 0.146	0.098 ± 0.161	0.101 ± 0.155	0.099 ± 0.144	**0.088 ± 0.128**
	t_p	H_{PDF}	0.319 ± 0.410	0.320 ± 0.413	0.307 ± 0.396	**0.281 ± 0.331**	0.292 ± 0.366	0.299 ± 0.361
		α , β	0.335 ± 0.405	0.327 ± 0.399	0.296 ± 0.387	0.305 ± 0.452	0.242 ± 0.374	**0.221 ± 0.355**
		H_{PDF}, α , β	0.333 ± 0.412	0.330 ± 0.409	0.331 ± 0.422	0.329 ± 0.438	0.242 ± 0.333	**0.218 ± 0.339**
		H_{hy}	0.321 ± 0.428	0.322 ± 0.430	0.318 ± 0.417	0.309 ± 0.401	0.273 ± 0.405	**0.244 ± 0.360**
		PVR	0.326 ± 0.424	0.332 ± 0.421	0.317 ± 0.405	0.318 ± 0.404	0.298 ± 0.388	**0.264 ± 0.426**
		H_{hy} , PVR	0.318 ± 0.417	0.323 ± 0.425	0.332 ± 0.443	0.347 ± 0.479	0.290 ± 0.413	**0.272 ± 0.365**
		Sk , Ku	0.314 ± 0.423	0.309 ± 0.407	0.294 ± 0.388	0.258 ± 0.369	0.265 ± 0.390	**0.223 ± 0.331**
		PVR, Sk , Ku	0.311 ± 0.401	0.303 ± 0.401	0.304 ± 0.402	0.265 ± 0.340	**0.256 ± 0.340**	0.266 ± 0.400
		Q_p/A	0.420 ± 0.430	0.416 ± 0.422	0.412 ± 0.415	0.392 ± 0.391	0.392 ± 0.357	**0.384 ± 0.360**
		V/A	0.294 ± 0.323	0.295 ± 0.318	0.294 ± 0.314	0.284 ± 0.295	0.271 ± 0.276	**0.221 ± 0.246**
		Q_p/A , V/A	0.405 ± 0.404	0.397 ± 0.389	0.394 ± 0.380	0.387 ± 0.373	**0.385 ± 0.349**	0.385 ± 0.379
Estimations using the **median** of the TSP parameters	Q_p	H_{PDF}	0.003 ± 0.111	**-0.002 ± 0.106**	-0.006 ± 0.103	-0.018 ± 0.105	-0.037 ± 0.123	-0.092 ± 0.142
		α , β	**-0.004 ± 0.099**	-0.005 ± 0.098	-0.011 ± 0.101	-0.033 ± 0.098	-0.048 ± 0.097	-0.065 ± 0.123
		H_{PDF}, α , β	0.002 ± 0.090	**0.001 ± 0.088**	-0.009 ± 0.090	-0.020 ± 0.101	-0.050 ± 0.130	-0.087 ± 0.135
		H_{hy}	0.014 ± 0.130	0.011 ± 0.125	**0.002 ± 0.120**	-0.020 ± 0.119	-0.059 ± 0.145	-0.089 ± 0.175
		PVR	0.007 ± 0.134	0.004 ± 0.130	**-0.001 ± 0.127**	-0.015 ± 0.123	-0.048 ± 0.119	-0.089 ± 0.133
		H_{hy} , PVR	0.006 ± 0.119	0.005 ± 0.115	**-0.003 ± 0.116**	-0.028 ± 0.121	-0.050 ± 0.114	-0.088 ± 0.142
		Sk , Ku	0.009 ± 0.099	0.008 ± 0.099	**0.001 ± 0.092**	-0.022 ± 0.094	-0.045 ± 0.101	-0.121 ± 0.139
		PVR, Sk , Ku	0.002 ± 0.100	**0.000 ± 0.100**	-0.009 ± 0.100	-0.030 ± 0.100	-0.052 ± 0.103	-0.093 ± 0.139
		Q_p/A	**-0.004 ± 0.148**	-0.009 ± 0.148	-0.009 ± 0.146	-0.010 ± 0.138	-0.031 ± 0.117	-0.046 ± 0.106
		V/A	0.010 ± 0.167	0.004 ± 0.163	**-0.003 ± 0.157**	-0.027 ± 0.146	-0.053 ± 0.136	-0.116 ± 0.155
		Q_p/A , V/A	-0.004 ± 0.138	**0.001 ± 0.137**	-0.005 ± 0.139	-0.009 ± 0.132	-0.017 ± 0.119	-0.037 ± 0.122
	t_p	H_{PDF}	0.198 ± 0.379	0.190 ± 0.376	0.172 ± 0.353	0.139 ± 0.294	0.103 ± 0.347	**-0.026 ± 0.375**
		α , β	0.205 ± 0.363	0.189 ± 0.351	0.148 ± 0.347	0.096 ± 0.370	0.066 ± 0.360	**0.000 ± 0.318**
		H_{PDF}, α , β	0.219 ± 0.383	0.206 ± 0.362	0.162 ± 0.371	0.116 ± 0.344	0.038 ± 0.334	**-0.028 ± 0.365**
		H_{hy}	0.226 ± 0.414	0.223 ± 0.415	0.213 ± 0.393	0.171 ± 0.358	0.051 ± 0.423	**-0.042 ± 0.311**
		PVR	0.217 ± 0.396	0.223 ± 0.392	0.184 ± 0.361	0.168 ± 0.347	0.107 ± 0.354	**0.010 ± 0.394**
		H_{hy} , PVR	0.223 ± 0.392	0.222 ± 0.398	0.223 ± 0.420	0.191 ± 0.458	0.097 ± 0.409	**0.013 ± 0.422**
		Sk , Ku	0.206 ± 0.388	0.200 ± 0.373	0.168 ± 0.344	0.091 ± 0.303	**0.057 ± 0.346**	-0.093 ± 0.304
		PVR, Sk , Ku	0.205 ± 0.376	0.191 ± 0.369	0.143 ± 0.324	0.098 ± 0.284	0.112 ± 0.441	**0.005 ± 0.320**
		Q_p/A	0.270 ± 0.396	0.259 ± 0.390	0.246 ± 0.384	0.214 ± 0.358	0.175 ± 0.292	**0.129 ± 0.306**
		V/A	0.203 ± 0.310	0.204 ± 0.306	0.199 ± 0.289	0.158 ± 0.278	0.126 ± 0.307	**-0.094 ± 0.306**
		Q_p/A , V/A	0.254 ± 0.370	0.234 ± 0.357	0.216 ± 0.344	0.190 ± 0.332	0.163 ± 0.302	**0.121 ± 0.283**

Table A.9: Mean and standard deviation of catchments' ε_R for the estimations of Q_p and t_p using a similarity as CO and using a Lognromal distribution

			mean ± std of catchments' ε_R					
			Similarity					
		Target	**0.025**	**0.05**	**0.1**	**0.2**	**0.3**	**0.4**
Estimations using the **mean** of the Lognormal parameters	Q_p	H_{PDF}	-0.044 ± 0.118	-0.043 ± 0.118	-0.042 ± 0.115	-0.038 ± 0.109	-0.032 ± 0.101	**-0.014 ± 0.089**
		α , β	-0.038 ± 0.096	-0.034 ± 0.091	-0.029 ± 0.085	-0.022 ± 0.086	-0.018 ± 0.086	**-0.002 ± 0.087**
		H_{PDF}, α , β	-0.036 ± 0.103	-0.034 ± 0.099	-0.030 ± 0.093	-0.029 ± 0.083	-0.022 ± 0.084	**-0.004 ± 0.075**
		H_{hy}	-0.036 ± 0.124	-0.036 ± 0.121	-0.034 ± 0.113	-0.026 ± 0.110	-0.018 ± 0.112	**-0.009 ± 0.116**
		PVR	-0.036 ± 0.135	-0.036 ± 0.133	-0.036 ± 0.135	-0.032 ± 0.131	-0.028 ± 0.122	**-0.014 ± 0.096**
		H_{hy} , PVR	-0.045 ± 0.109	-0.044 ± 0.105	-0.040 ± 0.102	-0.039 ± 0.085	-0.032 ± 0.083	**-0.029 ± 0.076**
		Sk , Ku	-0.044 ± 0.093	-0.041 ± 0.096	-0.036 ± 0.095	-0.033 ± 0.093	-0.027 ± 0.087	**-0.012 ± 0.083**
		PVR, Sk , Ku	-0.039 ± 0.092	-0.038 ± 0.089	-0.032 ± 0.090	-0.026 ± 0.089	-0.027 ± 0.086	**-0.016 ± 0.085**
		Q_p/A	-0.041 ± 0.142	-0.039 ± 0.142	-0.039 ± 0.139	-0.036 ± 0.135	**-0.027 ± 0.123**	-0.029 ± 0.104
		V/A	-0.029 ± 0.155	-0.034 ± 0.148	-0.037 ± 0.141	-0.032 ± 0.141	-0.023 ± 0.139	**-0.008 ± 0.136**
		Q_p/A , V/A	-0.041 ± 0.143	-0.044 ± 0.134	-0.040 ± 0.133	**-0.033 ± 0.127**	-0.034 ± 0.106	-0.036 ± 0.098
	t_p	H_{PDF}	0.213 ± 0.345	0.215 ± 0.339	0.223 ± 0.346	0.215 ± 0.334	0.190 ± 0.326	**0.159 ± 0.254**
		α , β	0.183 ± 0.331	0.176 ± 0.310	0.157 ± 0.276	0.143 ± 0.228	0.105 ± 0.185	**0.085 ± 0.187**
		H_{PDF}, α , β	0.170 ± 0.296	0.166 ± 0.270	0.149 ± 0.250	0.139 ± 0.243	0.128 ± 0.207	**0.124 ± 0.186**
		H_{hy}	0.222 ± 0.410	0.229 ± 0.407	0.227 ± 0.400	0.214 ± 0.379	0.204 ± 0.350	**0.169 ± 0.243**
		PVR	0.228 ± 0.398	0.230 ± 0.400	0.233 ± 0.411	0.198 ± 0.402	**0.185 ± 0.381**	0.188 ± 0.343
		H_{hy} , PVR	0.231 ± 0.391	0.229 ± 0.394	0.232 ± 0.404	0.249 ± 0.425	0.248 ± 0.477	**0.214 ± 0.313**
		Sk , Ku	0.215 ± 0.386	0.215 ± 0.379	0.190 ± 0.349	0.189 ± 0.337	0.168 ± 0.298	**0.160 ± 0.339**
		PVR, Sk , Ku	0.212 ± 0.357	0.212 ± 0.348	0.219 ± 0.342	0.199 ± 0.294	**0.191 ± 0.272**	0.192 ± 0.291
		Q_p/A	0.279 ± 0.391	0.282 ± 0.389	**0.276 ± 0.372**	0.276 ± 0.374	0.276 ± 0.366	0.276 ± 0.360
		V/A	0.200 ± 0.306	0.207 ± 0.299	0.211 ± 0.299	0.202 ± 0.285	0.203 ± 0.291	**0.187 ± 0.263**
		Q_p/A , V/A	0.273 ± 0.375	0.268 ± 0.352	0.270 ± 0.380	**0.259 ± 0.371**	0.268 ± 0.361	0.270 ± 0.376
Estimations using the **median** of the Lognormal parameters	Q_p	H_{PDF}	**0.037 ± 0.121**	0.045 ± 0.125	0.056 ± 0.127	0.058 ± 0.131	0.079 ± 0.147	0.081 ± 0.187
		α , β	0.035 ± 0.102	0.047 ± 0.099	0.067 ± 0.107	0.077 ± 0.105	0.046 ± 0.165	**0.001 ± 0.277**
		H_{PDF}, α , β	0.035 ± 0.115	0.043 ± 0.112	0.060 ± 0.110	0.074 ± 0.124	0.070 ± 0.188	**-0.028 ± 0.284**
		H_{hy}	**0.038 ± 0.135**	0.043 ± 0.133	0.061 ± 0.130	0.077 ± 0.120	0.073 ± 0.165	0.056 ± 0.232
		PVR	**0.052 ± 0.146**	0.061 ± 0.146	0.076 ± 0.153	0.074 ± 0.164	0.096 ± 0.190	0.096 ± 0.194
		H_{hy} , PVR	**0.039 ± 0.114**	0.053 ± 0.115	0.077 ± 0.129	0.079 ± 0.126	0.052 ± 0.123	0.079 ± 0.228
		Sk , Ku	**0.039 ± 0.099**	0.049 ± 0.103	0.054 ± 0.105	0.069 ± 0.110	0.064 ± 0.112	0.087 ± 0.183
		PVR, Sk , Ku	0.039 ± 0.100	0.046 ± 0.101	0.069 ± 0.111	0.076 ± 0.122	0.036 ± 0.143	**-0.004 ± 0.169**
		Q_p/A	**0.023 ± 0.159**	0.041 ± 0.162	0.050 ± 0.160	0.069 ± 0.161	0.101 ± 0.169	0.118 ± 0.171
		V/A	**0.024 ± 0.164**	0.031 ± 0.160	0.039 ± 0.162	0.029 ± 0.170	0.057 ± 0.198	0.068 ± 0.216
		Q_p/A , V/A	**0.032 ± 0.163**	0.046 ± 0.159	0.064 ± 0.158	0.102 ± 0.173	0.125 ± 0.189	0.118 ± 0.193
	t_p	H_{PDF}	0.247 ± 0.365	**0.241 ± 0.347**	0.248 ± 0.350	0.382 ± 0.770	0.309 ± 0.370	0.572 ± 0.973
		α , β	0.225 ± 0.356	0.211 ± 0.332	**0.193 ± 0.306**	0.389 ± 0.828	0.543 ± 0.821	0.915 ± 1.280
		H_{PDF}, α , β	0.216 ± 0.322	0.210 ± 0.298	**0.193 ± 0.264**	0.301 ± 0.482	0.489 ± 0.842	0.751 ± 1.062
		H_{hy}	0.264 ± 0.416	0.266 ± 0.417	**0.256 ± 0.411**	0.295 ± 0.444	0.467 ± 0.861	0.596 ± 0.943
		PVR	0.260 ± 0.415	0.257 ± 0.415	**0.256 ± 0.425**	0.267 ± 0.401	0.340 ± 0.533	0.463 ± 0.548
		H_{hy} , PVR	0.259 ± 0.394	0.254 ± 0.396	**0.251 ± 0.398**	0.381 ± 0.898	0.433 ± 0.653	0.678 ± 1.121
		Sk , Ku	0.249 ± 0.390	0.329 ± 0.772	**0.228 ± 0.361**	0.282 ± 0.482	0.385 ± 0.685	0.514 ± 0.501
		PVR, Sk , Ku	0.250 ± 0.371	**0.246 ± 0.365**	0.259 ± 0.357	0.368 ± 0.781	0.584 ± 0.905	0.826 ± 1.157
		Q_p/A	0.322 ± 0.428	0.314 ± 0.410	**0.296 ± 0.378**	0.298 ± 0.389	0.314 ± 0.428	0.334 ± 0.452
		V/A	0.267 ± 0.322	**0.267 ± 0.317**	0.274 ± 0.325	0.335 ± 0.404	0.394 ± 0.521	0.557 ± 0.777
		Q_p/A , V/A	0.315 ± 0.414	0.300 ± 0.393	0.288 ± 0.385	**0.271 ± 0.385**	0.297 ± 0.425	0.377 ± 0.521

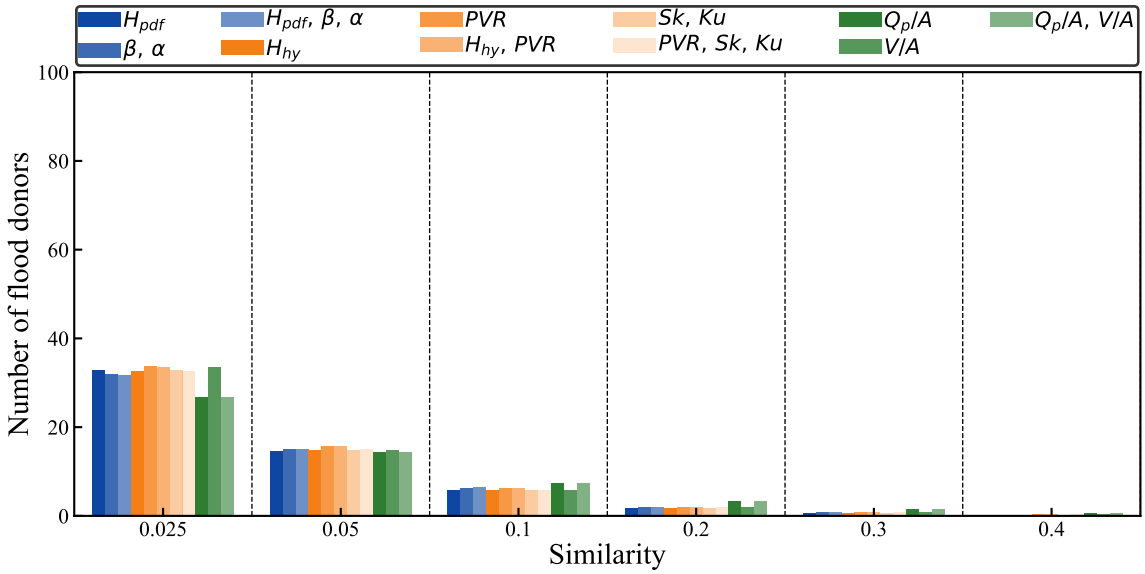

Figure A.2: Number of flood donors selected according to different similarity thresholds using $\bar{S}$ as the similarity matrix.

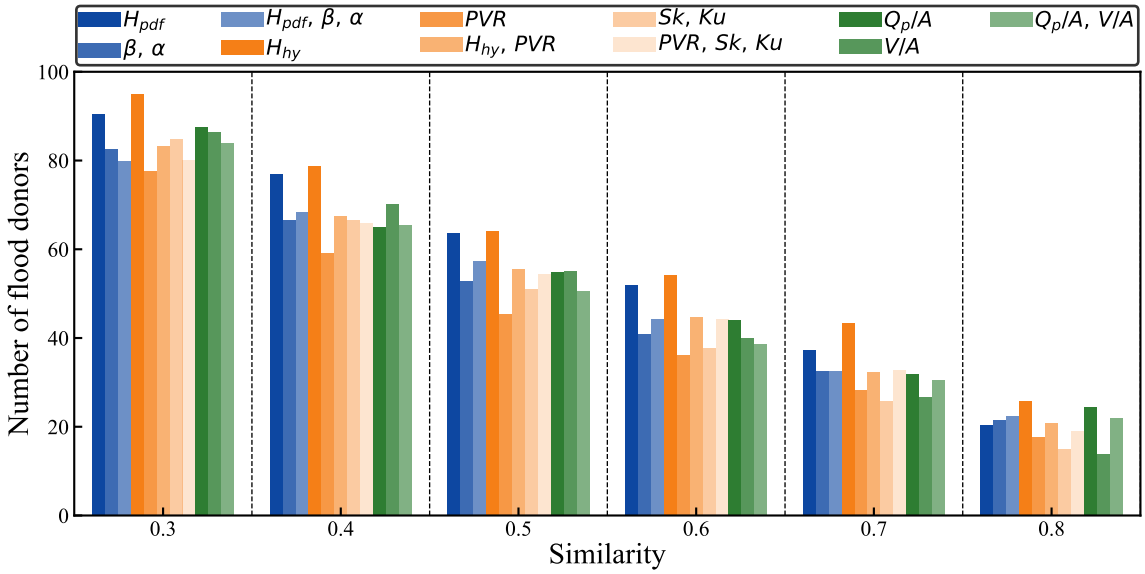

Figure A.3: Number of flood donors selected according to different similarity thresholds using CO as the similarity matrix.

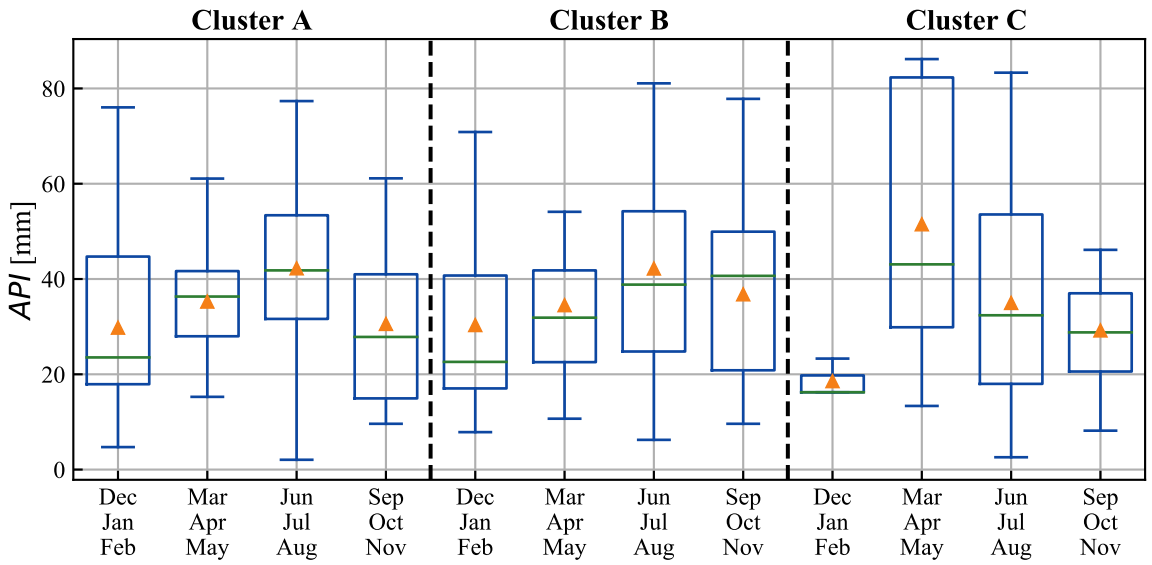

Figure A.4: Similarity of the API triggering a 1POT according to a supervised RF trained to estimate the parameters of the fitted PDF (H_{PDF}, α, β). Each box constructed with the events belonging to one cluster and one season.

Institut für Wasser- und Umweltsystemmodellierung
Universität Stuttgart

Pfaffenwaldring 61
70569 Stuttgart (Vaihingen)
Telefon (0711) 685 - 60156
Telefax (0711) 685 - 51073
E-Mail: iws@iws.uni-stuttgart.de
http://www.iws.uni-stuttgart.de

Verzeichnis der Mitteilungshefte

5 Plate, Erich: *Beitrag zur Bestimmung der Windgeschwindigkeitsverteilung in der durch eine Wand gestörten bodennahen Luftschicht*, und Röhnisch, Arthur; Marotz, Günter: *Neue Baustoffe und Bauausführungen für den Schutz der Böschungen und der Sohle von Kanälen, Flüssen und Häfen; Gestehungskosten und jeweilige Vorteile*, sowie Unny, T.E.: *Schwingungsuntersuchungen am Kegelstrahlschieber*, 1967

6 Seiler, Erich: *Die Ermittlung des Anlagenwertes der bundeseigenen Binnenschiffahrtsstraßen und Talsperren und des Anteils der Binnenschiffahrt an diesem Wert*, 1967

7 *Sonderheft anläßlich des 65. Geburtstages von Prof. Arthur Röhnisch mit Beiträgen von* Benk, Dieter; Breitling, J.; Gurr, Siegfried; Haberhauer, Robert; Honekamp, Hermann; Kuz, Klaus Dieter; Marotz, Günter; Mayer-Vorfelder, Hans-Jörg; Miller, Rudolf; Plate, Erich J.; Radomski, Helge; Schwarz, Helmut; Vollmer, Ernst; Wildenhahn, Eberhard; 1967

8 Jumikis, Alfred: *Beitrag zur experimentellen Untersuchung des Wassernachschubs in einem gefrierenden Boden und die Beurteilung der Ergebnisse*, 1968

9 Marotz, Günter: *Technische Grundlagen einer Wasserspeicherung im natürlichen Untergrund*, 1968

10 Radomski, Helge: *Untersuchungen über den Einfluß der Querschnittsform wellenförmiger Spundwände auf die statischen und rammtechnischen Eigenschaften*, 1968

11 Schwarz, Helmut: *Die Grenztragfähigkeit des Baugrundes bei Einwirkung vertikal gezogener Ankerplatten als zweidimensionales Bruchproblem*, 1969

12 Erbel, Klaus: *Ein Beitrag zur Untersuchung der Metamorphose von Mittelgebirgsschneedecken unter besonderer Berücksichtigung eines Verfahrens zur Bestimmung der thermischen Schneequalität*, 1969

13 Westhaus, Karl-Heinz: *Der Strukturwandel in der Binnenschiffahrt und sein Einfluß auf den Ausbau der Binnenschiffskanäle*, 1969

14 Mayer-Vorfelder, Hans-Jörg: *Ein Beitrag zur Berechnung des Erdwiderstandes unter Ansatz der logarithmischen Spirale als Gleitflächenfunktion*, 1970

15 Schulz, Manfred: *Berechnung des räumlichen Erddruckes auf die Wandung kreiszylindrischer Körper*, 1970

16 Mobasseri, Manoutschehr: *Die Rippenstützmauer. Konstruktion und Grenzen ihrer Standsicherheit*, 1970

17 Benk, Dieter: *Ein Beitrag zum Betrieb und zur Bemessung von Hochwasserrückhaltebecken*, 1970

18 Gàl, Attila: *Bestimmung der mitschwingenden Wassermasse bei überströmten Fischbauchklappen mit kreiszylindrischem Staublech*, 1971, vergriffen

19 Kuz, Klaus Dieter: *Ein Beitrag zur Frage des Einsetzens von Kavitationserscheinungen in einer Düsenströmung bei Berücksichtigung der im Wasser gelösten Gase*, 1971, vergriffen

20 Schaak, Hartmut: *Verteilleitungen von Wasserkraftanlagen*, 1971

21 *Sonderheft zur Eröffnung der neuen Versuchsanstalt des Instituts für Wasserbau der Universität Stuttgart mit Beiträgen von* Brombach, Hansjörg; Dirksen, Wolfram; Gàl, Attila; Gerlach, Reinhard; Giesecke, Jürgen; Holthoff, Franz-Josef; Kuz, Klaus Dieter; Marotz, Günter; Minor, Hans-Erwin; Petrikat, Kurt; Röhnisch, Arthur; Rueff, Helge; Schwarz, Helmut; Vollmer, Ernst; Wildenhahn, Eberhard; 1972

22 Wang, Chung-su: *Ein Beitrag zur Berechnung der Schwingungen an Kegelstrahlschiebern*, 1972

23 Mayer-Vorfelder, Hans-Jörg: *Erdwiderstandsbeiwerte nach dem Ohde-Variationsverfahren*, 1972

24 Minor, Hans-Erwin: *Beitrag zur Bestimmung der Schwingungsanfachungsfunktionen überströmter Stauklappen*, 1972, vergriffen

25 Brombach, Hansjörg: *Untersuchung strömungsmechanischer Elemente (Fluidik) und die Möglichkeit der Anwendung von Wirbelkammerelementen im Wasserbau*, 1972, vergriffen

26 Wildenhahn, Eberhard: *Beitrag zur Berechnung von Horizontalfilterbrunnen*, 1972

27 Steinlein, Helmut: *Die Eliminierung der Schwebstoffe aus Flußwasser zum Zweck der unterirdischen Wasserspeicherung, gezeigt am Beispiel der Iller*, 1972

28 Holthoff, Franz Josef: *Die Überwindung großer Hubhöhen in der Binnenschiffahrt durch Schwimmerhebewerke*, 1973

29 Röder, Karl: *Einwirkungen aus Baugrundbewegungen auf trog- und kastenförmige Konstruktionen des Wasser- und Tunnelbaues*, 1973

30 Kretschmer, Heinz: *Die Bemessung von Bogenstaumauern in Abhängigkeit von der Talform*, 1973

31 Honekamp, Hermann: *Beitrag zur Berechnung der Montage von Unterwasserpipelines*, 1973

32 Giesecke, Jürgen: *Die Wirbelkammertriode als neuartiges Steuerorgan im Wasserbau*, und Brombach, Hansjörg: *Entwicklung, Bauformen, Wirkungsweise und Steuereigenschaften von Wirbelkammerverstärkern*, 1974

33 Rueff, Helge: *Untersuchung der schwingungserregenden Kräfte an zwei hintereinander angeordneten Tiefschützen unter besonderer Berücksichtigung von Kavitation*, 1974

34 Röhnisch, Arthur: *Einpreßversuche mit Zementmörtel für Spannbeton - Vergleich der Ergebnisse von Modellversuchen mit Ausführungen in Hüllwellrohren*, 1975

35 *Sonderheft anläßlich des 65. Geburtstages von Prof. Dr.-Ing. Kurt Petrikat mit Beiträgen von*: Brombach, Hansjörg; Erbel, Klaus; Flinspach, Dieter; Fischer jr., Richard; Gàl, Attila; Gerlach, Reinhard; Giesecke, Jürgen; Haberhauer, Robert; Hafner Edzard; Hausenblas, Bernhard; Horlacher, Hans-Burkhard; Hutarew, Andreas; Knoll, Manfred; Krummet, Ralph; Marotz, Günter; Merkle, Theodor; Miller, Christoph; Minor, Hans-Erwin; Neumayer, Hans; Rao, Syamala; Rath, Paul; Rueff, Helge; Ruppert, Jürgen; Schwarz, Wolfgang; Topal-Gökceli, Mehmet; Vollmer, Ernst; Wang, Chung-su; Weber, Hans-Georg; 1975

36 Berger, Jochum: *Beitrag zur Berechnung des Spannungszustandes in rotationssymmetrisch belasteten Kugelschalen veränderlicher Wandstärke unter Gas- und Flüssigkeitsdruck durch Integration schwach singulärer Differentialgleichungen*, 1975

37 Dirksen, Wolfram: *Berechnung instationärer Abflußvorgänge in gestauten Gerinnen mittels Differenzenverfahren und die Anwendung auf Hochwasserrückhaltebecken*, 1976

38 Horlacher, Hans-Burkhard: *Berechnung instationärer Temperatur- und Wärmespannungsfelder in langen mehrschichtigen Hohlzylindern*, 1976

39 Hafner, Edzard: *Untersuchung der hydrodynamischen Kräfte auf Baukörper im Tiefwasserbereich des Meeres*, 1977, ISBN 3-921694-39-6

40 Ruppert, Jürgen: *Über den Axialwirbelkammerverstärker für den Einsatz im Wasserbau*, 1977, ISBN 3-921694-40-X

41 Hutarew, Andreas: *Beitrag zur Beeinflußbarkeit des Sauerstoffgehalts in Fließgewässern an Abstürzen und Wehren*, 1977, ISBN 3-921694-41-8, vergriffen

42 Miller, Christoph: *Ein Beitrag zur Bestimmung der schwingungserregenden Kräfte an unterströmten Wehren*, 1977, ISBN 3-921694-42-6

43 Schwarz, Wolfgang: *Druckstoßberechnung unter Berücksichtigung der Radial- und Längsverschiebungen der Rohrwandung*, 1978, ISBN 3-921694-43-4

44 Kinzelbach, Wolfgang: *Numerische Untersuchungen über den optimalen Einsatz variabler Kühlsysteme einer Kraftwerkskette am Beispiel Oberrhein*, 1978, ISBN 3-921694-44-2

45 Barczewski, Baldur: *Neue Meßmethoden für Wasser-Luftgemische und deren Anwendung auf zweiphasige Auftriebsstrahlen*, 1979, ISBN 3-921694-45-0

46 Neumayer, Hans: *Untersuchung der Strömungsvorgänge in radialen Wirbelkammerverstärkern*, 1979, ISBN 3-921694-46-9

47 Elalfy, Youssef-Elhassan: *Untersuchung der Strömungsvorgänge in Wirbelkammerdioden und -drosseln*, 1979, ISBN 3-921694-47-7

48 Brombach, Hansjörg: *Automatisierung der Bewirtschaftung von Wasserspeichern*, 1981, ISBN 3-921694-48-5

49 Geldner, Peter: *Deterministische und stochastische Methoden zur Bestimmung der Selbstdichtung von Gewässern*, 1981, ISBN 3-921694-49-3, *vergriffen*

50 Mehlhorn, Hans: *Temperaturveränderungen im Grundwasser durch Brauchwassereinleitungen*, 1982, ISBN 3-921694-50-7, *vergriffen*

51 Hafner, Edzard: *Rohrleitungen und Behälter im Meer*, 1983, ISBN 3-921694-51-5

52 Rinnert, Bernd: *Hydrodynamische Dispersion in porösen Medien: Einfluß von Dichteunterschieden auf die Vertikalvermischung in horizontaler Strömung*, 1983, ISBN 3-921694-52-3, *vergriffen*

53 Lindner, Wulf: *Steuerung von Grundwasserentnahmen unter Einhaltung ökologischer Kriterien*, 1983, ISBN 3-921694-53-1, *vergriffen*

54 Herr, Michael; Herzer, Jörg; Kinzelbach, Wolfgang; Kobus, Helmut; Rinnert, Bernd: *Methoden zur rechnerischen Erfassung und hydraulischen Sanierung von Grundwasserkontaminationen*, 1983, ISBN 3-921694-54-X

55 Schmitt, Paul: *Wege zur Automatisierung der Niederschlagsermittlung*, 1984, ISBN 3-921694-55-8, *vergriffen*

56 Müller, Peter: *Transport und selektive Sedimentation von Schwebstoffen bei gestautem Abfluß*, 1985, ISBN 3-921694-56-6

57 El-Qawasmeh, Fuad: *Möglichkeiten und Grenzen der Tropfbewässerung unter besonderer Berücksichtigung der Verstopfungsanfälligkeit der Tropfelemente*, 1985, ISBN 3-921694-57-4, *vergriffen*

58 Kirchenbaur, Klaus: *Mikroprozessorgesteuerte Erfassung instationärer Druckfelder am Beispiel seegangsbelasteter Baukörper*, 1985, ISBN 3-921694-58-2

59 Kobus, Helmut (Hrsg.): *Modellierung des großräumigen Wärme- und Schadstofftransports im Grundwasser*, Tätigkeitsbericht 1984/85 (DFG-Forschergruppe an den Universitäten Hohenheim, Karlsruhe und Stuttgart), 1985, ISBN 3-921694-59-0, *vergriffen*

60 Spitz, Karlheinz: *Dispersion in porösen Medien: Einfluß von Inhomogenitäten und Dichteunterschieden*, 1985, ISBN 3-921694-60-4, *vergriffen*

61 Kobus, Helmut: *An Introduction to Air-Water Flows in Hydraulics*, 1985, ISBN 3-921694-61-2

62 Kaleris, Vassilios: *Erfassung des Austausches von Oberflächen- und Grundwasser in horizontalebenen Grundwassermodellen*, 1986, ISBN 3-921694-62-0

63 Herr, Michael: *Grundlagen der hydraulischen Sanierung verunreinigter Porengrundwasserleiter*, 1987, ISBN 3-921694-63-9

64 Marx, Walter: *Berechnung von Temperatur und Spannung in Massenbeton infolge Hydratation*, 1987, ISBN 3-921694-64-7

65 Koschitzky, Hans-Peter: *Dimensionierungskonzept für Sohlbelüfter in Schußrinnen zur Vermeidung von Kavitationsschäden*, 1987, ISBN 3-921694-65-5

66 Kobus, Helmut (Hrsg.): *Modellierung des großräumigen Wärme- und Schadstofftransports im Grundwasser*, Tätigkeitsbericht 1986/87 (DFG-Forschergruppe an den Universitäten Hohenheim, Karlsruhe und Stuttgart) 1987, ISBN 3-921694-66-3

67 Söll, Thomas: *Berechnungsverfahren zur Abschätzung anthropogener Temperaturanomalien im Grundwasser*, 1988, ISBN 3-921694-67-1

68 Dittrich, Andreas; Westrich, Bernd: *Bodenseeufererosion, Bestandsaufnahme und Bewertung*, 1988, ISBN 3-921694-68-X, *vergriffen*

69 Huwe, Bernd; van der Ploeg, Rienk R.: *Modelle zur Simulation des Stickstoffhaushaltes von Standorten mit unterschiedlicher landwirtschaftlicher Nutzung*, 1988, ISBN 3-921694-69-8, *vergriffen*

70 Stephan, Karl: *Integration elliptischer Funktionen*, 1988, ISBN 3-921694-70-1

71 Kobus, Helmut; Zilliox, Lothaire (Hrsg.): *Nitratbelastung des Grundwassers, Auswirkungen der Landwirtschaft auf die Grundwasser- und Rohwasserbeschaffenheit und Maßnahmen zum Schutz des Grundwassers*. Vorträge des deutsch-französischen Kolloquiums am 6. Oktober 1988, Universitäten Stuttgart und Louis Pasteur Strasbourg (Vorträge in deutsch oder französisch, Kurzfassungen zweisprachig), 1988, ISBN 3-921694-71-X

72 Soyeaux, Renald: *Unterströmung von Stauanlagen auf klüftigem Untergrund unter Berücksichtigung laminarer und turbulenter Fließzustände*,1991, ISBN 3-921694-72-8

73 Kohane, Roberto: *Berechnungsmethoden für Hochwasserabfluß in Fließgewässern mit überströmten Vorländern*, 1991, ISBN 3-921694-73-6

74 Hassinger, Reinhard: *Beitrag zur Hydraulik und Bemessung von Blocksteinrampen in flexibler Bauweise*, 1991, ISBN 3-921694-74-4, *vergriffen*

75 Schäfer, Gerhard: *Einfluß von Schichtenstrukturen und lokalen Einlagerungen auf die Längsdispersion in Porengrundwasserleitern*, 1991, ISBN 3-921694-75-2

76 Giesecke, Jürgen: *Vorträge, Wasserwirtschaft in stark besiedelten Regionen; Umweltforschung mit Schwerpunkt Wasserwirtschaft*, 1991, ISBN 3-921694-76-0

77 Huwe, Bernd: *Deterministische und stochastische Ansätze zur Modellierung des Stickstoffhaushalts landwirtschaftlich genutzter Flächen auf unterschiedlichem Skalenniveau*, 1992, ISBN 3-921694-77-9, *vergriffen*

78 Rommel, Michael: *Verwendung von Kluftdaten zur realitätsnahen Generierung von Kluftnetzen mit anschließender laminar-turbulenter Strömungsberechnung*, 1993, ISBN 3-92 1694-78-7

79 Marschall, Paul: *Die Ermittlung lokaler Stofffrachten im Grundwasser mit Hilfe von Einbohrloch-Meßverfahren*, 1993, ISBN 3-921694-79-5, *vergriffen*

80 Ptak, Thomas: *Stofftransport in heterogenen Porenaquiferen: Felduntersuchungen und stochastische Modellierung*, 1993, ISBN 3-921694-80-9, *vergriffen*

81 Haakh, Frieder: *Transientes Strömungsverhalten in Wirbelkammern,* 1993, ISBN 3-921694-81-7

82 Kobus, Helmut; Cirpka, Olaf; Barczewski, Baldur; Koschitzky, Hans-Peter: *Versuchseinrichtung zur Grundwasser- und Altlastensanierung VEGAS, Konzeption und Programmrahmen*, 1993, ISBN 3-921694-82-5

83 Zang, Weidong: *Optimaler Echtzeit-Betrieb eines Speichers mit aktueller Abflußregenerierung*, 1994, ISBN 3-921694-83-3, *vergriffen*

84 Franke, Hans-Jörg: *Stochastische Modellierung eines flächenhaften Stoffeintrages und Transports in Grundwasser am Beispiel der Pflanzenschutzmittelproblematik*, 1995, ISBN 3-921694-84-1

85 Lang, Ulrich: *Simulation regionaler Strömungs- und Transportvorgänge in Karstaquiferen mit Hilfe des Doppelkontinuum-Ansatzes: Methodenentwicklung und Parameteridenti-fikation*, 1995, ISBN 3-921694-85-X, *vergriffen*

86 Helmig, Rainer: *Einführung in die Numerischen Methoden der Hydromechanik*, 1996, ISBN 3-921694-86-8, *vergriffen*

87 Cirpka, Olaf: *CONTRACT: A Numerical Tool for Contaminant Transport and Chemical Transformations - Theory and Program Documentation -*, 1996, ISBN 3-921694-87-6

88 Haberlandt, Uwe: *Stochastische Synthese und Regionalisierung des Niederschlages für Schmutzfrachtberechnungen*, 1996, ISBN 3-921694-88-4

89 Croisé, Jean: *Extraktion von flüchtigen Chemikalien aus natürlichen Lockergesteinen mittels erzwungener Luftströmung*, 1996, ISBN 3-921694-89-2, *vergriffen*

90 Jorde, Klaus: *Ökologisch begründete, dynamische Mindestwasserregelungen bei Ausleitungskraftwerken*, 1997, ISBN 3-921694-90-6, vergriffen

91 Helmig, Rainer: *Gekoppelte Strömungs- und Transportprozesse im Untergrund - Ein Beitrag zur Hydrosystemmodellierung-*, 1998, ISBN 3-921694-91-4, vergriffen

92 Emmert, Martin: *Numerische Modellierung nichtisothermer Gas-Wasser Systeme in porösen Medien,* 1997, ISBN 3-921694-92-2

93 Kern, Ulrich: *Transport von Schweb- und Schadstoffen in staugeregelten Fließgewässern am Beispiel des Neckars*, 1997, ISBN 3-921694-93-0, vergriffen

94 Förster, Georg: *Druckstoßdämpfung durch große Luftblasen in Hochpunkten von Rohrleitungen 1997*, ISBN 3-921694-94-9

95 Cirpka, Olaf: *Numerische Methoden zur Simulation des reaktiven Mehrkomponententransports im Grundwasser*, 1997, ISBN 3-921694-95-7, vergriffen

96 Färber, Arne: *Wärmetransport in der ungesättigten Bodenzone: Entwicklung einer thermischen In-situ-Sanierungstechnologie*, 1997, ISBN 3-921694-96-5

97 Betz, Christoph: *Wasserdampfdestillation von Schadstoffen im porösen Medium: Entwicklung einer thermischen In-situ-Sanierungstechnologie*, 1998, SBN 3-921694-97-3

98 Xu, Yichun: *Numerical Modeling of Suspended Sediment Transport in Rivers*, 1998, ISBN 3-921694-98-1, vergriffen

99 Wüst, Wolfgang: *Geochemische Untersuchungen zur Sanierung CKW-kontaminierter Aquifere mit Fe(0)-Reaktionswänden,* 2000, ISBN 3-933761-02-2

100 Sheta, Hussam: *Simulation von Mehrphasenvorgängen in porösen Medien unter Einbeziehung von Hysterese-Effekten*, 2000, ISBN 3-933761-03-4

101 Ayros, Edwin: *Regionalisierung extremer Abflüsse auf der Grundlage statistischer Verfahren*, 2000, ISBN 3-933761-04-2, vergriffen

102 Huber, Ralf: *Compositional Multiphase Flow and Transport in Heterogeneous Porous Media*, 2000, ISBN 3-933761-05-0

103 Braun, Christopherus: *Ein Upscaling-Verfahren für Mehrphasenströmungen in porösen Medien*, 2000, ISBN 3-933761-06-9

104 Hofmann, Bernd: *Entwicklung eines rechnergestützten Managementsystems zur Beurteilung von Grundwasserschadensfällen*, 2000, ISBN 3-933761-07-7

105 Class, Holger: *Theorie und numerische Modellierung nichtisothermer Mehrphasenprozesse in NAPL-kontaminierten porösen Medien,* 2001, ISBN 3-933761-08-5

106 Schmidt, Reinhard: *Wasserdampf- und Heißluftinjektion zur thermischen Sanierung kontaminierter Standorte*, 2001, ISBN 3-933761-09-3

107 Josef, Reinhold: *Schadstoffextraktion mit hydraulischen Sanierungsverfahren unter Anwendung von grenzflächenaktiven Stoffen*, 2001, ISBN 3-933761-10-7

108 Schneider, Matthias: *Habitat- und Abflussmodellierung für Fließgewässer mit unscharfen Berechnungsansätzen*, 2001, ISBN 3-933761-11-5

109 Rathgeb, Andreas: *Hydrodynamische Bemessungsgrundlagen für Lockerdeckwerke an überströmbaren Erddämmen*, 2001, ISBN 3-933761-12-3

110 Lang, Stefan: *Parallele numerische Simulation instätionärer Probleme mit adaptiven Methoden auf unstrukturierten Gittern*, 2001, ISBN 3-933761-13-1

111 Appt, Jochen; Stumpp Simone: *Die Bodensee-Messkampagne 2001, IWS/CWR Lake Constance Measurement Program 2001*, 2002, ISBN 3-933761-14-X

112 Heimerl, Stephan: *Systematische Beurteilung von Wasserkraftprojekten,* 2002, ISBN 3-933761-15-8, vergriffen

113 Iqbal, Amin: *On the Management and Salinity Control of Drip Irrigation,* 2002, ISBN 3-933761-16-6

114 Silberhorn-Hemminger, Annette: *Modellierung von Kluftaquifersystemen: Geostatistische Analyse und deterministisch-stochastische Kluftgenerierung,* 2002, ISBN 3-933761-17-4

115 Winkler, Angela: *Prozesse des Wärme- und Stofftransports bei der In-situ-Sanierung mit festen Wärmequellen,* 2003, ISBN 3-933761-18-2

116 Marx, Walter: *Wasserkraft, Bewässerung, Umwelt - Planungs- und Bewertungsschwerpunkte der Wasserbewirtschaftung,* 2003, ISBN 3-933761-19-0

117 Hinkelmann, Reinhard: *Efficient Numerical Methods and Information-Processing Techniques in Environment Water,* 2003, ISBN 3-933761-20-4

118 Samaniego-Eguiguren, Luis Eduardo: *Hydrological Consequences of Land Use / Land Cover and Climatic Changes in Mesoscale Catchments*, 2003, ISBN 3-933761-21-2

119 Neunhäuserer, Lina: *Diskretisierungsansätze zur Modellierung von Strömungs- und Transportprozessen in geklüftet-porösen Medien*, 2003, ISBN 3-933761-22-0

120 Paul, Maren: *Simulation of Two-Phase Flow in Heterogeneous Poros Media with Adaptive Methods*, 2003, ISBN 3-933761-23-9

121 Ehret, Uwe: *Rainfall and Flood Nowcasting in Small Catchments using Weather Radar*, 2003, ISBN 3-933761-24-7

122 Haag, Ingo: *Der Sauerstoffhaushalt staugeregelter Flüsse am Beispiel des Neckars - Analysen, Experimente, Simulationen -,* 2003, ISBN 3-933761-25-5

123 Appt, Jochen: *Analysis of Basin-Scale Internal Waves in Upper Lake Constance,* 2003, ISBN 3-933761-26-3

124 Hrsg.: Schrenk, Volker; Batereau, Katrin; Barczewski, Baldur; Weber, Karolin und Koschitzky, Hans-Peter: *Symposium Ressource Fläche und VEGAS - Statuskolloquium 2003, 30. September und 1. Oktober 2003,* 2003, ISBN 3-933761-27-1

125 Omar Khalil Ouda: *Optimisation of Agricultural Water Use: A Decision Support System for the Gaza Strip,* 2003, ISBN 3-933761-28-0

126 Batereau, Katrin: *Sensorbasierte Bodenluftmessung zur Vor-Ort-Erkundung von Schadensherden im Untergrund*, 2004, ISBN 3-933761-29-8

127 Witt, Oliver: *Erosionsstabilität von Gewässersedimenten mit Auswirkung auf den Stofftransport bei Hochwasser am Beispiel ausgewählter Stauhaltungen des Oberrheins*, 2004, ISBN 3-933761-30-1

128 Jakobs, Hartmut: *Simulation nicht-isothermer Gas-Wasser-Prozesse in komplexen Kluft-Matrix-Systemen*, 2004, ISBN 3-933761-31-X

129 Li, Chen-Chien: *Deterministisch-stochastisches Berechnungskonzept zur Beurteilung der Auswirkungen erosiver Hochwasserereignisse in Flussstauhaltungen,* 2004, ISBN 3-933761-32-8

130 Reichenberger, Volker; Helmig, Rainer; Jakobs, Hartmut; Bastian, Peter; Niessner, Jennifer: *Complex Gas-Water Processes in Discrete Fracture-Matrix Systems: Up-scaling, Mass-Conservative Discretization and Efficient Multilevel Solution,* 2004, ISBN 3-933761-33-6

131 Hrsg.: Barczewski, Baldur; Koschitzky, Hans-Peter; Weber, Karolin; Wege, Ralf: *VEGAS - Statuskolloquium 2004,* Tagungsband zur Veranstaltung am 05. Oktober 2004 an der Universität Stuttgart, Campus Stuttgart-Vaihingen, 2004, ISBN 3-933761-34-4

132 Asie, Kemal Jabir: *Finite Volume Models for Multiphase Multicomponent Flow through Porous Media*. 2005, ISBN 3-933761-35-2

133 Jacoub, George: *Development of a 2-D Numerical Module for Particulate Contaminant Transport in Flood Retention Reservoirs and Impounded Rivers,* 2004, ISBN 3-933761-36-0

134 Nowak, Wolfgang: *Geostatistical Methods for the Identification of Flow and Transport Parameters in the Subsurface,* 2005, ISBN 3-933761-37-9

135 Süß, Mia: *Analysis of the influence of structures and boundaries on flow and transport processes in fractured porous media*, 2005, ISBN 3-933761-38-7

136 Jose, Surabhin Chackiath: *Experimental Investigations on Longitudinal Dispersive Mixing in Heterogeneous Aquifers,* 2005, ISBN: 3-933761-39-5

137 Filiz, Fulya: *Linking Large-Scale Meteorological Conditions to Floods in Mesoscale Catchments,* 2005, ISBN 3-933761-40-9

138 Qin, Minghao: *Wirklichkeitsnahe und recheneffiziente Ermittlung von Temperatur und Spannungen bei großen RCC-Staumauern*, 2005, ISBN 3-933761-41-7

139 Kobayashi, Kenichiro: *Optimization Methods for Multiphase Systems in the Subsurface - Application to Methane Migration in Coal Mining Areas*, 2005, ISBN 3-933761-42-5

140 Rahman, Md. Arifur: *Experimental Investigations on Transverse Dispersive Mixing in Heterogeneous Porous Media,* 2005, ISBN 3-933761-43-3

141 Schrenk, Volker: *Ökobilanzen zur Bewertung von Altlastensanierungsmaßnahmen,* 2005, ISBN 3-933761-44-1

142 Hundecha, Hirpa Yeshewatesfa: *Regionalization of Parameters of a Conceptual Rainfall-Runoff Model*, 2005, ISBN: 3-933761-45-X

143 Wege, Ralf: *Untersuchungs- und Überwachungsmethoden für die Beurteilung natürlicher Selbstreinigungsprozesse im Grundwasser,* 2005, ISBN 3-933761-46-8

144 Breiting, Thomas: *Techniken und Methoden der Hydroinformatik - Modellierung von komplexen Hydrosystemen im Untergrund*, 2006, ISBN 3-933761-47-6

145 Hrsg.: Braun, Jürgen; Koschitzky, Hans-Peter; Müller, Martin: *Ressource Untergrund: 10 Jahre VEGAS: Forschung und Technologieentwicklung zum Schutz von Grundwasser und Boden,* Tagungsband zur Veranstaltung am 28. und 29. September 2005 an der Universität Stuttgart, Campus Stuttgart-Vaihingen, 2005, ISBN 3-933761-48-4

146 Rojanschi, Vlad: *Abflusskonzentration in mesoskaligen Einzugsgebieten unter Berücksichtigung des Sickerraumes,* 2006, ISBN 3-933761-49-2

147 Winkler, Nina Simone: *Optimierung der Steuerung von Hochwasserrückhaltebeckensystemen,* 2006, ISBN 3-933761-50-6

148 Wolf, Jens: *Räumlich differenzierte Modellierung der Grundwasserströmung alluvialer Aquifere für mesoskalige Einzugsgebiete*, 2006, ISBN: 3-933761-51-4

149 Kohler, Beate: *Externe Effekte der Laufwasserkraftnutzung*, 2006, ISBN 3-933761-52-2

150 Hrsg.: Braun, Jürgen; Koschitzky, Hans-Peter; Stuhrmann, Matthias: *VEGAS-Statuskolloquium 2006,* Tagungsband zur Veranstaltung am 28. September 2006 an der Universität Stuttgart, Campus Stuttgart-Vaihingen, 2006, ISBN 3-933761-53-0

151 Niessner, Jennifer: *Multi-Scale Modeling of Multi-Phase - Multi-Component Processes in Heterogeneous Porous Media*, 2006, ISBN 3-933761-54-9

152 Fischer, Markus: *Beanspruchung eingeerdeter Rohrleitungen infolge Austrocknung bindiger Böden,* 2006, ISBN 3-933761-55-7

153 Schneck, Alexander: *Optimierung der Grundwasserbewirtschaftung unter Berücksichtigung der Belange der Wasserversorgung, der Landwirtschaft und des Naturschutzes*, 2006, ISBN 3-933761-56-5

154 Das, Tapash: *The Impact of Spatial Variability of Precipitation on the Predictive Uncertainty of Hydrological Models,* 2006, ISBN 3-33761-57-3

155 Bielinski, Andreas: *Numerical Simulation of CO_2 sequestration in geological formations*, 2007, ISBN 3-933761-58-1

156 Mödinger, Jens: *Entwicklung eines Bewertungs- und Entscheidungsunterstützungssystems für eine nachhaltige regionale Grundwasserbewirtschaftung*, 2006, ISBN 3-933761-60-3

157 Manthey, Sabine: *Two-phase flow processes with dynamic effects in porous media - parameter estimation and simulation,* 2007, ISBN 3-933761-61-1

158 Pozos Estrada, Oscar: *Investigation on the Effects of Entrained Air in Pipelines,* 2007, ISBN 3-933761-62-X

159 Ochs, Steffen Oliver: *Steam injection into saturated porous media – process analysis including experimental and numerical investigations*, 2007, ISBN 3-933761-63-8

160 Marx, Andreas: *Einsatz gekoppelter Modelle und Wetterradar zur Abschätzung von Niederschlagsintensitäten und zur Abflussvorhersage, 2007,* ISBN 3-933761-64-6

161 Hartmann, Gabriele Maria: *Investigation of Evapotranspiration Concepts in Hydrological Modelling for Climate Change Impact Assessment*, 2007, ISBN 3-933761-65-4

162 Kebede Gurmessa, Tesfaye: *Numerical Investigation on Flow and Transport Characteristics to Improve Long-Term Simulation of Reservoir Sedimentation*, 2007, ISBN 3-933761-66-2

163 Trifković, Aleksandar: *Multi-objective and Risk-based Modelling Methodology for Planning, Design and Operation of Water Supply Systems*, 2007, ISBN 3-933761-67-0

164 Götzinger, Jens: *Distributed Conceptual Hydrological Modelling - Simulation of Climate, Land Use Change Impact and Uncertainty Analysis*, 2007, ISBN 3-933761-68-9

165 Hrsg.: Braun, Jürgen; Koschitzky, Hans-Peter; Stuhrmann, Matthias: *VEGAS – Kolloquium 2007,* Tagungsband zur Veranstaltung am 26. September 2007 an der Universität Stuttgart, Campus Stuttgart-Vaihingen, 2007, ISBN 3-933761-69-7

166 Freeman, Beau: *Modernization Criteria Assessment for Water Resources Planning; Klamath Irrigation Project, U.S.*, 2008, ISBN 3-933761-70-0

167 Dreher, Thomas: *Selektive Sedimentation von Feinstschwebstoffen in Wechselwirkung mit wandnahen turbulenten Strömungsbedingungen*, 2008, ISBN 3-933761-71-9

168 Yang, Wei: *Discrete-Continuous Downscaling Model for Generating Daily Precipitation Time Series*, 2008, ISBN 3-933761-72-7

169 Kopecki, Ianina: *Calculational Approach to FST-Hemispheres for Multiparametrical Benthos Habitat Modelling,* 2008*,* ISBN 3-933761-73-5

170 Brommundt, Jürgen: *Stochastische Generierung räumlich zusammenhängender Niederschlagszeitreihen*, 2008, ISBN 3-933761-74-3

171 Papafotiou, *Alexandros: Numerical Investigations of the Role of Hysteresis in Heterogeneous Two-Phase Flow Systems*, 2008, ISBN 3-933761-75-1

172 He, Yi: *Application of a Non-Parametric Classification Scheme to Catchment Hydrology*, 2008, ISBN 978-3-933761-76-7

173 Wagner, Sven: *Water Balance in a Poorly Gauged Basin in West Africa Using Atmospheric Modelling and Remote Sensing Information*, 2008, ISBN 978-3-933761-77-4

174 Hrsg.: Braun, Jürgen; Koschitzky, Hans-Peter; Stuhrmann, Matthias; Schrenk, Volker: *VEGAS-Kolloquium 2008 Ressource Fläche III*, Tagungsband zur Veranstaltung am 01. Oktober 2008 an der Universität Stuttgart, Campus Stuttgart-Vaihingen, 2008, ISBN 978-3-933761-78-1

175 Patil, Sachin: *Regionalization of an Event Based Nash Cascade Model for Flood Predictions in Ungauged Basins*, 2008, ISBN 978-3-933761-79-8

176 Assteerawatt, Anongnart: *Flow and Transport Modelling of Fractured Aquifers based on a Geostatistical Approach,* 2008, ISBN 978-3-933761-80-4

177 Karnahl, Joachim Alexander: *2D numerische Modellierung von multifraktionalem Schwebstoff- und Schadstofftransport in Flüssen*, 2008, ISBN 978-3-933761-81-1

178 Hiester, Uwe: *Technologieentwicklung zur In-situ-Sanierung der ungesättigten Bodenzone mit festen Wärmequellen,* 2009, ISBN 978-3-933761-82-8

179 Laux, Patrick: *Statistical Modeling of Precipitation for Agricultural Planning in the Volta Basin of West Africa,* 2009, ISBN 978-3-933761-83-5

180 Ehsan, Saqib: *Evaluation of Life Safety Risks Related to Severe Flooding,* 2009, ISBN 978-3-933761-84-2

181 Prohaska, Sandra: *Development and Application of a 1D Multi-Strip Fine Sediment Transport Model for Regulated Rivers,* 2009, ISBN 978-3-933761-85-9

182 Kopp, Andreas: *Evaluation of CO_2 Injection Processes in Geological Formations for Site Screening,* 2009, ISBN 978-3-933761-86-6

183 Ebigbo, Anozie: *Modelling of biofilm growth and its influence on CO_2 and water (two-phase) flow in porous media,* 2009, ISBN 978-3-933761-87-3

184 Freiboth, Sandra: *A phenomenological model for the numerical simulation of multiphase multicomponent processes considering structural alterations of porous media*, 2009, ISBN 978-3-933761-88-0

185 Zöllner, Frank: *Implementierung und Anwendung netzfreier Methoden im Konstruktiven Wasserbau und in der Hydromechanik*, 2009, ISBN 978-3-933761-89-7

186 Vasin, Milos: *Influence of the soil structure and property contrast on flow and transport in the unsaturated zone*, 2010, ISBN 978-3-933761-90-3

187 Li, Jing: *Application of Copulas as a New Geostatistical Tool*, 2010, ISBN 978-3-933761-91-0

188 AghaKouchak, Amir: *Simulation of Remotely Sensed Rainfall Fields Using Copulas*, 2010, ISBN 978-3-933761-92-7

189 Thapa, Pawan Kumar: *Physically-based spatially distributed rainfall runoff modelling for soil erosion estimation*, 2010, ISBN 978-3-933761-93-4

190 Wurms, Sven: *Numerische Modellierung der Sedimentationsprozesse in Retentionsanlagen zur Steuerung von Stoffströmen bei extremen Hochwasserabflussereignissen*, 2011, ISBN 978-3-933761-94-1

191 Merkel, Uwe: *Unsicherheitsanalyse hydraulischer Einwirkungen auf Hochwasserschutzdeiche und Steigerung der Leistungsfähigkeit durch adaptive Strömungsmodellierung*, 2011, ISBN 978-3-933761-95-8

192 Fritz, Jochen: *A Decoupled Model for Compositional Non-Isothermal Multiphase Flow in Porous Media and Multiphysics Approaches for Two-Phase Flow*, 2010, ISBN 978-3-933761-96-5

193 Weber, Karolin (Hrsg.): *12. Treffen junger WissenschaftlerInnen an Wasserbauinstituten*, 2010, ISBN 978-3-933761-97-2

194 Bliefernicht, Jan-Geert: *Probability Forecasts of Daily Areal Precipitation for Small River Basins,* 2011, ISBN 978-3-933761-98-9

195 Hrsg.: Koschitzky, Hans-Peter; Braun, Jürgen: *VEGAS-Kolloquium 2010 In-situ-Sanierung - Stand und Entwicklung Nano und ISCO -,* Tagungsband zur Veranstaltung am 07. Oktober 2010 an der Universität Stuttgart, Campus Stuttgart-Vaihingen*,* 2010*,* ISBN 978-3-933761-99-6

196 Gafurov, Abror: *Water Balance Modeling Using Remote Sensing Information - Focus on Central Asia,* 2010, ISBN 978-3-942036-00-9

197 Mackenberg, Sylvia: *Die Quellstärke in der Sickerwasserprognose: Möglichkeiten und Grenzen von Labor- und Freilanduntersuchungen,* 2010, ISBN 978-3-942036-01-6

198 Singh, Shailesh Kumar: *Robust Parameter Estimation in Gauged and Ungauged Basins,* 2010, ISBN 978-3-942036-02-3

199 Doğan, Mehmet Onur: *Coupling of porous media flow with pipe flow,* 2011, ISBN 978-3-942036-03-0

200 Liu, Min: *Study of Topographic Effects on Hydrological Patterns and the Implication on Hydrological Modeling and Data Interpolation,* 2011, ISBN 978-3-942036-04-7

201 Geleta, Habtamu Itefa: *Watershed Sediment Yield Modeling for Data Scarce Areas,* 2011, ISBN 978-3-942036-05-4

202 Franke, Jörg: *Einfluss der Überwachung auf die Versagenswahrscheinlichkeit von Staustufen,* 2011, ISBN 978-3-942036-06-1

203 Bakimchandra, Oinam: *Integrated Fuzzy-GIS approach for assessing regional soil erosion risks,* 2011, ISBN 978-3-942036-07-8

204 Alam, Muhammad Mahboob: *Statistical Downscaling of Extremes of Precipitation in Mesoscale Catchments from Different RCMs and Their Effects on Local Hydrology,* 2011, ISBN 978-3-942036-08-5

205 Hrsg.: Koschitzky, Hans-Peter; Braun, Jürgen: *VEGAS-Kolloquium 2011 Flache Geothermie - Perspektiven und Risiken,* Tagungsband zur Veranstaltung am 06. Oktober 2011 an der Universität Stuttgart, Campus Stuttgart-Vaihingen*,* 2011*,* ISBN 978-3-933761-09-2

206 Haslauer, Claus: *Analysis of Real-World Spatial Dependence of Subsurface Hydraulic Properties Using Copulas with a Focus on Solute Transport Behaviour,* 2011, ISBN 978-3-942036-10-8

207 Dung, Nguyen Viet: *Multi-objective automatic calibration of hydrodynamic models – development of the concept and an application in the Mekong Delta,* 2011, ISBN 978-3-942036-11-5

208 Hung, Nguyen Nghia: *Sediment dynamics in the floodplain of the Mekong Delta, Vietnam,* 2011, ISBN 978-3-942036-12-2

209 Kuhlmann, Anna: *Influence of soil structure and root water uptake on flow in the unsaturated zone,* 2012, ISBN 978-3-942036-13-9

210 Tuhtan, Jeffrey Andrew: *Including the Second Law Inequality in Aquatic Ecodynamics: A Modeling Approach for Alpine Rivers Impacted by Hydropeaking,* 2012, ISBN 978-3-942036-14-6

211 Tolossa, Habtamu: *Sediment Transport Computation Using a Data-Driven Adaptive Neuro-Fuzzy Modelling Approach,* 2012, ISBN 978-3-942036-15-3

212 Tatomir, Alexandru-Bodgan: *From Discrete to Continuum Concepts of Flow in Fractured Porous Media,* 2012, ISBN 978-3-942036-16-0

213 Erbertseder, Karin: *A Multi-Scale Model for Describing Cancer-Therapeutic Transport in the Human Lung,* 2012, ISBN 978-3-942036-17-7

214 Noack, Markus: *Modelling Approach for Interstitial Sediment Dynamics and Reproduction of Gravel Spawning Fish,* 2012, ISBN 978-3-942036-18-4

215 De Boer, Cjestmir Volkert: *Transport of Nano Sized Zero Valent Iron Colloids during Injection into the Subsurface*, 2012, ISBN 978-3-942036-19-1

216 Pfaff, Thomas: *Processing and Analysis of Weather Radar Data for Use in Hydrology*, 2013, ISBN 978-3-942036-20-7

217 Lebrenz, Hans-Henning: *Addressing the Input Uncertainty for Hydrological Modeling by a New Geostatistical Method*, 2013, ISBN 978-3-942036-21-4

218 Darcis, Melanie Yvonne: *Coupling Models of Different Complexity for the Simulation of CO_2 Storage in Deep Saline Aquifers*, 2013, ISBN 978-3-942036-22-1

219 Beck, Ferdinand: *Generation of Spatially Correlated Synthetic Rainfall Time Series in High Temporal Resolution - A Data Driven Approach*, 2013, ISBN 978-3-942036-23-8

220 Guthke, Philipp: *Non-multi-Gaussian spatial structures: Process-driven natural genesis, manifestation, modeling approaches, and influences on dependent processes*, 2013, ISBN 978-3-942036-24-5

221 Walter, Lena: *Uncertainty studies and risk assessment for CO_2 storage in geological formations*, 2013, ISBN 978-3-942036-25-2

222 Wolff, Markus: *Multi-scale modeling of two-phase flow in porous media including capillary pressure effects,* 2013, ISBN 978-3-942036-26-9

223 Mosthaf, Klaus Roland: *Modeling and analysis of coupled porous-medium and free flow with application to evaporation processes,* 2014, ISBN 978-3-942036-27-6

224 Leube, Philipp Christoph: *Methods for Physically-Based Model Reduction in Time: Analysis, Comparison of Methods and Application*, 2013, ISBN 978-3-942036-28-3

225 Rodríguez Fernández, Jhan Ignacio: *High Order Interactions among environmental variables: Diagnostics and initial steps towards modeling*, 2013, ISBN 978-3-942036-29-0

226 Eder, Maria Magdalena: *Climate Sensitivity of a Large Lake*, 2013, ISBN 978-3-942036-30-6

227 Greiner, Philipp: *Alkoholinjektion zur In-situ-Sanierung von CKW Schadensherden in Grundwasserleitern: Charakterisierung der relevanten Prozesse auf unterschiedlichen Skalen*, 2014, ISBN 978-3-942036-31-3

228 Lauser, Andreas: *Theory and Numerical Applications of Compositional Multi-Phase Flow in Porous Media*, 2014, ISBN 978-3-942036-32-0

229 Enzenhöfer, Rainer: *Risk Quantification and Management in Water Production and Supply Systems*, 2014, ISBN 978-3-942036-33-7

230 Faigle, Benjamin: *Adaptive modelling of compositional multi-phase flow with capillary pressure*, 2014, ISBN 978-3-942036-34-4

231 Oladyshkin, Sergey: *Efficient modeling of environmental systems in the face of complexity and uncertainty*, 2014, ISBN 978-3-942036-35-1

232 Sugimoto, Takayuki: *Copula based Stochastic Analysis of Discharge Time Series*, 2014, ISBN 978-3-942036-36-8

233 Koch, Jonas: *Simulation, Identification and Characterization of Contaminant Source Architectures in the Subsurface*, 2014, ISBN 978-3-942036-37-5

234 Zhang, Jin: *Investigations on Urban River Regulation and Ecological Rehabilitation Measures, Case of Shenzhen in China*, 2014, ISBN 978-3-942036-38-2

235 Siebel, Rüdiger: *Experimentelle Untersuchungen zur hydrodynamischen Belastung und Standsicherheit von Deckwerken an überströmbaren Erddämmen,* 2014, ISBN 978-3-942036-39-9

236 Baber, Katherina: *Coupling free flow and flow in porous media in biological and technical applications: From a simple to a complex interface description,* 2014, ISBN 978-3-942036-40-5

237 Nuske, Klaus Philipp: *Beyond Local Equilibrium — Relaxing local equilibrium assumptions in multiphase flow in porous media,* 2014, ISBN 978-3-942036-41-2

238 Geiges, Andreas: *Efficient concepts for optimal experimental design in nonlinear environmental systems*, 2014, ISBN 978-3-942036-42-9

239 Schwenck, Nicolas: *An XFEM-Based Model for Fluid Flow in Fractured Porous Media*, 2014, ISBN 978-3-942036-43-6

240 Chamorro Chávez, Alejandro: *Stochastic and hydrological modelling for climate change prediction in the Lima region, Peru*, 2015, ISBN 978-3-942036-44-3

241 Yulizar: *Investigation of Changes in Hydro-Meteorological Time Series Using a Depth-Based Approach*, 2015, ISBN 978-3-942036-45-0

242 Kretschmer, Nicole: *Impacts of the existing water allocation scheme on the Limarí watershed – Chile, an integrative approach*, 2015, ISBN 978-3-942036-46-7

243 Kramer, Matthias: *Luftbedarf von Freistrahlturbinen im Gegendruckbetrieb*, 2015, ISBN 978-3-942036-47-4

244 Hommel, Johannes: *Modeling biogeochemical and mass transport processes in the subsurface: Investigation of microbially induced calcite precipitation*, 2016, ISBN 978-3-942036-48-1

245 Germer, Kai: *Wasserinfiltration in die ungesättigte Zone eines makroporösen Hanges und deren Einfluss auf die Hangstabilität*, 2016, ISBN 978-3-942036-49-8

246 Hörning, Sebastian: *Process-oriented modeling of spatial random fields using copulas*, 2016, ISBN 978-3-942036-50-4

247 Jambhekar, Vishal: *Numerical modeling and analysis of evaporative salinization in a coupled free-flow porous-media system,* 2016, ISBN 978-3-942036-51-1

248 Huang, Yingchun: *Study on the spatial and temporal transferability of conceptual hydrological models*, 2016, ISBN 978-3-942036-52-8

249 Kleinknecht, Simon Matthias: *Migration and retention of a heavy NAPL vapor and remediation of the unsaturated zone*, 2016, ISBN 978-3-942036-53-5

250 Kwakye, Stephen Oppong: *Study on the effects of climate change on the hydrology of the West African sub-region*, 2016, ISBN 978-3-942036-54-2

251 Kissinger, Alexander: *Basin-Scale Site Screening and Investigation of Possible Impacts of CO_2 Storage on Subsurface Hydrosystems*, 2016, ISBN 978-3-942036-55-9

252 Müller, Thomas: *Generation of a Realistic Temporal Structure of Synthetic Precipitation Time Series for Sewer Applications*, 2017, ISBN 978-3-942036-56-6

253 Grüninger, Christoph: *Numerical Coupling of Navier-Stokes and Darcy Flow for Soil-Water Evaporation*, 2017, ISBN 978-3-942036-57-3

254 Suroso: *Asymmetric Dependence Based Spatial Copula Models: Empirical Investigations and Consequences on Precipitation Fields*, 2017, ISBN 978-3-942036-58-0

255 Müller, Thomas; Mosthaf, Tobias; Gunzenhauser, Sarah; Seidel, Jochen; Bárdossy, András: *Grundlagenbericht Niederschlags-Simulator (NiedSim3)*, 2017, ISBN 978-3-942036-59-7

256 Mosthaf, Tobias: *New Concepts for Regionalizing Temporal Distributions of Precipitation and for its Application in Spatial Rainfall Simulation,* 2017, ISBN 978-3-942036-60-3

257 Fenrich, Eva Katrin: *Entwicklung eines ökologisch-ökonomischen Vernetzungsmodells für Wasserkraftanlagen und Mehrzweckspeicher,* 2018, ISBN 978-3-942036-61-0

258 Schmidt, Holger: *Microbial stabilization of lotic fine sediments*, 2018, ISBN 978-3-942036-62-7

259 Fetzer, Thomas: *Coupled Free and Porous-Medium Flow Processes Affected by Turbulence and Roughness – Models, Concepts and Analysis*, 2018, ISBN 978-3-942036-63-4

260 Schröder, Hans Christoph: *Large-scale High Head Pico Hydropower Potential Assessment*, 2018, ISBN 978-3-942036-64-1

261 Bode, Felix: *Early-Warning Monitoring Systems for Improved Drinking Water Resource Protection*, 2018, ISBN 978-3-942036-65-8

262 Gebler, Tobias: *Statistische Auswertung von simulierten Talsperrenüberwachungsdaten zur Identifikation von Schadensprozessen an Gewichtsstaumauern*, 2018, ISBN 978-3-942036-66-5

263 Harten, Matthias von: *Analyse des Zuppinger-Wasserrades – Hydraulische Optimierungen unter Berücksichtigung ökologischer Aspekte*, 2018, ISBN 978-3-942036-67-2

264 Yan, Jieru: *Nonlinear estimation of short time precipitation using weather radar and surface observations*, 2018, ISBN 978-3-942036-68-9

265 Beck, Martin: *Conceptual approaches for the analysis of coupled hydraulic and geomechanical processes*, 2019, ISBN 978-3-942036-69-6

266 Haas, Jannik: *Optimal planning of hydropower and energy storage technologies for fully renewable power systems*, 2019, ISBN 978-3-942036-70-2

267 Schneider, Martin: *Nonlinear Finite Volume Schemes for Complex Flow Processes and Challenging Grids*, 2019, ISBN 978-3-942036-71-9

268 Most, Sebastian Christopher: *Analysis and Simulation of Anomalous Transport in Porous Media*, 2019, ISBN 978-3-942036-72-6

269 Buchta, Rocco: *Entwicklung eines Ziel- und Bewertungssystems zur Schaffung nachhaltiger naturnaher Strukturen in großen sandgeprägten Flüssen des norddeutschen Tieflandes*, 2019, ISBN 978-3-942036-73-3

270 Thom, Moritz: *Towards a Better Understanding of the Biostabilization Mechanisms of Sediment Beds*, 2019, ISBN 978-3-942036-74-0

271 Stolz, Daniel: *Die Nullspannungstemperatur in Gewichtsstaumauern unter Berücksichtigung der Festigkeitsentwicklung des Betons*, 2019, ISBN 978-3-942036-75-7

272 Rodriguez Pretelin, Abelardo: *Integrating transient flow conditions into groundwater well protection*, 2020, ISBN: 978-3-942036-76-4

273 Weishaupt, Kilian: *Model Concepts for Coupling Free Flow with Porous Medium Flow at the Pore-Network Scale: From Single-Phase Flow to Compositional Non-Isothermal Two-Phase Flow*, 2020, ISBN: 978-3-942036-77-1

274 Koch, Timo: *Mixed-dimension models for flow and transport processes in porous media with embedded tubular network systems*, 2020, ISBN: 978-3-942036-78-8

275 Gläser, Dennis: *Discrete fracture modeling of multi-phase flow and deformation in fractured poroelastic media*, 2020, ISBN: 978-3-942036-79-5

276 Seitz, Lydia: *Development of new methods to apply a multi-parameter approach – A first step towards the determination of colmation*, 2020, ISBN: 978-3-942036-80-1

277 Ebrahim Bakhshipour, Amin: *Optimizing hybrid decentralized systems for sustainable ur-ban drainage infrastructures planning*, 2021, ISBN: 978-3-942036-81-8

278 Seitz, Gabriele: *Modeling Fixed-Bed Reactors for Thermochemical Heat Storage with the Reaction System CaO/Ca(OH)$_2$*, 2021, ISBN: 978-3-942036-82-5

279 Emmert, Simon: *Developing and Calibrating a Numerical Model for Microbially Enhanced Coal-Bed Methane Production*, 2021, ISBN: 978-3-942036-83-2

280 Heck, Katharina Klara: *Modelling and analysis of multicomponent transport at the interface between free- and porous-medium flow - influenced by radiation and roughness*, 2021, ISBN: 978-3-942036-84-9

281 Ackermann, Sina: *A multi-scale approach for drop/porous-medium interaction*, 2021, ISBN: 978-3-942036-85-6

282 Beckers, Felix: *Investigations on Functional Relationships between Cohesive Sediment Erosion and Sediment Characteristics*, 2021, ISBN: 978-3-942036-86-3

283 Schlabing, Dirk: *Generating Weather for Climate Impact Assessment on Lakes*, 2021, ISBN: 978-3-942036-87-0

284 Becker, Beatrix: *Efficient multiscale multiphysics models accounting for reversible flow at various subsurface energy storage sites*, 2021, ISBN: 978-3-942036-88-7

285 Reuschen, Sebastian: *Bayesian Inversion and Model Selection of Heterogeneities in Geo-statistical Subsurface Modeling*, 2021, ISBN: 978-3-942036-89-4

286 Michalkowski, Cynthia: *Modeling water transport at the interface between porous GDL and gas distributor of a PEM fuel cell cathode*, 2022, ISBN: 978-3-942036-90-0

287 Koca, Kaan: *Advanced experimental methods for investigating flow-biofilm-sediment interactions*, 2022, ISBN: 978-3-942036-91-7

288 Modiri, Ehsan: *Clustering simultaneous occurrences of extreme floods in the Neckar catchment*, 2022, ISBN: 978-3-942036-92-4

289 Mayar, Mohammad Assem: *High-resolution spatio-temporal measurements of the colmation phenomenon under laboratory conditions*, 2022, ISBN: 978-3-942036-93-1

290 Schäfer Rodrigues Silva, Aline: *Quantifying and Visualizing Model Similarities for Multi-Model Methods*, 2022, ISBN: 978-3-942036-94-8

291 Moreno Leiva, Simón: *Optimal planning of water and renewable energy systems for copper production processes with sector coupling and demand flexibility*, 2022, ISBN 978-3-942036-95-5

292 Schönau, Steffen: *Modellierung von Bodenerosion und Sedimentaustrag bei Hochwasserereignissen am Beispiel des Einzugsgebiets der Rems*, 2022, ISBN 978-3-942036-96-2

293 Glatz, Kumiko: *Upscaling of Nanoparticle Transport in Porous Media,* 2022, ISBN 978-3-942036-97-9

294 Pavía Santolamazza, Daniela: *Event-based flood estimation using a random forest algorithm for the regionalization in small catchments,* 2022, ISBN 978-3-942036-98-6

Die Mitteilungshefte ab der Nr. 134 (Jg. 2005) stehen als pdf-Datei über die Homepage des Instituts: www.iws.uni-stuttgart.de zur Verfügung.